Adhesive Joints in Wind Turbine Blades

Jørgensen, Jeppe Bjørn

Link to article, DOI:
10.11581/DTU:00000027

Publication date:
2017

Document Version
Publisher's PDF, also known as Version of record

Adhesive Joints in Wind Turbine Blades

Department of Wind Energy
PhD Report 2017

Jeppe Bjørn Jørgensen

DTU Wind Energy PhD-0079(EN)
DOI number: 10.11581/DTU:00000027

September 2017

DTU Wind Energy
Department of Wind Energy

Prepared by:
Jeppe Bjørn Jørgensen, Industrial PhD student
LM Wind Power, Department of Composites Engineering and Technology
Technical University of Denmark, Department of Wind Energy
Mail:jeppbj@dtu.dk/jbj@lmwindpower.com

Main supervisors:
Bent F. Sørensen, Dr.Techn., Head of Section
Technical University of Denmark
Department of Wind Energy, Section of Composite and Materials Mechanics
Mail:bsqr@dtu.dk

Casper Kildegaard, PhD, Chief Engineer
LM Wind Power
Department of Composites Engineering and Technology
Mail:ck@lmwindpower.com

Technical University of Denmark
DTU Wind Energy
Section of Composite and Materials Mechanics

DTU Risø Campus
Frederiksborgvej 399 Building 228
4000 Roskilde, Denmark
www.vindenergi.dtu.dk

Preface

This thesis was prepared at LM Wind Power (LM) and at the department of Wind Energy at the Technical University of Denmark (DTU) in fulfillment of the requirements for acquiring a PhD degree. Furthermore, the thesis was prepared in accordance with the requirements of the industrial PhD programme in Denmark that is regulated by Innovation Fund Denmark.

The research described in this thesis is based on the work of an industrial PhD project in a collaboration between LM Wind Power, Department of Composites Engineering & Technology, and DTU Wind Energy, Section of Composites Mechanics & Materials. The main topic is adhesive joints in wind turbine blades with the primary objective of developing novel design rules to improve the existing joint design for the three primary joint types in the wind turbine blade; the leading-edge joint, the trailing-edge joint and the web joint. The need for developing larger and more cost effective wind turbine blades was a motivation to work in the field of fracture mechanics for adhesive joints used in wind turbine blades. Personally, it was challenging and motivating to couple model predictions with lab scale experiments in order to predict the response on full scale wind turbine blade joints.

This research was primarily supported by grant no. 4135-00010B from Innovation Fund Denmark. This research was also supported by the Danish Centre for Composite Structures and Materials for Wind Turbines (DCCSM), grant no. 0603-00301B, from Innovation Fund Denmark. The project has primarily been supervised by Bent F. Sørensen (DTU Wind Energy) and Casper Kildegaard (LM Wind Power).

Risø campus, Roskilde, November 15, 2017

Jeppe Bjørn Jørgensen

Acknowledgements

During this PhD project several persons have supported me such that I could keep the motivation high. Without this support it would not have been possible to overcome the challenges and obstacles on the way. This section is assigned the institutions that supported the project and the people that helped me on the way to complete the PhD project.

First of all, I would like to thank my two main supervisors, Bent F. Sørensen and Casper Kildegaard for the supervision, guidance and for pointing in the right direction. There has been many non-trivial problems to solve and I believe we all learned something new. Also thanks to my colleagues at LM Wind Power and DTU Wind Energy for creating a great working environment and a nice approachable atmosphere. This openness formed the basis for many valuable discussions e.g. about composites, adhesives and fracture mechanics.

In the duration of the PhD project more than 400 test specimens were manufactured at the laboratory of LM Wind Power and tested at the laboratories of LM Wind Power, DTU Wind Energy and University of Michigan. The valuable discussions with the staff in the laboratories gave me valuable inputs for the project as well as personal learnings. Especially, thanks to the technicians for supervision and guidance during the laboratory work.

A research stay at University of Michigan, Ann Arbor under supervision of prof. Michael D. Thouless were arranged to work on crack deflection at interfaces experimentally. The topics in this PhD project were within the research field of prof. Thouless e.g. adhesive joints, crack deflection and cohesive laws. Thus, it was possible to share different viewpoints, methods, experimental approaches and experience on the applicability of the methods on adhesive joints. These valuable discussions are gratefully acknowledged. Further, acknowledgements to Fulbright for supporting the research stay at the University of Michigan. Thanks to James Gorman, University of Michigan for his help when preparing some of the Python scripts used for the DIC data analysis and for his help during the laboratory work at the Department of Mechanical Engineering, University of Michigan, MI, USA. Also, thanks to William LePage for guidance in the lab at University of Michigan and for the social events during the stay.

A special thank to my wife Nanna Amorsen for delivering two lovely kids (Lili and Aksel) in the duration of the project and for reminding me that there is other things in life than adhesive joints. Finally, thanks to Nanna and Lili for travelling with me to USA and for making the research stay at University of Michigan unforgettable.

Abstract

The industrial goal of this PhD project is to enable manufacturing of larger wind turbine blades by improving the existing design methods for adhesive joints. This should improve the present joint design such that more efficient wind turbine blades can be produced. The main scientific goal of the project is to develop new- and to improve the existing design rules for adhesive joints in wind turbine blades. The first scientific studies of adhesive joints were based on stress analysis, which requires that the bond-line is free of defects, but this is rarely the case for a wind turbine blade. Instead linear-elastic fracture mechanics are used in this project since it is appropriate to assume that a crack can initiate and propagate from a pre-existing defect.

The project was divided into three sub-projects. In the first sub-project, the effect of different parameters (e.g. laminate thickness, post curing and test temperatures) on the formation of transverse cracks in the adhesive were tested experimentally. It was assumed that the transverse cracks evolved due to a combination of mechanical- and residual stresses in the adhesive. A new approach was developed that allows the residual stress to be determined in several different ways. The accuracy of different ways of measuring residual stresses in the adhesive was tested by applying five different methods on a single sandwich test specimen (laminate/adhesive/laminate) that was instrumented with strain gauges and fiber Bragg gratings. Quasi-static tensile tests of sandwich specimens showed that higher post curing temperature and lower test temperature had a negative effect on the formation of transverse cracks in the adhesive i.e. transverse cracks initiated at lower applied mechanical loadings. The effect of increased laminate thickness was minimal under both static and cyclic loading.

In the second sub-project, tunneling cracks in adhesive joints were analyzed numerically and experimentally. Simulations with a new tri-material finite element model showed that the energy release rate of the tunneling crack could be reduced by embedding a so-called buffer-layer with a well-chosen stiffness and -thickness. However, it was found for adhesive joints in wind turbine blades that the laminates were already sufficiently stiff. Thus, the effect of a stiffer buffer-layer was small in comparison with the effect of reducing the thickness of the adhesive layer. A new approach was in combination with a generic tunneling crack tool used to predict the cyclic crack growth rate for tunneling cracks in the adhesive joint of a full scale wind turbine blade. Model predictions were tested on a full scale wind turbine blade that was loaded excessively in an edgewise fatigue test in a laboratory. It was demonstrated that the model predictions were in agreement with measurements on the full scale test blade.

In the third sub-project crack deflection at interfaces in adhesive joints was investigated experimentally. Therefore, it was necessary to design a test specimen, where a crack could propagate stable and orthogonal towards a bi-material interface. A four-point

single-edge-notch-beam (SENB) test specimen loaded in displacement control (fixed grip) was designed and manufactured for the purpose. In order to design the test specimen, new models were established to ensure stable crack growth and thus enable that crack deflection could be observed during loading (in-situ). A new analytical model of the four-point SENB specimen was derived, and together with numerical models it was found that the test specimen should be short and thick and the start-crack length relatively deep for the crack to propagate in a stable manner. Using the design from the developed models, crack deflection at interfaces for different material systems was tested successfully. For test specimens in selected test series it was observed that a new crack initiated at the interface before the main crack propagated and reached the interface. This cracking mechanism was used to develop a novel approach to determine the cohesive strength of the interface. The novel approach was applied to determine the cohesive strength of different material systems including an adhesive/laminate interface. It was found that the cohesive strength of the interfaces was small in comparison with the macroscopic strength of the adhesive.

Resume

Det industrielle formål med dette ph.d. projekt er at muliggøre fremstilling af større vindmøllevinger ved at forbedre de eksisterende designmetoder for limsamlinger. Dette skal føre til en forbedring af det nuværende design for limsamlinger således mere effektive vindmøllevinger kan produceres. Det overordnede videnskabelige formål med projektet er at udvikle nye- samt forbedre de eksisterende designregler for limsamlinger i vindmøllevinger. De første videnskabelige studier af limsamlinger var baseret på spændingsanalyse, som forudsætter at limsamlingen er fremstillet uden defekter, hvilket dog sjældent er tilfældet i en vindmøllevinge. I dette projekt anvendes istedet en fremgangsmåde baseret på lineær-elastisk brudmekanik, da det med rimelighed kan antages at en revne kan initiere og vokse fra en allerede eksisterende defekt i limen.

Projektet blev opdelt i tre delprojekter. I det første delprojekt blev dannelsen af tværgående revner i limen testet eksperimentelt og effekten af forskellige parametre blev undersøgt (f.eks. laminattykkelse, efterhærdningstemperatur og testtemperatur). Det blev antaget at de tværgående revner initierede som følge af en kombination af mekaniske- og residualspændinger i limen. En ny fremgangsmåde muliggjorde at residual spændinger i limen kunne bestemmes på forskellige måder. Nøjagtigheden af fem forskellige metoder til at måle residualspændinger i limen blev testet vha. et sandwich testemne (laminat/lim/laminat), som var instrumenteret med strain gauges og fiber Bragg gratings. Statiske træktests af sandwichemnerne viste at højere efterhærdningstemperatur og lavere testtemperatur havde en negativ effekt på dannelsen af tværgående revner i limen, dvs. tværgående revner initierede ved lavere mekanisk belastning. Effekten af tykkere laminat var minimal under både statisk og cyklisk belastning.

I det andet delprojekt blev tunnelrevner i limsamlinger analyseret numerisk og eksperimentelt. Simuleringer vha. en ny symmetrisk finite element model med tre forskellige materialer viste at energifrigørelsesgraden for tunnelrevnen kunne reduceres ved at inkludere et såkaldt buffer-lag med en velvalgt stivhed og -tykkelse. Dog viste det sig for limsamlinger i vindmøllevinger, at stivheden af laminaterne allerede var tilstrækkeligt stor således effekten af et buffer-lag var lille sammenlignet med effekten af at reducere tykkelsen af limlaget. En ny fremgangsmåde blev anvendt sammen med et generisk tunnelrevneværktøj til at forudsige cyklisk revnevæksthastighed for en række af tunnelrevner i en limsamling på en vindmøllevinge. Modelforudsigelserne blev testet på en fuldskalavinge, som blev belastet ekstremt højt cyklisk under en kantvis udmattelsestest i et laboratorie. Revnelængden for 27 tunnelrevner blev løbende opmålt på bagkantslimsamlingen under den cyklisk belastede test og det blev demonstreret at modelforudsigelserne var i overensstemmelse med målingerne på fuldskala-testvingen.

I det tredje delprojekt blev revneafbøjning ved grænseflader i limsamlinger undersøgt eksperimentelt. Derfor var det nødvendigt at designe et testemne, hvor en revne kunne

vokse stabilt og vinkelret ind mod en bi-materiale grænseflade. Til formålet blev et testemne med en sidekærv fremstillet. Testemnet blev belastet i firepunktsbøjning med en påtrykt flytning. Modeller blev udviklet til at designe testemnets geometri for at sikre stabil revnevækst og således muliggøre observation af revneafbøjning under belastning (in-situ). En ny analytisk model af testemnet blev udledt og sammen med numeriske modeller blev det bestemt at testemnet skulle være kort og tykt samt at start-revnelængden skulle være dyb for at revnen kunne vokse stabilt. På baggrund af modellerne blev succesfulde forsøg med revneafbøjning udført for forskellige materialesystemer med lim. For testemner i udvalgte testserier blev det observeret at en ny revne initierede i grænsefladen inden hovedrevnen nåede at vokse frem. Denne revnemekanisme blev anvendt til at udvikle en ny metode til at bestemme den kohæsive styrke af grænsefladen. Metoden blev anvendt til at bestemme den kohæsive styrke af grænsefladen for forskellige materialesystemer, herunder en lim/laminat grænseflade. De målte kohæsive styrker af grænsefladerne var små sammenlignet med den makroskopiske styrke af limen.

Publications

List of publications appended to the thesis and presented in Appendix A:

P1 Jeppe B. Jørgensen, Bent F. Sørensen and Casper Kildegaard. "The effect of residual stresses on the formation of transverse cracks in adhesive joints for wind turbine blades." Submitted to: *International Journal of Solids and Structures* (2017).

P2 Jeppe B. Jørgensen, Bent F. Sørensen and Casper Kildegaard. "The effect of buffer-layer on the steady-state energy release rate of a tunneling crack in a wind turbine blade joint". Submitted to: *Composite Structures* (2017).

P3 Jeppe B. Jørgensen, Bent F. Sørensen and Casper Kildegaard. "Tunneling cracks in full scale wind turbine blade joints". Accepted for: *Engineering Fracture Mechanics* (2017).

P4 Jeppe B. Jørgensen, Casper Kildegaard and Bent F. Sørensen. "Design of four-point SENB specimens with stable crack growth". Submitted to: *Engineering Fracture Mechanics* (2017).

P5 Jeppe B. Jørgensen, Bent F. Sørensen and Casper Kildegaard. "Crack deflection at interfaces in adhesive joints for wind turbine blades". Submitted to: *Composites Part A: Applied Science and Manufacturing* (2017).

P6 Jeppe B. Jørgensen, Michael D. Thouless, Bent F. Sørensen and Casper Kildegaard. "Determination of mode-I cohesive strength of interfaces". In: *IOP Conf. Series: Materials Science and Engineering*, 139, 012024 (2016).

Contents

CHAPTER 1

Introduction

The main parts of wind turbine blades are two aerodynamic shells (upwind, downwind) and two webs made of glass fibre reinforced composites produced by a vacuum-assisted-resin-transfer-moulding (VARTM) process. In the typical blade concept, the shells and webs are moulded separately and then bonded together in an assembly process using a structural adhesive. During the curing process, the adhesive shrinks and builds up residual stresses (tensile) that is caused by the constraining effect from the laminates since the adhesive cannot freely contract. Residual stresses can also rise due to thermal effects if there is a mismatch in coefficient of thermal expansion between the adhesive and the laminate. The main load carrying adhesive joints are located at the leading-edge, trailing-edge and at the webs as shown in Figure 1.1. The stress state in the adhesive is three dimensional since geometries are complex (curvature- and thickness variations) and the mechanical stresses interact with the residual stresses in the adhesive.

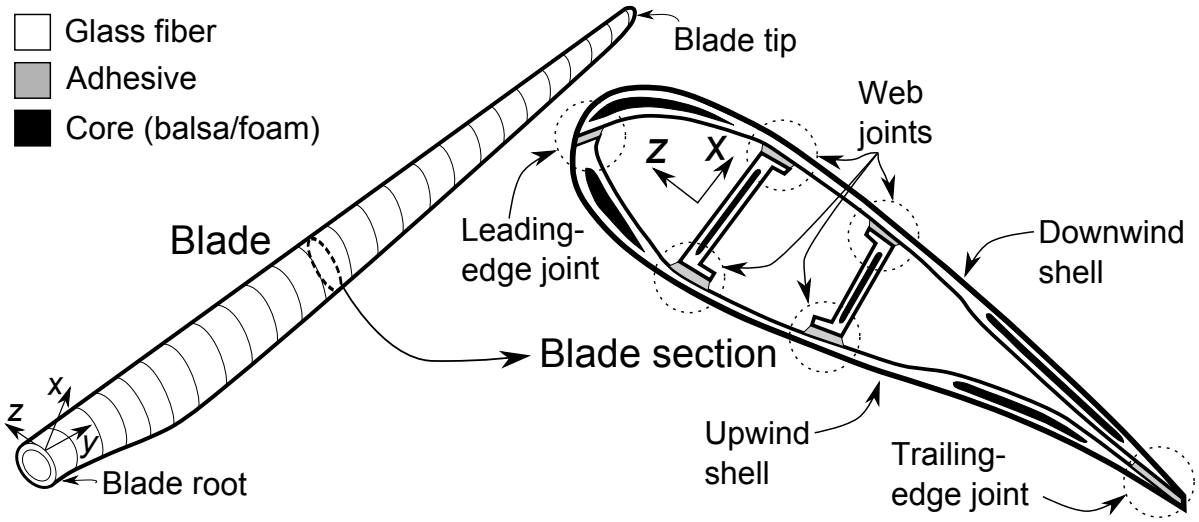

Figure 1.1: Blade and cross section to illustrate the location of the adhesive joints.

During the life-time of the wind turbine, which is more than 20 years [52, 92, 90, 60, 47, 83], the adhesive joints are loaded cyclic by wind- and gravitational loads that can be separated into a flapwise- and an edgewise load, respectively [85, 90]. Furthermore, the joints should be designed against extreme loads i.e. a few high static loads, but also be able to resist the demanding operational conditions such as temperatures, lightning strikes, moisture and erosion [51].

1.1 Motivation and Problem Statement

In the recent decades, technology developments and improvements have increased the power ratings for wind turbines. Thus, the levelized cost of energy (LCOE) has decreased and further capacity of wind energy were installed [54]. In order to reduce the LCOE, wind turbines, and particular the blades have increased in size over the past years as illustrated in Figure 1.2.

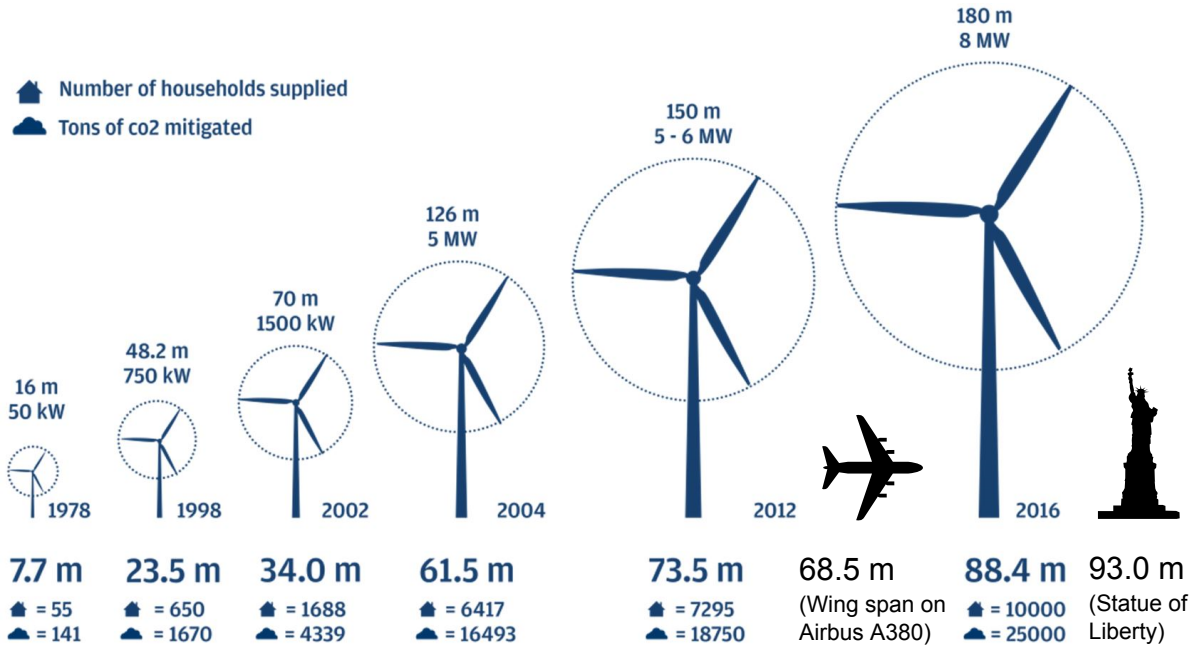

Figure 1.2: The increase in blade sizes over the last four decades (LM Wind Power).

Larger wind turbines means that for the same level of energy production, fewer units are required, which reduces the operation costs of the wind farm [29]. The power ratings are now above 8 MW and the length of the blades has exceeded 85 m. It is expected that even longer blades will be produced in the near future to fit wind turbines with power ratings of about 12-15 MW [5]. Even concept designs of wind turbines up to 20 MW are being explored, where one of the most important challenges is to limit the blade weight [61]. Another benefit of manufacturing lighter blades is the cost reduction for the remaining components (hub, nacelle, tower, foundation [32]) in the wind turbine since the loadings on these components become smaller.

Historically, the weight of the blades measured in kg, has increased to the power of about 2.1 of the rotor diameter in meters as shown in Figure 1.3 [19, 65]. With increasing size and weight of the blades, the structural performance requirements become more difficult to achieve. For wind turbine blades, two important design requirements are sufficiently bending stiffness to maintain tip clearance towards the tower and sufficiently blade bending strength against extreme static loadings e.g. a 50-year gust. Furthermore,

the fatigue life for the blades should usually be minimum 20 years corresponding to approx. 10^8 cycles [29]. Full scale blade tests are used to verify the static/fatigue strength of the blade according to the requirements of IEC 61400-23 that includes the following tests [25]: Blade properties (weight, natural frequencies, elastic properties etc.), static strength, fatigue strength and static strength after fatigue tests. The strength tests are separated into flapwise and edgewise tests. Usually only one full scale blade test is conducted for each blade type [25].

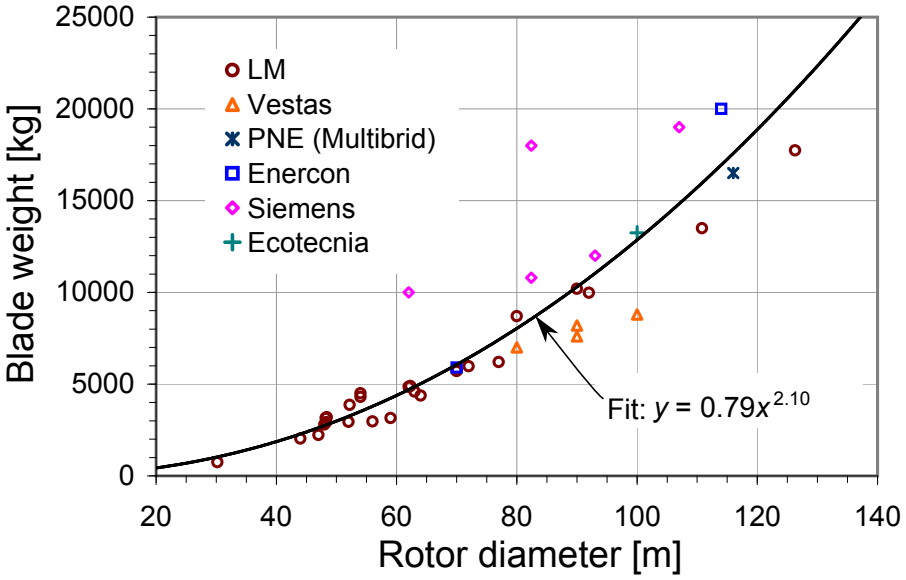

Figure 1.3: The trend in blade mass with rotor diameter [19].

The overall business objective of this project is to reduce the cost of energy by enabling manufacturing of longer and more cost efficient wind turbine blades. More specifically, it is aimed at developing new- and improving existing analysis tools for adhesive joints in wind turbine blades. This will enable the industry to design closer to the actual structural limits. The main scientific aim of the project can be stated as:

- Develop novel design rules and generic models of adhesive bonded joints in wind turbine blades.

A way to achieve the overall business objective is to develop novel design rules, for an improved joint design, that can significantly reduce the cost by not only saving material, but also allowing larger loading of the joints. In relation to the design of the joints, there are mainly two ways of fulfilling this:

- Allow the joint design limit to be closer to the actual strength based on improved understanding of the failure modes. Thus, material savings are achieved and lighter blades can be manufactured.
- Increasing material and process performance in a cost effectively way.

The work in this project is related to the first point by applying an approach based on linear-elastic fracture mechanics (LEFM) since the aero shells in a wind turbine

rotor blade are bonded by a structural adhesive and it is appropriate to assume that the adhesive contains manufacturing flaws from which a crack can initiate and propagate. This means that cost reductions can be achieved by improved understanding of the cracking mechanisms in the joints, which enable a design closer to the actual structural/material limits. As exemplified in Figure 1.4, the larger design margin, the more safe or conservative design, but too large design margins adds unnecessary, and costly, material to the blade.

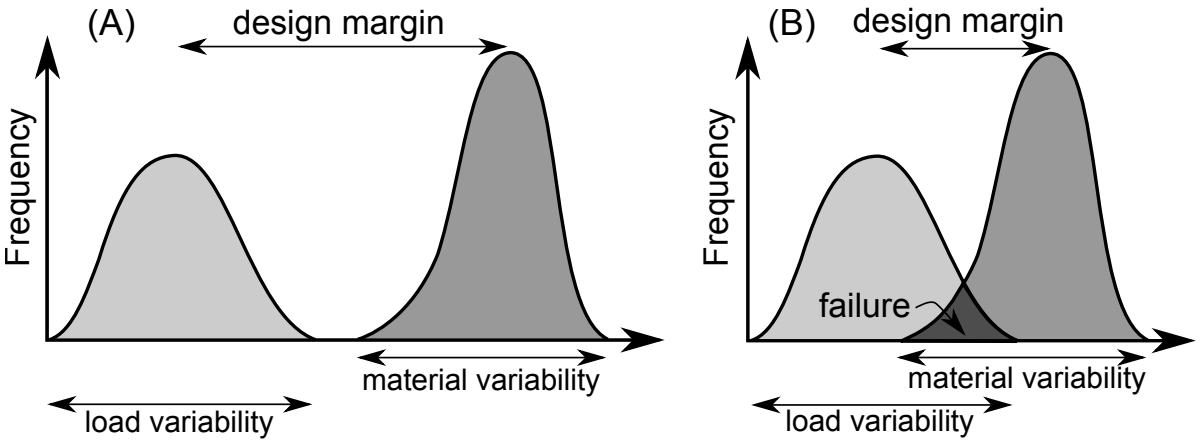

Figure 1.4: (A) Overly conservative joint design. (B) Joint design with desired probability of failure (modified from Straalen *et al.* [94]).

The variable nature of both the loadings (e.g. energy release rate) and the adhesive joint resistance (e.g. fracture toughness) complicates the development of design rules [94]. The variation of the loadings, i.a. caused by the random nature of the wind, cannot directly be changed. The load distribution can be translated (reduced) by adding material, but this increases the blade weight in an undesired manner. Alternatively, the load distribution can be translated (reduced) e.g. by reducing the residual stresses in the adhesive. The residual stress magnitude can be reduced by improved understanding of the residual stress development in the adhesive during the manufacturing process. The joint material distribution can be translated (enhanced/increased) by improving the mechanical properties of the joints e.g. by using a better but more expensive adhesive material systems.

Design based solely on probabilistic considerations is an old fashioned way of designing adhesive bonded joints. Another way of improving the structural performance of an adhesive joint is to apply a modern fracture mechanics based approach to design the joint, such that, if an isolated crack initiates and starts to grow, then crack propagation is stable i.e. the energy release rate decreases with crack length. A good damage tolerant design for wind turbine blade joints contains only cracks that deflects or arrests before reaching a critical length. This can be achieved by improved understanding of the cracking mechanisms in the joint, which is the main problem to investigate in this thesis.

1.1.1 Cracking Mechanisms and Damage Tolerance of Adhesive Joints

Adhesive joints are typically one of the first structural details in a blade to develop damage that is defined as distributed adhesive cracks [90]. If several distributed cracks initiate and evolve simultaneously, then a damage based design approach can be applied to improve the joint design [75, 64].

Although, the joints are designed properly according to the structural design limits for crack initiation, it is advantageous to ensure that the joint design is damage tolerant i.e. building in an extra safety feature. Thus, the damage develops in a stable manner and is detectable before it reaches a critical state i.e. joint failure [90]. The term failure defines the critical state where the joint loses its capability to carry load. Models and experimental test results of damage development are also desirable since they can be used to plan maintenance by evaluating the damage growth rates and -sizes [37].

Adhesive joints can develop damage or fail in several different ways (failure modes) depending on material properties, temperatures, environmental conditions, loadings and geometry. Accounting for these parameters are necessary in order to design a reliable and damage tolerant adhesive joint. Especially, adhesive joints made of composite materials can fail in a number of ways since cracks can develop in both the adhesive and the laminate, and these can even interact and thereby complicate the design process further. Thus, the blade designer has to consider a broad range of different potential failure modes as elaborated next.

1.2 Design Failure Mode and Effects Analysis

Design Failure Mode and Effects Analysis (DFMEA) is a methodology to identify the ways a given product potentially can fail and it includes a prioritization of the potential modes of failure evaluated based on the severity of the failure, the occurrence of the failure and the detectability of the failure [63]. For the present analysis, the product is the adhesive joint component in a wind turbine blade. Generally, about ten steps are needed to complete a full DFMEA [63]. Since it is out of the scope to conduct a full DFMEA, a brief (mini) DFMEA of adhesive joints in wind turbine blades will be presented. Therefore, only the first two steps in the DFMEA methodology presented by McDermott *et al.* [63] is applied:

(1) Review the product.

(2) Brainstorm potential failure modes.

The main idea of step (1) is to be familiar with the product e.g. by drawings or prototypes. The primary purpose of this mini DFMEA is to identify potential failure modes that are generic i.e. frequent in the three main structural adhesive joints (the leading-edge, trailing-edge and web joints).

1.2.1 Potential Failure Modes

The first step in the mini DFMEA presented here is a brief review of the manufacturing procedure and the typical design of the adhesive joints. From a geometrical point of view, the leading-edge, trailing-edge and web joints are different as shown in Figure 1.5. The leading-edge joint is connecting the upwind and downwind shells that are produced of glass fibre reinforced laminates in a VARTM process. The leading-edge joint is designed with a flange to support the joint in order to re-direct the load transfer from peel stresses to shear stresses. The trailing-edge joint is manufactured by bonding the upwind- and downwind shells (two laminates) that are produced of glass fibre reinforced laminates. The web joint is manufactured by bonding the web foot onto the main laminate of the blade. The main laminate is primarily made of a thick stack of uni-directional glass fibre layers. The web body is produced by infusion of a balsa/foam core with thin skin laminates, whereas the web foot is primarily made of different types of glass fibre.

The second step in the mini DFMEA is a brief brainstorm of the potential failure modes that can be thought to be identified for the leading-edge, trailing-edge and web joints. From a fracture mechanics point of view, the three joints are similar as shown by comparing the types of potential cracking modes in Figure 1.5. The potential cracks in the x-z plane of the adhesive joints are numbered (#1.i) and those in the x-y plane are numbered (#2.i), where i is an integer between 1 and 6. The potential types of cracks are listed below:

1.1 Cohesive failure of the adhesive.

1.2 Debond crack in the laminate-adhesive interface.

1.3 Debond crack that is kinking into the laminate.

1.4 Delamination in the laminate.

2.1 Transverse crack (tunneling crack loaded in tension (mode-I)).

2.2 Singly deflected crack (L-shaped tunneling crack with debonding).

2.3 One-sided doubly deflected crack (T-shaped tunneling crack with debonding).

2.4 Two-sided doubly deflected crack (H-shaped tunneling crack with debonding).

2.5 Crack penetration into laminate (tunneling crack penetrating the laminate).

2.6 Oblique crack (tunneling crack loaded in shear (mode-II)).

The description of the potential cracking mode outside the parenthesis of the list is the 2D version and the description inside the parenthesis of the list is the 3D version of the potential cracking mode. The coordinate system is oriented such that the y-axis is pointing from the blade root towards the blade tip according to Figure 1.1. The loading components are named according to:

- P: Normal force
- T: Shear force (longitudinal shear)
- M: Bending moment (in transverse plane)

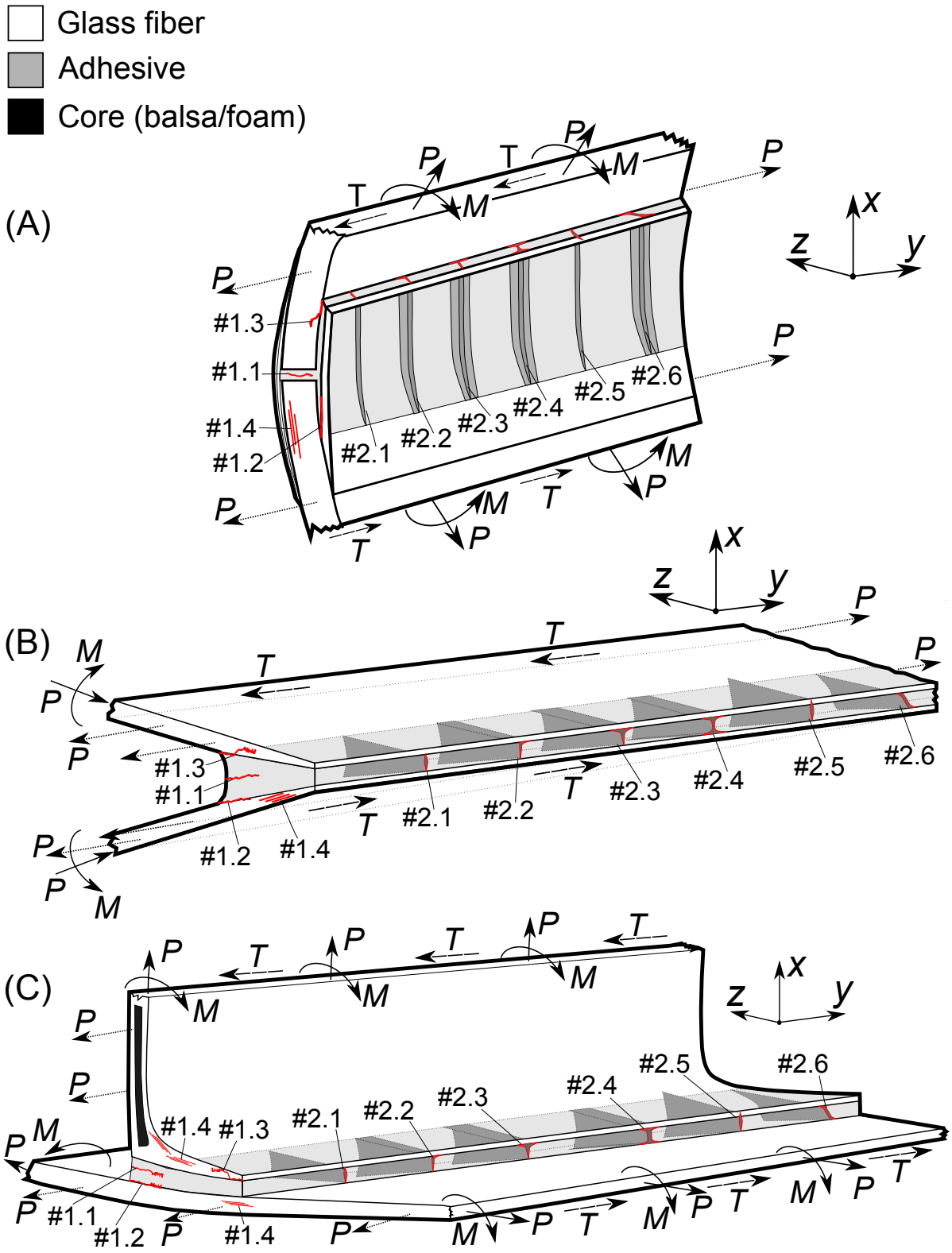

Figure 1.5: Potential cracking modes in: (A) leading-edge joint, (B) trailing-edge joint, (C) web joint.

1.2.2 Evaluation of Potential Failure Modes and Identification of a Family of Joints

The potential failure modes identified and presented in Figure 1.5 (A-C) are found to be comparable, especially the types of cracks named #2.i. Since the leading-edge, trailing-edge and web joints contain similar potential failure modes, they are referred to as a "family of joints". Although the geometrical and structural details of the joints are different, from a fracture mechanics point of view the joints are similar.

In order to cover the most important failure modes in the joint design process with the least amount of different models/tests, it is desirable to select and analyze failure modes that are present in all three members of the "family of joints". Since the transverse cracking mode (#2.1 in Figure 1.6) is one of the first steps in the cracking process and potentially can be found in all three members of the "family of joints" i.e. the leading-edge, the trailing-edge and the web joints, it is advantageous to analyze this particular cracking mode in details. Thus, it is aimed at analyzing transverse cracking of the adhesive using the same model concept for the three members of the "family of joints". When a transverse crack in the bondline of the "family of joints" is fully developed, it may deflect along the interface (#2.2, #2.3 and #2.4 in Figure 1.6) or penetrate into the laminate (#2.5 in Figure 1.6).

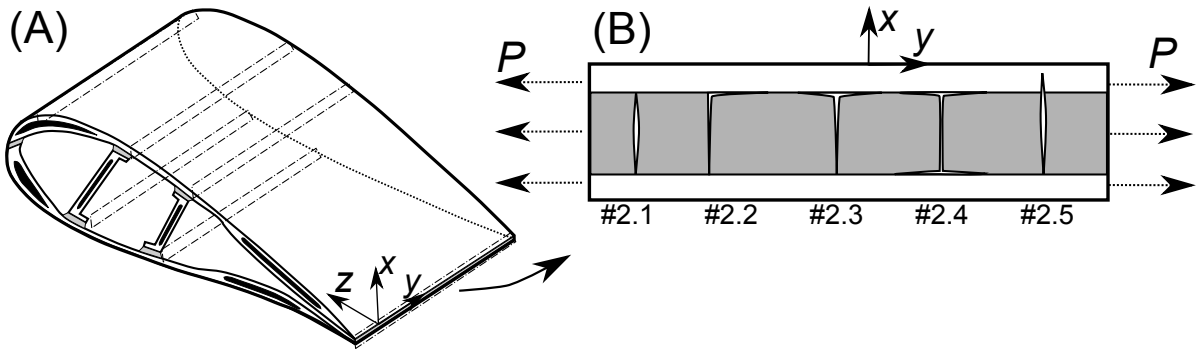

Figure 1.6: (A) Blade section. (B) Potential cracking modes in the x-y plane of the adhesive joint under loading by the normal force, P.

According to Figure 1.5, the main loading components on the different types of cracks named #2.i are the normal force, P, and the shear force, T. The forces P and T are causing longitudinal tension and -shearing deformation of the joint, respectively. To simplify the analysis, the shear loading component is neglected meaning that the potential cracking mode numbered #2.6 in Figure 1.5 is not considered. Thus, the primary cracking modes to be analyzed in the present work are those presented in Figure 1.6 (#2.1, #2.2, #2.3, #2.4 and #2.5). There will be a primary focus on the fundamental cracking mode numbered #2.1 in Figure 1.6. In order to analyze these cracking modes and -phenomena for adhesive joints in wind turbine blades novel approaches, test methods and model concepts are desired.

1.3 State of the Art for Adhesive Bonded Joints

Some of the first scientific studies of adhesive bonded joints, by Volkersen [109], Goland & Reissner [26] and Hart-Smith [35], were closed form solutions based on stress for single lap joints. Later, other joint types were modeled using a similar approach [33] and according to Figure 1.7 by Hart-Smith [34], a double scarf joint was the preferable joint type if the adherends were thick and high strength was a requirement. More advanced elastic-plastic models were also developed by Hart-Smith [36] in order to account for plasticity of the adhesive and the effect of flaws at the adhesive-substrate interface. Another application of modeling based on stress was the interaction between an elliptical shaped crack and a plane of weakness (such as an interface) under various conditions as demonstrated by Cook and Gordon [18]. They established a criterion (Cook-Gordon criterion) stating that the interface fails if the interface-to-substrate strength ratio is less than about 1/3 to 1/5.

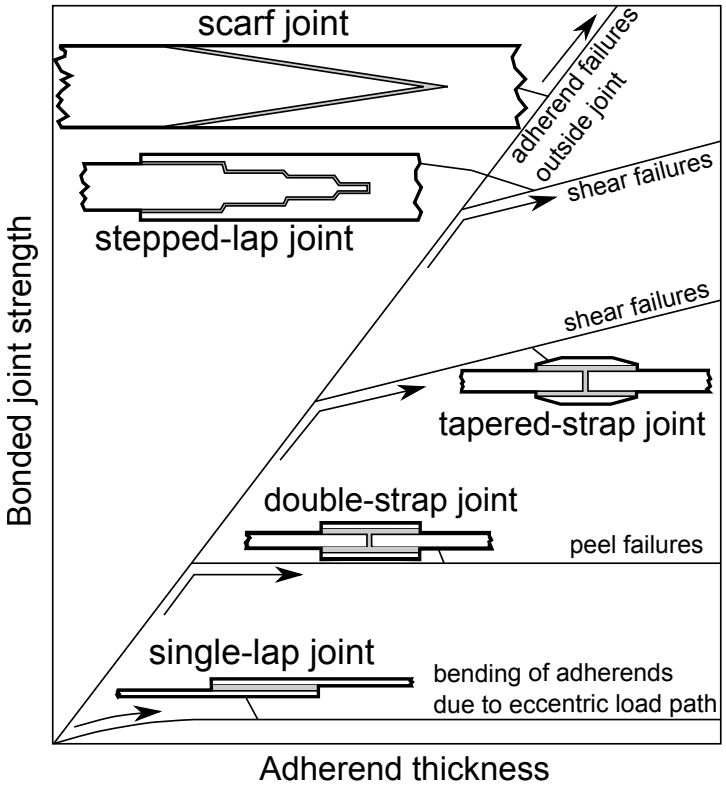

Figure 1.7: Bonded joint strength for various joint types with different thickness of adherends. The failure modes on the diagram represent the limit on efficient design for each joint type (modified from Hart-Smith [34]).

Design based on stress analysis requires that the bond line is free of manufacturing flaws and defects, which is rarely the case in a wind turbine blade joint. It is therefore appropriate to assume that the joint contains manufacturing flaws [91]. Classical linear-elastic fracture mechanics (LEFM) can be applied if a flaw or a pre-crack is present. For

LEFM to be accurate the materials must deform in a linear-elastic manner, be isotropic and the plastic zone size and the fracture process zone at the crack tip must be small [44, 42]. When these assumptions are satisfied, the energy release rate approach by Griffith [28] is related to the stress intensity approach through the Irwin relation [45]. Solutions for practical crack problems have been developed based on LEFM to predict crack propagation [101, 43, 104]. One of the important applications of LEFM is the modeling of a channeling crack propagating through a thin film [11]. A related problem is that of a tunneling crack propagating through an adhesive layer constrained in-between two substrates as demonstrated by Ho and Suo [100, 41]. The energy release rate of a steady-state tunneling crack can be determined using a plane strain solution although the tunneling crack problem is a 3D process [41]. In turn, 3D finite element (FE) models are needed for transient modeling of channeling/tunneling cracks since the crack length must reach a certain length for the crack to become steady-state [68, 111, 4, 6]. For a tunneling crack in a homogenous solid this length is about twice the thickness of the cracked layer [68, 41]. For tunneling crack models, delamination between the adhesive and the substrate can be included as well [17, 97].

LEFM can also be applied for the prediction of crack deflection at interfaces [39, 40, 38, 30, 62]. He and Hutchinson [39] established a criterion for crack deflection stating that the interface-to-substrate toughness ratio should be less than 1/4 for the crack to deflect at the interface. For cyclic crack propagation, the Paris law can be used to couple the stress intensity factor range to the crack growth rate [69]. These models are important for the prediction of crack propagation in adhesive joints for wind turbine blades [22]. The analytical methods based on LEFM are useful since they are reliable and quick to apply, but they have their limitations.

The recent studies have found a way to account for the influence of non-linear effects in the fracture process zone and to predict the initiation of a new crack. The non-linearities can be accounted for by using a cohesive law, which is relating the separation of the crack surfaces with the prescribed tractions [90]. The cohesive law can be measured experimentally, e.g. by the J-integral approach [59, 88, 89, 7, 27]. Alternatively, Mohammed and Liechti [66] measured the cohesive law parameters for a bi-material interface using a calibration procedure. The cohesive law can, based on cohesive zone modeling (CZM) and inputs from small scale test specimens, be used to predict the failure strength of larger adhesive joints [87]. Cohesive zone modeling with finite element simulations can also be used to predict both crack initiation and crack propagation for adhesive bonded joints [114, 113, 66]. Another application of cohesive zone modeling is crack deflection at interfaces as demonstrated in the studies by Parmigiani and Thouless [72] and Brinckmann *et al.* [13]. They concluded that both the fracture toughness and the cohesive strength are important parameters in an accurate crack deflection criterion.

As demonstrated, methodologies exist for the modeling of cracking mechanisms in adhesive bonded joints, although primarily for simplified geometries and loadings. However, the methodologies applicability on the complicated cracking mechanisms in adhesive joints for wind turbine blades needs to be further investigated. Therefore, the theme of this thesis is, based the fundamental methodologies, to develop novel approaches and to test their applicability on adhesive joints for wind turbine blades.

1.4 Scientific Objectives and Sub-projects based on a Family of Joints

As mentioned, the structural details of the "family of joints" are different, but from a fracture mechanics point of view, the cracking sequence is the same (see Figure 1.8):

1. A crack initiates from a pre-exising defect in the adhesive and evolves to a transverse crack.
2. The transverse crack propagates as a tunneling crack across the adhesive layer.
3. When the transverse crack reaches the interface, it can deflect along the interface or penetrate into the laminate.

This sequence of potential cracking defines the three main sub projects of the present work, see Figure 1.8. It is assumed that cracks in the adhesive propagate under combined mechanical stress, σ_m, and residual stress, σ_r. This should be taken into account in the development of generic design rules and model concepts for the "family of joints".

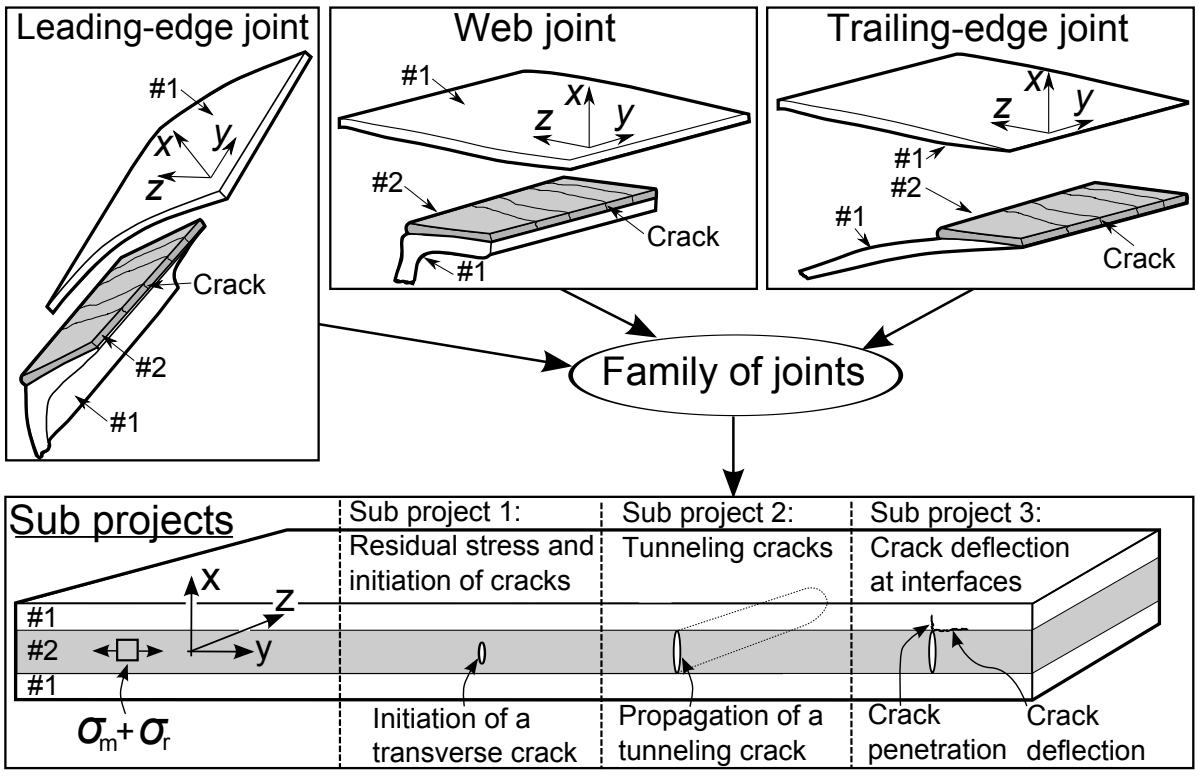

Figure 1.8: Sub projects and the "family of joints" (#1: Laminate/substrate, #2: Adhesive).

1.4.1 Definition of Scientific Objectives

For each sub project, scientific objectives should be defined based on the gaps identified in the state of the art literature.

Sub project 1: The evolution of transverse cracks is promoted by residual stresses in the adhesive. Therefore, it is the aim to improve the measuring techniques for determination of residual stresses and establish a robust method where the residual stress measurement can be included in the determination of the stress in the adhesive at first transverse crack. Furthermore, it is the goal to investigate the effect of different parameters such as temperatures on the evolution of transverse cracks in adhesive joints. General techniques for the measurement of residual stresses is well known in the literature [110] e.g. by using different types of beam specimens [67]. However, the applicability and accuracy of the different methods for the particular adhesive joints needs to be tested experimentally. Furthermore, it is desired to measure the residual stress during the manufacturing of the adhesive joints such that the manufacturing step where the largest part of the residual stress builds up in the adhesive can be identified. Other complicating factors are the specific joint geometry and the constraining effect of the laminates on the adhesive (during curing), which might affect the residual stress magnitude. Therefore, it is needed to develop a new type of test specimen and approach where these effects can be included.

Sub project 2: The existing tunneling crack models found in the literature [100, 43, 41, 97, 98, 10] are limited to bi-material models e.g. a layer of adhesive constrained in-between two substrates. In turn, for a wind turbine blade joint the substrates are made of several different layers of materials that for some cases needs to be modeled as orthotropic. Therefore, the existing tunneling crack models needs to be expanded and tailored to the applicability on adhesive joints for wind turbine blades. The applicability of tunneling crack models on real full scale structures are limited and complicated due to the many parameters (e.g. environments, loads, geometries, material variations) that needs to be accounted for in an accurate analysis. Also, the difficulty of collecting data (e.g. crack lengths, geometries, loadings) on structures in operation makes measurements of tunneling cracks challenging, especially under cyclic loading. Therefore, a generic tunneling crack tool is desired that is easy to apply (with sufficient accuracy) on real engineering structures that are loaded cyclic e.g. wind turbine blades.

Sub project 3: Modeling the deflection of a crack meeting an interface were, at first, based on either stress criteria [18, 31] or energy criteria [40, 38, 30, 62, 106]. The stress criteria and energy based approach can be unified using a cohesive law with cohesive zone finite element simulations [72, 13]. The parameters for the cohesive law can e.g. be measured by the J-integral approach [59, 27], but accurate experimental determination of cohesive strength magnitude for bi-material interfaces is challenging. Furthermore, stable crack growth experiments where the crack deflection process are clearly documented are limited [57]. It is therefore the aim to design an experiment to test crack deflection at interfaces, where the crack deflection process can be clearly identified. Thus, novel models need to be developed in order to design the experiment properly i.e. with stable crack propagation. A successful crack deflection experiment should be demonstrated in

practice. Finally, it is the aim to develop a novel approach to determine the cohesive strength of a bi-material interface, $\hat{\sigma}_i$, since this is an important parameter in an accurate crack deflection criterion.

1.4.2 Addressing the Scientific Objectives

As visualized by the three sub projects in Figure 1.8, the main research objective is to develop a generic model concept based on linear-elastic fracture mechanics that can predict the primary cracking mechanisms for the "family of joints". This should lead to novel design rules for adhesive bonded joints in order to fulfill the main scientific aim. The scientific objectives for the three main sub projects were addressed by the work in the papers appended to this thesis as:

- Sub project 1:
  - The effect of residual stresses on the formation of transverse cracks in adhesive joints for wind turbine blades (Paper P1).
- Sub project 2:
  - The effect of buffer-layer on the steady-state energy release rate of a tunneling crack in a wind turbine blade joint (Paper P2).
  - Tunneling cracks in full scale wind turbine blade joints (Paper P3).
- Sub project 3:
  - Design of four-point SENB specimens with stable crack growth (Paper P4).
  - Crack deflection at interfaces in adhesive joints for wind turbine blades (Paper P5).
  - Determination of mode-I cohesive strength for interfaces (Paper P6).

The fracture mechanics models and methods should be integrated into design rules that can improve the joint design for large wind turbine blades. Thus, the desired industrial outcome is design criteria that can expand the existing joint design envelopes. The primary academic goal is to contribute to the current research within adhesive bonded joints for wind turbine blades e.g. through novel approaches, methodologies, experimental tests and models.

1.5 Thesis Outline

This thesis is divided into six chapters, where the first chapter is the introduction. The second chapter presents the needed background for adhesive joints in wind turbine blades, primarily from a materials perspective. Chapter 3, 4 and 5 will be dedicated the three sub projects, respectively. In chapter 3, experimental determination of residual stress and its effect on the formation of transverse cracks in the adhesive will be investigated experimentally. In chapter 4, a numerical model of a tunneling crack will be developed to improve the joint design and to predict tunneling crack growth rates on a full scale wind

turbine blade joint. Chapter 5 presents investigations of the problem of crack deflection at interfaces through modeling and experimental tests. Finally in chapter 6, the novel model concepts and experimental results will be discussed in relation to the existing knowledge in the literature. Furthermore, in this last part of the thesis, the papers will be summarized and the main findings will be combined in order to provide a broader perspective and to establish novel design rules for adhesive bonded joints. To conclude, the future challenges for adhesive joints in wind turbine blades will be discussed and a brief conclusion will sum up the major results.

CHAPTER 2
Background

In this chapter the background of adhesive joints for wind turbine blade and materials will be presented beginning with an introduction of structural adhesives.

2.1 Structural Adhesives for Wind Turbine Blades

According to Slütter [84], in a typical wind turbine blade with a length of 43 meter, the shells are bonded by applying about 165 kg adhesive and the adhesive layer thickness can be up to 30 mm. Therefore, the price- and properties of the adhesive, e.g. strength, stiffness and fracture toughness, are important parameters when selecting the right structural adhesive for the wind turbine blade. Some of the largest suppliers of structural adhesives for the wind turbine blade industry are: Huntsman, ITW Plexus, SciGrip, Reichhold, Sika and Scott Bader.

Structural adhesives are load-bearing adhesives since they are capable of adding strength to the adherends [46]. Structural adhesives are usually two-component resin-hardener systems, where a thermosetting resin and a hardener are mixed to start the chemical reaction (sometimes accelerated by heat). During the reaction the molecules are linked together and the material becomes solid such that a permanent bond is created. Fillers can be added to the adhesive in order to tailor specific properties such as chemical shrinkage, stiffness or toughness [8]. Heat treatment is another way to enhance certain properties. The main types of structural adhesives, commonly used for wind turbine blade joints, are [84]:

- Epoxy adhesives (EP)
- Polyurethane adhesives (PU)
- Methyl methacrylate adhesives (MMA)
- Vinylester adhesives (VE)

The choice of adhesive type is important since the mechanical properties of the adhesive affects the reliability of the joint significantly. Schematic stress-strain curves for different groups of adhesives are presented in Figure 2.1.

In general, epoxy adhesives are the most widely used structural adhesive and have been used longer than other structural adhesives [46]. Epoxy adhesives can bond a wide range of materials e.g. composites, metals, ceramics and rubber [8]. The shear strength of epoxy adhesives are generally high in comparison with other structural adhesives. Both the curing temperature and post curing temperature have an effect on the Young's modulus and tensile strength of the epoxy adhesive [16, 15]. Post curing of epoxy

adhesives at elevated temperatures can also enhance surface hardness, tensile strength and flexural strength if the appropriate temperature conditions are present [118].

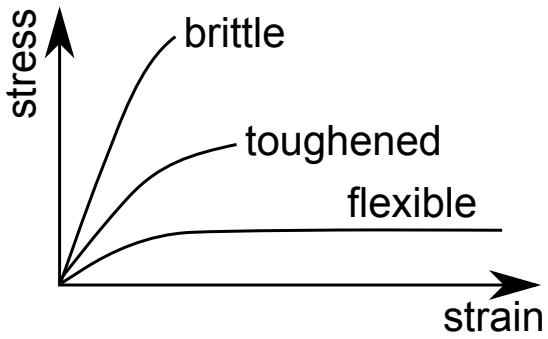

Figure 2.1: Schematic illustration of stress-strain curves for different types of adhesives (modified from Straalen *et al.* [94]).

PU adhesives are known for high toughness and flexibility even at low temperatures, but sensitive to moisture and temperature in uncured state [46]. Furthermore, PU adhesives can adhere to a wide range of substrates with a moderate shear strength [8].

Unmodified MMA adhesives are brittle, but MMA adhesives in modified state provide high elongation to break, sometimes up to 130% [84]. The strength of MMA adhesives are typically low, but the adhesion to surfaces is great even on unprepared surfaces [84]. The short curing times that can be achieved with MMA adhesives are advantageous to reduce cycle times in the production [8].

VE adhesives are recommended when bonding composites made of polyester- or vinylester resin [84]. The mechanical properties of VE adhesives are close to those of epoxy adhesives since VE adhesives are based on epoxy systems [8, 84]. VE adhesives can cure at room temperature, but particular properties can typically be enhanced by post curing at elevated temperatures [3].

2.2 Material Assumptions

In order to apply linear-elastic fracture mechanics within an acceptable accuracy for modeling of crack propagation in adhesive joints, the following assumptions must be fulfilled:

- Linear-elastic and isotropic material properties.
- Plasticity is limited to small-scale yielding near the crack tip.

If these assumptions are fulfilled, the energy- and stress intensity approach are related by the Irwin relation [45]:

$$G_I = \frac{K_I^2}{\bar{E}} \tag{2.1}$$

where the Young's modulus $\bar{E} = E$ is for plane stress and $\bar{E} = E/(1-\nu^2)$ is for plane strain. G_I is the mode-I energy release rate and K_I is the mode-I stress intensity factor.

To satisfy small-scale yielding, the plastic zone size near the crack tip must be small in comparison with the characteristic length scale in the problem, which is typically the crack length, a, or the start-crack length, a_0, in the adhesive. The first order estimation of the radius of the plastic zone size, r_p, can be determined by [42]:

$$r_p = \frac{1}{3\pi}\left(\frac{K_{IC}}{\sigma_{YS}}\right)^2 \qquad \text{(plane strain)} \tag{2.2}$$

$$r_p = \frac{1}{\pi}\left(\frac{K_{IC}}{\sigma_{YS}}\right)^2 \qquad \text{(plane stress)} \tag{2.3}$$

where σ_{YS} is the yield strength of the material and K_{IC} is the mode-I critical stress intensity factor. Dependent on the specimen geometry, material properties and loading configuration, the crack will propagate stable or dynamic once the magnitude of the critical energy release rate, G_{IC}, (or K_{IC}) is reached [42]. For a material exhibiting R-curve behavior, i.e. a material with rising fracture resistance as shown in Figure 2.2, the condition for continued crack extension is; $G = G_R(\Delta a)$, where G is the applied energy release rate. G_R versus Δa is the resistance curve of a material when the crack has extended an amount Δa to the current crack length, a, under quasi-static loading. To ensure stable crack propagation (not dynamic), the following generalized condition must be satisfied [42, 104]:

$$\left[\frac{\partial G}{\partial a}\right]_{\mathrm{L}} < \left[\frac{dG_R}{d\Delta a}\right] \tag{2.4}$$

where L is the loading parameter (prescribed dead load or prescribed fixed displacement). A mode-I crack in a perfectly brittle material will propagate under constant $G_I = G_{IC}$ as illustrated in Figure 2.2. Thus, the condition for stable crack growth reduces to [42]:

$$\left[\frac{\partial G_I}{\partial a}\right]_{\mathrm{L}} < 0 \tag{2.5}$$

This means that G_I must decrease with crack length for the crack to propagate in a stable manner.

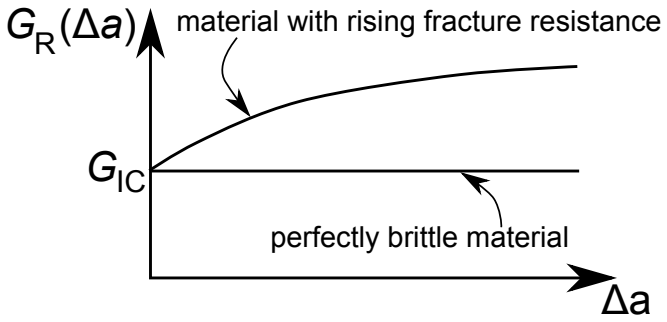

Figure 2.2: Resistance curves (modified from Hutchinson [42]).

In the present project, the materials are assumed to be perfectly brittle, i.e. no R-curve behavior as shown in Figure 2.2, such that the assumptions of small-scale yielding

and a small fracture process zone are satisfied. Furthermore, it is assumed that the adhesive is deforming elastic (not visco-elastic) and phenomena such as creep and stress relaxation are negligible.

2.3 Material Parameters

In order to simplify the modeling, non-dimensional parameters can be introduced to reduce the number of material parameters in the specific problem.

2.3.1 Laminate Parameters

The number of stiffness parameters for an orthotropic material can be reduced by introducing the dimensionless parameters proposed by Suo [99, 102] that for in-plane material orientations are:

$$\lambda_{x'y'} = \frac{E_{y'y'}}{E_{x'x'}}, \qquad \rho_{x'y'} = \frac{\sqrt{E_{x'x'}E_{y'y'}}}{2G_{x'y'}} - \sqrt{\nu_{x'y'}\nu_{y'x'}} \tag{2.6}$$

or for out-of-plane material orientation:

$$\lambda_{x'z'} = \frac{E_{z'z'}}{E_{x'x'}}, \qquad \rho_{x'z'} = \frac{\sqrt{E_{x'x'}E_{z'z'}}}{2G_{x'z'}} - \sqrt{\nu_{x'z'}\nu_{z'x'}} \tag{2.7}$$

where E_{ij} is the Young's modulus, ν_{ij} is the Poisson's ratio and G_{ij} is the shear modulus. The material orientations are shown in Figure 2.3. The structural coordinate system (x, y, z) and the material coordinate system (x', y', z') are not oriented in the same way. The structural coordinate system (x, y, z) is oriented such that z is pointing in the direction where the plane strain assumption typically is applied in the modeling and the material coordinate system (x', y', z') is oriented such that x' is pointing in the typical uni-directional (UD) fiber direction of the laminate, see Figure 2.3.

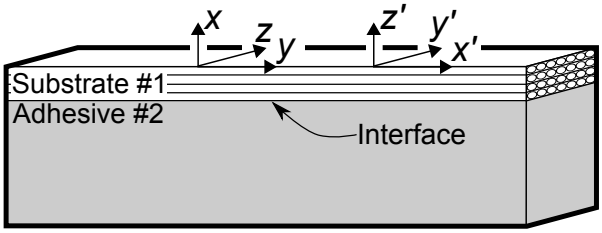

Figure 2.3: Bi-material specimen with adhesive bonded to a uni-directional glass fiber laminate including material coordinate system (x', y', z') and structural coordinate system (x, y, z).

The material properties of the glass fibre reinforced epoxy laminates presented by Leong *et al.* [58] and the material properties of the carbon fibre reinforced epoxy laminate from Yang *et al.* [115] are representative for wind turbine blades. The values for λ and ρ

for a bi-axial glass fiber laminate (Glass Biax), for a uni-directional glass fiber laminate (Glass UD), and for uni-directional carbon fiber laminate (Carbon UD) can be found in Table 2.1.

Material name	$\lambda_{x'y'}$	$\rho_{x'y'}$	$\lambda_{x'z'}$	$\rho_{x'z'}$
Glass Biax	0.92	0.06	0.85	2.79
Glass UD	0.33	2.43	0.33	2.75
Carbon UD	0.08	4.12	0.08	4.41

Table 2.1: Typical material properties for wind turbine blade relevant materials (based on values from Leong *et al.* [58] and Yang *et al.* [115]).

Typical values of $\lambda_{x'y'}$ and $\rho_{x'y'}$ for various materials are presented in Figure 2.4 including the values of Glass Biax, Glass UD and Carbon UD that are marked by "x". If the laminate is assumed isotropic then $E_{x'x'}$ and $\nu_{x'z'}$ are the only stiffness parameters used in the models i.e. $\lambda = \rho = 1$ [102].

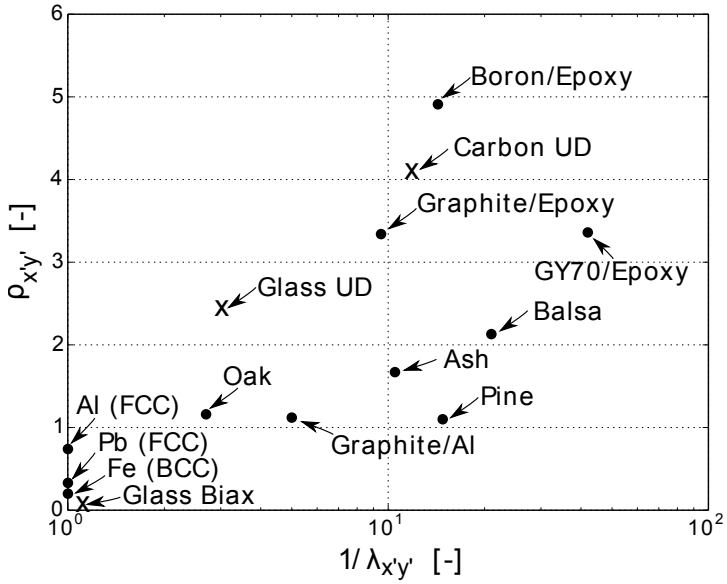

Figure 2.4: Orthotropy parameters $\lambda_{x'y'}$ and $\rho_{x'y'}$ for selected materials. Materials marked by dots are from Suo [99] and materials marked by "x" are the blade relevant materials in Table 2.1.

2.3.2 Bi-material Parameters

When loadings are prescribed as displacements, the stiffness mismatch (elastic) for the bi-material models, e.g. the specimen shown in Figure 2.3, can be presented in terms of three non-dimensional parameters E_1/E_2, ν_1, and ν_2 for the substrate/adhesive. The typical elastic mismatch between the adhesive and an isotropic substrate with stiffness of a uni-directional glass fibre reinforced polyester laminate is $E_1/E_2 \approx 12$.

In turn, when loadings are prescribed as tractions for a bi-material problem, Dundurs' parameters (α, β) can be introduced to reduce the number of non-dimensional parameters from three to two [21, 20, 43]. To apply Dundurs' parameters it is furthermore required that the materials are linear-elastic, isotropic and deformations are planer i.e. plane strain or plane stress. If these requirements are fulfilled, the stress field of bi-material problems with stresses as boundary conditions (not displacement boundary conditions) depends on only two (α, β), and not three (E_1/E_2, ν_1, ν_2), non-dimensional elastic parameters (Dundurs' parameters):

$$\alpha_{12} = \frac{\bar{E}_1 - \bar{E}_2}{\bar{E}_1 + \bar{E}_2}, \qquad \beta_{12} = \frac{\bar{E}_1 f(\nu_2) - \bar{E}_2 f(\nu_1)}{\bar{E}_1 + \bar{E}_2} \tag{2.8}$$

where $\bar{E}_i = E_i/(1-\nu_i^2)$ and $f(\nu_i) = (1-2\nu_i)/[2(1-\nu_i)]$ are for plane strain, and $\bar{E}_i = E_i$ and $f(\nu_i) = (1-2\nu_i)/2$ are for plane stress [71]. If the Poisson's ratios are set constant ($\nu_1 = \nu_2 = 1/3$) then Dundurs' parameters reduce to $\beta = \alpha/4$ in plane strain and $\beta = \alpha/3$ in plane stress [20, 43].

In plane strain the physically admissible values of α and β are restricted to lie within a parallelogram [20]. This parallelogram is enclosed by $\alpha = \pm 1$ and $\alpha - 4\beta = \pm 1$ in the α, β-plane when assuming non-negative values of Poisson's ratio. α and β values for different materials are presented in Figure 2.5. It is illustrated that typical material combinations are enclosed by the parallelogram. Realistic values of Dundurs' parameters (α, β) for the bi-material combination of adhesive-to-substrate (isotropic), where the substrate is Glass Biax, Glass UD or Carbon UD, are marked by "x" in Figure 2.5. It is the laminate stiffness parameter E_{yy} that is used in the computation of α and β for these relevant wind turbine blade materials.

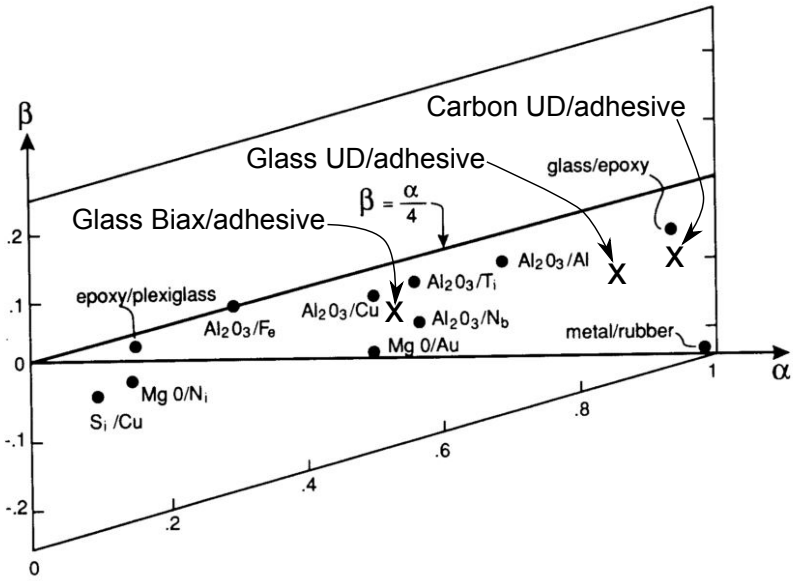

Figure 2.5: Dundurs' parameters in plane strain for selected materials (modified from Suga *et al.* [96] and Hutchinson and Suo [43]).

CHAPTER 3

The Effect of Residual Stresses on the Formation of Transverse Cracks

Residual stresses in the adhesive layer of a bonded joint can build up during the manufacturing process since two pre-manufactured glass fibre laminated shells are produced in a VARTM process and subsequently bonded by a structural adhesive. During the curing process, the structural adhesive heats up and shrinks. Since the adhesive is constrained between stiffer laminates, tensile residual stresses builds up. It is expected that the main contributors to the residual stress is the chemical shrinkage of the adhesive and the differences in elastic strains due to mismatch in coefficients of thermal expansion between the laminate and the adhesive $(\alpha_1 - \alpha_2)$. Often adhesive joints are post cured at higher temperatures in a subsequent process to enhance certain mechanical properties of the adhesive [16, 3], but this elevated temperature can increase the magnitude of residual stresses even further.

Under tensile mechanical straining of the adhesive joint, ϵ_{yy}, the propagation of transverse cracks from small pre-existing voids in the adhesive layer is promoted by residual stresses. Thus, transverse cracks might propagate due to a combination of mechanical stresses, σ_m, and residual stresses, σ_r, in the adhesive as illustrated in Figure 3.1. It is the purpose to measure the residual stresses in a blade relevant component, such as the sandwich specimen in Figure 3.1, and use that measurement to determine the stress at which the first crack propagates and turns into a transverse crack in the adhesive layer. It is the aim to analyze the initiation and propagation of transverse cracks from small pre-existing voids in the adhesive under both static and cyclic loadings.

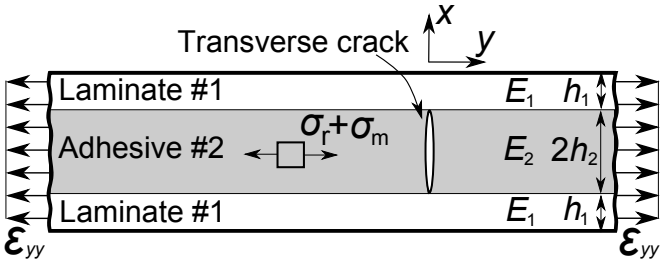

Figure 3.1: Sandwich specimen loaded by tensile strains in the y-direction.

Two sandwich specimen configurations with laminates of different type (Laminate A and Laminate B) will be used for the present study. Both laminates were primarily

made of uni-directional glass fibres oriented in the y-direction and the stiffness were comparable. The same type of adhesive was used for all specimens. The exact properties of the laminates and adhesive are confidential and therefore the results will be presented in a non-dimensional form.

This chapter is organized as follows. First, a new approach will be presented for determination of stress in the adhesive at first crack in the sandwich specimen. The results of a bi-material FE model of the center cracked test specimen will be presented and included as a part of the approach. Hereafter, the residual stress will be determined in five different ways. Experimental tests of sandwich specimens loaded in quasi-static tension will be presented. A model prediction will be compared with the experimental determination of stress in the adhesive at first crack. Furthermore, the sandwich specimens will be loaded cyclic and multiple cracking of the adhesive will be studied.

3.1 Introduction of Residual Stress Model

To measure a realistic value of residual stresses in a wind turbine blade joint, the test specimen must reflect the manufacturing process that is used for adhesive joints in wind turbine blades in order to ensure that the curing conditions, constraining of the adhesive and thermal boundary conditions are realistic. Therefore, the sandwich specimen in Figure 3.1 is a relevant component to analyze in details. It is convenient to relate the residual stress, σ_r, to a socalled misfit stress, σ_T, through a non-dimensional function, q [23]:

$$\sigma_r = q\sigma_T \tag{3.1}$$

where σ_T is defined as the stress induced in an infinitely thin film adhered to an infinitely thick substrate. q is a non-dimensional function accounting for e.g. geometry and elastic properties. The misfit stress cannot be predicted by modeling - it must be measured experimentally [23].

A relation between the misfit stress and the residual stress in the adhesive of the sandwich specimen shown in Figure 3.1 can be derived by equilibrium considerations (interface perfectly bonded) and by Hooke's law in plane stress (x-direction) [93]:

$$\sigma_r = \frac{\sigma_T}{1 + \zeta_2 \Sigma_2} \tag{3.2}$$

where $\Sigma_2 = \left[E_2/(1-\nu_2)\right]/\left[E_1/(1-\nu_1)\right]$ and $\zeta_2 = h_2/h_1$ are the parameters for the sandwich specimen shown in Figure 3.1. The misfit stress, σ_T, of the adhesive can be measured in different ways as demonstrated in section 3.4.

3.2 Approach for Determination of Stress in the Adhesive at First Crack

The approach for determination of stress in the adhesive at first crack, σ_{fc}, in static tensile tests of the sandwich specimen, shown in Figure 3.1, is presented schematic in

Figure 3.2. The determination of σ_{fc} for "(i) Model prediction" and "(ii) Experimental test" will be compared in "(iii) Comparison". These three main elements of the approach will be presented in the next sections.

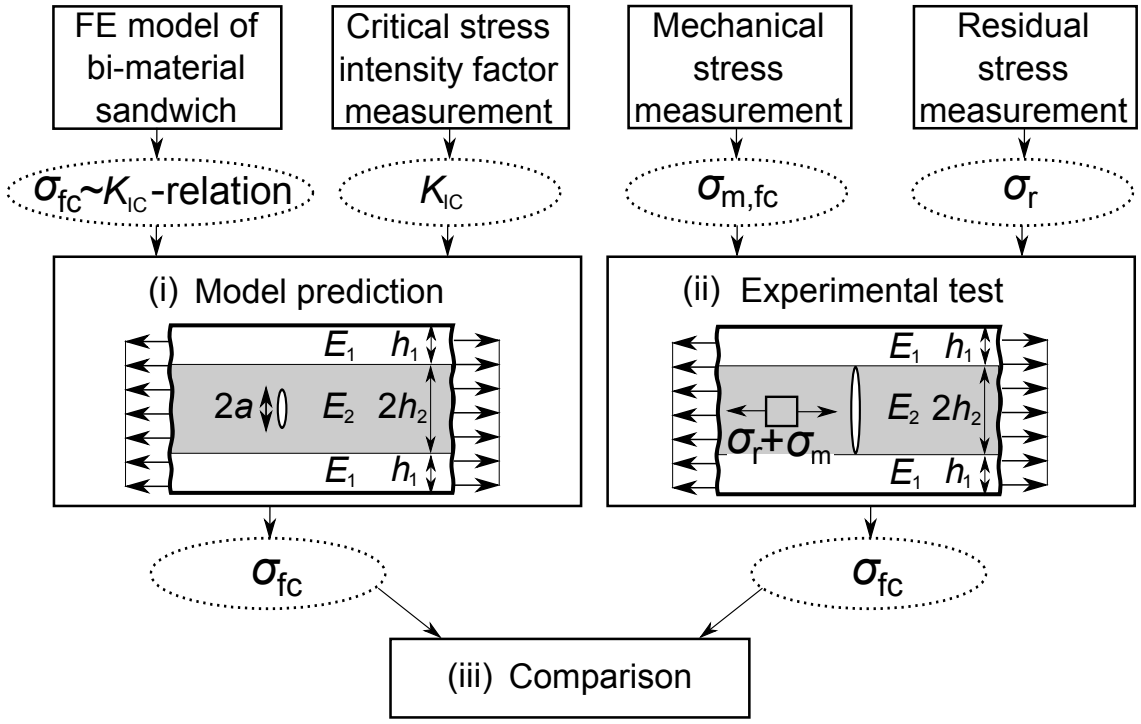

Figure 3.2: Approach for determination of stress in the adhesive at first crack, σ_{fc}. (i) Model prediction. (ii) Experimental test. (iii) Comparison.

3.2.1 Model Prediction

It is assumed that the stress level at which first crack of length, $2a$, in the adhesive of the sandwich specimen in Figure 3.2 (i) can propagate, can be predicted by a relation between the stress in the adhesive at first crack, σ_{fc}, and the mode-I critical stress intensity factor of the adhesive, K_{IC}:

$$\sigma_{fc} = \frac{K_{IC}}{\sqrt{\pi a} F(a/(h_1+h_2), h_1/h_2, E_1/E_2, \nu_1, \nu_2)} \qquad \text{(prediction)} \qquad (3.3)$$

which is a relation on a similar form as for the center cracked test specimen presented by Tada *et al.* [104]. The non-dimensional function, F, accounts for the geometry and the stiffness mismatch between the substrates and the adhesive, and it needs to be determined numerically for this bi-material specimen. K_{IC} of the bulk adhesive should be measured experimentally. Other inputs for the model prediction are the crack length, $2a$, the thickness ratio, h_1/h_2, the stiffness ratio, E_1/E_2, the Poisson's ratio of the substrate, ν_1, and the Poisson's ratio of the adhesive, ν_2.

3.2.2 Experimental Test

For the experimental tests of the sandwich specimens (static tensile loading), shown in Figure 3.2 (ii), the stress in the adhesive at first crack, i.e. the onset of growth of a crack with length, $2a$, is assumed to be the sum of the residual stress, σ_r, and the mechanical stress in the adhesive at first crack, $\sigma_{m,fc}$, as:

$$\sigma_{fc} = \sigma_{m,fc} + \sigma_r \qquad \text{(experimental)} \tag{3.4}$$

where $\sigma_{m,fc}$ can be determined based on the measured strain at first crack, $\epsilon_{m,fc}$, and Hooke's law in plane strain:

$$\sigma_{m,fc} = \bar{E}_2 \epsilon_{m,fc} \tag{3.5}$$

where $\bar{E}_2$ is the plane strain Young's modulus of the adhesive. When the residual stress is determined by (3.2), the stress in the adhesive at onset of first crack can be determined by (3.4).

3.2.3 Comparison of Model Prediction and Experimental Test

In order to test the accuracy of the methods ("Model prediction" and "Experimental test" in Figure 3.2), a comparison will be made at two different temperatures (23°C and −40°C) according to the last step in the approach i.e. Figure 3.2 (iii). The material properties of the adhesive (K_{IC} and E_2) are taken to depend on temperature, T, meaning that σ_{fc} will be a function of $K_{IC}(T)$ and $E_2(T)$. Furthermore, the experimental test method in Figure 3.2 (ii) to determine the stress in the adhesive at first crack experimentally will be applied on other sandwich specimens in order to test the effect of different parameters such as post curing temperature, test temperature and laminate thickness.

3.3 Modeling of the Center Cracked Test Specimen

If a pre-existing crack exists in the adhesive, LEFM with FE simulations can be applied to predict the propagation of the crack.

3.3.1 Methods

The sandwich specimen in Figure 3.1 is comparable to the center cracked test specimen presented by Tada *et al.* [104] where the mode-I stress intensity factor, K_I, is given on the form:

$$K_I = \sigma_{yy,2}\sqrt{\pi a} F(a/h_2) \tag{3.6}$$

where $\sigma_{yy,2}$ is the stress in the adhesive and $2a$ is the crack length, see Figure 3.1 and Figure 3.3. However, the non-dimensional function, F, from Tada *et al.* [104] is only valid in absence of elastic mismatch between the substrate and the adhesive i.e. for the

homogenous specimen. If elastic mismatch is included, the stress intensity factor depends on additional parameters and (3.6) should be modified to:

$$K_I = \sigma_{yy,2}\sqrt{\pi a}F(a/(h_1+h_2), h_1/h_2, E_1/E_2, \nu_1, \nu_2) \tag{3.7}$$

The non-dimensional function, F, is determined numerically by the use of a parametric 2D FE model, simulated in Abaqus CAE 6.14 (Dassault Systemes) with eight-noded plane strain elements.

3.3.2 Results from FE model of the center cracked test specimen

Finite element results are presented in Figure 3.3 in terms of the non-dimensional function, F, and for different elastic mismatch, E_1/E_2. For the homogenous case ($E_1/E_2 = 1.0$), F is compared with the results presented in Tada *et al.* [104] and the maximum deviation is 0.81%. The trend in Figure 3.3 is comparable to the partial cracked film problem from Beuth [11] i.e. F increases with crack length for compliant substrates ($E_1/E_2 \lesssim 1$) and decreases with crack length for stiffer substrates ($E_1/E_2 \gtrsim 4$). Note, $F \to 1.0$ for $a/(h_1+h_2) \to 0$, which is similar to the solution for a center crack in an infinitely large plate of a homogenous material [104].

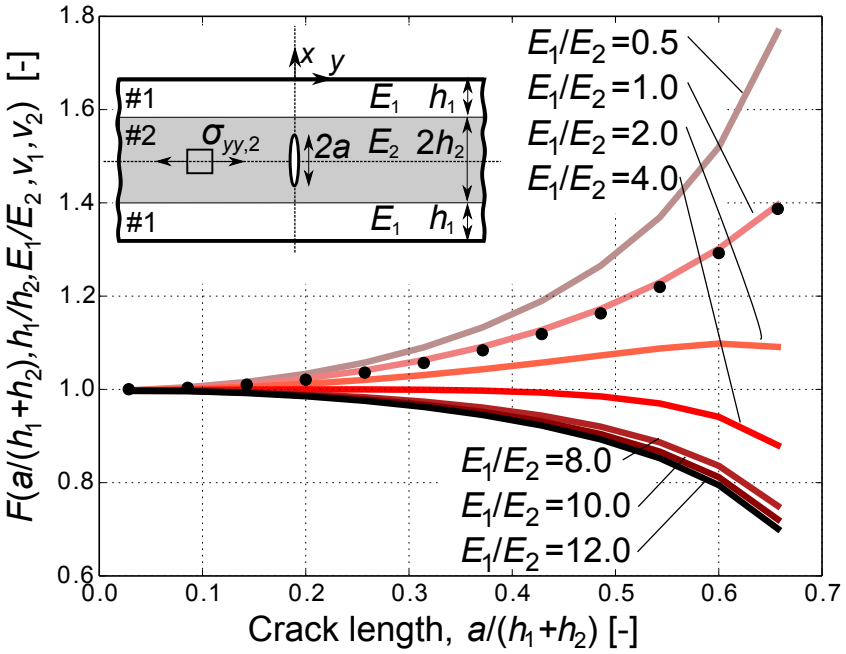

Figure 3.3: Finite element modeling results where $\nu_1 = \nu_2 = 1/3$ and $h_1/h_2 = 0.4$. The interface is located near $a/(h_1+h_2) \approx 0.7$. The FE results are compared with the results (dots) from Tada *et al.* [104] for $E_1/E_2 = 1$.

3.4 Determination of Residual Stresses

3.4.1 Methods and Experimental Procedure

In this section, a new approach is presented that allows the residual stress to be determined in several different ways. The accuracy of four different experimental methods to measure the residual stresses in the adhesive is tested on a single sandwich test specimen (laminate/adhesive/laminate) that is instrumented with strain gauges and fiber Bragg gratings (FBG). Furthermore, FBGs embedded in a symmetric sandwich specimen enable measuring the residual stresses in the different steps in the bonding process. Method 5 is a theoretical estimate that is based on a measured reference temperature and the mismatch in coefficients of thermal expansion.

The sandwich specimen is manufactured (Step 1 to Step 3 shown in Figure 3.4) by applying a structural adhesive between two laminates. The specimens are then cured and post cured. The contraction of the adhesive in the y-direction is indicated by ΔL in Figure 3.4 and Figure 3.5. The stresses in Figure 3.4, $\sigma_{yy,1}$ is compressive and $\sigma_{yy,2}$ is tensile ($\sigma_r = \sigma_{yy,2}$) since the adhesive contracts under the curing process. The four different experimental methods are demonstrated on a single sandwich specimen to determine the misfit stress. Method 1 to 4 that are used to determine the misfit stress experimentally are presented graphically in Figure 3.5. The four experimental methods and the theoretical estimate in Method 5 are summarized as:

- Method 1 - based on strains measured by FBG on sandwich specimen.
- Method 2 - based on dial gauge to measure curvature of bi-layer specimen.
- Method 3 - based on strain gauge and FBG to measure curvature of bi-layer specimen.
- Method 4 - based on strains measured by strain gauge on free laminate.
- Method 5 - based on estimate using a reference temperature.

The principles behind the methods are as follows. After manufacturing, the contraction of the sandwich specimen is measured by the FBG that is embedded in the sandwich specimen as shown in Figure 3.5 (Method 1). One of the laminates is removed and the curvature is measured as shown in Figure 3.5 (Method 2) using a dial gauge. The FBG is now embedded in the adhesive as shown in Figure 3.5 (Method 3) and the strain signals from strain gauge, SG1, and FBG are recorded in order to determine the curvature. Furthermore, strain gauge, SG2, measures a strain on the free laminate as shown in Figure 3.5 (Method 4). The measured curvatures and strains can be used to determine the misfit stress in the adhesive using different analytical models that are presented in Paper P1.

Based on Method 1 to 4 the actual residual stress magnitude in the adhesive is determined unaffected of the mechanism behind i.e. chemical shrinkage, thermal, creep or others. In turn, for Method 5 it is assumed that the only contribution to the residual stress comes from a temperature difference (between curing and test) and the mismatch in coefficient of thermal expansion. The methods are described in Paper P1, where

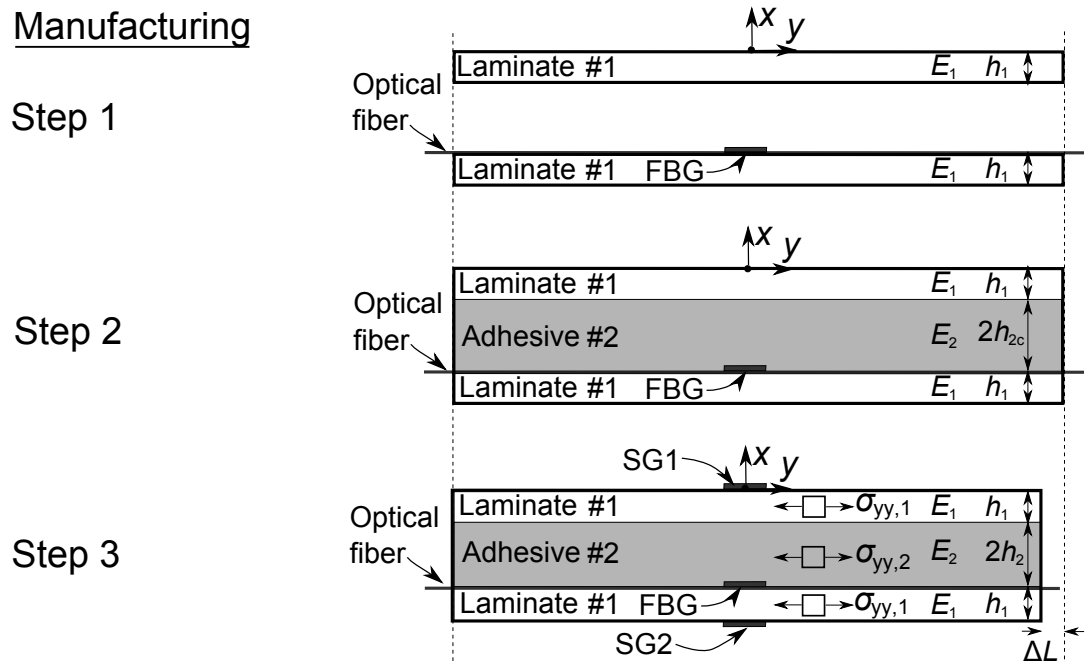

Figure 3.4: Manufacturing procedure. Step 1: Mounting of FBG before injection of the adhesive. Step 2: After injection of the adhesive, but before curing of the adhesive. Step 3: After curing of the adhesive.

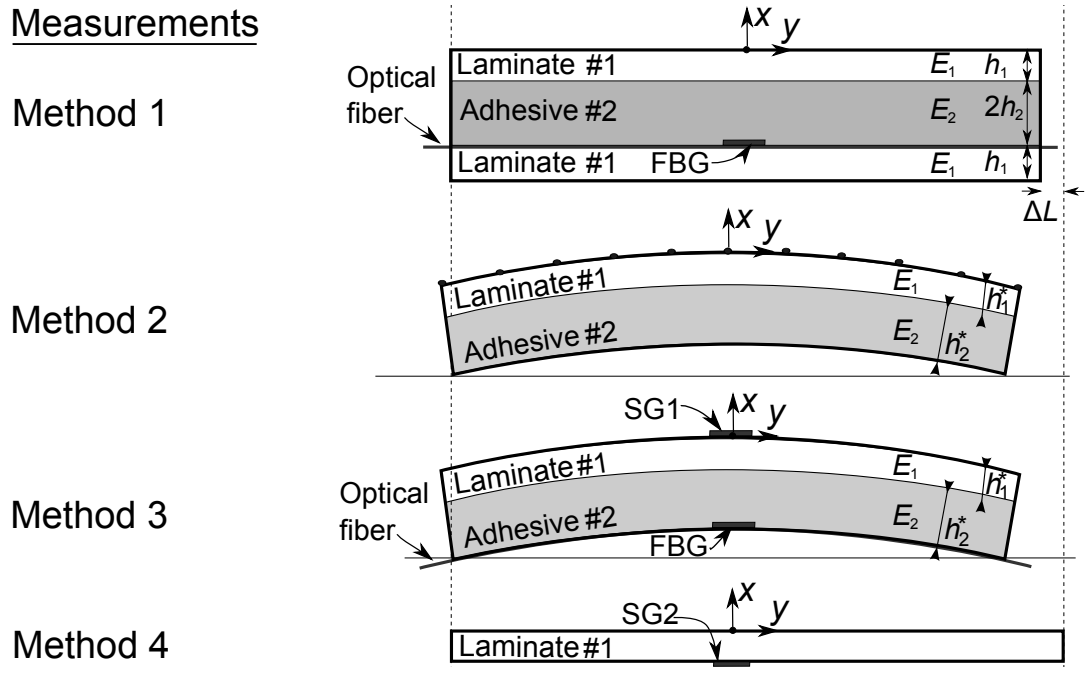

Figure 3.5: Measurement principles after curing. Method 1: Measure strains with FBG. Method 2: Measure curvature of specimens. Method 3: Determine curvature with FBG and SG1. Method 4: Measure strains by SG1 on free laminate.

the specific equations, manufacturing procedure, instrumentation and test setup are presented in details. Only Method 5 is presented here for convenience since this misfit stress result is used for normalization of the measurements by the other methods.

3.4.2 Method 5 - Based on Estimate using a Reference Temperature

The misfit stress in the adhesive can be estimated based the temperature difference between a reference temperature, T_r, e.g. the curing or the post curing temperature, and the current test temperature, T_t [23]. Thus, the misfit stress estimated based on Method 5 is denoted $\sigma_T^{\Delta\alpha}$ and it can be calculated by:

$$\sigma_T^{\Delta\alpha} = \epsilon_T^{\Delta\alpha} \frac{E_2}{(1-\nu_2)} = (\alpha_1 - \alpha_2)(T_t - T_r) \frac{E_2}{(1-\nu_2)} \tag{3.8}$$

where α_1 and α_2 are the coefficients of thermal expansion of the substrate and the bulk adhesive, respectively. The misfit strain by Method 5 is denoted $\epsilon_T^{\Delta\alpha}$. If T_r is assumed to be the peak curing temperature of the adhesive then it can be measured by a thermo-couple inside the adhesive of the joint. In Method 5, it is assumed that the chemical shrinkage of the adhesive is zero and all deformation is elastic [23].

3.4.3 Misfit Stress Reference Value

The misfit stress determined by Method 5 ($\sigma_T^{\Delta\alpha}$) is a theoretical estimate. Beside material properties (α_1, α_2, E_2, ν_2) that were measured experimentally in the lab, the only experimental input to Method 5 is the measured temperatures; $T_R = 23°\text{C}$ and $T_{PC} = 50°\text{C}$, where T_R is the room temperature and T_{PC} is the post curing temperature. The predicted result by Method 5 for $\sigma_T^{\Delta\alpha}$ is used as reference value and therefore used for normalization of the misfit stress measurements obtained by the other methods.

3.4.4 Experimental Results - FBG Strain Measurements during Manufacturing

During manufacturing, the FBG was measuring a uni-axial straining of the sandwich specimen. The interpretation of the results in Figure 3.6 (A-B) are: (numbers indicate manufacturing step according to Figure 3.4 where Step 3 is divided into sub steps)

1. After mounting of the FBG on the laminate.
   - FBGs were mounted and the recorded strain (wavelength) was used as reference for zero since the optical fibre was taken to be stress free.
2. After injection of the adhesive.
   - A few minutes after injection of the adhesive, the measured strain increased.

3a. After curing at room temperature (before demoulding).

- The measured strain decreased after the adhesive had cured at room temperature for 20 hours.

3b. After demoulding (plates were removed from bonding fixture).

- The measured strain was not affected significantly by demoulding (no trend identified).

3c. After post curing (the specimens were still in one sandwich plate).

- The measured strain decreased after post curing.

3d. After cutting of the sandwich plate into specimens.

- When the sandwich specimens were cut out from the sandwich plate, the measured strains decreased.

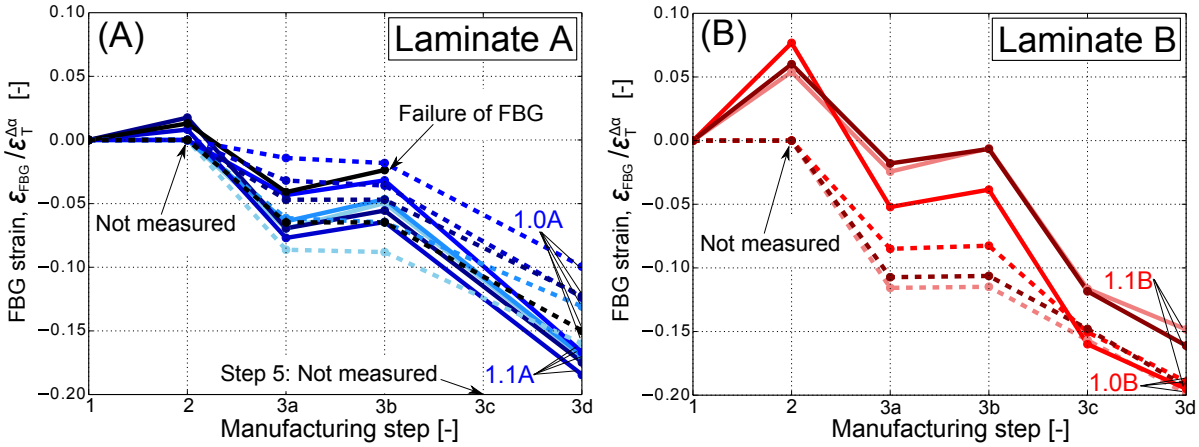

Figure 3.6: Strain measured with FBG during the manufacturing steps with four different test series of sandwich specimens: (A) Laminate A (1.0A with dashed line and 1.1A with solid line). (B) Laminate B (1.0B with dashed line and 1.1B with solid line).

All FBG strains were measured at room temperature in the laboratory, but in Step 2 the adhesive had just started to generate exothermal heat. This temperature effect explains why the measured strain increased for Step 2 in Figure 3.6. The manufacturing Step 3c (post curing) is identified, based on Figure 3.6, as the step in the manufacturing process where the primary residual stress builds up. Manufacturing Step 3a (curing at room temperature) is identified as the second most important step in the manufacturing step wrt. residual stress.

3.4.5 Experimental Results - Misfit Stress for Method 1 to 5

The misfit stress results determined using Method 1 to 5 are presented in Figure 3.7 for Laminate A and Laminate B, where Method 1 to 4 is shown graphically in Figure 3.5.

The results from test series 1.0A, 1.0B, 1.1A and 1.1B in Figure 3.7 are taken from the last measurement (manufacturing Step 3d) with FBG in Figure 3.6 i.e. for four different test series (1.0A, 1.0B, 1.1A, 1.1B) with 3-6 samples each.

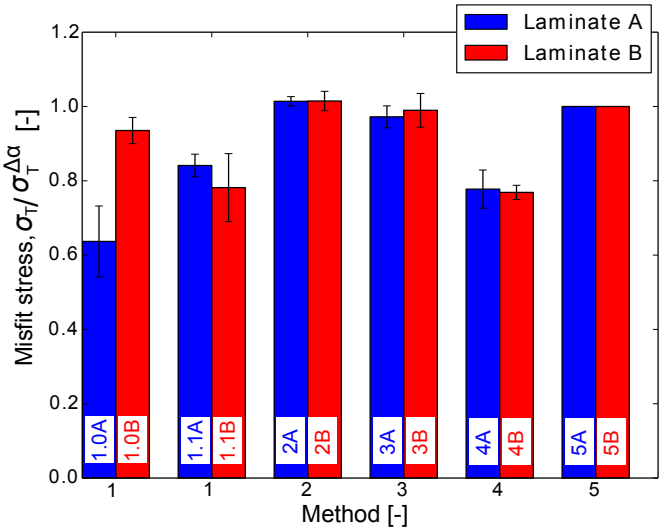

Figure 3.7: Misfit stress results determined experimentally by Method 1 to 5.

The misfit stress results from Method 1 and 4, which are based on strain measurements (FBG and SG2), are lower than the misfit stress results determined by the other methods. The results from Method 2 and 3 are based on the determined curvature of the bi-layer specimen, which could be an explanation of the similarity between these results. It is noticeably that the results from Method 2, 3 and 5 are relatively close and with a small standard deviation as indicated by the error bars in Figure 3.7.

3.5 The Formation of Transverse Cracks in Adhesive Joints

Specimens with a layer of structural adhesive sandwiched in between two laminates, see Figure 3.1, were tested in quasi-static tension. The details of the manufacturing procedure and experimental test setup can be read in Paper P1. The main results from the tests will be presented here.

3.5.1 Results for Stress in the Adhesive at First Crack - Comparison of Prediction with Experimental Tests

Propagation of a crack from a small void in the adhesive of the sandwich specimens was observed on images taken during the experimental tensile tests e.g. as shown in Figure 3.8. However, crack propagation from the void towards the adhesive-laminate interface was rapid, and instantaneously the crack propagated across the width of the specimen (in z-direction). The stress in the adhesive at onset of propagation of first transverse crack

from a small void, σ_{fc}, was determined at temperatures of 23°C and −40°C using the two different methods of the approach in Figure 3.2 i.e. based on "(i) Model predictions" and based on "(ii) Experimental tests".

The input parameters for the two methods were measured experimentally on the bulk materials in the laboratory. The material properties of the adhesive were measured at temperatures of 23°C and −40°C on specimens that were manufactured under similar process conditions as the sandwich specimens. The mode-I critical stress intensity factor, K_{IC}, was measured by a compact tension test of the bulk adhesive using the standard "ASTM D5045" at temperatures of 23°C and −40°C. The Young's modulus of the adhesive, E_2, was measured by a dog bone specimen using the standard "ISO 527-2: 2012" at temperatures of 23°C and −40°C.

(i) Prediction: The stress in the adhesive at first crack of the sandwich specimen shown in Figure 3.1 can be predicted based on the FE model and equation 3.3. As an approximation the crack length, $2a$, was taken to be the maximum measured void size in the adhesive of the sandwich specimens. The size of the six largest voids in the adhesive of the sandwich specimen in Figure 3.8 was measured to an average of $a/(h_1+h_2) \approx 0.042$ with a standard deviation of ± 0.01. Thus, the value of the non-dimensional function, F, could be determined based on the modeling result in Figure 3.3 to $F \approx 1$. Having determined K_{IC}, F and a, the value of σ_{fc} was determined by equation 3.3 and presented in Figure 3.9.

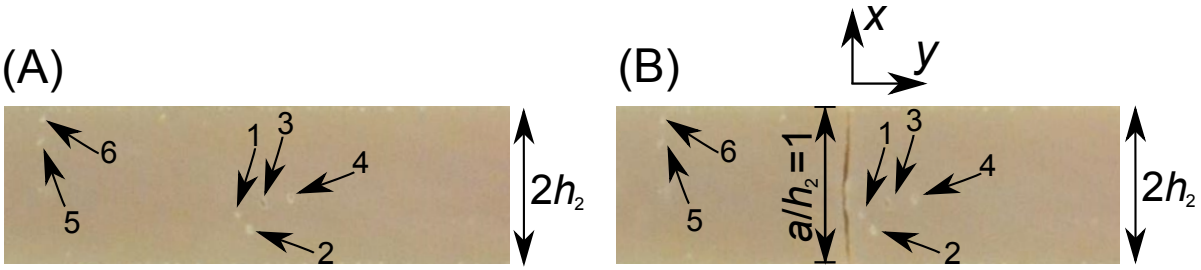

Figure 3.8: The sizes of six voids in the adhesive layer of a sandwich specimen loaded in tension were measured on a photo. (A) Before transverse cracking. (B) After transverse cracking.

(ii) Experimental test: For experimental tests of two series of sandwich test specimens (23°C and −40°C), the stress in the adhesive at first crack, σ_{fc}, was taken to be the sum of the residual stress and the mechanical stress as shown in equation 3.4. For the experimental tests, $\sigma_{m,fc}$ was determined based on the measured mechanical strain from the clip gauge, $\epsilon_{m,fc}$, using equation 3.5. The misfit stress was determined at 23°C by Method 2 and at −40°C by Method 5 (section 3.4.2). Thus, the residual stress, σ_r, could be determined based on equation 3.2 and finally σ_{fc} could be calculated by equation 3.4. This experimental result are presented in Figure 3.9.

(iii) Comparison: A comparison between the predicted results and the experimental results for σ_{fc} at temperatures of 23°C and −40°C is presented in Figure 3.9. It was

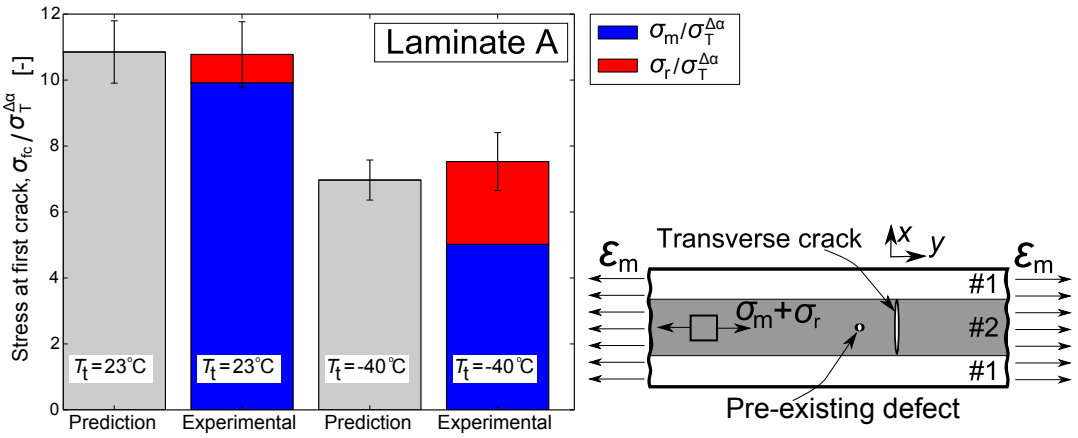

Figure 3.9: Results for stress in the adhesive at first crack for temperatures of 23°C and −40°C. Benchmark of prediction with experimental test results using the approach in Figure 3.2.

a hypothesis that equation 3.3 could be used to predict σ_{fc} although the FE model was developed for an infinitely sharp start-crack based on LEFM whereas the shape of the pre-existing cracks in the adhesive layer of the sandwich specimens were more uncertain. However, this hypothesis cannot be rejected since the error bars for the "Experimental" and "Prediction" in Figure 3.9 overlaps i.e. the prediction is close to the experimental results for both 23°C and −40°C. Since results from two independent methods determined at two very different temperatures are consistent, the methods seems to be promising for the determination of σ_{fc} for the sandwich specimens. Therefore, in the next sections, the experimental method in Figure 3.2 (ii) is applied to investigate the effect of different parameters (post curing temperature, test temperature, laminate thickness) on the magnitude of σ_{fc}.

3.5.2 Results from Tensile Tests of Sandwich Specimens under Quasi-Static Loading

The effect of post curing temperature on the stress in the adhesive at first crack of the adhesive joint was tested experimentally under quasi-static loading using the sandwich specimen shown in Figure 3.1. The sandwich specimens were post cured at 50°C, 70°C, and 90°C for 24 hours. The misfit stresses for the corresponding post curing temperatures were determined using bi-layer specimens cut out from the same plate as the sandwich specimens. The residual stress, σ_r, was then calculated based on equation 3.2. The determination of residual stress and the experimental test setup for testing the sandwich specimens can be read in details in Paper P1.

The results for the stress in the adhesive at first crack are presented in Figure 3.10 (A) for different post curing temperatures. From the results presented in Figure 3.10 (A), it is seen that with increasing post curing temperature, the stress in the adhesive at first crack decreases in a nearly linear manner. This trend can to some extend be explained

by an increase in residual stresses since the residual stresses increased with increasing post curing temperature. The residual stress, σ_r, was determined to approx. 8-14 % of σ_{fc} in the tests with different post curing temperature.

The results, presented in Figure 3.10 (B) show that as the test temperature decreases, the stress in the adhesive at first crack decreases. This trend can also (to a certain extend) be explained by an increase in residual stresses. Since the magnitude of σ_{fc} differs for the different tests, the fracture toughness of the adhesive is most likely affected by the low temperatures (or the high post curing temperatures). The residual stress, σ_r, was determined to approx. 25-40 % of σ_{fc} in the low temperature tests.

The results for the stress in the adhesive at first crack for laminate thickness of $h_1/h_2 = 0.45$, $h_1/h_2 = 0.65$, and $h_1/h_2 = 0.85$ are presented in Paper P1. The main finding was that the effect of laminate thickness on the stress in the adhesive at first crack was small for the configurations tested.

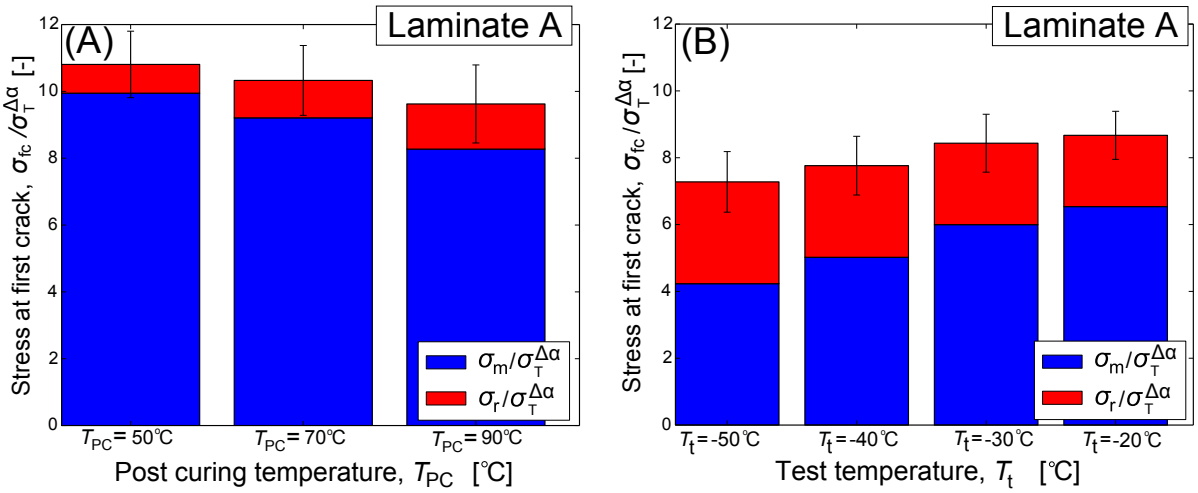

Figure 3.10: Results from static tensile tests for the stress in the adhesive at first crack of the sandwich specimens. (A) The effect of post curing temperature. (B) The effect of test temperature.

3.5.3 Results from Tensile Tests of Sandwich Specimens under Cyclic Loading

The effect of laminate thickness on the cycles to first crack in the adhesive layer of the sandwich specimens with Laminate B were tested for three configurations ($h_1/h_2 = 0.45$, $h_1/h_2 = 0.65$, and $h_1/h_2 = 0.85$). The residual stress in the adhesive of the sandwich specimen was determined from the misfit stress measurement by Method 2 and by equation 3.2. The residual stress increased the mean stress in the adhesive, but not the stress amplitude. This means that the residual stress increased the load R-ratio ($R = \sigma_{min}/\sigma_{max}$) experienced by the adhesive from $R = 0.1$ to $R \approx 0.22 - 0.30$ for the present tests.

The maximum mechanical strain, $\epsilon_{m,max}$, applied in the fatigue test is normalized by the average mechanical static strain at first crack, $\bar{\epsilon}_{m,st}$, and the numbers on the second axis in Figure 3.11 are removed due to confidentiality. It is shown in Figure 3.11 (by the triangles) that the number of cycles for the first transverse crack to initiate in the adhesive of the sandwich specimen is comparable for the different laminate thickness tested ($h_1/h_2 = 0.45$, $h_1/h_2 = 0.65$, and $h_1/h_2 = 0.85$). This suggests that crack initiation in the adhesive is primarily driven by stress level and defect size, and less sensitive to the thickness of the laminate. A tendency of the subsequent cracks in the adhesive is difficult to identify. However, it seems like the transverse cracks appears earlier for the smaller ratios of h_1/h_2. The results in Figure 3.11 show that multiple transverse cracks in the adhesive developed in a stable manner and were measurable.

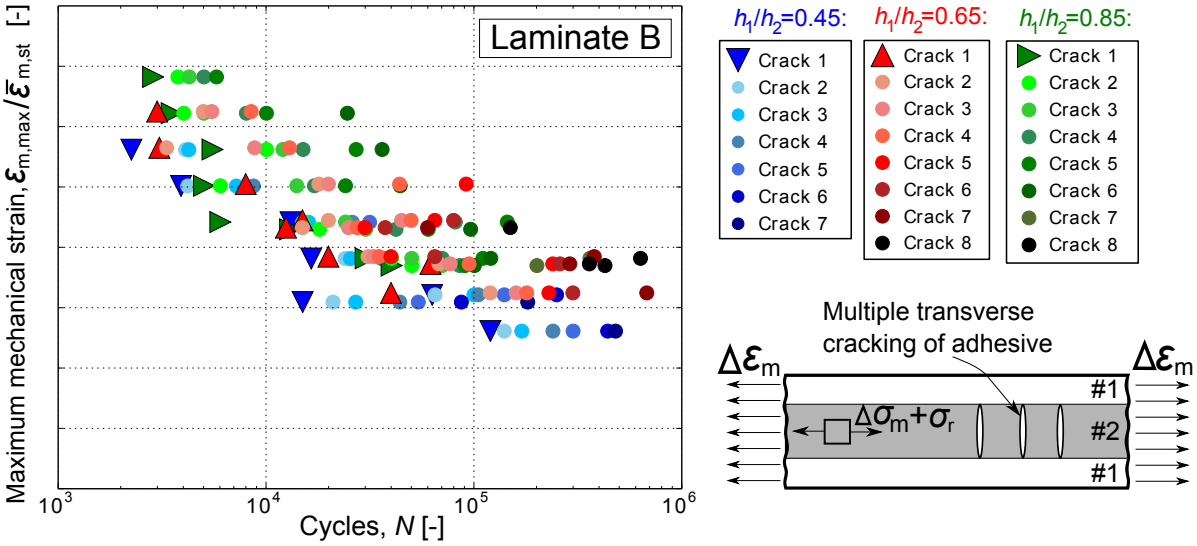

Figure 3.11: Transverse crack measurements from fatigue tests of sandwich specimens with different thickness of laminates. The orientation of the triangles indicate first crack in the adhesive for $h_1/h_2 = 0.45$, $h_1/h_2 = 0.65$ and $h_1/h_2 = 0.85$. Dots indicate multiple cracks from Crack 2 and onwards.

3.6 Conclusions

Prediction of stress in the adhesive at first crack in the sandwich specimen loaded in tension (using a new bi-material FE model) were found to agree well with experimental results obtained at temperatures of 23°C and −40°C. Dependent on the test temperature and processing conditions, the residual stress was determined to ∼8-40% of the stress in the adhesive at first crack of the sandwich specimens meaning that the residual stresses were relatively significant. The cyclic loaded tests confirmed that the design of the sandwich specimen was damage tolerant since multiple cracks in the adhesive developed in a stable manner.

CHAPTER 4
Tunneling Cracks in Adhesive Bonded Joints

Tunneling cracks have been modeled extensively through the last three decades using the concepts of LEFM [100, 43, 41, 97, 98, 6, 10]. From a modeling perspective, tunneling cracks are closely related to channeling cracks in thin films [105, 11, 108, 107, 9]. As introduced in the state of the art literature in section 1.3, one of the first models of a single tunneling crack embedded in-between two substrates were developed using 2D FE simulations and LEFM by Ho and Suo [100, 41].

Material orthotropy of the substrates and the adhesive layers can also be accounted for using FE simulations as demonstrated by Yang *et al.* [115] and Beom *et al.* [10]. In the work of Beom *et al.* [10], orthotropy was only modeled for the adhesive layer meaning that the tunneling crack model was limited to isotropic substrates of infinitely thickness. In a wind turbine blade joint the adhesive can be assumed isotropic, but the substrates are laminates of finite thickness manufactured of several layers of different types of materials. These materials are typically uni-directional (UD) and bi-axial (Biax) glass fibre reinforced laminates that can be assumed to be orthotropic.

This chapter is organized in two main sections. The first section covers a numerical study of a tunneling crack in a wind turbine blade joint with focus on the effect of embedding a buffer-layer to reduce the tunneling crack energy release rate. In the second section, the tunneling crack model will be included in a novel approach to predict the cyclic crack growth rate for tunneling cracks propagating across the adhesive layer of a wind turbine blade joint.

4.1 The Effect of a Buffer-layer on the Propagation of a Tunneling Crack

A trailing-edge joint in a wind turbine blade consists of an adhesive layer constrained in-between stiffer laminates as shown in Figure 4.1. Observations from this joint loaded in tension show that cracks may initiate at the free-edge and propagate through the adhesive layer as a tunneling crack constrained by the laminates. A potential way to prevent tunneling crack propagation across the adhesive layer of the joint is to add a new layer, called a buffer-layer, near the adhesive and control the stiffness- and thickness of this layer in order to reduce the steady-state energy release rate.

Therefore, the objective is to study the effect of in-plane stiffness, $\bar{E}_i$, and thickness, h_i, on the steady-state energy release rate for a structural adhesive joint with material properties that are realistic for wind turbine blade joints. More specifically, it is the aim

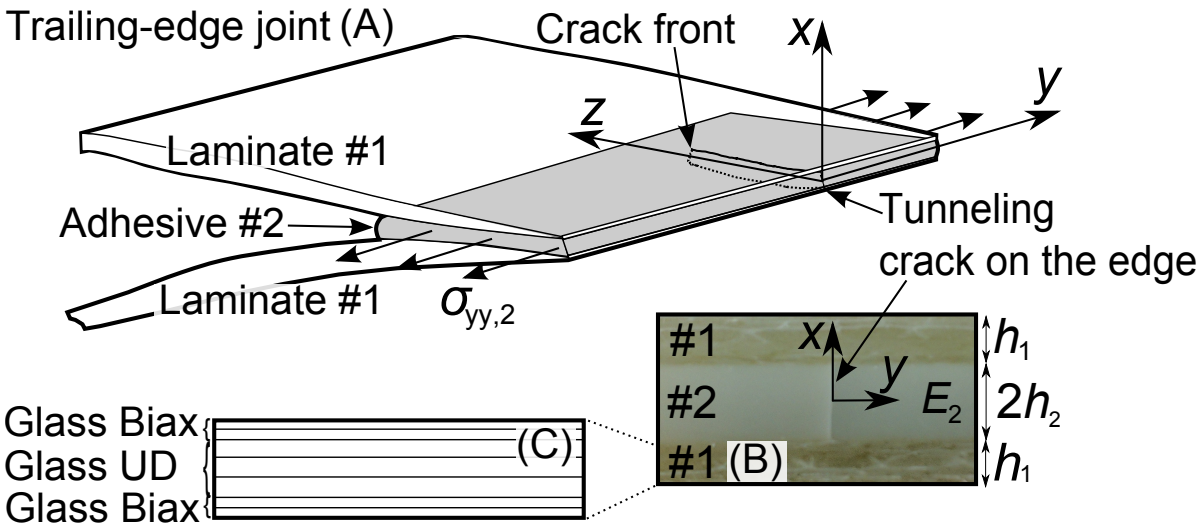

Figure 4.1: (A) Trailing-edge joint with a tunneling crack propagating across the adhesive layer in z-direction. (B) Photo of a tunneling crack in a trailing-edge wind turbine blade joint. (C) Typical layers in a laminate of a trailing-edge joint.

to determine the effect of a buffer-layer on the steady-state energy release rate for an isolated tunneling crack in the adhesive layer. This should lead to design rules for an improved joint design.

The design idea of embedding a buffer-layer for improvement of the joint is novel, but the implications and effects of this buffer-layer needs to be investigated. Therefore, a new symmetric tri-material FE model is developed for the purpose with the geometry presented in Figure 4.2, where h_1 is the thickness of the substrate, $2h_2$ is the thickness of the adhesive and h_3 is the thickness of the buffer-layer. E_2 is the Young's modulus of the adhesive.

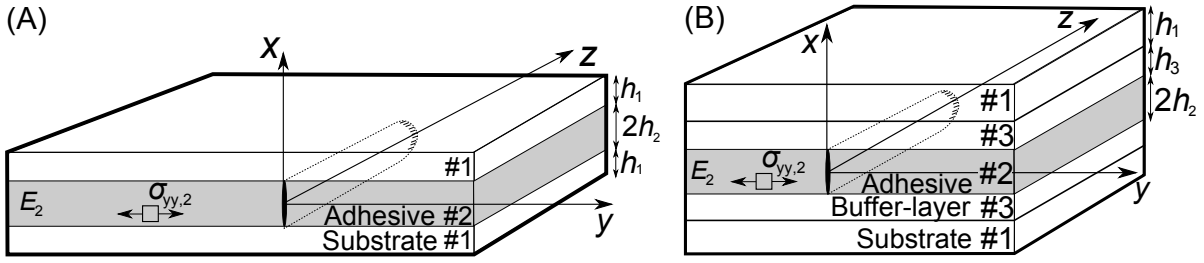

Figure 4.2: (A) Bi-material model. (B) Tri-material model.

The material properties used in the study are presented in Table 4.1 and are comparable to the values provided by Leong *et al.* [58] for Glass Biax and Glass UD and by Yang *et al.* [112] for Carbon UD, see also section 2.3.1. For the substrate $i = 1$ and for the

buffer-layer $i = 3$ according to Figure 4.2. The Poisson's ratio is set to $\nu_1 = \nu_2 = \nu_3 = 1/3$ meaning that Dundurs' second parameter is $\beta = \alpha/4$ in plane strain. The bi-material properties in Table 4.1 for α_{i2} and β_{i2} are characterizing the elastic mismatch between the substrate and the structural adhesive.

	Isotropic				Orthotropic			
Material name	α_{i2}	β_{i2}	λ	ρ	α_{i2}	β_{i2}	λ	ρ
Glass Biax	0.54	0.13	1.00	1.00	0.54	0.13	1.00	0.67
Glass UD	0.85	0.21	1.00	1.00	0.85	0.21	0.26	1.62
Carbon UD	0.94	0.23	1.00	1.00	0.94	0.23	0.11	2.69

Table 4.1: Material properties for "blade relevant materials". For α_{i2} and β_{i2}, material #2 is a typical structural adhesive.

4.1.1 Methods - Finite Element Modeling of a Tunneling Crack

Typically, tunneling cracks initiate from a penny shaped flaw or an edge defect [41]. When the tunneling crack in Figure 4.1 (A) reaches a certain length from the edge (in z-direction), the energy release rate becomes steady-state. The general problem of steady-state tunneling cracking was analyzed by Ho and Suo [41, 100]. The steady-state energy release rate of a tunneling crack, $\mathcal{G}_{ss}$, can be determined by [41, 100]:

$$\mathcal{G}_{ss} = \frac{1}{2}\frac{\sigma_{yy,2}}{2h_2}\int_{-h_2}^{+h_2}\delta_{cod}(x)dx \tag{4.1}$$

where $\sigma_{yy,2}$ is the far field stress in the cracked adhesive layer and $\delta_{cod}(x)$ is the crack opening displacement profile for the plane strain crack. In this work, $\delta_{cod}(x)$ will be determined by a 2D FE model with eight-noded plane strain elements simulated in Abaqus CAE 6.14 (Dassault Systemes). Numerical integration will be used to evaluate the integral in (4.1).

Alternatively, for the elementary case of a central crack in a homogenous and infinitely large plate, i.e. a Griffith crack [28] with $\alpha_{12} = 0.0$ and $h_1/h_2 \to \infty$, the crack opening displacement can be determined by [100]:

$$\delta_{cod} = \frac{4\sigma_{yy,2}}{\bar{E}_2}\sqrt{(h_2^2 - x^2)} \tag{4.2}$$

Inserting equation 4.2 into equation 4.1 gives [41, 100]:

$$\mathcal{G}_{ss} = \frac{\pi}{4}\frac{\sigma_{yy,2}^2 2h_2}{\bar{E}_2} \qquad \text{(asymptotic limit)} \tag{4.3}$$

This asymptotic limit, established by Ho and Suo [41, 100], is representing the mode-I steady-state energy release rate of a tunneling crack in a homogenous structure with infinitely thick substrates. Therefore, it is convenient to normalize other energy release rate results with this elementary case i.e. $[(\sigma_{yy,2}^2 2h_2)/(\bar{E}_2)]$.

4.1.2 Results from Finite Element Modeling

Finite element results are presented in Figure 4.3 and compared with the modeling results by Ho and Suo [41] in order to test the accuracy of the model implementation. For $\alpha_{12} = 0.0$ in Figure 4.3 (A), the deviation between the numerical solution and the *asymptotic limit* (Ho and Suo [41]) of $\pi/4$ in equation 4.3 is less than 0.3% when $h_1/h_2 \geq 6.0$. The trend of the modeling results in Figure 4.3 (B) is that the steady-state energy release rate, $\mathcal{G}_{ss}$, decreases with increasing substrate stiffness and -thickness. The maximum deviation between the curve for $h_1/h_2 = 2.0$ in Figure 4.3 (B) and the modeling results by Ho and Suo is below 2%.

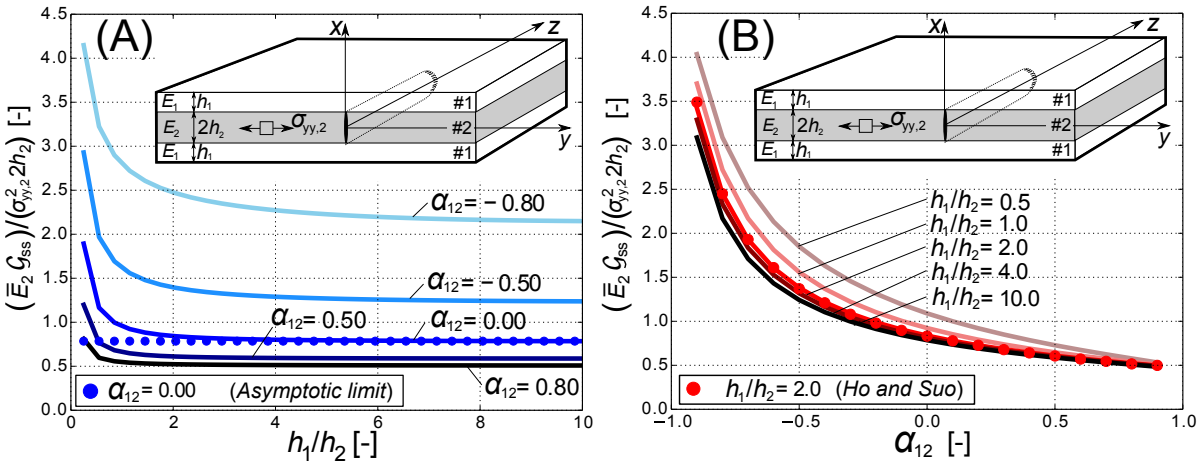

Figure 4.3: (A) FE results from bi-material model compared with the asymptotic limit ($\pi/4$) from Ho and Suo [41]. (B) FE results from bi-material model compared with the results by Ho and Suo [41]. Materials are modeled as isotropic and $\beta_{12} = \alpha_{12}/4$.

The bi-material model in Figure 4.2 (A) is extended by embedding a buffer-layer, named #3 in Figure 4.2 (B), to investigate the effect of buffer-layer stiffness and -thickness on $\mathcal{G}_{ss}$. For the tri-material model, design curves are presented in Figure 4.4 where α_{32} is varied for different h_3/h_2 and α_{12}. The design curves in Figure 4.4 for each stiffness mismatch, α_{12}, intersect at a specific point, namely the "point of intersection" (PoI) that is marked with "X" in Figure 4.4. On the right hand side of the "point of intersection" ($\alpha_{32} >$ PoI), it is advantageous to increase the buffer-layer thickness. In turn, on the left hand side of the "point of intersection" ($\alpha_{32} <$ PoI), it is advantageous to decrease the buffer-layer thickness. It can also be seen in Figure 4.4 that with increasing α_{12} the "point of intersection" moves to the right (to a larger α_{32} value).

Another study with the tri-material FE model is presented in Figure 4.5. The substrates are modeled as both isotropic and orthotropic with the properties in Table 4.1 in order to investigate the effect of material orthotropy on $\mathcal{G}_{ss}$. Glass Biax and Carbon UD are used as buffer-layers in the study and the properties of the basis substrate are

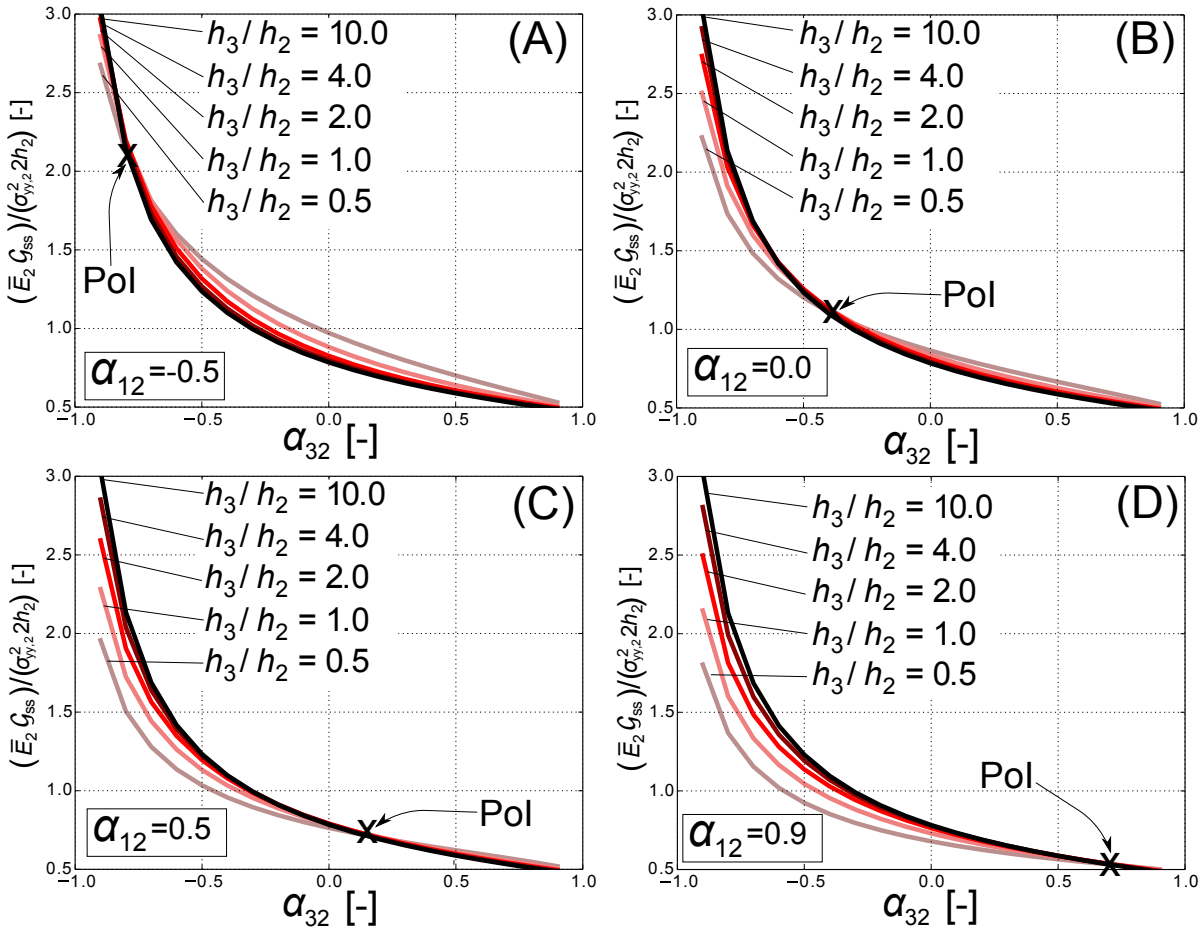

Figure 4.4: Steady-state energy release rate results from a symmetric tri-material FE model with isotropic materials and selected parameters fixed: $\beta_{i2} = \alpha_{i2}/4$, $h_1/h_2 = 1.0$. Substrate stiffness mismatch of: (A) $\alpha_{12} = -0.5$, (B) $\alpha_{12} = 0.0$, (C) $\alpha_{12} = 0.5$ and (D) $\alpha_{12} = 0.9$.

taken from Glass UD. As shown in Table 4.1, the stiffness of Glass Biax is lower than the stiffness of the substrate (Glass UD), whereas the stiffness of Carbon UD is higher than that of the substrate (Glass UD).

In the first case, the stiffness of the substrate is comparable to a uni-directional glass fibre reinforced laminate and the stiffness of the buffer-layer is similar to a glass fibre reinforced bi-axial laminate according to the material properties for Glass UD and Glass Biax in Table 4.1. The buffer-layer thus has a lower stiffness than the (original) substrate. Figure 4.5 shows that an increase of h_3 increases $\mathcal{G}_{ss}$ although the total thickness of the substrate $(h_1 + h_3)$ increases. This can be explained by the stiffer substrate is moved further away from the tunneling crack tip and by the lower stiffness of the buffer-layer closest to the adhesive that is reducing the constraint. The effect of material orthotropy when Glass Biax is used as buffer layer is small (below 2%).

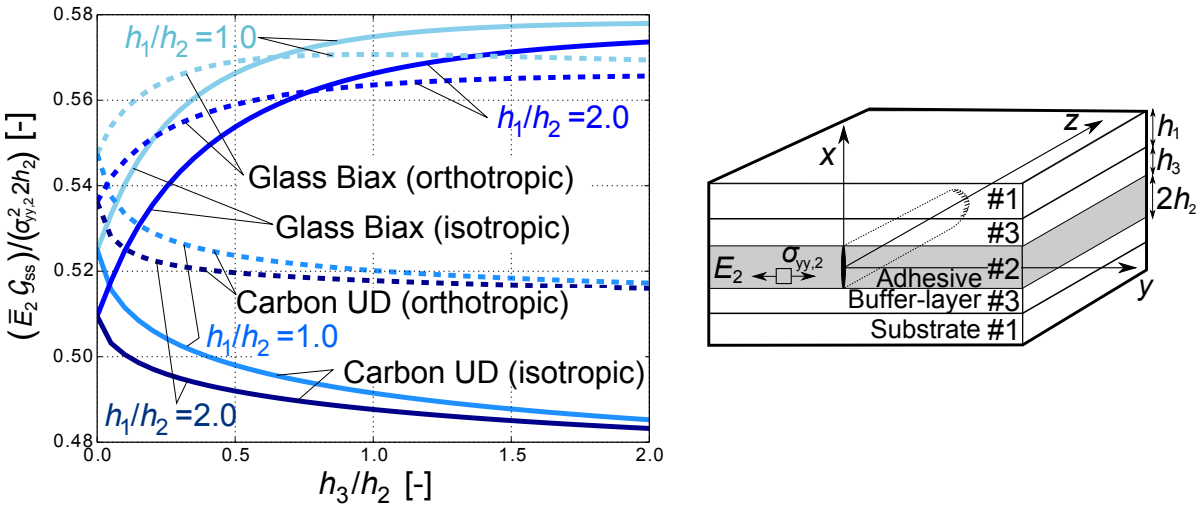

Figure 4.5: Steady-state energy release rate results from a symmetric tri-material FE model with blade relevant material combinations. Solid lines and dashed lines represent isotropic- and orthotropic material properties, respectively. The FE model is simulated with $\alpha_{12} = 0.85$ and $\beta_{i2} = \alpha_{i2}/4$. For the model with the less stiff Glass Biax (isotropic): $\alpha_{32} = 0.54$, and for model with the stiffer Carbon UD (isotropic): $\alpha_{32} = 0.94$.

For the second case, presented in Figure 4.5, the in-plane stiffness of the buffer-layer is increased meaning that the stiffness is comparable to that of a unidirectional carbon fibre reinforced laminate with material properties of Carbon UD in Table 4.1. In this case, the stiffness of the buffer-layer is higher than the stiffness of the substrate. The thickness of the buffer-layer, h_3, is varied, which shows that an improved design for reducing $\mathcal{G}_{ss}$ would be to embed a thick- and stiff layer closest to the adhesive. The effect of material orthotropy when Carbon UD is used as buffer layer is relatively small (below 7%), whereas the largest difference between buffer-layers of Glass Biax (isotropic) and Carbon UD (isotropic) in Figure 4.5 is about 18%.

The results in Figure 4.5 can also be used to determine the best compromise between buffer-layer thickness, -stiffness and -price since too many carbon layers would be costly in comparison with the constraining effect achieved. However, adding carbon layers to an already stiff uni-directional glass fibre laminate will only decrease $\mathcal{G}_{ss}$ by approx. 5-6% (for the isotropic case) according to Figure 4.5. Instead, from a practical point of view, it is more beneficial to decrease the adhesive thickness, $2h_2$, since $\mathcal{G}_{ss}$ scales linearly with $2h_2$ when all other non-dimensional parameters are kept fixed.

4.2 Prediction of Crack Growth Rates for Tunneling Cracks

A generic tunneling crack tool is presented for the prediction of crack growth rates for tunneling cracks propagating across a bond-line in a wind turbine blade under high cyclic loadings. The main input to the tool is the mode-I Paris law for the adhesive that is measured experimentally in the laboratory using a moment-loaded double cantilever beam specimen. Another input is the residual stresses in the adhesive that are determined from measured curvature of bi-layer specimens. Additionally, the generic tunneling crack tool takes input from blade geometry, -loads, and -constitutive properties, see Figure 4.6. Here, the dashed square at position $z = a_i(N_i)$ shows the crack configuration that is analyzed using a plane strain condition (in z-direction) and LEFM modeling. To apply Dundurs parameters (α, β) in the x-y plane [21, 20], it is also a prerequisite that the materials are isotropic, linear-elastic and deformations are planar i.e. either plane stress or plane strain. These prerequisites are satisfied for the sandwich in Figure 4.1 (B) if the adhesive and laminates are assumed isotropic, linear-elastic and the tunneling crack has reached a certain length from the edge (in z-direction) i.e. the crack propagates under steady-state conditions.

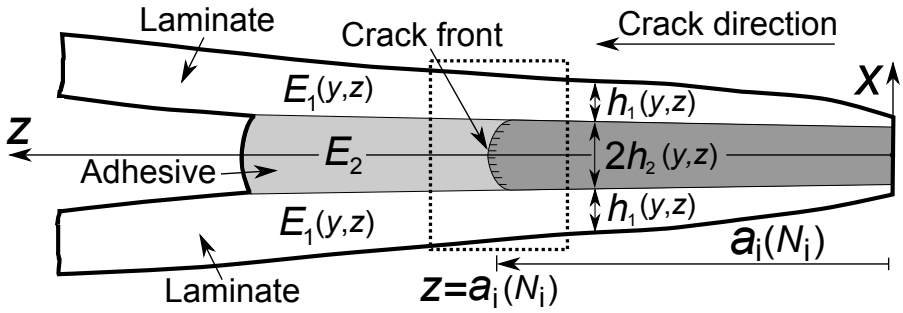

Figure 4.6: Tunneling crack configuration in the trailing-edge joint.

In order to demonstrate the applicability of the tool, model predictions are compared with measured crack growth rates from a full scale blade tested in an edgewise fatigue test in the laboratory. Tunneling cracks in the adhesive layer of the trailing-edge joint are monitored as they propagate under excessive high cyclic loadings.

4.2.1 Approach

The tunneling crack tool takes the local -stiffness and -geometry input from blade models/measurements including the mechanical stress, σ_m, and the residual stress, σ_r, in the adhesive, see e.g. Figure 3.1. In the real structural blade application shown in Figure 4.6, these many parameters depend on the crack tip location (y, z). This dependence on (y, z) for each tunneling crack complicates the modeling significantly. Therefore, the mode-I steady-state energy release rate, $\mathcal{G}_{ss}$, for a single isolated tunneling crack, shown

in Figure 4.6, should be determined by [41]:

$$\mathcal{G}_{ss}(y,z) = \frac{[\sigma_m(y) + \sigma_r(y,z)]^2 2h_2(y,z)}{\bar{E}_2} f\left[\alpha(y,z), \beta(y,z), h_1(y,z)/h_2(y,z)\right] \qquad (4.4)$$

where subscripts 1 and 2 refer to substrate and adhesive, respectively. f is a non-dimensional function that is determined by 2D FE simulations. Since the loading is cyclic, $\mathcal{G}_{ss}$ varies in between a minimum and a maximum value that are denoted $\mathcal{G}_{ss}^{min}$ and $\mathcal{G}_{ss}^{max}$, respectively. $\mathcal{G}_{ss}^{min}$ and $\mathcal{G}_{ss}^{max}$ are converted to a cyclic stress intensity factor range, ΔK, using an analytical model and the Irwin relation [45] in equation 2.1. The tunneling crack modeling results, the measured residual stresses and the measured Paris law for the adhesive are combined in the approach in Figure 4.7 to predict the crack growth rate for each tunneling crack along the length of the blade section. The steps of the approach, presented in Figure 4.7, are summarized:

(i) **DCB**: Double cantilever beam specimen fatigue tested in laboratory to measure Paris law (da/dN, ΔK) for a mode-I crack in the adhesive.

(ii) **Bi-layer**: Residual stress (σ_r) determination in the adhesive of the joint using misfit stress (σ_T) that is determined by measuring the curvature of bi-layer specimens.

(iii) **Blade**: Characterization of geometry ($h_1, 2h_2$), crack length for each crack (a_i), cycles for each crack (N_i), constitutive properties (E_1, E_2, ν_1, ν_2), and mechanical stresses ($\sigma_m^{min}, \sigma_m^{max}$) from blade inspection/model, CAD model, aero/FE model or similar.

(iv) **Modeling**: Tunneling cracks modeled using finite elements to determine ΔK_i as a function of blade geometry/properties, mechanical stress, and residual stress ($h_1, 2h_2, E_1, E_2, \nu_1, \nu_2, \Delta\sigma_m, \sigma_r$) for each tunneling crack configuration (a_i, N_i) dependent on location (y, z).

(v) **Blade prediction**: Prediction of da_i/dN_i for each tunneling crack in the blade using ΔK_i from tunneling crack model and Paris law (da/dN) for the adhesive that is measured by a DCB test in laboratory. Note, F is a function that relates ΔK with da/dN.

The methods and results for step (i) to step (iv) in the above list are presented in details in Paper P3. The main results determined in step (i) and step (v) in the approach in Figure 4.7 are presented next and compared with cyclic crack growth rates measured on the trailing-edge joint of the full scale blade tested in the laboratory. The generic full scale research blade was loaded excessively high in the fatigue test in order to propagate the tunneling cracks.

4.2.2 Results

For the prediction of cyclic tunneling crack growth rates on the blade, the parameters for the mode-I Paris law of the adhesive were measured by a cyclic moment-loaded DCB specimen. The Paris law for the adhesive were measured for different load R-ratio and presented in Figure 4.8. The Paris law parameters (C, m) were determined by a least

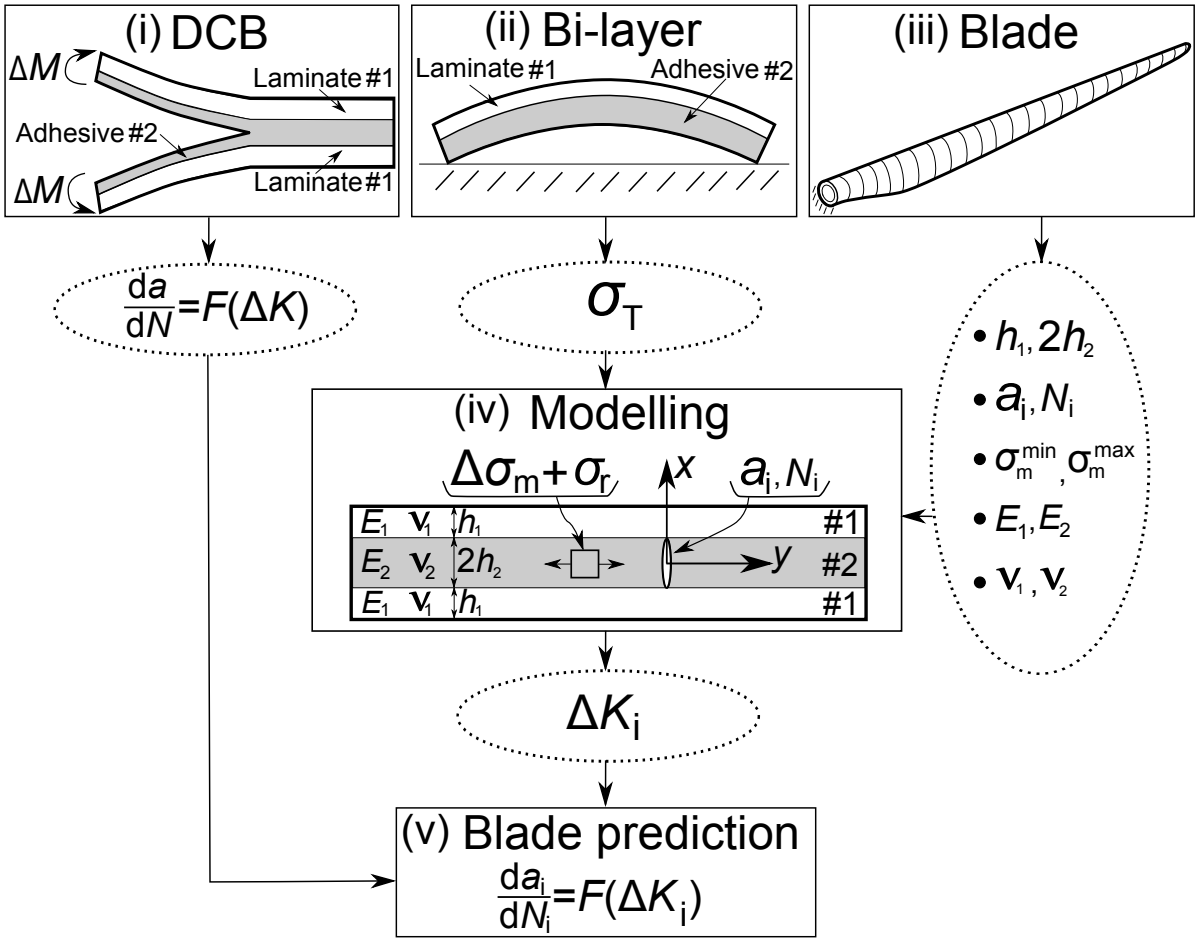

Figure 4.7: Approach for the prediction of tunneling crack growth rates.

square fit to the measured data points in the log-log space (ΔK, da/dN) on the form given by [69, 73]:

$$da/dN = C(\Delta K)^m \tag{4.5}$$

The best fit in Figure 4.8 was used to determine the parameters C and m. The upper- and lower fit gave the upper- and lower bounds for da/dN as shown in Figure 4.8 by the dashed and dotted lines, respectively. The mode-I Paris law for the adhesive was found to be comparable to those published for epoxy resin systems [50, 14, 12, 53].

Tunneling crack growth rates were predicted using the approach in Figure 4.7 and presented in Figure 4.9 together with the measured crack growth rates on the trailing-edge joint from the full scale test of the full scale test blade. The dashed lines in Figure 4.9 indicate the upper limits and the dotted lines the lower limits for the uncertainty of the predictions based on the corresponding bounds in Figure 4.8 from the DCB test. The da/dN predictions and measurements are normalized by the average thickness of the adhesive measured on the blade section, $2\bar{h}_2$.

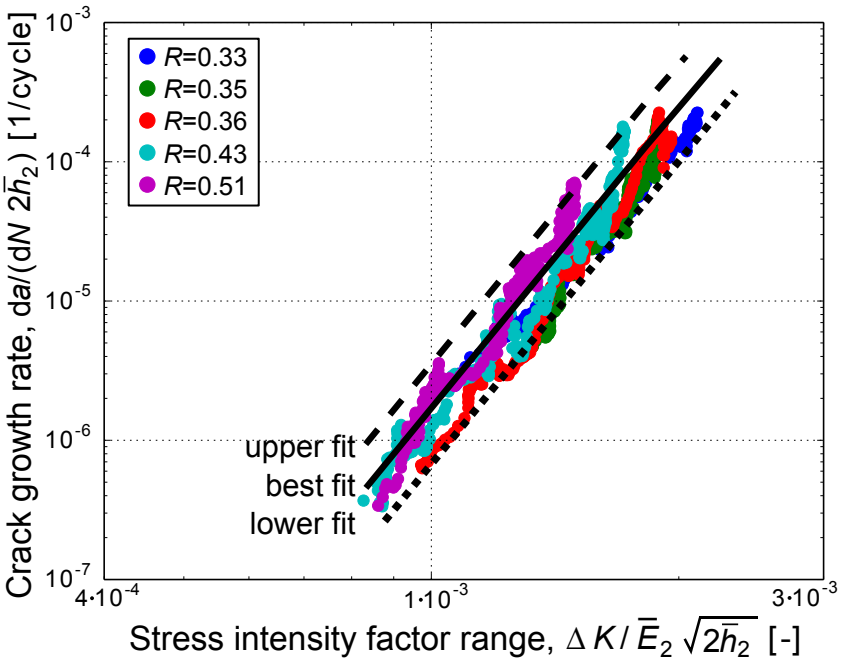

Figure 4.8: Results from cyclic loaded DCB test of the adhesive including Paris law best fit. The axes are normalized by the average thickness of the adhesive measured on the blade section, $2\bar{h}_2$.

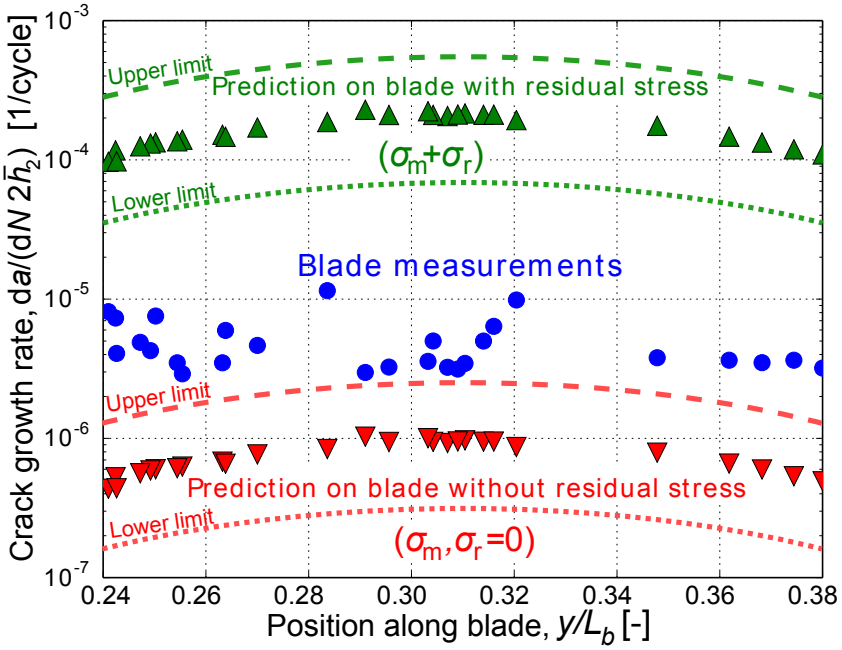

Figure 4.9: Comparison of predicted crack growth rates (triangles) with the crack growth rates measured (circles) on the full scale blade joint.

The predicted crack growth rates vary relative to crack location (y, z) due to the variations in the parameters α, h_1/h_2, $\Delta\sigma_m$ and σ_r. However, the variation of $\Delta\sigma_m$ is small meaning that the cyclic stress state of each individual tunneling crack is similar. On the other hand, the effect of σ_r on da/dN is significant. The crack growth rates measured individually for each tunneling crack in the blade are similar, which can be explained by the small variations in load levels and geometry along the blade section. As shown in Figure 4.8 and elaborated in Paper P3, the slope of the Paris law was relatively steep meaning that the resulting crack growth rates were sensitive to small variations in loadings. Thus, the main uncertainty comes from the measured Paris law for the adhesive.

The crack growth rates predicted on the blade joint falls above and below the crack growth rates measured on the blade. The crack growth rates predicted without including residual stress are closest to the crack growth rates measured on the blade. The inclusion of residual stress increased the level of the stress intensity factor range since the R-ratio changed from $R = -1$ to between $R \approx 0.3$ and $R \approx 0.5$. Therefore, the inclusion of residual stress increased da/dN as shown in Figure 4.9. The influence of this effect is elaborated in Paper P3.

4.3 Conclusions

It was found advantageous to embed a stiff buffer-layer near the adhesive with controllable thickness- and stiffness properties in order to improve the joint design against the propagation of tunneling cracks. However, for wind turbine blade specific materials, this effect was found to be relatively small since the substrate to adhesive stiffness mismatch was already high. Instead, it was proposed to reduce the thickness of the adhesive layer since this parameter had a higher effect on the steady-state energy release rate of the tunneling crack.

The tunneling crack growth rates predicted with- and without accounting for the residual stress in the adhesive were interpreted as upper- and lower-bounds for the crack growth rates in the wind turbine blade joint. The crack growth rates, measured for a several metre long section along the trailing-edge joint during an edgewise fatigue test, were found to be in-between the upper- and lower-bound predictions. This suggests that the tunneling crack tool can predict crack growth rates for tunneling cracks in a trailing-edge joint of a wind turbine blade sufficiently accurate.

CHAPTER 5
Crack Deflection at Interfaces in Adhesive Bonded Joints

If it is assumed that the bond-line of an adhesive joint contains pre-existing defects then a crack might be able to initiate and evolve into a transverse crack in the adhesive. After a small crack is formed in the adhesive, the typical cracking sequence is as shown schematically in Figure 5.1. The main crack in the adhesive propagates towards the adhesive/laminate interface (Figure 5.1 (A)). The main crack might reach the interface (Figure 5.1 (B)) or initiate a new crack at the adhesive/laminate interface (Figure 5.1 (C)). If the crack reaches the interface it may stop here (Figure 5.1 (B)), but it can also penetrate into the laminate (Figure 5.1 (D)) or deflect along the adhesive/laminate interface (Figure 5.1 (E)).

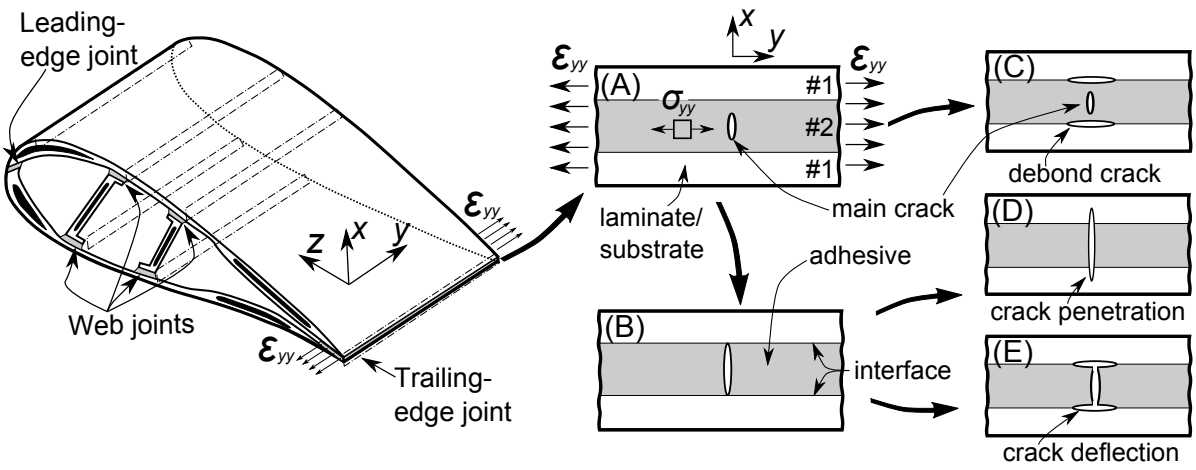

Figure 5.1: Crack deflection mechanisms in adhesive joints for wind turbine blades.

One of the first models for the cracking mechanism in Figure 5.1 (C) were developed by Cook and Gordon [18]. A stress based criterion (Cook-Gordon criterion) was established for an elliptical shaped crack in a homogenous solid. The Cook-Gordon deflection criterion states that the interface will fail if the interface strength is less than about 1/3 to 1/5 of the bulk material strength.

Later, a fracture mechanics based approach was applied to predict crack deflection for the cracking mechanism in Figure 5.1 (B), by introducing an infinitesimal small crack at the interface and in the substrate [40, 38, 106]. In absence of elastic mismatch, the

deflection criterion states that the interface-to-substrate toughness ratio should be one fourth or less for the crack to deflect.

Modeling the deflection of a crack meeting an interface were, at first, based on either stress [18, 31] or energy [40, 38, 30, 62, 106]. The stress based and fracture mechanics based approach can be unified using a cohesive law combined with cohesive zone FE modeling [72, 70, 95, 13, 2, 1]. The cohesive law can be measured experimentally, e.g. by the J-integral approach [59, 88, 89, 7, 27]. Alternatively, Mohammed and Liechti [66] measured the cohesive law parameters for an aluminum-epoxy bi-material interface using an iterative calibration procedure where cohesive zone modeling by FE simulations were combined with measurements from an experimental test of a four-point bend specimen.

It was demonstrated in the literature that crack deflection at interfaces can be modeled using approaches based on stress, fracture energy or cohesive zone modeling. In turn, rigorous experimental tests of crack deflection at interfaces, where the crack deflection process is clearly documented, are limited [57]. Therefore, it is desired to design a robust experimental test setup in order to study the problem of crack deflection at interfaces.

This chapter is organized as follows. First an experiment will be designed using analytical/numerical models in order to test crack deflection at interfaces. Hereafter, experimental tests will be used to test crack deflection and a new approach will be applied to measure the cohesive strength of a bi-material interface. Lastly, these measurements will be discussed in relation to existing results from the literature.

5.1 Design of Four-point SENB Specimens with Stable Crack Growth

In order to investigate crack deflection at interfaces experimentally, the four-point single-edge-notch-beam (SENB) specimen in Figure 5.2 is selected like in the studies by Zhang and Lewandowski [117]. However, in their experiments, crack propagation was unstable and crack deflection could only be seen as a sudden decrease in the measured moment. Therefore, further investigations are needed in order to design the experiment such that the crack in the displacement-loaded four-point SENB specimen grows stable in mode-I. This means that for the bi-material four-point SENB specimen in Figure 5.2, it is necessary that the crack can propagate stable towards the interface in order to enable observation of the crack deflection mechanism.

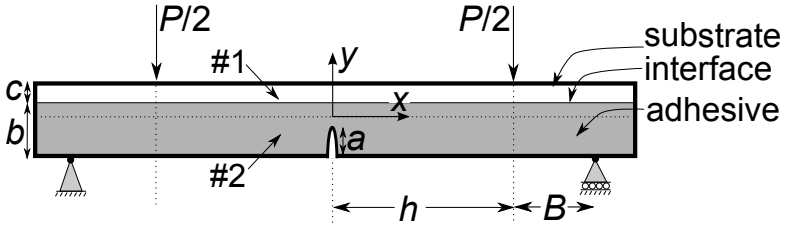

Figure 5.2: Bi-material four-point SENB specimen (here shown with fixed load, P).

The parameters defining the bi-material four-point SENB test specimen geometry are presented in Figure 5.2 and can be written on a non-dimensional form as; a/b, h/b, B/b and c/b, where a is the actual crack length, h is the horizontal distance between load point and main crack, B is the horizontal distance between load- and support point and c is the substrate thickness. Furthermore, a_0 is the start-crack length, b is the thickness of the adhesive layer and δ is the load point displacement.

The models and methods will developed for a class of materials that satisfy LEFM assumptions (isotropic, linear-elastic material and small plastic zone size and small fracture process zone at crack tip compared with crack length), see also section 2.2. The general condition for stable crack growth in equation 2.5 in a perfectly brittle material can be specified for fixed displacement loading (fixed grip) as:

$$\left[\frac{\partial G_I}{\partial a}\right]_\delta < 0 \tag{5.1}$$

where δ is the displacement at the force/grip. Thus, the mode-I energy release rate, G_I, must decrease with crack length for the crack to propagate stable.

5.1.1 The Homogenous Four-Point SENB Specimen

The homogenous four-point SENB specimen in Figure 5.3 is a special case of the bi-material specimen where $c/b = 0$. Since it is a simpler specimen than the bi-material version, it can be used to clarify the effect of different parameters in a convenient way. An analytical model of the homogenous four-point SENB specimen, loaded by displacements (fixed grip), is derived since the experimental tests are controlled by fixed grip and analysis of this is not available in the literature.

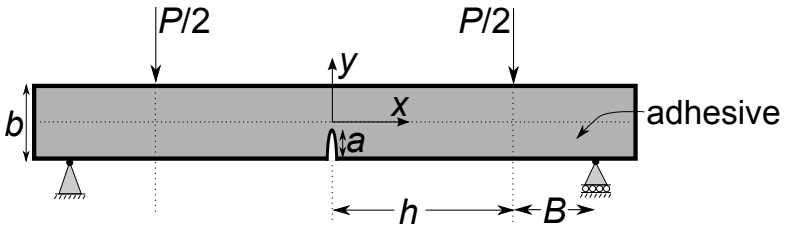

Figure 5.3: Homogenous four-point SENB specimen (here shown with fixed load, P).

The model was derived in Paper P4 based on the work of Tada *et al.* [104] and the assumptions from LEFM and Bernoulli-Euler beam theory. Thus, an expression for the mode-I energy release rate, G_I, as a function of applied displacement, δ, is:

$$\frac{G_I b}{\bar{E}\delta^2} = \pi\frac{ab}{B^2}\left[\frac{3}{2}\frac{F(a/b)}{\left[\frac{B}{b}+3\frac{h}{b}+\frac{3}{5}\frac{b}{B}\bar{\nu}+3S(a/b)\right]}\right]^2 \tag{5.2}$$

where $\bar{E} = E/(1-\nu^2)$ and $\bar{\nu} = 1/(1-\nu)$ is for plane strain, and $E = \bar{E}$ and $\bar{\nu} = (1+\nu)$ is for plane stress. $F(a/b)$ and $S(a/b)$ are non-dimensional functions that can be found

in the work of Tada *et al.* [104] or Paper P4. Note, in displacement control the energy release rate is coupled to the applied displacement through the elastic constants and the geometrical parameters according to equation 5.2.

A FE model is used to test the accuracy of the analytical derivation of the energy release rate for the homogenous four-point SENB specimen. The FE model, simulated in Abaqus CAE 6.14 (Dassault Systemes) with eight-noded plane strain elements, is parametrized with the non-dimensional groups; a/b, h/b and B/b. A symmetry condition is imposed along the vertical center line at $x = 0$ (see Figure 5.2) to reduce the computational time. A focused mesh is applied in the region of $0.5b$ in the x-direction of the beam and 100 elements are used over the distance b.

The curves for energy release rate of the crack in the SENB specimen under fixed grip loading (displacement control), presented in Figure 5.4, start from zero at $a/b = 0$, increase to a peak and finally decrease to zero again at $a/b = 1$. Thus, $G_I \to 0$ when $a/b \to 1$ since the crack approaches a free surface and the load is applied with fixed displacements. The largest difference observed in Figure 5.4 between the results of the analytical- (red lines) and the numerical model (red symbols) is for the short and thick specimen ($h/b = 0.5$) loaded in displacement control. When h/b is relatively large, the results of the analytical model (red lines) are close to the results from the numerical model (red symbols) as shown in Figure 5.4. As h/b decreases, i.e. the specimen becomes more compact, the analytical derivation becomes inaccurate.

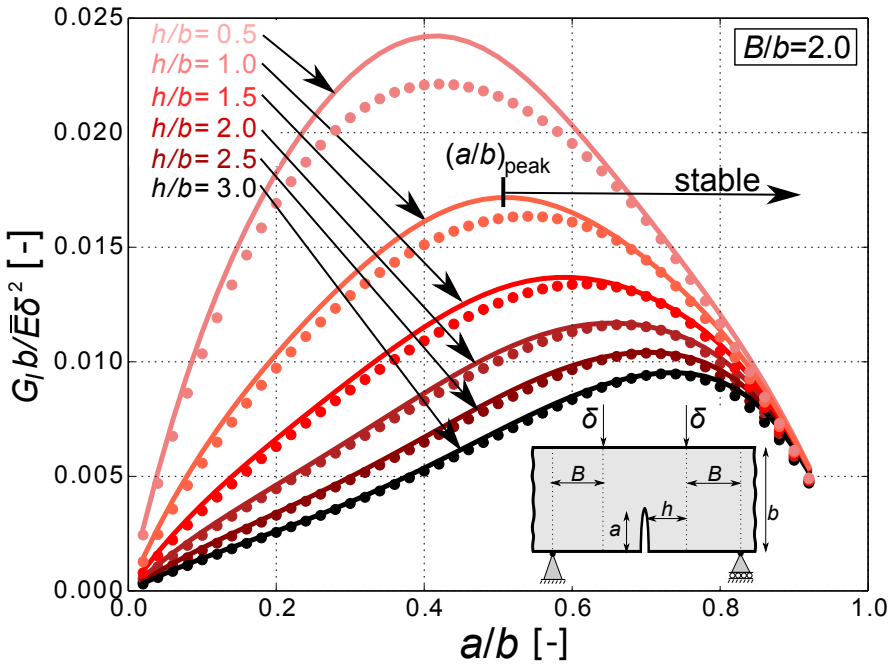

Figure 5.4: Energy release rate results determined by the plane strain FE model and the analytical model for different h/b and a/b for displacement control with $B/b = 2.0$, $E_1/E_2 = 1.0$, $\nu = 1/3$ (lines are analytic results; symbols are FE results).

It is the aim to design the test specimen such that the criterion for stable crack growth in equation 5.1 is satisfied. From Figure 5.4 it is seen that equation 5.1 is fullfilled when a exceeds a critical value, denoted $(a/b)_{peak}$. The crack grows stable if the start-crack length is $a_0/b \geq (a/b)_{peak}$ hence the energy release rate decreases with crack length in accordance with (5.1). It is desired that $(a/b)_{peak}$ is as small as possible such that the crack can grow stable for a long distance before reaching the free surface. This is to enlarge the design space with stable crack growth. As an example, take the curve for $h/b = 1.0$ in Figure 5.4 where $(a/b)_{peak} \approx 0.5$. For this case, the start-crack length should be $a_0/b \geq 0.5$ for the crack to propagate stable as exemplified in Figure 5.4.

5.1.2 The Bi-material Four-Point SENB Specimen

A function similar to $F(a/b)$ from Tada *et al.* [104] can be established for the bi-material four-point SENB specimen in Figure 5.2 to account for the presence of a substrate with thickness, c and Young's modulus, E_1. Thus, for the bi-material specimen in load control and with the adhesive and the substrate assumed isotropic:

$$G_I = \frac{1}{\bar{E}_2}\sigma_{xx}^2 \pi a F(a/(b+c), c/b, E_1/E_2)^2, \quad \sigma_{xx} = \frac{M E_2 \Omega}{E_1 I_1 + E_2 I_2} \tag{5.3}$$

where subscript 1 and 2 represent the substrate and adhesive, respectively. As shown in Figure 5.5, Ω is the distance from the bottom of the beam and to the global neutral axis of the beam (in the beam specimen without crack) [101]. I_1 and I_2 are the local area moment of inertia for the substrate and adhesive, respectively:

$$I_1 = \frac{c^3}{12} + c\left(\frac{c}{2} + b - \Omega\right)^2, \quad I_2 = \frac{b^3}{12} + b\left(\Omega - \frac{b}{2}\right)^2, \quad \Omega = c\frac{1 + 2\frac{E_1}{E_2}\frac{c}{b} + \frac{E_1}{E_2}\left(\frac{c}{b}\right)^2}{2\frac{c}{b}\left(1 + \frac{E_1}{E_2}\frac{c}{b}\right)} \tag{5.4}$$

The function, F, in equation 5.3 is determined as shown in Figure 5.5 by FE simulations, which is compared with the solution by Tada *et al.* [104] for $E_1/E_2 = 1$. It can be seen that when $a/(b+c) \to 0$ then $F(a/(b+c)) \to 1.12$ (independently of elastic mismatch). This limit is similar to the solution for a side-crack in an infinitely large homogenous plate under uni-directional tension [104, 24]. The trend in Figure 5.5 is comparable to the partial cracked film problem from Beuth [11]. For compliant substrates ($E_1/E_2 \lesssim 3$), F increases monotonic with increasing crack length, whereas for stiffer substrates ($E_1/E_2 \gtrsim 9$), F reaches a peak and subsequently starts decreasing (close to $a/(b+c) = 0.8$).

Dimension analysis reveals that the energy release rate of the crack for the bi-material specimen presented in Figure 5.2 can, when loaded in displacement control, be written as:

$$\frac{G_I(b+c)}{\bar{E}_2\delta^2} = \frac{9\pi}{4}\frac{a(b+c)}{B^2}F_\delta(a/(b+c), h/b, B/b, c/b, E_1/E_2)^2 \tag{5.5}$$

where the non-dimensional function, F_δ, is determined numerically. F_δ is introduced as a numerical function since it is out of the scope to derive an expression analytically for the

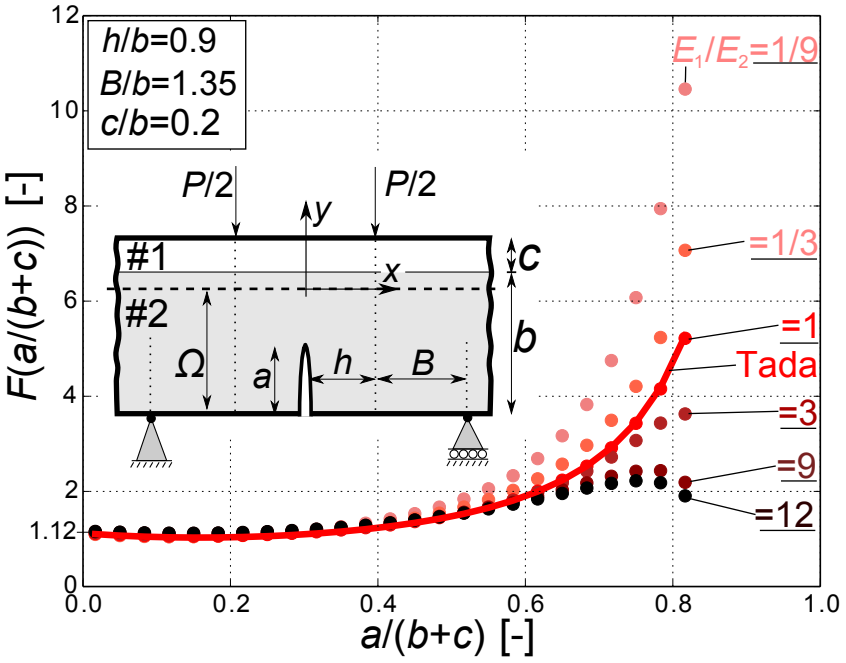

Figure 5.5: Results from FE model of bi-material SENB specimen with; $c/b = 0.2$, $h/b = 0.9$, $B/b = 1.35$ (line is result by Tada *et al.* [104], symbols are FE results, #1 is substrate, #2 is adhesive). The bi-material interface is located near $a/(b+c) \approx 0.83$.

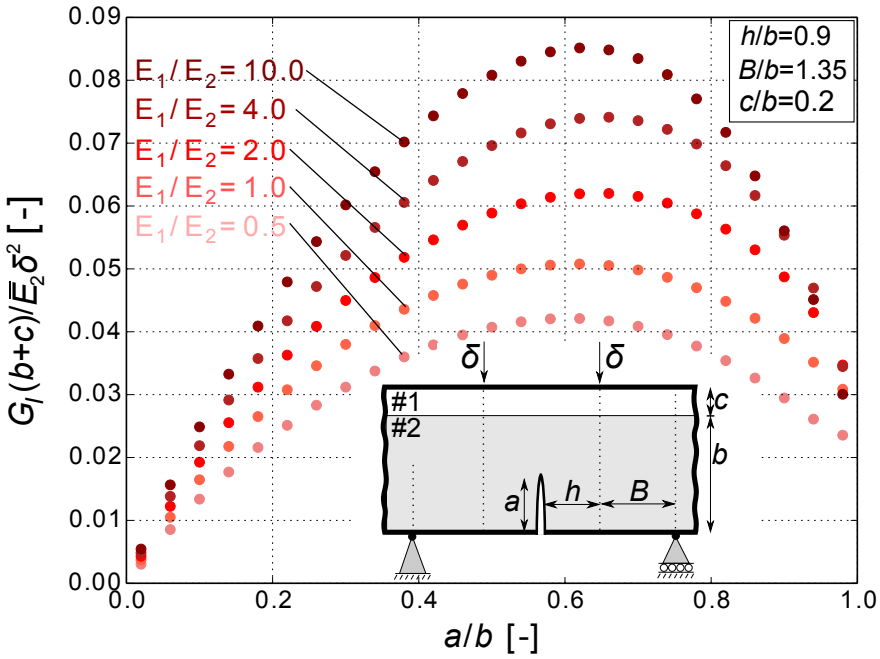

Figure 5.6: Energy release rate results from bi-material FE model loaded in displacement control for different E_1/E_2. Other parameters are: $\nu_1 = \nu_2 = 1/3$, $h/b = 0.9$, $B/b = 1.35$ and $c/b = 0.2$.

bi-material specimen like in equation 5.2 for the homogenous specimen. To determine a start-crack length, a_0/b, that gives stable crack growth, the requirement in equation 5.1 needs to be satisfied for the results of the bi-material FE model in Figure 5.6. From Figure 5.6 it is also clear that an increase of the substrate stiffness (E_1/E_2), increases the energy release rate when the load is applied in fixed grip. The effect of elastic mismatch on the magnitude of $(a/b)_{peak}$ is more complex and investigated further in Paper P4.

5.2 Experimental Test of Crack Deflection at Interfaces in Adhesive Joints

The four-point SENB specimen, shown in Figure 5.7, was analyzed in the last section since it was found that the first derivative of the mode-I energy release rate of the main crack depends on load conditions, geometry, and stiffness mismatch. For the experimental tests, presented in this section, the parameters $h/b = 0.9$ and $B/b = 1.35$ were utilized, and the bi-material specimens were manufactured such that $0.2 \leq c/b \leq 0.3$.

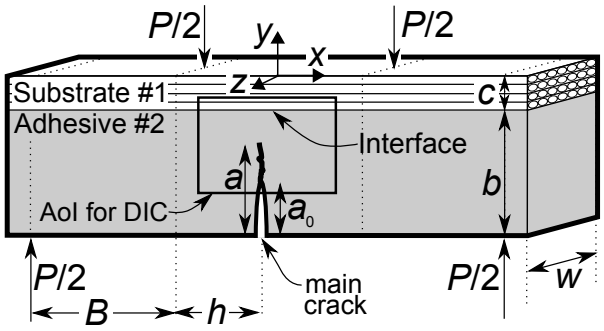

Figure 5.7: The bi-material four-point SENB test specimen geometry with symbols describing the geometry.

To enable observations of the crack deflection mechanism, the main crack should grow in a stable manner towards the interface meaning that the energy release rate of the main crack must decrease with crack length according to the requirement in equation 5.1. Using this criterion, the start-crack length is determined in Figure 5.6 based on FE simulations dependent on elastic mismatch, E_1/E_2, and substrate thickness, c/b. Thus, for the four-point SENB specimens with $E_1/E_2 = 1.0$ and $E_1/E_2 = 10.0$, the start-crack length should approx. be $a_0 \gtrsim 0.65$.

5.2.1 Test Setup and Manufacturing of Four-point SENB Specimens

Different groups of four-point SENB specimens were manufactured as illustrated in Figure 5.8. Here, only procedure (and results) for two groups, test series A and test series D, will be presented. The manufacturing procedure is elaborated in Paper P5 where the other types of test series are presented as well. The specimens of test series A (A1+A2)

are referred to as "model experiments" and designed for testing crack deflection, whereas the specimens in test series D are referred to as "cohesive strength experiments", see Figure 5.8.

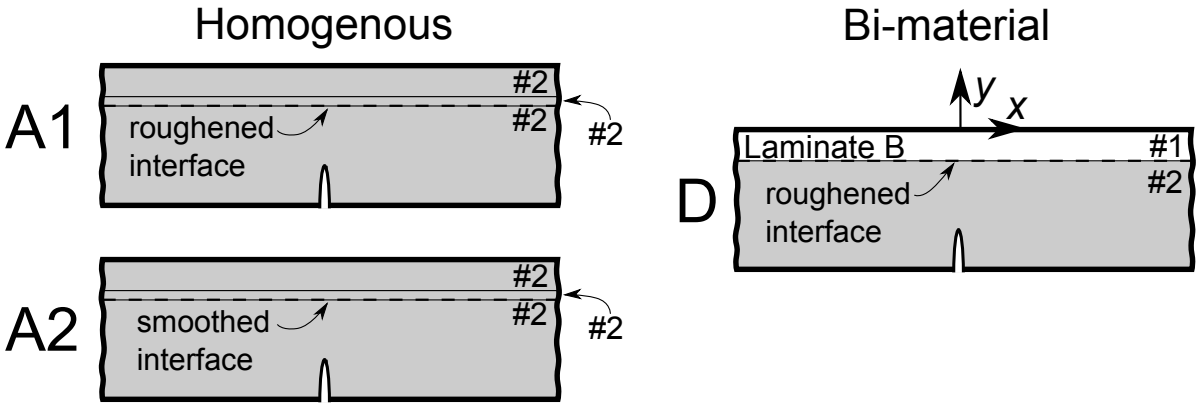

Figure 5.8: Test specimens for: A1: Model experiments with roughened interface. A2: Model experiments with smoothed interface. D: Cohesive strength experiments with roughened interface (Laminate B).

For test series A, two pre-cast adhesive plates of different thickness were subsequently bonded using the same type of adhesive. This process enabled that different interfaces could be manufactured; the roughened surface (A1: roughened interface) and the smooth surface (A2: smooth interface). "Roughened interface" means that the surface at the interface was roughened with sandpaper of grid 180. "Smooth interface" means that the interface was left untreated, but cleaned. Thus, this surface finish was prepared by the surface of the smooth glass plate. The adhesive, applied in viscous form to bond the two pre-cast adhesive plates, were left for 20 hours to harden at room temperature. Finally, the tri-layer specimens were post cured and cut into beams.

The specimens in test series D are bi-materials manufactured of an adhesive that was bonded to a glass-fibre reinforced laminate. The laminates were produced of non-crimp-fabrics of glass-fiber using a VARTM process. Subsequently, a structural adhesive was cast onto the laminate hence a zero-thickness interface was created. The plies were primarily uni-directional with main fiber-orientation in x-direction according to Figure 5.8. Prior to the casting, the surface on the laminate was roughened with sandpaper to ensure a proper bonding of the adhesive to the surface of the laminate. Start-cracks of length, a_0, were cut using first a thin hack saw, followed by a standard razor blade, and finally an ultra-thin razor blade of thickness 74 microns.

The test setup and equipment can be seen in Figure 5.9. Vic 2D DIC system (Correlated Solutions) was used to measure the displacement field. In order to determine the DIC setup and speckle pattern, initial experiments were conducted and practical guidelines for measuring with DIC were consulted [103]. The settings were inspired primarily by the work of Reu [80, 82, 81, 79, 78, 76, 77], but also by Lava [56], and Pierron & Barton [74], and the guidelines in the Vic manual [86]. The description of

speckle pattern preparation and the settings used for the DIC measurements can be read in details in Paper P5.

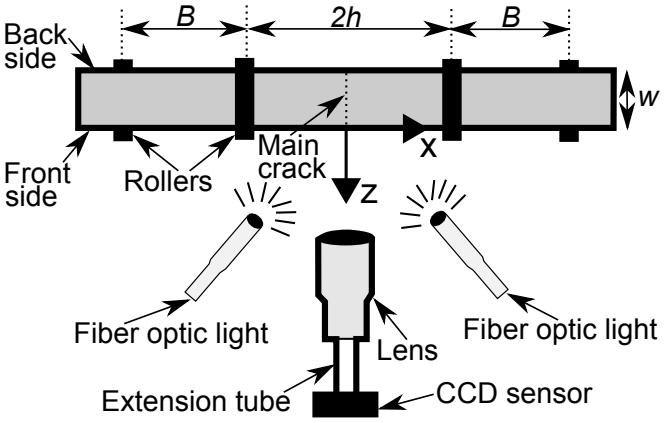

Figure 5.9: Top-view of the four-point bend test setup and equipment.

A MTS 858 Mini Bionix II servo-hydraulic test machine applied the load through a constant displacement rate. A load cell, calibrated for 1.5 kN, measured the load, P. A CCD sensor of type Grasshopper GRAS-50S5M (2448x2048 pixels) was mounted to a tri-pod and to the Fujinon CCTV Lens (HF50SA-1, 1:1.8/50mm) as shown in Figure 5.9. Extension tubes were used to achieve a proper magnification [81].

5.2.2 Experimental Results

Highlights of the results from the experimental tests of the four-point SENB specimens are presented here; a complete presentation of the results are given in Paper P5. The primary result of test series A1 was that the main crack propagated through the roughened interface of the specimen i.e. penetrated into the substrate. For test series A2, the crack deflected along the smoothed interface. Test specimen A2-1 is selected for further analysis. The moment and crack length measured for test A2-1 are presented in Figure 5.10 (A). The moment increased linearly with time until the main crack started to grow at time $t \approx 1200$ s. The main crack grew stable towards the interface until time $t \approx 1402$ s, see the image in Figure 5.10 (B). ϵ_{yy}^{max} is the maximum vertical strain in Figure 5.10 (B) measured by DIC and used for normalization of the strains in the figure. The crack length was measured to $a/b = 0.92$. Next, at time $t \approx 1404$ s, it was observed that the main crack deflected along the interface, see Figure 5.10 (C). As elaborated in Paper P5, it was observed that the main crack, in test series A2, first reached the interface and then deflected along the interface.

The results for all specimens in test series D (bi-material) can be found in Paper P5. For these tests, the main crack grew stable towards the interface until the interface suddenly debonded as indicated by the sudden drop in measured moment. Test specimen D-9 was selected for further analysis. The moment and crack length were measured and presented in Figure 5.11 (A) for test D-9.

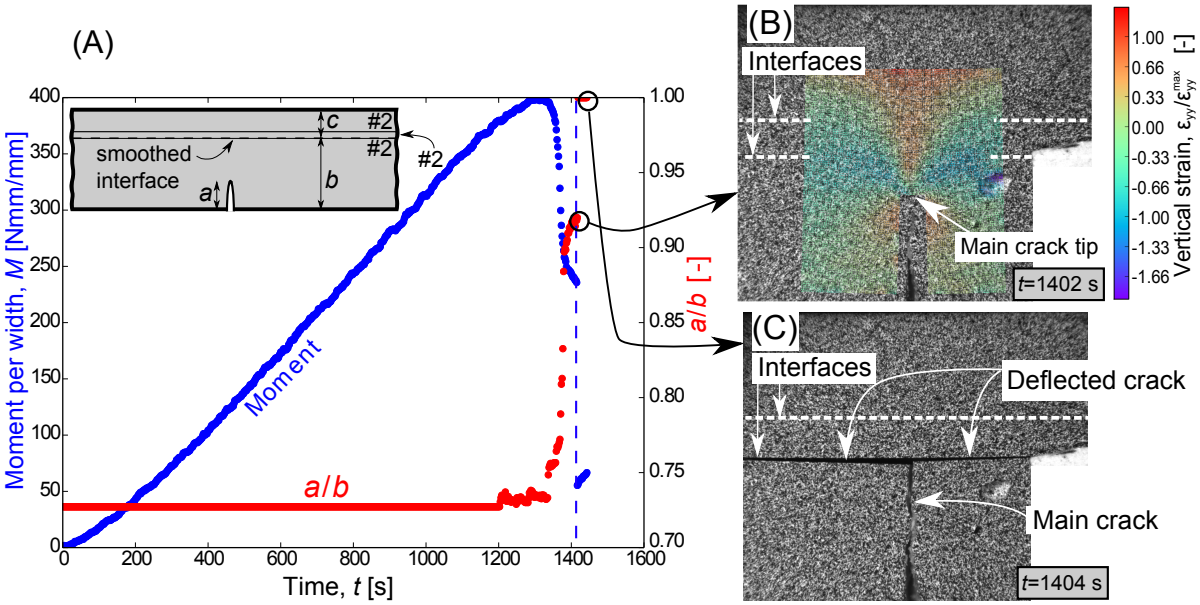

Figure 5.10: Measurements for test specimen A2-1 with crack deflection. (A) Moment and crack length. (B) Vertical strain contour. (C) After crack deflection.

Figure 5.11 shows that the main crack grew stable towards the interface until time, $t \approx 957$ s. On the next image at time, $t \approx 958$ s, the main crack has reached the interface ($a/b = 1.0$). The crack initiation appeared as a localized strain at the interface in the DIC analysis and it was captured by DIC as seen by the vertical strain contour plot in Figure 5.11 (B) for $t = 957$ s for test D-9. This localized strain indicated that the interface crack initiated before the main crack reached the interface. Note, ϵ_{yy}^{max} is the maximum vertical strain in Figure 5.11 (B) and used for normalization of the strain contours in the figure. As shown in Figure 5.11 (B) a localized strain (crack initiation) was captured by DIC measurements at the interface before the main crack reached the interface. This localized strain measurement is basically a displacement difference measured across substrate, interface and adhesive. Therefore, the localized strain can more precisely be denoted a "displacement difference" since it is measured across a bi-material interface and therefore different from a strain measured in a homogenous material. This cracking mechanism, where the crack initiated in the interface before the onset of main crack propagation (see also Figure 5.1 (C)), can be used to determine the mode-I cohesive strength of the interface by using a novel approach. This will be described next.

5.3 Determination of the Mode-I Cohesive Strength for Interfaces

The approach for determination of the mode-I cohesive strength of a bi-material interface is presented in short here, but can be read in details in Paper P5 and Paper P6. Paper P6

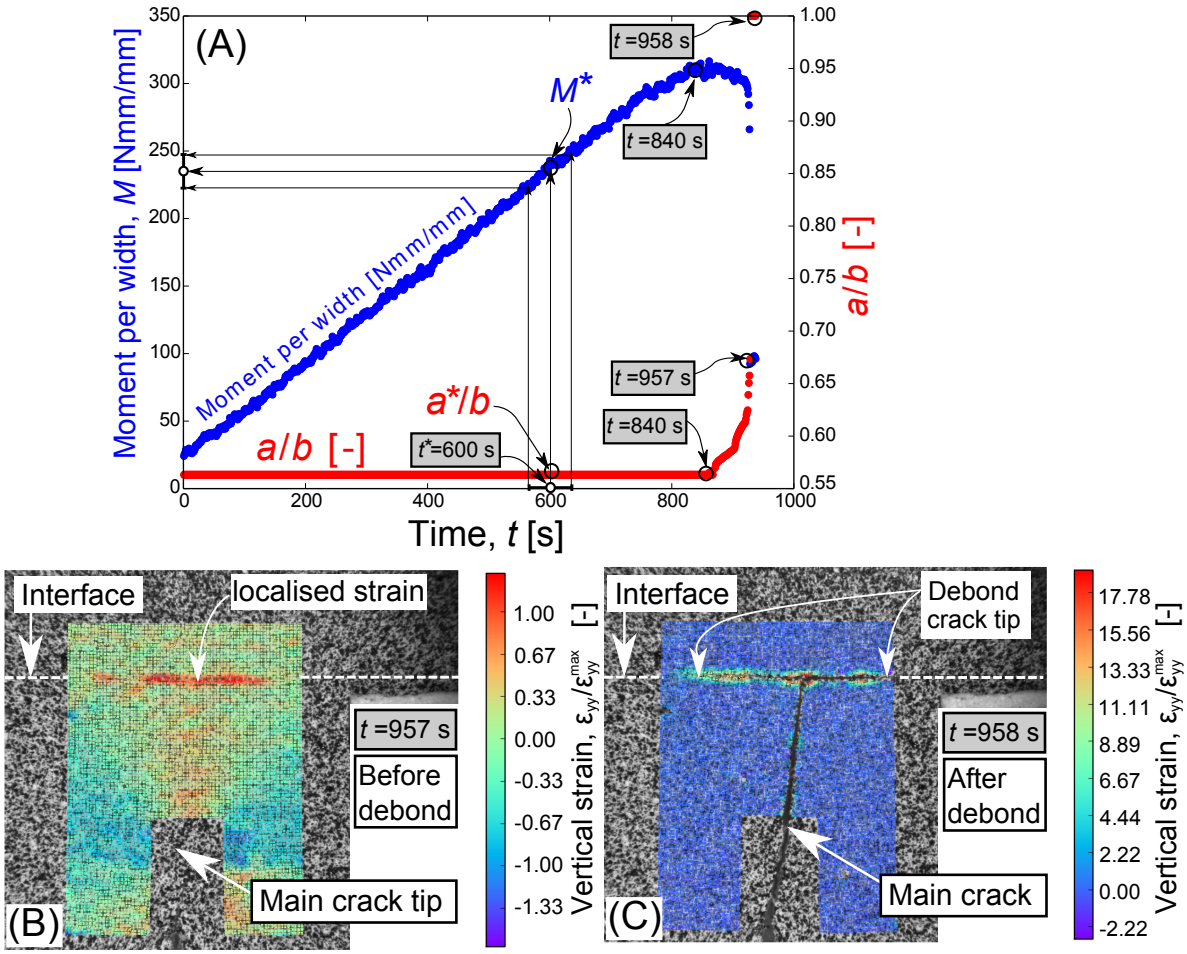

Figure 5.11: Measurements from test D-9: (A) Moment and crack length. (B) DIC vertical strain contour plot of AoI before debond at time $t = 957$ s. (C) DIC vertical strain contour plot of AoI after debond at time $t = 958$ s.

is the paper introducing the approach. The approach is further refined and demonstrated in Paper P5. The approach is based on the stress field of a crack tip close to an interface that has the purpose of initiating a new crack at the interface. The displacement difference, $\Delta\delta$, across the zero-thickness interface is measured by DIC over the gauge length, l_g, as shown in Figure 5.12. During loading the spacing between two points on each side of the interface in Figure 5.12 increases due to elastic deformation and initiation of the interface crack. The displacement difference, $\Delta\delta$, across the interface increases linearly with applied load (and time, t), but becomes non-linear at the onset of interface crack initiation. The onset of non-linear displacement difference is denoted $\Delta\delta^*$ according to Figure 5.12. Assuming linear-elastic materials and a zero-thickness interface, the non-linearity in measured displacement difference across the interface is attributed interface separation only.

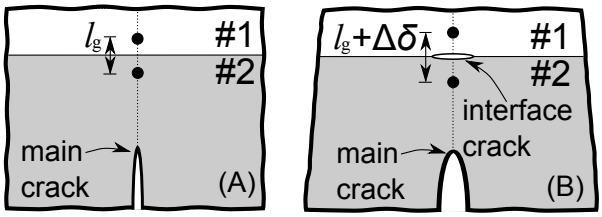

Figure 5.12: Illustration of l_g and $\Delta\delta$: (A) Initial undeformed state. (B) Deformed state, where the interface crack has formed.

At the time of crack initiation, t^*, the associated moment, M^*, and crack length, a^*, are measured from the experiment. These measurements (M^*, a^*/b) are used as inputs to a 2D linear-elastic FE model of the experiment. The stress across the interface, $\sigma_{yy,i}$, is determined by:

$$\frac{\sigma_{yy,i}b^2}{M} = f(a/b, c/b, E_1/E_2) \tag{5.6}$$

where the non-dimensional function, f, is determined using the result of a finite element model presented in Figure 5.13. The calculation procedure to determine the cohesive strength of the interface, $\hat{\sigma}_i$, is listed in short here [49]:

- Capture the time of interface crack initiation, t^*, (onset of interface separation) e.g. by digital image correlation, visually or by other methods.
- Determine M^* and a^*/b at the time of interface crack initiation (onset of interface separation).
- Use measured M^* and a^*/b with the FE results in Figure 5.13 and equation 5.6 to determine the stress across the interface, $\sigma_{yy,i}$, at the onset of interface separation.

Moment, M, and crack length, a/b, are the only parameters varying during the test of the four-point SENB specimen. The stress across the interface, $\sigma_{yy,i}$, scales linearly with M, but non-linearly with a/b as shown in Figure 5.13. Thus, by using the measured values of M^* and a^*/b at the time of crack initiation together with the FE simulation results in Figure 5.13 and equation 5.6, the resulting cohesive strength of a material interface, $\hat{\sigma}_i$, can be determined.

5.3.1 Example of Determination of Cohesive Strength

The approach to determine the cohesive strength of the interface is exemplified by test D-9 presented in Figure 5.11. For test D-9, a displacement difference, $\Delta\delta$, is measured by DIC over the gauge length, $l_g = 0.1b$, as shown in Figure 5.14.

The result in Figure 5.14 is used to identify the time where the interface crack initiates in a more accurate way than what can be seen from the strain contour plots. A straight line is fitted to the first linear part of the measured non-dimensional displacement difference, $\Delta\delta/\Delta\delta^*$, and it is judged that the measurements deviate from the fitted straight line at time $t \approx 600$ s. Thus, time $t^* \approx 600$ s is identified as the onset of non-linearity in measured displacement difference and thus the time where the interface crack

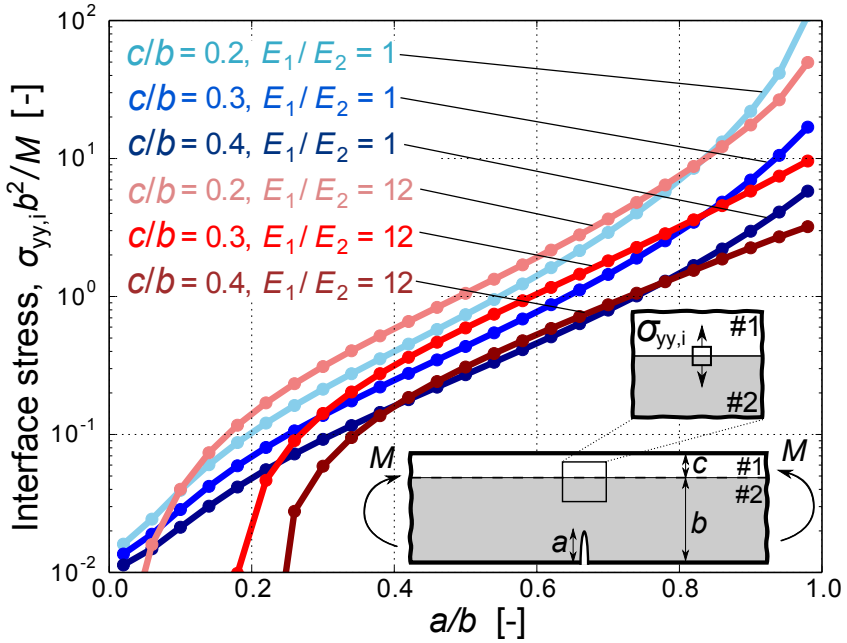

Figure 5.13: FE results for normalized interface stress determined numerically for different E_1/E_2 and c/b. Other parameters are: $h/b = 0.9$ and $B/b = 1.35$.

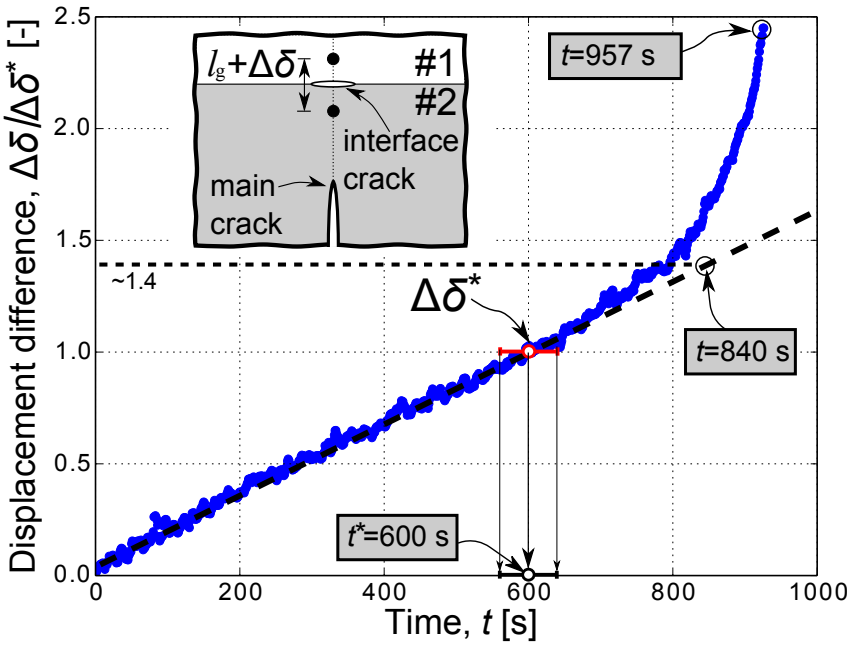

Figure 5.14: Experimental result of test D-9 measured by DIC. The displacement difference is normalized by the value of the displacement difference at the onset of non-linearity, $\Delta\delta^*$.

initiated. The onset of interface separation begins at time $t^* = 600$ s whereas the main crack started to propagate at time $t = 840$ s. This time measurement ($t^* = 600$ s) is used in Figure 5.11 (A) to determine $M^* = 240$ Nmm/mm and $a^*/b = 0.57$. These parameters ($M^* = 240$ Nmm/mm, $a^*/b = 0.57$) together with $E_1/E_2 = 12.0$ and $c/b = 0.2$ are the inputs to equation 5.6. From the results in Figure 5.13, the mode-I cohesive strength of the interface can be determined to $\hat{\sigma}_i/\bar{\sigma}_a = 0.078 \pm 0.004$ for test D-9, where $\hat{\sigma}_i$ is normalized with the macroscopic strength of the adhesive, $\bar{\sigma}_a$, that was measured by a uni-directional tensile test of a dog bone specimen.

5.3.2 Discussion of Cohesive Strength Results

Further results for the non-dimensional cohesive strength, $\hat{\sigma}_i/\bar{\sigma}_a$, are presented in Paper P5 and ranges between $0.05 < \hat{\sigma}_i/\bar{\sigma}_a < 0.20$ for the different material interfaces tested.

Mohammed and Liechti [66] measured the cohesive strength of an aluminum-epoxy bi-material interface to $\hat{\sigma}_i = 3$ MPa, which can be normalized by the bulk strength of the epoxy adhesive of $\bar{\sigma}_a = 13.4$ MPa (provided by Mohammed and Liechti [66]) to give $\hat{\sigma}_i/\bar{\sigma}_a = 0.22$. Although the material systems are different, the non-dimensional result by Mohammed and Liechti [66] are close to the range of the cohesive strengths measured in Paper P5 of $0.05 < \hat{\sigma}_i/\bar{\sigma}_a < 0.20$. This consistency leads to confidence in the novel approach applied in the present work.

Normalization of $\hat{\sigma}_i$ by $\bar{\sigma}_a$ is equivalent to the way Cook and Gordon [18] presented their modeling results based on stress. They [18] suggested that the interface strength should be less than about 1/3 to 1/5 of the bulk material strength in order to ensure that a new crack initiates along the weaker interface ahead of the main crack. Although the Cook and Gordon model was established for a homogenous solid, the criterion is consistent with the experimental test results presented in Paper P5 since all measured normalized cohesive strengths of the interfaces were below 1/5. Since crack penetration into the substrate was observed in test series A1, it is expected based on the Cook-Gordon criterion that the cohesive strength of the interfaces for the specimens in test series A1 is $\hat{\sigma}_i/\bar{\sigma}_a > 1/3$.

5.4 Conclusions

An analytical model of the displacement loaded four-point SENB test specimen was derived and found to agree well with FE simulations. The models (analytical and numerical) were found appropriate to design the experiment with stable crack growth since it was found that $\partial G_I/\partial a$ depends on load configuration, crack length and geometry. These models suggested that the beam should be short and thick, and the start-crack length should be relatively deep for the main crack to propagate stable.

A model experiment of four-point SENB specimens with different interfaces, were designed, manufactured, and tested. The tests were successful in that crack propagation was stable and the crack deflection at interfaces could be observed during loading (in-situ). For bi-material test specimens, it was observed that a new crack initiated at the interface. This cracking mechanism enabled determination of the cohesive strength of the interface

using a novel approach. The cohesive strength of the interfaces were found to be small in comparison with the macroscopic strength of the adhesive and found to be consistent with the measurements by Mohammed and Liechti [66] and the Cook-Gordon criterion [18].

CHAPTER 6
Summary of Results and Concluding Remarks

In this chapter, the six papers addressing the main goals of the project will be summarized and the findings in the papers will be used to establish novel design rules for adhesive bonded joints. The outcome of the papers will be discussed in relation to the existing knowledge in the literature. To conclude, the future challenges will be discussed and a final conclusion completes the thesis.

6.1 Summary of Results

In this section summaries of the six appended papers are presented. The main results and conclusions are highlighted, but details should be read in the full papers listed below.

P1 Jeppe B. Jørgensen, Bent F. Sørensen and Casper Kildegaard. "The effect of residual stresses on the formation of transverse cracks in adhesive joints for wind turbine blades." Submitted to: *International Journal of Solids and Structures* (2017).

P2 Jeppe B. Jørgensen, Bent F. Sørensen and Casper Kildegaard. "The effect of buffer-layer on the steady-state energy release rate of a tunneling crack in a wind turbine blade joint". Submitted to: *Composite Structures* (2017).

P3 Jeppe B. Jørgensen, Bent F. Sørensen and Casper Kildegaard. "Tunneling cracks in full scale wind turbine blade joints". Accepted for: *Engineering Fracture Mechanics* (2017).

P4 Jeppe B. Jørgensen, Casper Kildegaard and Bent F. Sørensen. "Design of four-point SENB specimens with stable crack growth". Submitted to: *Engineering Fracture Mechanics* (2017).

P5 Jeppe B. Jørgensen, Bent F. Sørensen and Casper Kildegaard. "Crack deflection at interfaces in adhesive joints for wind turbine blades". Submitted to: *Composites Part A: Applied Science and Manufacturing* (2017).

P6 Jeppe B. Jørgensen, Michael D. Thouless, Bent F. Sørensen and Casper Kildegaard. "Determination of mode-I cohesive strength of interfaces". In: *IOP Conf. Series: Materials Science and Engineering*, 139, 012024 (2016).

6.1.1 Summary of Paper P1: The effect of residual stresses on the formation of transverse cracks in adhesive joints for wind turbine blades

An experimental approach was applied to test the effect of different parameters on the formation of transverse cracks in an adhesive joint. Transverse cracks were assumed to evolve due to a combination of mechanical- and residual stresses. A new approach was developed that allows the residual stress to be determined in several different ways. The accuracy of different methods to measure residual stresses in the adhesive was tested on a single bi-layer/sandwich test specimen (laminate/adhesive/laminate) that was instrumented with strain gauges and fiber Bragg gratings (FBG). One of the methods with FBGs was used to clarify which of the steps in the bonding process that had the largest contribution to the residual stress.

A bi-material FE model of the sandwich specimen were developed to predict the stress in the adhesive at first crack from knowledge of fracture energy and geometry. Transverse cracking of the adhesive was investigated experimentally by manufacturing different series of sandwich test specimens made of two laminates that were bonded by a thick layer of structural adhesive. The sandwich specimens were tested in quasi-static tension to explore the effect of test temperature, post curing temperature and thickness of the laminate. The effect of laminate thickness on the formation of transverse cracks in the adhesive was also tested under cyclic loading.

Using the measured residual stress as input to the model, the predictions of the stress in the adhesive at first crack were made. The predictions were found to agree well with the experimental results from tensile tests of the sandwich specimens at 23°C and −40°C. The residual stress in the adhesive was found to contribute to the formation of transverse cracks in the sandwich specimens, especially at low test temperatures. The static tensile tests of the sandwich specimens showed that higher post curing temperature and lower test temperature had a negative effect on the formation of transverse cracks in the adhesive in the sense that transverse cracks initiated at lower applied mechanical loadings. The effect of increased laminate thickness was minimal under both static and cyclic loading. The cyclic loaded tests confirmed that the design of the sandwich specimen was damage tolerant since multiple cracking of the adhesive developed in a stable manner.

6.1.2 Summary of Paper P2: The effect of buffer-layer on the steady-state energy release rate of a tunneling crack in a wind turbine blade joint

A new tri-material FE model was developed in order to design the wind turbine blade joint such that the energy release rate of a tunneling crack, propagating across the adhesive layer, was reduced. Results from the tri-material FE model was found comparable with the results of Ho and Suo [41] for the simplified case of a bi-material model. Other simulations showed that the energy release rate of the tunneling crack could be reduced by embedding a so-called buffer-layer near the adhesive with a well-chosen stiffness and

-thickness. It was found that the appropriate thickness of the buffer-layer depended on the stiffness of the buffer-layer. In any case it was found advantageous to increase the stiffness of the buffer-layer in order to reduce the energy release rate of the tunneling crack. However, it was found for adhesive joints with properties comparable to materials used for wind turbine blades that the laminates were already sufficiently stiff. Thus, the effect of the buffer-layer was small in comparison with the effect of reducing the thickness of the adhesive layer.

6.1.3 Summary of Paper P3: Tunneling cracks in full scale wind turbine blade joints

A generic tunneling crack tool was presented and used in a novel approach for the prediction of crack growth rates for tunneling cracks propagating across a bond-line in a wind turbine blade under high cyclic loadings. Inputs to the generic tool was the Paris law for the adhesive, the residual stresses in the adhesive, and information about the loadings, geometry and material properties for the adhesive joint in the blade. First, a DCB specimen was fatigue tested in the laboratory to measure Paris law for a mode-I crack in the adhesive. The parameters for Paris law of the adhesive was found comparable to those of epoxy resin systems reported in the literature. Residual stresses in the adhesive of the joint was determined based on misfit stress that was measured using a curvature experiment of bi-layer specimen tested in the laboratory.

The model prediction of crack growth rates on the joint with and without residual stresses included were taken to be the upper and lower bounds, respectively. The model predictions by the generic tunneling crack tool was tested on a full scale wind turbine blade that was loaded cyclic in an edgewise fatigue test in a laboratory. The full scale blade, which was more than 40 meter long, was tested with cyclic loads that was significantly higher than standard design loads in order to propagate the tunneling cracks in the trailing-edge joint. The crack length for 27 tunneling cracks was measured on the trailing-edge during the edgewise fatigue test. It was demonstrated that the upper- and lower bounds for the model predictions were in agreement with the measurements on the full scale test blade.

6.1.4 Summary of Paper P4: Design of four-point SENB specimens with stable crack growth

In order to investigate crack deflection at interfaces experimentally, it was necessary to design a test specimen where a crack could propagate stable and orthogonal towards a bi-material interface. A four-point single-edge-notch-beam (SENB) test specimen loaded by applied displacements was developed and manufactured for the purpose. In order to design the test specimen, models were established to ensure stable crack growth and thus enable that crack deflection at the interface could be observed (in-situ) during loading. To explore a parameter space an analytical model was derived for the homogenous four-point SENB specimen, and it was found that the test specimen should be short and thick and the start-crack length relatively deep for the crack to propagate in a stable manner. The

analytical model was compared with a numerical model. The results from the numerical model of the bi-material four-point SENB specimen showed the same tendencies. An experiment with the homogenous four-point SENB specimen showed that the crack could grow stable if the start-crack-length was made sufficiently long and unstable if not. This was in agreement with the model prediction.

6.1.5 Summary of Paper P5: Crack deflection at interfaces in adhesive joints for wind turbine blades

Crack deflection at interfaces for different material systems was tested experimentally. A four-point SENB specimen was manufactured by bonding two pre-cast beams of structural adhesive. Thus, different interfaces could be prepared by varying the roughness of the surface prior to casting. It was found that the main crack penetrated into the substrate if the surface of the interface was roughened, but deflected along the interface if the surface of the interface was smooth. The test specimens used for studying crack deflection at interfaces were tested successfully since the crack deflection mechanism could be observed by DIC during loading (in-situ).

Other four-point SENB test specimens of different materials systems (adhesive/laminate, adhesive/adhesive) were manufactured with different interface properties and tested experimentally. For some of the test series it was observed that a new crack initiated at the interface before the main crack propagated and reached the interface. This cracking mechanism was used to develop a novel approach to determine the mode-I cohesive strength of the interface.

The novel approach were first presented in Paper P6, where it was demonstrated on a bi-material SENB specimen. The approach was further refined and demonstrated in Paper P5 for SENB specimens with different interface properties. The novel approach was based on measuring the displacement field across the interface during loading using DIC. Initially, the relative displacement across the interface increased linearly with the applied loading, but became non-linear at the time where the new crack at the interface initiated. At this time, the measured crack length and moment from the experimental test were applied to a FE model such that the stress across the interface could be determined numerically. Assuming that the measured non-linearity was the onset of separation (crack initiation) then the stress across the interface were taken to be the cohesive strength of the interface. The method was applied to determine the mode-I cohesive strength of different bi-material interfaces. The cohesive strength of these interfaces was found to be low in comparison with the macroscopic strength of the adhesive.

6.1.6 Summary of Paper P6: Determination of mode-I cohesive strength for interfaces

This is the first paper introducing the novel approach for determination of the cohesive strength of a bi-material interface. The cohesive strength of the interface is one of the governing properties for crack deflection at interfaces as demonstrated by the cohesive zone models by Parmigiani and Thouless [72]. The novel approach for determination of

the cohesive strength of a bi-material interface was successfully applied and demonstrated on a four-point SENB specimen made of an adhesive that was cast onto a glass fiber laminate. This bi-material four-point SENB specimen was tested experimentally and it was observed that a new crack initiated in the bi-material interface before the main started to grow. DIC was applied to identify the onset of interface separation (crack initiation) and, at this time, a 2D finite element model was used to determine the stress across the interface. At the time of crack initiation, this stress can be associated with the cohesive strength of the interface. It was found that the mode-I cohesive strength of the tested adhesive/laminate interface was low in comparison with the macroscopic strength of the adhesive.

6.2 Discussion of Contributions and Impact

The results of Paper P1 in section 3.4 and section 3.5 showed that the processing parameters (e.g. post curing temperatures in Figure 3.10) used in the manufacturing of adhesive joints are important parameters in order to control the magnitude of residual stress in the adhesive layer. These findings could also be relevant in other applications (e.g. aircrafts or cars) where the adhesive is constrained between stiffer substrates and therefore cannot freely contract. Under cyclic loading it was shown by the results in Figure 3.11 in section 3.5.3 that the adhesive joint (sandwich specimen) was a damage tolerant component since multiple cracking of the adhesive evolved in a stable manner. Since it was found that the evolution of multiple transverse cracks in the adhesive were slow and measurable, it is proposed to use structural health monitoring systems to detect and monitor the development of transverse cracks. FBGs could be one way to first measure the residual strains (stresses) and subsequently monitor the stable development of multiple cracks in the adhesive.

A new tri-material FE model was used to design a structural adhesive joint against the propagation of a tunneling crack as demonstrated in section 4.1. For wind turbine blade specific materials the stiffness of the substrates were already sufficiently high meaning that the effect of increasing the substrate stiffness was small. Although the effect of embedding a buffer-layer in a wind turbine blade joint was small, the buffer-layer idea and -model could be applied to other engineering structures where the effect of a buffer-layer is more pronounced. Especially, the identification of the point of intersection (PoI) in Figure 4.4 (in section 4.1.2 for the tri-material FE model and in Paper P2) is an important scientific contribution since it can be used to select the optimal properties of the buffer-layer in order reduce the risk of tunneling crack propagation in the specific application.

Another important scientific result is the approach and tunneling crack tool for the prediction of crack growth rates of tunneling cracks in an adhesive joint of a wind turbine blade in section 4.2 (Paper P3). The tunneling crack tool is not just limited to wind turbine blade joints under cyclic loading. Basically, the approach can be adapted to other types of propagating fatigue cracks, where the energy release rate can be determined by a model and the inputs to the model are measurable e.g. by using lab scale experiments

to characterize the needed material properties, like demonstrated in Paper P3.

As presented in chapter 5 and Paper P4, rigorous experimental studies of crack deflection at interfaces were identified as a gap in the literature. One of the challenges, which was not addressed in the literature, was to design an experiment with stable crack growth so that the crack deflection mechanism could be observed during loading. Four-point SENB geometries found in the literature vary significantly from test to test and no justifications for the chosen geometry were presented. An analytical model of the four-point SENB specimen was derived and compared with numerical models in order to design an experiment where crack propagation towards the bi-material interface was stable (see e.g. Figure 5.4 in section 5.1.1). These models were comparable and found applicable on experiments. The new results, presented in Paper P4, explored and clarified the complexity of the problem since stable crack growth of the crack in the four-point SENB specimen depends on the test specimen geometry, test setup and start-crack length (section 5.1). The parameter studies presented in Paper P4 are of significant scientific importance since it is difficult to design a crack deflection experiment where the crack grows stable and orthogonal towards a bi-material interface. Therefore, the modeling results and experimental demonstration will be valuable to others working on crack growth experiments, particularly with experimental test of crack deflection at interfaces.

Accurate experimental determination of cohesive strength for bi-material interfaces is challenging, especially for material interfaces with small separations [48], and therefore novel methodologies are desired (chapter 5). Thus, it is a valuable scientific contribution that a novel approach to determine the mode-I cohesive strength of a bi-material interface were developed and presented in Paper P6 and further refined and applied in Paper P5 (section 5.3). One of the advantages of the novel approach is that there is no need for a complicated calibration procedure or CZM model. Only a linear-elastic solution is required. Furthermore, it is not necessary to use advanced microscope equipment since a standard four-point bend rig with a DIC camera system is the primary equipment needed. The new approach is not limited to the four-point SENB specimen and it could be applicable on other test specimens, provided the initiation of the interface crack can be captured by DIC (or another method) and the interface stress can be accurately determined using a model (e.g. FE or analytical). Therefore, this new approach could win popularity on other types of test specimens where it is difficult to measure the cohesive strength of the interface.

6.3 Determination of Novel Design Rules for Adhesive Bonded Joints

This section has the purpose of addressing the main scientific goal of the project that, in short, was to develop new- and to improve the existing design rules for adhesive joints in wind turbine blades. This section is divided into design rules based on each of the three sub-projects and finally a section dedicated the three most important design rules.

6.3.1 Design Rules based on Sub-project 1

In Paper P1, it was assumed that the stress in the adhesive at first crack was a combination of tensile residual stress and tensile mechanical stress (section 3.2). Thus, by reducing the tensile residual stress, the mechanical load to initiate the first crack in the adhesive can be increased. For the low temperature tensile tests of sandwich specimens (laminate/adhesive/laminate) in Figure 3.10, presented in section 3.5.2, the residual stresses were measured to between 8-40% of the mechanical stress in the adhesive to initiate the first crack. Therefore, if the residual stress could be removed, e.g. in the manufacturing process, the mechanical stress can potentially be increased by up to 40%. However, it would be even better to manufacture adhesive joints with compressive residual stresses in the adhesive since this gives room for loading the joint even further.

Based on the conclusions in Paper P1, it was found desirable to post cure at temperatures that are not too high in order to reduce residual stresses. If possible, low operation temperatures should be avoided in order to keep the residual stresses small.

Beside the standard desired adhesive properties of high strength and fracture toughness, for the application on wind turbine blade joints, it is desirable that the chemical shrinkage of the adhesive and the mismatch in coefficient of thermal expansion is low since the adhesive is constrained in-between stiffer laminates (and are therefore not free to contract). Reducing the chemical shrinkage and the mismatch in coefficient of thermal expansion are two ways to reduce the residual stress in the adhesive. Lowering the chemical shrinkage might be achievable by adding different fillers to the adhesive, but this might affect the other material properties of the adhesive negatively. In practice for wind turbine blade joints, it might be challenging to eliminate the mismatch in coefficient of thermal expansion since various types of layups are used in different regions of the blade.

6.3.2 Design Rules based on Sub-project 2

Since it is the layer closest to the adhesive that has the main constraining effect on the tunneling crack, it was found advantageous to embed a stiff buffer-layer near the adhesive (section 4.1.2). However, the effect was small for adhesive joints with stiff substrates. The optimal properties (thickness and stiffness) of the buffer-layer can be determined based on the new tri-material models in Paper P2. To exemplify a design rule, take the results in Figure 4.5 in section 4.1.2 for the adhesive joint with substrates of Glass UD with thickness $h_1/2h_2 = 1$ and include a buffer-layer of Carbon UD. By increasing the buffer-layer thickness (starting from zero thickness), the energy release rate can be reduced until the buffer-layer thickness is about the same as the adhesive thickness i.e. $h_3/2h_2 = 1$. At this point, the energy release rate cannot be reduced much further. Thus, one applicability of the models is to determine the appropriate buffer-layer thickness according to a desired energy release rate level. Furthermore, a price constraint can be included since adding extra material can be costly in comparison with the effect achieved.

The use of tunneling crack models for design criteria is conservative since the load to propagate a tunneling crack is lower than the load to initiate a tunneling crack according to the homogenous models by Ho and Suo [41]. Since the stiffness of the laminates

in a wind turbine blade joint is relatively high, the most efficient way of reducing the tunneling crack energy release rate is to decrease the thickness of the adhesive layer.

It was demonstrated in Paper P3 that for an edgewise full scale blade test with load R-ratio of $R = -1$, residual stresses increased the R-ratio in the adhesive in an undesirable manner (to $R > 0$) and enhanced the crack growth rates of the tunneling cracks, see also section 4.2.2. In this perspective, elimination of residual stress in the adhesive is advantageous in order to reduce the crack growth rates for the tunneling cracks. This is particularly important since the measured slope of the Paris law curve of the adhesive, presented in Figure 4.8, is relatively steep meaning that small variations of the loadings give large variations of the crack growth rates (section 4.2.2).

6.3.3 Design Rules based on Sub-project 3

The cohesive strength is one of the governing properties for crack deflection at interfaces [72, 13]. The cohesive zone modeling results for crack deflection by Parmigiani and Thouless [72] were found consistent with the stress based Cook-Gordon criterion [18] (if interface-to-substrate toughness ratio was a constant of one). The Cook-Gordon criterion states that the interface will fail if the interface strength is less than about 1/3 to 1/5 of the bulk material strength. Although, the Cook-Gordon criterion was established by stress analysis of a homogenous solid, the criterion is consistent with the experimental test results presented in Paper P5 and Paper P6 since all measured normalized cohesive strengths of the interfaces were below 1/5. Therefore, it is judged that the Cook-Gordon criterion can be used as a good approximation for the prediction of crack deflection at interfaces. Although, it is a rather simple design rule, the experimental test results in Paper P5 and Paper P6 (and section 5.3.1) indicate that it can be applied with sufficiently accuracy in practice.

6.3.4 Main Design Rules

Based on the present work, the three most important design rules for adhesive bonded joints are identified to be:

- Sub project 1: Eliminate residual stresses - this can potentially enhance the stress in the adhesive at first crack by up to 40% based on the experimental tensile tests of the sandwich specimens.
- Sub project 2: Reduce the thickness of the adhesive layer since the energy release rate of a tunneling crack in the adhesive is proportional to the adhesive thickness.
- Sub project 3: Ensure that the cohesive strength of the interface is less than 1/5 of the cohesive strength of the bulk material (or substrate) for the crack to deflect at the interface.

6.4 Future Work and Challenges for Adhesive Joints in Wind Turbine Blades

Although the PhD project has contributed to the research within adhesive joints for wind turbine blades, there are still many challenges to face in the future. This section is dedicated a discussion about the future challenges based on the findings in the present work and the gaps identified in the state of the art literature.

The adhesive materials used in the present work were analyzed by different test methods, but further material related challenges for adhesive bonded joints in wind turbine blades exists. The small scale test specimens used in the present work were manufactured under process conditions in the laboratory that were different from the manufacturing of a full scale wind turbine blade.

Temperature was found to be an important parameter affecting the properties of the adhesive. This was demonstrated by the tensile tests of the sandwich specimens (laminate/adhesive/laminate) where the results were presented in Figure 3.9 and Figure 3.10 in section 3.5.2. It was found that the approach in Figure 3.2 could predict the stress in the adhesive at first crack at temperatures of 23°C and −40°C relatively accurate (see Figure 3.9) if the input parameters were measured at the same temperatures. A relevant extension of this study could explore the effect of elevated test temperatures e.g. 40°C. This would require to measure K_{IC}, E_2 and ν_2 for the adhesive at similar temperatures.

Another complicating factor is the time dependency of the adhesive (stress relaxation, creep, visco-elasticity). These effects might be present in the real application, but they were assumed to be negligible in the modeling (section 2.2). Therefore, it would be relevant to look further into the time dependency of the adhesive i.a. since this will affect the residual stresses in the adhesive.

In the present work residual stresses were measured on adhesive test specimens that were tested within a few weeks after manufacturing whereas typical wind turbine blades in the field operate in harsh conditions for more than 20 years. Since the life time of wind turbine blades is more than 20 years, the effect of creep and stress relaxation of the adhesive might be significant and thus reduce the residual stress magnitude in the adhesive of a full scale blade. Therefore, the problem of residual stresses might be smaller in reality than what was measured on the test specimens in the laboratory. A future study could investigate the contradictory effects of residual stresses and the level of creep over time. This could possibly be tested using the bi-layer specimen (e.g. with FBGs) where the curvature over time could be measured and compared with creep experiments. The measurements could be supported by visco-elastic models. Another material related challenge is the effect of residual stresses on the R-ratio and on the parameters in Paris law, which is not well documented in the literature for polymeric materials. Further understanding and testing of adhesives loaded cyclic by different R-ratio and residual stress levels are proposed as a future study.

The tunneling crack tool, in combination with the approach presented in Paper P3 and Figure 4.7, can predict crack growth rates for tunneling cracks in a trailing-edge joint of a wind turbine blade within acceptable accuracy, see Figure 4.9 in section 4.2.2. The

tunneling crack tool could be extended to account for delamination during the tunneling process [17, 97, 98], to handle gel coat channeling cracks in wind turbine blade surfaces during cyclic loading [116], or be applied on tunneling cracks in grid-scored balsa/foam panels used in wind turbine blades, where the crack tunnels through the resin filled grid-scores [55]. The range of proposed applications are broad.

In Paper P5 and Paper P6, a novel approach was presented to determine the cohesive strength of a bi-material interface. The approach were summarized in section 5.3. Alternatively, the cohesive strength could be determined with environmental scanning-electron microscopy (ESEM) using a J-integral based approach [27]. A benchmark of these two distinct approaches is proposed as a future study to evaluate the accuracy of the methods. The geometry of the four-point SENB specimen, used to determine the cohesive strength, could be changed by machining an elliptical-shaped notch instead of a sharp start crack. The advantage of the geometry with an elliptical-shaped notch is that the stress concentration factor would be known, and it will be harder for the main crack to start propagating. This might simplify the analysis.

During this PhD project, novel approaches were developed and their applicability on adhesive joints for wind turbine blades were tested experimentally in order to establish novel design rules. In Paper P3 the approach were tested and compared with actual measurements from a full scale blade fatigue test. The approaches developed in the other papers were primarily compared with lab scale experiments. Generally, these approaches should be compared with tests on full scale blades since this is an important step towards integration of the design rules into the current joint design package. Furthermore, the process related design rules needs to be tested in a real production environment before they can be implemented in the manufacturing technology such that the advantages of these design rules can be fully utilized.

6.5 Conclusion

Based on residual stress measurements and experimental tensile tests of adhesive bonded joints, it was found that residual stresses were of relative significant magnitude, primarily at low temperatures. The cyclic loaded tests confirmed that the design of the adhesive joint was damage tolerant since multiple cracking of the adhesive evolved in a stable manner. Using a new tunneling crack tool (approach) and accounting for the residual stresses in the adhesive, crack growth rates predicted for tunneling cracks in a trailing-edge joint were found to agree well with crack growth rates measured on a full scale blade tested with high cyclic loadings. By applying a novel approach, the cohesive strength measured for a number of model interfaces, were found to be low in comparison with the macroscopic strength of the adhesive. These experimental results were found to be consistent with the Cook-Gordon criterion for crack deflection.

The experimental-, analytical- and numerical results can, in combination with the novel approaches, be used to improve the current design methods for adhesive joints. Thus, the design limits for adhesive joints in wind turbine blades can, safely, be pushed closer towards the actual structural limits.

Bibliography

[1] M. Alam, B. Grimm, and J. P. Parmigiani. "Effect of incident angle on crack propagation at interfaces". In: *Engineering Fracture Mechanics* 162 (2016), pages 155–163.

[2] M. Alam and J. P. Parmigiani. "Crack propagation at bi-material interfaces". In: *Proc. Appl. Math. Mech.* Volume 15. 2015, pages 143–144. DOI: 10.1002/pamm.201510062.

[3] C. Aliá et al. "Influence of post-curing temperature on the structure, properties, and adhesion of vinyl ester adhesive". In: *Journal of Adhesion Science and Technology* 29.6 (2015), pages 518–531. ISSN: 15685616. DOI: 10.1080/01694243.2014.995910.

[4] J. M. Ambrico and M. R. Begley. "The role of initial flaw size, elastic compliance and plasticity in channel cracking of thin films". In: *Thin Solid Films* 419 (2002), pages 144–153. ISSN: 00406090. DOI: 10.1016/S0040-6090(02)00718-6.

[5] J. Ambrose. *World's largest wind turbines may double in size before 2024*. 2017.

[6] J. Andersons, P. H. M. Timmermans, and J. Modniks. "Mechanics of tunnelling cracks in trilayer elastic materials in tension". In: *International Journal of Fracture* 148.3 (April 2008), pages 233–241. ISSN: 0376-9429. DOI: 10.1007/s10704-008-9197-3.

[7] T. Andersson and U. Stigh. "The stress-elongation relation for an adhesive layer loaded in peel using equilibrium of energetic forces". In: *International Journal of Solids and Structures* 41.2 (2004), pages 413–434. ISSN: 00207683. DOI: 10.1016/j.ijsolstr.2003.09.039.

[8] Scott Bader. *Crystic Composites Handbook*. Technical report. Wollaston, UK, 2005, pages 1–90.

[9] H. G. Beom and H. S. Jang. "Effect of elastic constants on crack channeling in a thin film bonded to an orthotropic substrate". In: *Archive of Applied Mechanics* 83.11 (2013), pages 1577–1589. ISSN: 0939-1533. DOI: 10.1007/s00419-013-0766-1.

[10] H. G. Beom, X. R. Zhuo, and C. B. Cui. "Tunneling cracks in the adhesive layer of an orthotropic sandwich structure". In: *International Journal of Engineering Science* 63 (February 2013), pages 40–51. ISSN: 00207225. DOI: 10.1016/j.ijengsci.2012.11.001.

[11] J. L. Beuth. "Cracking of thin bonded films in residual tension". In: *Int. J. Solid Structures* 2.13 (1992), pages 1657–1675.

[12] A. Boonyapookana, K. Nagata, and Y. Mutoh. “Fatigue crack growth behavior of silica particulate reinforced epoxy resin composite”. In: *Composites Science and Technology* 71.8 (2011), pages 1124–1131. ISSN: 02663538. DOI: 10.1016/j.compscitech.2011.02.015.

[13] S. Brinckmann, B. Völker, and G. Dehm. “Crack deflection in multi-layered four-point bending samples”. In: *International Journal of Fracture* 190.1-2 (2014), pages 167–176. ISSN: 15732673. DOI: 10.1007/s10704-014-9981-1.

[14] E. N. Brown, S. R. White, and N. R. Sottos. “Fatigue crack propagation in microcapsule-toughened epoxy”. In: *Journal of Materials Science* 41.19 (2006), pages 6266–6273. ISSN: 00222461. DOI: 10.1007/s10853-006-0512-y.

[15] R. J. C. Carbas, E. A. S. Marques, and L. F. M. da Silva. “Effect of Cure Temperature on the Glass Transition Temperature and Mechanical Properties of Epoxy Adhesives”. In: *The Journal of Adhesion* 90 (2014), pages 104–119. DOI: 10.1080/00218464.2013.779559.

[16] R. J. C. Carbas et al. “Effect of post-cure on the glass transition temperature and mechanical properties of epoxy adhesives.” In: *Journal of Adhesion Science & Technology* 27.23 (2013), pages 2542–2557. ISSN: 01694243. DOI: 10.1080/01694243.2013.790294.

[17] K. S. Chan, M. Y. He, and J. W. Hutchinson. “Cracking and stress redistribution in ceramic layered composites”. In: *Materials Science and Engineering* A167 (1993), pages 57–64.

[18] J. Cook et al. “A mechanism for the control of crack propagation in all-brittle systems”. In: *Mathematical and Physical Sciences* 282.1391 (1964), pages 508–520.

[19] C. A. Crawford. “The Path from Functional to Detailed Design of a Coning Rotor Wind Turbine Concept”. In: *Proceedings of the Canadian Engineering Education Association* (2011), pages 1–10. DOI: 10.24908/pceea.v0i0.3768.

[20] J. Dundurs. “Edge-Bonded Dissimilar Orthogonal Elastic Wedges Under Normal and Shear Loading”. In: *Journal of Applied Mechanics* (1969), pages 650–652.

[21] J. Dundurs. “Effect of elastic constants on stress in a composite under plane deformation”. In: *Journal of Composite Materials* 1 (1967), pages 310–322. ISSN: 00137944. DOI: 10.1177/002199836700100306.

[22] M. A. Eder and R. D. Bitsche. “Fracture Analysis of Adhesive Joints in Wind Turbine Blades”. In: *Wind Energy* 00 (2012), pages 1–18. DOI: 10.1002/we.

[23] A. G. Evans and J. W. Hutchinson. “The Thermomechanical Integrity of Thin Films and Multilayers”. In: *Acta metall. mater.* 43.7 (1995), pages 2507–2530.

[24] S. Fenster and A. Ugural. *Advanced Strength and Applied Elasticity*. 4th. Upper Saddle River, New Jersey: Prentice Hall, 2003, pages 1–545. ISBN: 0-13-047392-8.

[25] G. Fernandez, H. Usabiaga, and D. Vandepitte. "Subcomponent development for sandwich composite wind turbine blade bonded joints analysis". In: *Composite Structures* 180 (2017), pages 41–62. ISSN: 02638223. DOI: 10.1016/j.compstruct.2017.07.098.

[26] M. Goland and E. Reissner. "The Stresses in Cemented Joints". In: *Journal of Applied Mechanics* 11 (1944), pages 17–27.

[27] S. Goutianos et al. "Effect of Processing Conditions on Fracture Resistance and Cohesive Laws of Binderfree All-Cellulose Composites". In: *Applied Composite Materials* 21.6 (2014), pages 805–825. ISSN: 0929189X. DOI: 10.1007/s10443-013-9381-0.

[28] A. A. Griffith. "The phenomena of Rupture and Flow in solids". In: *Royal Soc. of London* 221 (A 587 (1920), pages 163–198.

[29] M. Grujicic et al. "Multidisciplinary design optimization for glass-fiber epoxy-matrix composite 5 MW horizontal-axis wind-turbine blades". In: *Journal of Materials Engineering and Performance* 19.8 (2010), pages 1116–1127. ISSN: 10599495. DOI: 10.1007/s11665-010-9596-2.

[30] V. Gupta, A. S. Argon, and Z. Suo. "Crack Deflection at an Interface Between Two Orthotropic Media". In: *Journal of Applied Mechanics* 59 (1992), pages 79–87.

[31] V. Gupta, J. Yuan, and D. Martinez. "Calculation, measurements, and control of interface strength in composites". In: *J. Am. Ceram. Soc* 76.2 (1993), pages 305–315.

[32] J. Z. Hansen. "The effects of fibre architecture on fatigue life-time of composite materials". PhD thesis. Technical University of Denmark. Dept. of Wind Energy, 2013. ISBN: 9788792896483.

[33] L. J. Hart-Smith. *Adhesive bonded double-lap Joints*. Technical report. 1973, pages 1–106.

[34] L. J. Hart-Smith. "Adhesive Bonded Joints for Composites - Phenomenological Considerations". In: *Conference on Advanced Composites Technology*. 1978, pages 1–18.

[35] L. J. Hart-Smith. *Adhesive bonded single lap joints*. Technical report. 1973, pages 1–104.

[36] L. J. Hart-Smith. "Further Developments in Design and Analysis of Adhesive-Bonded Structural Joints". In: *ASTM Symposium on Joining of Composite Materials*. 1980, pages 1–26.

[37] B. Hayman, J. Wedel-Heinen, and P. Brøndsted. "Materials Challenges in Present and Future Wind Energy". In: *MRS Bulletin* 33.04 (2008), pages 343–353. ISSN: 1938-1425. DOI: 10.1557/mrs2008.70.

[38] M. Y. He, A. G. Evans, and J. W. Hutchinson. "Crack deflection at an interface between dissimilar elastic materials: Role of residual stresses". In: *International Journal of Solids and Structures* 31.24 (December 1994), pages 3443–3455. ISSN: 00207683. DOI: 10.1016/0020-7683(94)90025-6.

[39] M. Y. He and J. W. Hutchinson. "Crack deflection at an interface between dissimilar elastic materials". In: *Int. J. Solid Structures* 25.9 (1989), pages 1053–1067.

[40] M. Y. He and J. W. Hutchinson. "Kinking of a crack out of an interface". In: *Journal of Applied Mechanics* 111 (1989).

[41] S. Ho and Z. Suo. "Tunneling cracks in constrained layers". In: *J. Appl. Mech* 60 (1993), pages 890–894.

[42] J. W. Hutchinson. "Fundamentals of the Phenomenological Theory of Nonlinear Fracture Mechanics". In: *Journal of Applied Mechanics* 50.4 (1983), pages 1042–1051. ISSN: 0021-8936. DOI: 10.1115/1.3167187.

[43] J. W. Hutchinson and Z. Suo. "Mixed Mode Cracking in Layered Materials". In: *Advances in Applied Mechanics* 29 (1992), pages 63–191.

[44] G. Irwin. "Linear fracture mechanics, fracture transition, and fracture control". In: *Engineering Fracture Mechanics* 1.2 (1968), pages 241–257. ISSN: 00137944. DOI: 10.1016/0013-7944(68)90001-5.

[45] G. Irwin and D. Washington. "Analysis of Stresses and Strains Near the End of a Crack Traversing a Plate". In: *Journal of Applied Mechanics* 24 (1957), pages 361–364.

[46] ITW Plexus. *Plexus Guide To Bonding of Plastics, Composites and Metals*. Technical report. ITW Plexus, 2017, pages 1–46.

[47] K. K. Jin et al. "International Conferences on Composite Materials". In: *Life Prediction of Wind Turbine Blades*. 2009, pages 1–12.

[48] R. K. Joki et al. "Determination of a cohesive law for delamination modelling - Accounting for variation in crack opening and stress state across the test specimen width". In: *Composites Science and Technology* 128 (2016), pages 49–57. ISSN: 02663538. DOI: 10.1016/j.compscitech.2016.01.026.

[49] J. B. Jørgensen et al. "Determination of mode-I cohesive strength for interfaces". In: *IOP Conference Series: Materials Science and Engineering* 139 (2016), pages 267–274. ISSN: 1757-8981. DOI: 10.1088/1757-899X/139/1/012025.

[50] C. Kanchanomai and A. Thammaruechuc. "Effects of stress ratio on fatigue crack growth of thermoset epoxy resin". In: *Polymer Degradation and Stability* 94.10 (2009), pages 1772–1778. ISSN: 01413910. DOI: 10.1016/j.polymdegradstab.2009.06.012.

[51] K. B. Katnam et al. "Composite Repair in Wind Turbine Blades: An Overview". In: *The Journal of Adhesion* 91.1-2 (2014), pages 113–139. ISSN: 0021-8464. DOI: 10.1080/00218464.2014.900449.

[52] C. Kong et al. “Investigation of fatigue life for a medium scale composite wind turbine blade”. In: *International Journal of Fatigue* 28.10 SPEC. ISS. (2006), pages 1382–1388. ISSN: 01421123. DOI: 10.1016/j.ijfatigue.2006.02.034.

[53] M. H. Kothmann et al. “Fatigue crack propagation behaviour of epoxy resins modified with silica-nanoparticles”. In: *Polymer (United Kingdom)* 60 (2015), pages 157–163. ISSN: 00323861. DOI: 10.1016/j.polymer.2015.01.036.

[54] S. Krohn, P. E. Morthorst, and S. Awerbuch. *The Economics of Wind Energy*. Technical report 6-7. 2012, pages 714–728. DOI: 10.1016/j.renene.2014.01.017.

[55] S. Laustsen et al. “Development of a high-fidelity experimental substructure test rig for grid-scored sandwich panels in wind turbine blades”. In: *Strain* 50.2 (2014), pages 111–131. ISSN: 14751305. DOI: 10.1111/str.12072.

[56] P. Lava and D. Debruyne. “Practical considerations in DIC measurements MatchID : new spin-off company of KULeuven”. In: *Practical considerations in DIC measurements*. Edinburgh, 2015, pages 1–79.

[57] W. Lee and W. J. Clegg. “The Deflection of Cracks at Interfaces”. In: *Key Engineering Materials* 116-117 (1996), pages 193–208. ISSN: 10139826. DOI: 10.4028/www.scientific.net/KEM.132-136.1886.

[58] M. Leong et al. “Fatigue failure of sandwich beams with face sheet wrinkle defects”. In: *Composites Science and Technology* 72.13 (2012), pages 1539–1547. ISSN: 02663538. DOI: 10.1016/j.compscitech.2012.06.001.

[59] V. C. Li and R. J. Ward. “A novel testing technique for post peak tensile behaviour of cementitious materials”. In: *Fracture Toughness and Fracture Energy*. Edited by Mihashi et a. (eds). 1989, pages 183–195. ISBN: 9061919886.

[60] X. Liu et al. “Dynamic Response Analysis of the Blade of Horizontal Axis Wind Turbines”. In: *Journal of Mechanical Engineering* 46.12 (2010), page 128. ISSN: 0577-6686. DOI: 10.3901/JME.2010.12.128.

[61] E. Loth et al. “Downwind pre-aligned rotors for extreme-scale wind turbines”. In: *Wind Energy* 20 (2017), pages 1241–1259.

[62] D. Martinez and V. Gupta. “Energy Criterion for Crack Deflection at an Interface Between Two Orthotropic Media”. In: *J. Mech. Phys. Solids* 42.8 (1994), pages 1247–1271.

[63] R. E. McDermott, R. J. Mikulak, and M. R. Beauregard. *The Basics of FMEA*. Second edi. New York: CRC Press, 2008, pages 1–91. ISBN: 9781563273773.

[64] G. Meneghetti, M. Quaresimin, and M. Ricotta. “Life prediction for bonded joints in composite material based on actual fatigue damage”. In: *Advances in structural adhesive bonding*. Edited by David A. Dillard. Cambirdge: Woodhead Publishing Limited, 2010. Chapter 12, pages 316–349. ISBN: 978-1-84569-435-7.

[65] L. P. Mikkelsen. "A simplified model predicting the weight of the load carrying beam in a wind turbine blade". In: *IOP Conference Series: Materials Science and Engineering* 139 (2016), pages 1–8. ISSN: 1757-8981. DOI: 10.1088/1757-899X/139/1/012038.

[66] I. Mohammed and K. M. Liechti. "Cohesive zone modeling of crack nucleation at bimaterial corners". In: *Journal of the Mechanics and Physics of Solids* 48.4 (April 2000), pages 735–764. ISSN: 00225096. DOI: 10.1016/S0022-5096(99)00052-6.

[67] J. A. Nairn. "Energy release rate analysis for adhesive and laminate double cantilever beam specimens emphasizing the effect of residual stresses". In: *International Journal of Adhesion and Adhesives* 20 (1999), pages 59–70.

[68] T. Nakamura and S. M. Kamath. "Three-dimensional effects in thin film fracture mechanics". In: *Mechanics of Materials* 13.1 (March 1992), pages 67–77. ISSN: 01676636. DOI: 10.1016/0167-6636(92)90037-E.

[69] P. C. Paris and F. Erdogan. "A Critical Analysis of Crack Propagation Laws". In: *Journal of Basic Engineering* 85.4 (1963), pages 528–534.

[70] J. P. Parmigiani. "Delamination and deflection at interfaces". PhD thesis. University of Michigan, 2006, pages 1–129.

[71] J. P. Parmigiani and M. D. Thouless. "The effects of cohesive strength and toughness on mixed-mode delamination of beam-like geometries". In: *Engineering Fracture Mechanics* 74.17 (November 2007), pages 2675–2699. ISSN: 00137944. DOI: 10.1016/j.engfracmech.2007.02.005.

[72] J. P. Parmigiani and M. D. Thouless. "The roles of toughness and cohesive strength on crack deflection at interfaces". In: *Journal of the Mechanics and Physics of Solids* 54.2 (February 2006), pages 266–287. ISSN: 00225096. DOI: 10.1016/j.jmps.2005.09.002.

[73] J. A. Pascoe, R. C. Alderliesten, and R. Benedictus. "Methods for the prediction of fatigue delamination growth in composites and adhesive bonds - A critical review". In: *Engineering Fracture Mechanics* 112-113 (2013), pages 72–96. ISSN: 00137944. DOI: 10.1016/j.engfracmech.2013.10.003.

[74] F. Pierron. *Metrology and uncertainty quantification in DIC*. Technical report. Southampton: University of Southampton, 2015.

[75] M. Quaresimin. "Modelling the fatigue behaviour of bonded joints in composite materials". In: *Multi-Scale Modelling of Composite Material Systems*. Edited by C. Soutis and P. W. R. Beaumont. Cambridge: Woodhead Publishing Limited, 2005. Chapter 16, pages 469–494. ISBN: 9781855739369. DOI: 10.1533/9781845690847.469.

[76] P. Reu. "All about speckles: Contrast". In: *Experimental Techniques* 39.1 (2015), pages 1–2. ISSN: 17471567. DOI: 10.1111/ext.12126.

[77] P. Reu. "All about speckles: Speckle density". In: *Experimental Techniques* 39.3 (2015), pages 1–2. ISSN: 17471567. DOI: 10.1111/ext.12161.

[78] P. Reu. "Points on Paint". In: *Experimental Techniques* 39.4 (2015), pages 1–2. ISSN: 0732-8818. DOI: 10.1111/ext.12147.

[79] P. Reu. "Speckles and their relationship to the digital camera". In: *Experimental Techniques* 38.4 (2014), pages 1–2. ISSN: 1747-1567. DOI: 10.1111/ext.12105.

[80] P. Reu. "Stereo-rig design: Camera selection-part 2". In: *Experimental Techniques* 36.6 (2012), pages 3–4. ISSN: 07328818. DOI: 10.1111/j.1747-1567.2012.00872.x.

[81] P. Reu. "Stereo-rig design: Lens selection - Part 3". In: *Experimental Techniques* 37.1 (2013), pages 1–3. ISSN: 07328818. DOI: 10.1111/ext.12000.

[82] P. Reu. "Stereo-rig design: Lighting - Part 5". In: *Experimental Techniques* 37.3 (2013), pages 1–2. ISSN: 07328818. DOI: 10.1111/ext.12020.

[83] D. Salimi-Majd, V. Azimzadeh, and B. Mohammadi. "Loading Analysis of Composite Wind Turbine Blade for Fatigue Life Prediction of Adhesively Bonded Root Joint". In: *Applied Composite Materials* 22.3 (2014), pages 269–287. ISSN: 0929189X. DOI: 10.1007/s10443-014-9405-4.

[84] S. M. M. Slütter. *Crack formation of adhesive bonded joints in wind turbine blades*. Technical report. Aeronautical Engineering of Inholland University of Applied Sciences at Delft, 2013, pages 1–164. DOI: http://www.royalcommission.vic.gov.au/finaldocuments/summary/PF/VBRC_Summary_PF.pdf.

[85] H. Söker. "Loads on wind turbine blades". In: *Advances in Wind Turbine Blade Design and Materials*. 2013, pages 29–58. ISBN: 9780857094261. DOI: 10.1533/9780857097286.1.29.

[86] Correlated Solutions. *Vic-2D Reference Manual*. Technical report. Correlated Solutions, 2009, pages 1–58.

[87] B. F. Sørensen, S. Goutianos, and T. K. Jacobsen. "Strength scaling of adhesive joints in polymer matrix composites". In: *International Journal of Solids and Structures* 46 (February 2009), pages 741–761. ISSN: 00207683. DOI: 10.1016/j.ijsolstr.2008.09.024. URL: http://linkinghub.elsevier.com/retrieve/pii/S0020768308003971.

[88] B. F. Sørensen and T. K. Jacobsen. "Large-scale bridging in composites: R-curves and bridging laws". In: *Composites Part A: Applied Science and Manufacturing* 29 (1998), pages 1443–1451. ISSN: 1359835X. DOI: 10.1016/S1359-835X(98)00025-6.

[89] B. F. Sørensen et al. "A general mixed mode fracture mechanics test specimen : The DCB-specimen loaded with uneven bending moments". In: *Int J Fract* 141 (2006), pages 163–176.

[90] B. F. Sørensen et al. "Blade materials, testing methods and structural design". In: *Wind Power Generation and Wind Turbine Design*. Edited by Wei Tong. Volume 44. Boston: WIT Press, 2010. Chapter 13, pages 417–460. ISBN: 978-1-84564-205-1. DOI: 10.2495/978-1-84564-.

[91] B. F. Sørensen et al. "From interface laws to composite behaviour". In: *Interface Design of Polymer Matrix Composites – Mechanics, Chemistry, Modelling and Manufacturing*. Risø, 2007, pages 55–74.

[92] B. F. Sørensen et al. *Improved design for large wind turbine blades of fibre composites (Phase 3) Summary report*. Technical report June. 2009, pages 1–30.

[93] B. F. Sørensen et al. "Strength and failure modes of ceramic multilayers". In: *Journal of the European Ceramic Society* 32.16 (2012), pages 4165–4176. ISSN: 09552219. DOI: 10.1016/j.jeurceramsoc.2012.06.012.

[94] IJ. J. van Straalen et al. "Structural adhesive bonded joints in engineering–drafting design rules". In: *International Journal of Adhesion and Adhesives* 18 (1998), pages 41–49. ISSN: 01437496. DOI: 10.1016/S0143-7496(97)00068-7.

[95] J. L. Strom and J. P. Parmigiani. "Transition of crack path at bi-material interfaces". In: *Engineering Fracture Mechanics* 115 (2014), pages 13–21. ISSN: 00137944. DOI: 10.1016/j.engfracmech.2013.11.015.

[96] T. Suga, G. Elssner, and S. Schmauder. "Composite Parameters and Mechanical Compatibility of Material Joints". In: *Journal of Composite Materials* 22.10 (1988), pages 917–934. ISSN: 0021-9983. DOI: 10.1177/002199838802201002.

[97] A. S. J. Suiker and N. A. Fleck. "Crack tunneling and plane-strain delamination in layered solids". In: *International Journal of Fracture* 125.1 (January 2004), pages 1–32. ISSN: 0376-9429. DOI: 10.1023/B:FRAC.0000021064.52949.e2.

[98] A. S. J. Suiker and N. A. Fleck. "Modelling of fatigue crack tunneling and delamination in layered composites". In: *Composites Part A: Applied Science and Manufacturing* 37.10 (October 2006), pages 1722–1733. ISSN: 1359835X. DOI: 10.1016/j.compositesa.2005.09.006.

[99] Z. Suo. "Delamination specimens for orthotropic materials". In: *Journal of Applied Mechanics* 57 (1990), pages 627–634.

[100] Z. Suo. "Failure of brittle adhesive joints". In: *Appl. Mech. Rev.* 43.5 (1990), pages 275–279.

[101] Z. Suo and J. W. Hutchinson. "Interface crack between two elastic layers". In: *International Journal of Fracture* 43 (1990), pages 1–18.

[102] Z. Suo et al. "Orthotropy rescaling and implications for fracture in composites". In: *Int. J. Solid Structures* 28.2 (1991), pages 235–248.

[103] M. A. Sutton, J.J. Orteu, and H. W. Schreier. *Image Correlation for Shape, Motion and Deformation Measurements*. Volume 1. Springer, 2009. ISBN: 9788578110796. DOI: 10.1017/CBO9781107415324.004. arXiv: arXiv:1011.1669v3.

[104] H. Tada, P. C. Paris, and G. R. Irwin. *The Stress Analysis of Cracks Handbook*. Third. Volume 3. New York: ASME Press, 2000, pages 1–677.

[105] M. D. Thouless. "Crack Spacing in Brittle Films on Elastic Substrates". In: *J. Am. Ceram. Soc.* 73.7 (1990), pages 2144–46.

[106] M. D. Thouless, H. C. Cao, and P. A. Mataga. “Delamination from surface cracks in composite materials”. In: *Journal of Materials Science* 24 (1989), pages 1406–1412.

[107] T. Y. Tsui, A. J. McKerrow, and J. J. Vlassak. “Constraint Effects on Thin Film Channel Cracking Behavior”. In: *Journal of Materials Research* 20 (2005), pages 2266–2273. ISSN: 0884-2914. DOI: 10.1557/jmr.2005.0317.

[108] J. J. Vlassak. “Channel cracking in thin films on substrates of finite thickness”. In: *International Journal of Fracture* 119/120.1979 (2003), pages 299–323. ISSN: 0376-9429. DOI: 10.1023/A:1024962825938.

[109] O. Volkersen. “Nietkraftverteiligung in zugbeanspruchten nietverbindungen mit konstanten Laschenquerschnitten”. In: *Luftfahrtforschung* (1938), pages 15–41.

[110] P. J. Withers and H. K. D. H. Bhadeshia. “Residual stress part 1 - Measurement techniques”. In: *Materials Science and Technology* 17.4 (2001), pages 355–365. ISSN: 02670836. DOI: 10.1179/026708301101509980.

[111] Z. C. Xia and J. W. Hutchinson. “Crack patterns in thin films”. In: *Journal of the Mechanics and Physics of Solids* 48 (2000), pages 1107–1131.

[112] J. Yang et al. “Structural investigation of composite wind turbine blade considering structural collapse in full-scale static tests”. In: *Composite Structures* 97 (2013), pages 15–29. ISSN: 02638223. DOI: 10.1016/j.compstruct.2012.10.055.

[113] Q. D. Yang and M. D. Thouless. “Mixed-mode fracture analyses of plastically-deforming adhesive joints”. In: *International Journal of Fracture* 110.2 (2001), pages 175–187. ISSN: 03769429. DOI: 10.1023/A:1010869706996.

[114] Q. D. Yang, M. D. Thouless, and S. M. Ward. “Numerical Simulations of Adhesively-bonded Beams Failing with Extensive Plastic Deformation”. In: *Journal of the Mechanics and Physics of Solids* 47 (1999), pages 1337–1353.

[115] T. Yang, Y. Liu, and J. Wang. “A study of the propagation of an embedded crack in a composite laminate of finite thickness”. In: *Composite Structures* 59.4 (March 2003), pages 473–479. ISSN: 02638223. DOI: 10.1016/S0263-8223(02)00284-2.

[116] H. Zhang and J. Jackman. “Feasibility of Automatic Detection of Surface Cracks in Wind Turbine Blades”. In: *Wind Engineering* 38.6 (2014), pages 575–586.

[117] J. Zhang and J. J. Lewandowski. “Delamination study using four-point bending of bilayers”. In: *Journal of Materials Science* 32.14 (1997), pages 3851–3856. ISSN: 00222461.

[118] Y. Zhang, R. D. Adams, and L. F. M. da Silva. “Effects of curing cycle and thermal history on the glass transition temperature of adhesives”. In: *Journal of Adhesion* 90.4 (2014), pages 327–345. ISSN: 00218464. DOI: 10.1080/00218464.2013.795116.

APPENDIX A
Appended papers

List of appended papers in the thesis:

P1 Jeppe B. Jørgensen, Bent F. Sørensen and Casper Kildegaard. "The effect of residual stresses on the formation of transverse cracks in adhesive joints for wind turbine blades." Submitted to: *International Journal of Solids and Structures* (2017).

P2 Jeppe B. Jørgensen, Bent F. Sørensen and Casper Kildegaard. "The effect of buffer-layer on the steady-state energy release rate of a tunneling crack in a wind turbine blade joint". Submitted to: *Composite Structures* (2017).

P3 Jeppe B. Jørgensen, Bent F. Sørensen and Casper Kildegaard. "Tunneling cracks in full scale wind turbine blade joints". Accepted for: *Engineering Fracture Mechanics* (2017).

P4 Jeppe B. Jørgensen, Casper Kildegaard and Bent F. Sørensen. "Design of four-point SENB specimens with stable crack growth". Submitted to: *Engineering Fracture Mechanics* (2017).

P5 Jeppe B. Jørgensen, Bent F. Sørensen and Casper Kildegaard. "Crack deflection at interfaces in adhesive joints for wind turbine blades". Submitted to: *Composites Part A: Applied Science and Manufacturing* (2017).

P6 Jeppe B. Jørgensen, Michael D. Thouless, Bent F. Sørensen and Casper Kildegaard. "Determination of mode-I cohesive strength of interfaces". In: *IOP Conf. Series: Materials Science and Engineering*, 139, 012024 (2016).

APPENDED PAPER P1

The effect of residual stresses on the formation of transverse cracks in adhesive joints for wind turbine blades

Jeppe B. Jørgensen, Bent F. Sørensen and Casper Kildegaard
International Journal of Solids and Structures
Submitted, 2017

The effect of residual stresses on the formation of transverse cracks in adhesive joints for wind turbine blades

Jeppe B. Jørgensen[a,b,*], Bent F. Sørensen[b], Casper Kildegaard[a]

[a] *LM Wind Power, Østre Alle 1, 6640 Lunderskov, Denmark.*
[b] *The Technical University of Denmark, Dept. of Wind Energy, Frederiksborgvej 399, 4000 Roskilde, Denmark.*

Abstract

Transverse cracks in adhesive bonded joints evolve typically due to a combination of mechanical- and residual stresses. In this paper, a new approach that allows the residual stress to be determined in several different ways is presented. The residual stress measurements were used in combination with a novel bi-material model to predict the stress at first transverse crack in the adhesive layer of a sandwich specimen (laminate/adhesive/laminate).

The model prediction was consistent with measurements from quasi-static tensile tests of the sandwich specimens. These experimental results showed that higher post curing temperature and lower test temperature had a negative effect on the formation of transverse cracks in the adhesive layer i.e. residual stresses were higher and transverse cracks initiated at lower applied mechanical loading. The effect of increased laminate thickness was found to be small under both static and cyclic loading of the sandwich specimens. Furthermore, the cyclic loaded tests confirmed that the design of the sandwich specimen was damage tolerant since multiple cracking of the adhesive developed in a stable manner.

Keywords: Residual stress, Fracture, Crack, Adhesion, Finite element

Nomenclature

a	crack length
E_1, E_2	Young's modulus (substrate, adhesive)
$\bar{E}_1, \bar{E}_2$	plane strain Young's modulus (substrate, adhesive)
F	non-dimensional function (for crack model)
G_I	mode-I energy release rate

*Corresponding author
Email address: jbj@lmwindpower.com (Jeppe B. Jørgensen)

h_1, h_2	thickness for sandwich specimen (substrate, adhesive)
h_1^*, h_2^*	thickness for bi-layer specimen (substrate, adhesive)
K_I	mode-I stress intensity factor
K_{IC}	mode-I critical stress intensity factor
N	number of cycles
P	applied force
q	non-dimensional function (for misfit stress model)
r	radius of curvature
R	load R-ratio
t	time
T	temperature
T_C	curing temperature
T_{PC}	post curing temperature
T_r	reference temperature
T_R	room temperature
T_t	test temperature
U_t	total strain energy
U_{crack}	strain energy caused by the formation of a crack
$U_{no,crack}$	strain energy of specimen without crack
V_t	total work done by external forces
x, y, z	coordinates
α_1, α_2	coefficient of thermal expansion (substrate, adhesive)
δ	displacement
ϵ_{fc}	strain in adhesive at first crack
ϵ_{FBG}	strain measured by fiber Bragg grating
ϵ_{SG1}	strain measured by strain gauge number 1
ϵ_{SG2}	strain measured by strain gauge number 2
ϵ_m	mechanical strain

$\epsilon_{m,fc}$	mechanical strain at first crack in the adhesive
$\epsilon_{m,max}$	maximum mechanical strain in cyclic tests
$\bar{\epsilon}_{m,st}$	average mechanical strain at first crack in the adhesive for static tests
ϵ_{yy}	normal strain
ϵ_T	misfit strain
$\epsilon_T^{\Delta\alpha}$	misfit strain for Method 5 (reference value)
ζ_2, ζ_{2*}	adhesive to substrate thickness ratio (sandwich, bi-layer)
η_{yy}	surface traction in the y-direction in the finite element model
κ	curvature of the bi-layer specimen
ν_1, ν_2	Poisson's ratio (substrate, adhesive)
σ_m	mechanical stress in the adhesive
$\sigma_{m,fc}$	mechanical stress in the adhesive at first crack
σ_{fc}	stress in the adhesive at first crack
σ_r	residual stress in the adhesive
σ_T	misfit stress
$\sigma_T^{\Delta\alpha}$	misfit stress for Method 5 (reference value)
$\sigma_{yy,1}$	generalised normal stress in the substrate in y-direction
$\sigma_{yy,2}$	generalised normal stress in the adhesive in y-direction
Σ_2	adhesive to substrate stiffness ratio
FBG	fiber Bragg grating
FE	finite element
LEFM	linear-elastic fracture mechanics
VARTM	vacuum-assisted-resin-transfer-moulding

1. Introduction

The primary adhesive joints in wind turbine blades are the leading edge-, trailing edge-, and web-joints as shown in the blade section in Figure 1 (A). These joints connect the upwind- and downwind-shells that are usually manufactured of glass-fibre reinforced laminates produced by a vacuum-assisted-resin-transfer-moulding (VARTM) process. During the curing process, the structural adhesive shrinks and since the adhesive is constrained in-between stiffer laminates tensile residual stresses builds up. It is expected that the main contributors to the residual stress is the chemical shrinkage of the adhesive and the mismatch in coefficient of thermal expansion between the laminate and the adhesive ($\alpha_1 - \alpha_2$). The latter occurs primarily since there is a mismatch in the coefficient of thermal expansion between the laminate and the adhesive and since the structural adhesive is cured at a temperature above the operating temperature [1]. Often adhesive joints are post cured at higher temperatures in a subsequent process to enhance certain mechanical properties of the adhesive [2, 3], but this elevated temperature can also increase the magnitude of residual stresses.

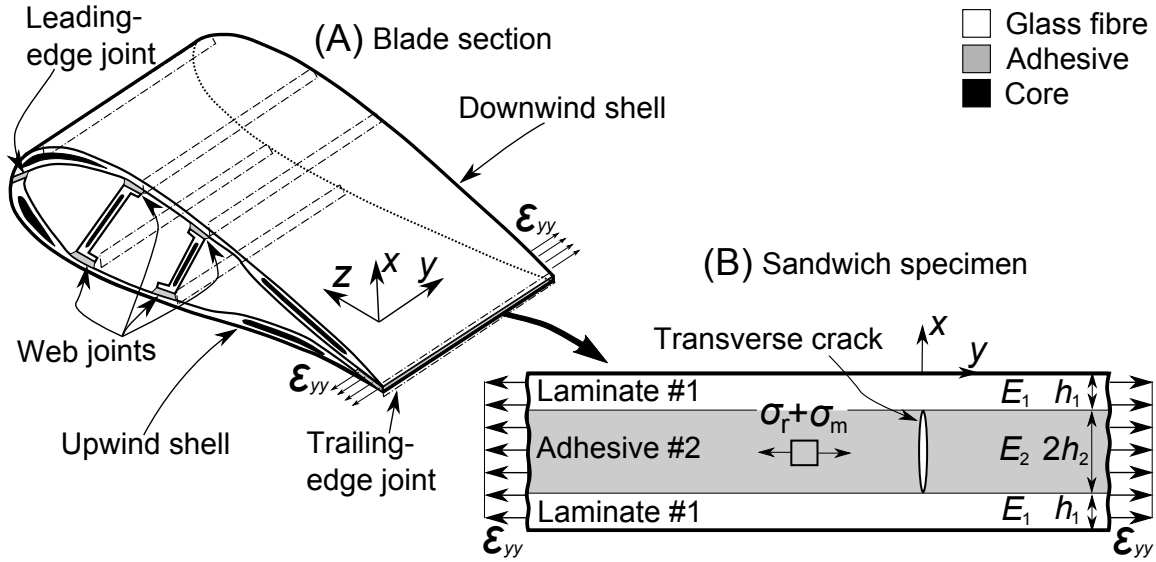

Figure 1: (A) Blade section and adhesive joints. (B) Sandwich specimen loaded in tension.

The residual stresses can be large and can, if combined critically with mechanical loadings, promote crack formation and crack growth in adhesive bonded joints [4, 5, 6]. Residual stresses in adhesive joints can be analysed e.g. using finite element (FE) modelling [7, 8, 9, 10, 11] or laminate theory [12]. Different methods for measuring residual stresses are available [4, 5, 6, 12]. The residual stress, σ_r, can be related to the misfit stress, σ_T, through a non-dimensional function, q [13]:

$$\sigma_r = q\sigma_T \tag{1}$$

The misfit stress is defined as the stress induced in a thin film adhered to an infinitely thick substrate. The use of misfit stress is convenient since the residual stress in a structure can be expressed through a non-dimensional function, q, that accounts for e.g. geometry and elastic properties. Without comprehensive models of curing, solidification and creep of the adhesive, the misfit stress cannot be predicted by modelling - it must be determined experimentally [13]. When the material response to temperature changes is elastic, the misfit stress can be related to the misfit strain, ϵ_T, by [13]:

$$\epsilon_T = \sigma_T(1 - \nu_2)/E_2 \tag{2}$$

where E_2 and ν_2 are the Young's modulus and the Poisson's ratio of the adhesive, respectively.

For wind turbine blade joints, debonding between the adhesive and one of the laminated shells is one of the most frequently analysed and modeled cracking mechanisms in the literature [14, 15, 16, 17]. In turn, analyses, models and tests of transverse cracking of the adhesive of wind turbine blade joints are limited in the literature [18]. As shown in Figure 1 (B), edgewise loadings of the blade induce longitudinal strains, ϵ_{yy}, of the trailing-edge joint. The materials of the sandwich configuration in Figure 1 (B) are assumed to be isotropic with substrate Young's modulus, E_1, substrate Poisson's ratio, ν_1, substrate thickness, h_1, adhesive Young's modulus, E_2, adhesive Poisson's ratio, ν_2 and adhesive thickness, $2h_2$. It is assumed that the resulting stress in the adhesive is the sum of the mechanical stress, σ_m, and the residual stress, σ_r. For this edgewise load case, the damage development in the trailing-edge joint typically starts with the initiation of a transverse crack in the adhesive as shown in Figure 1 (B).

Cracks in the trailing-edge joint, including transverse cracks, observed in full scale blades in operation were reported by Ataya *et al.* [19]. The transverse cracks were identified in the trailing-edge joint with a relatively high crack density at the aerodynamic part of the blade, at a position of about 0.8 of the blade length from the root, for working lifes of 17-22 years [19]. From a fracture mechanics perspective, transverse cracking of the adhesive bond line is comparable to the crack formation in a tile core sandwich structure [20, 21, 22, 23] or off-axis matrix cracks in cross ply laminates [24, 25, 26, 27, 28, 29].

Adhesive joints are typically one of the first structural details in a blade to develop damage. Damage is defined as distributed adhesive cracks (multiple cracking) [30]. The adhesive joints in wind turbine blades are typically damage tolerant, implying that the damage develops in a stable manner and is detectable before it reaches a critical state i.e. joint failure [30].

Structural adhesive joints are typically designed against first crack (no damage) since a safe design must be conservative. Thus, the damage tolerance of the joint can be used as an extra safety feature. The difficult and costly repair of adhesive joints [31, 32], especially for off-shore wind turbines, emphasise the importance of using robust design criteria such that the blade can achieve an operating life of 20 years or more [33, 34, 35, 36].

Structural health monitoring systems are desirable in order to identify damage before it reaches a critical state and cause catastrophic failure of a joint or a full structure e.g. a wind turbine blade [37, 38, 39, 40, 41]. The use of optical fibers with fiber Bragg gratings (FBG) in structural adhesive joints is attractive since residual strains during manufacturing can be measured, and subsequently the FBG can potentially be used as a part of a structural health monitoring system during operation [40, 42, 43]. The FBG measures a wavelength that can through the FBGs gauge factor be converted to a strain value [42]. Advantages of the use of optical fibers with FBGs are described in the work of Güemes *et al.* [44, 45].

The problem studied in the present work is transverse cracking of the adhesive layer of the structural adhesive joint shown in Figure 1 (B), where crack formation and growth are expected to be driven by a combination of mechanical- and residual stresses. The study includes the effect of residual stresses, laminate type, laminate thickness, post curing temperature, and operational (test) temperature. Furthermore, the effect of laminate thickness on the evolution of multiple cracking of the adhesive under cyclic loading is studied. Additionally in this work, a new approach that allows the residual stress in the adhesive to be determined in several different ways is presented. The accuracy of four different methods to measure residual stress is tested on a single sandwich test specimen (laminate/adhesive/laminate). The instrumentation of the test specimen includes strain gauges and FBGs. FBGs are also embedded in the adhesive to determine residual stresses during the different manufacturing steps in the bonding process.

The paper is structured as follows. First, a new approach to predict the stress in the adhesive at which the first crack can propagate from a void in the adhesive layer of the sandwich specimen will be introduced. Secondly, a novel bi-material FE model of the sandwich specimen in Figure 1 (B) will be presented and included in the approach. The principles of measuring residual stresses will then be described. Hereafter, the materials and manufacturing procedures for preparation of the test specimens will be described including the experimental procedures. The results section includes a comparison of the different residual stress measurements and a comparison between predicted and experimentally determined stress in the adhesive at first transverse crack in the sandwich specimen. Additionally, results from the static- and cyclic loaded tests of the different sandwich specimen configurations will be presented. Finally, the results will be discussed and the major findings will be used to propose novel design rules for adhesive bonded joints.

2. Problem definition

The adhesive joint in Figure 1 (B) is basically a sandwich specimen (laminate/adhesive/laminate) loaded in tension. Experimental tests of this sandwich specimen should lead to novel design rules for

structural adhesive joints. Two types of laminates (Laminate A and Laminate B) that are presented in section 6, are used to investigate the effect of different variables:

- The effect of variables on the magnitude of residual stresses in the adhesive layer of the sandwich specimen:
  - Test temperature (-50^{o}C, -40^{o}C, -30^{o}C, -20^{o}C, 23^{o}C).
  - Post curing temperature (50^{o}C, 70^{o}C, 90^{o}C).
  - Laminate thickness (Laminate B).
- The effect of variables to initiate a transverse crack in the adhesive layer of the sandwich specimens loaded in static tension:
  - Test temperature (-50^{o}C, -40^{o}C, -30^{o}C, -20^{o}C, 23^{o}C).
  - Post curing temperature (50^{o}C, 70^{o}C, 90^{o}C).
  - Laminate type (Laminate A, Laminate B).
  - Laminate thickness (Laminate B).
- The effect of variables on the evolution of multiple cracking of the adhesive layer of the sandwich specimen loaded cyclic:
  - Laminate thickness (Laminate B).

3. Approach for determination of stress in the adhesive at first crack

The approach for determination of stress in the adhesive at first crack, σ_{fc}, in static tensile tests of the sandwich specimen, shown in Figure 1 (B), is presented schematic in Figure 2.

3.1. Model prediction

It is assumed that the stress level at which first crack of length, $2a$, in the adhesive of the sandwich specimen in Figure 2 (i) can propagate, can be predicted by a relation between the stress in the adhesive at first crack, σ_{fc}, and the mode-I critical stress intensity factor of the adhesive, K_{IC}:

$$\sigma_{fc} = \frac{K_{IC}}{\sqrt{\pi a} F(a/(h_1+h_2), h_1/h_2, E_1/E_2, \nu_1, \nu_2)} \qquad \text{(prediction)} \tag{3}$$

which is a relation on a similar form as for the center cracked test specimen presented by Tada *et al.* [46]. The non-dimensional function, F, accounts for the geometry and the stiffness mismatch between the substrates and the adhesive. F needs to be determined numerically for this bi-material specimen. K_{IC} of the bulk adhesive should be measured experimentally.

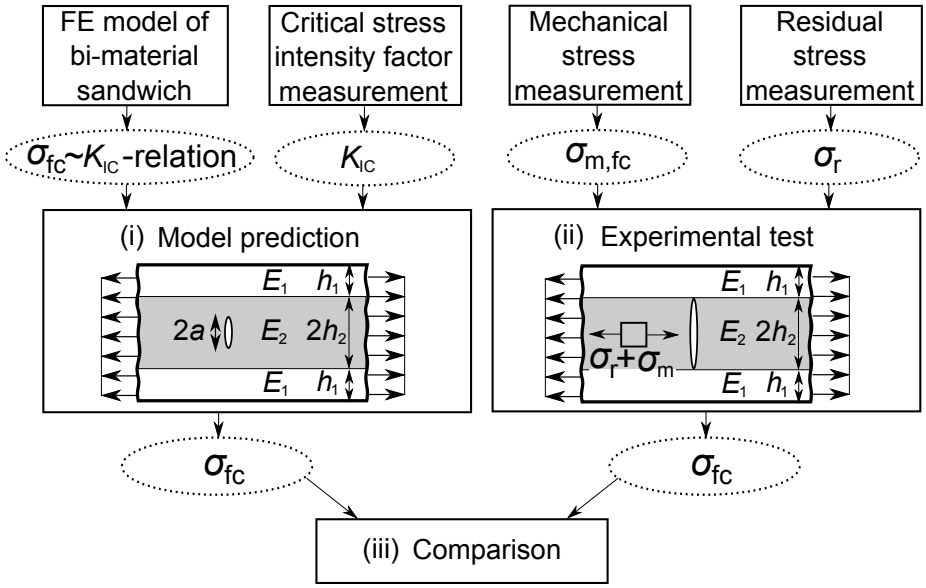

Figure 2: Approach for determination of stress in the adhesive at first crack, σ_{fc}. (i) Model prediction. (ii) Experimental test. (iii) Comparison of model prediction and experimental test.

3.2. Experimental test

For the experimental tests of the sandwich specimens (static), shown in Figure 2 (ii), the stress in the adhesive at first crack, i.e. the onset of growth of a crack with length, $2a$, is assumed to be the sum of the residual stress, σ_r, and the mechanical stress in the adhesive at first crack, $\sigma_{m,fc}$, as:

$$\sigma_{fc} = \sigma_{m,fc} + \sigma_r \qquad \text{(experimental)} \tag{4}$$

where $\sigma_{m,fc}$ can be determined based on the measured strain at first crack, $\epsilon_{m,fc}$, and Hooke's law:

$$\sigma_{m,fc} = \bar{E}_2 \epsilon_{m,fc} \tag{5}$$

where $\bar{E}_2$ is the plane strain Young's modulus of the adhesive. A relation between the misfit stress and the residual stress in the adhesive of the sandwich specimen shown in Figure 1 (B) can be derived by equilibrium considerations (interface perfectly bonded) and by Hooke's law in plane stress (x-direction) [47]:

$$\sigma_r = \frac{\sigma_T}{1 + \zeta_2 \Sigma_2} \tag{6}$$

where $\Sigma_2 = [E_2/(1-\nu_2)] \,/\, [E_1/(1-\nu_1)]$ and $\zeta_2 = h_2/h_1$ are for the sandwich specimen shown in Figure 1 (B). The misfit stress, σ_T, of the adhesive can be measured by different methods as demonstrated in section 5. When the residual stress is determined, the magnitude of σ_{fc} can be determined by equation 4.

3.3. Comparison of model prediction and experimental test

In order to test the accuracy of the methods ("Model prediction" and "Experimental test" in Figure 2), a comparison will be made at two different temperatures (23°C and −40°C) according to the last step in the approach i.e. Figure 2 (iii). The material properties of the adhesive (K_{IC} and E_2) are taken to depend on temperature, T, meaning that σ_{fc} will be a function of $K_{IC}(T)$ and $E_2(T)$. Furthermore, the experimental method in Figure 2 (ii) will be applied on other sandwich specimens in order to test the effect of different parameters e.g. post curing temperature, test temperature and laminate thickness.

4. Modelling of the center cracked test specimen

If pre-existing cracks are present in the adhesive, linear-elastic fracture mechanics (LEFM) with finite element simulations can be applied to predict the propagation of the crack.

4.1. Methods

The sandwich specimen in Figure 1 (B) is comparable to the center cracked test specimen presented by Tada *et al.* [46] where the mode-I stress intensity factor, K_I, is given on the form:

$$K_I = \sigma_{yy,2}\sqrt{\pi a}F(a/h_2) \tag{7}$$

where $\sigma_{yy,2}$ is the stress in the adhesive and $2a$ is the crack length, see Figure 3 and Figure 4. The non-dimensional function, F, from Tada *et al.* [46] is however only valid in absence of elastic mismatch between substrate and adhesive i.e. for the homogenous specimen. If including elastic mismatch, the stress intensity factor depends on additional parameters and (7) should be modified to:

$$K_I = \sigma_{yy,2}\sqrt{\pi a}F(a/(h_1+h_2), h_1/h_2, E_1/E_2, \nu_1, \nu_2) \tag{8}$$

The non-dimensional function, F, is determined numerically by the use of a parametric 2D FE model, simulated in Abaqus CAE 6.14 (Dassault Systemes) with eight-noded plane strain elements. A quarter of the sandwich geometry is modelled by imposing a symmetry condition in both the x- and y-directions as shown in Figure 3. A surface traction, η_{yy}, is applied on the free boundary in the y-direction. 100 elements are used over distance h_2 near the crack in the quarter of the model. A focused mesh were used in the y-direction in a distance of h_2 from the crack tip. The model is parametric with the non-dimensional groups of $a/(h_1+h_2)$, h_1/h_2, E_1/E_2, ν_1 and ν_2.

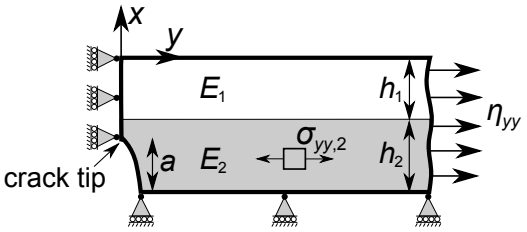

Figure 3: Boundary conditions for the FE model, where a quarter of the full model is analysed by finite element simulations.

4.2. Results from FE model of center cracked test specimen

Finite element results are presented in Figure 4 in terms of the non-dimensional function, F, and for different elastic mismatch. For the homogenous case ($E_1/E_2 = 1.0$), F is compared with the results presented by Tada *et al.* [46]. The maximum deviation between the two results is 0.81%. The trend in Figure 4 is comparable to the partial cracked film problem from Beuth [48] i.e. F increases with crack length for compliant substrates ($E_1/E_2 \lesssim 1$) and decreases with crack length for stiff substrates ($E_1/E_2 \gtrsim 4$). Note, $F \to 1.0$ for $a/(h_1 + h_2) \to 0$, which is similar to the solution for a center crack in an infinitely large plate [46] of a homogenous material.

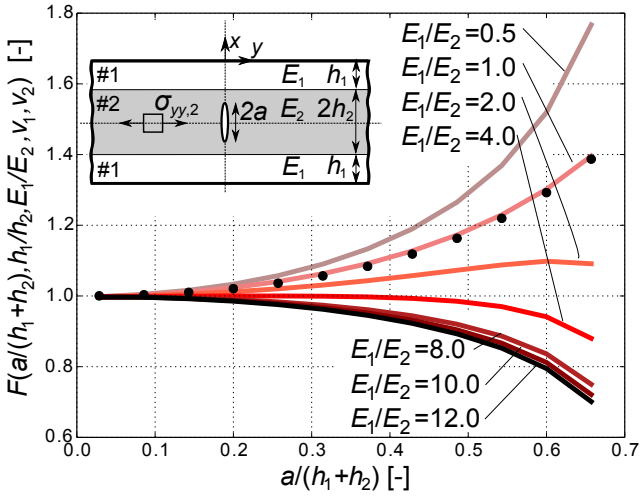

Figure 4: Finite element modelling results where $\nu_1 = \nu_2 = 1/3$ and $h_1/h_2 = 0.4$. The interface is located near $a/(h_1 + h_2) \approx 0.7$. The FE results are compared with the results (dots) from Tada *et al.* [46] for $E_1/E_2 = 1$.

5. Methods

5.1. Methods - determination of strain energies

The strain energies of the sandwich specimen in Figure 1 (B) will be analysed. In general for a linear relationship between applied force, P, and displacement, δ, of an elastic body the work done by

the external force, V_t, to deform the body is [49, 50]:

$$V_t = \frac{1}{2} P\delta \tag{9}$$

In a linear-elastic body without energy dissipation (such as heat), the work done by the external force, V_t, can be equated with the total elastic strain energy, U_t [49, 50]:

$$U_t = V_t \tag{10}$$

This relation is also known as Clapeyron's theorem [51, 52]. The total elastic strain energy, U_t, stored in the body of the sandwich specimen in Figure 1 (B) can be written as the sum of the elastic strain energy for the specimen without crack, $U_{no,crack}$, and the elastic strain energy for the introduction of the transverse crack, U_{crack}, see Tada *et al.* [46] (Appendix B) or Rice *et al.* [53]:

$$U_t = U_{no,crack} + U_{crack} \tag{11}$$

The change in strain energy due to the introduction of the transverse crack in the sandwich specimen in Figure 1 (B) can be determined by the principles presented by Beuth [48] as:

$$U_{crack} = \int_{x=-a}^{x=+a} G_I da = 2\int_{x=0}^{x=a} G_I da \tag{12}$$

where U_{crack} can be interpreted as the change in strain energy when the crack extends over the length from $x = -a$ to $x = +a$. Using the Irwin relation [54], $G_I = K_I^2/\bar{E}_2$, and equation 8 for K_I, the strain energy, U_{crack}, becomes:

$$U_{crack} = \frac{2\pi\sigma_{yy,2}^2}{\bar{E}_2} \int_{x=0}^{x=a} \left[a \left[F(a/(h_1+h_2), h_1/h_2, E_1/E_2, \nu_1, \nu_2) \right]^2 \right] da \tag{13}$$

The integral in equation 13 can e.g. be evaluated by numerical integration over the crack length, $2a$, using the finite element modeling result for F in Figure 4. Thus, if the input parameters to equation 13 are known, the increase of strain energy due to the formation of a transverse crack in the adhesive can be predicted.

5.2. Methods - determination of residual stresses

A new approach is proposed that allows the residual stress to be determined in several different ways. With this approach, it is possible to mimic the process conditions and constraints of the structural adhesive joint i.e. reproduce the thermal boundary conditions and the constraining effect from the laminates on the adhesive. Thus, an advantage of the new approach is that all process related effects contributing to the residual stress will be included in the measurement. As a part of the new approach, five different methods can be applied on the same sandwich specimen/bi-layer specimen (in Figure 5 and 6) in order to test the accuracy of each method. Method 1 to 4 to determine the misfit stress experimentally are presented graphically in Figure 6, whereas Method 5 is a theoretical estimate:

- Method 1 - based on strains measured by FBG in sandwich specimens.
- Method 2 - based on dial gauge to measure curvature of bi-layer specimens.
- Method 3 - based on strain gauge and FBG to measure curvature of bi-layer specimens.
- Method 4 - based on strains measured by strain gauge on free laminates (debonded).
- Method 5 - based on theoretical estimate using a reference temperature.

First the sandwich specimen is manufactured (Step 1-3) in Figure 5. The contraction of the sandwich specimen in the y-direction after curing in Figure 5 and Figure 6 is indicated by ΔL. The contraction of the adhesive in the x-direction is indicated by the adhesive thickness before curing, $2h_{2c}$, (liquid state) and the thickness of the adhesive after curing, $2h_2$ (solid state). After manufacturing, the contraction of the specimen is measured with the FBG in the sandwich specimen (see Method 1 in Figure 6). The bottom laminate is removed and the curvature is measured (see Method 2 in Figure 6). The FBG is now embedded in the adhesive (see Method 3 in Figure 6) and the strains are measured by the strain gauge, SG1, and the FBG. The strain gauge, SG2, measures a strain on the free laminate (Method 4 in Figure 6). Method 5 is a direct estimate of the misfit stress based on a reference temperature, the test (operational) temperature, and the coefficients of thermal expansion.

Method 1 to 4 is used to determine the actual residual stress magnitude in the adhesive irrespective of the mechanism behind i.e. chemical shrinkage, thermal expansion mismatch, creep or other phenomena. In turn, for Method 5 it is assumed that the only contribution to the residual stress comes from the temperature and the coefficient of thermal expansion. The methods are presented in details in the next sections where dimensionless parameters are introduced to reduce the number of variables (see symbols in Figure 6):

$$\Sigma_2 = \frac{E_2/(1-\nu_2)}{E_1/(1-\nu_1)}, \quad \zeta_2 = \frac{h_2}{h_1} \quad \text{(sandwich specimen)}, \quad \zeta_{2*} = \frac{h_2^*}{h_1^*} \quad \text{(bi-layer specimen)} \tag{14}$$

where h_1^* and h_2^* are the thickness of the substrate and adhesive for the bi-layer specimen, respectively. Note, the relations in Figure 6 between the sandwich and the bi-layers specimens, $h_1^* = h_1$ and $h_2^* = 2h_2$.

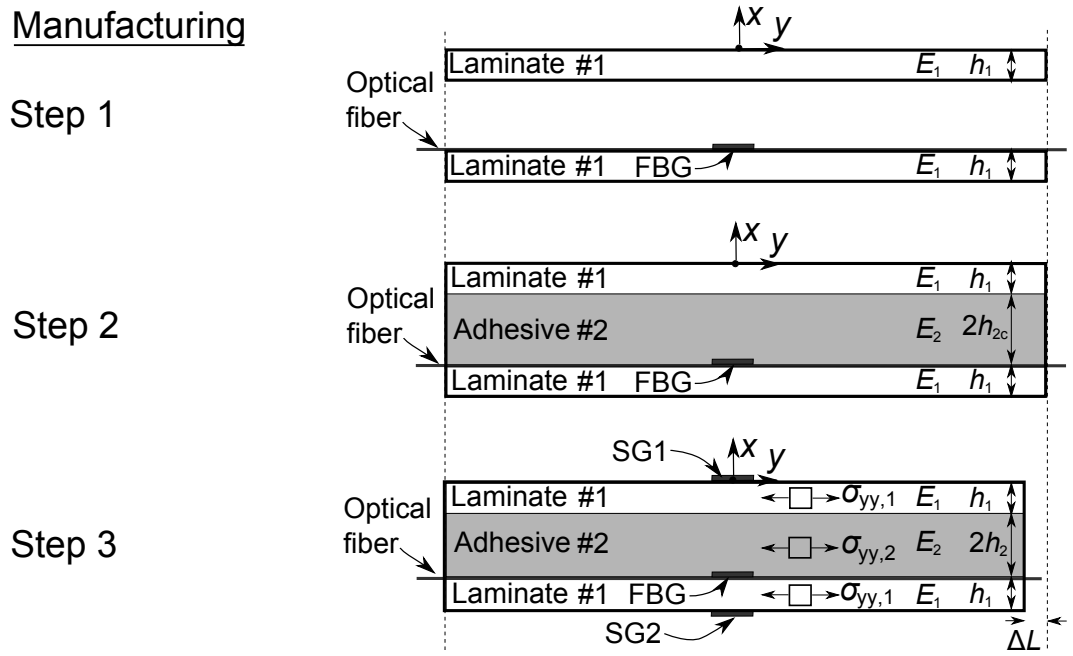

Figure 5: Manufacturing principle. Step 1: Mounting of FBG before injection of the adhesive. Step 2: After injection of the adhesive, but before curing of the adhesive. Step 3: After curing of the adhesive. Note, $\sigma_{yy,1}$ will be compressive and $\sigma_{yy,2}$ will be tensile ($\sigma_r = \sigma_{yy,2}$) since the adhesive contracts during the curing process.

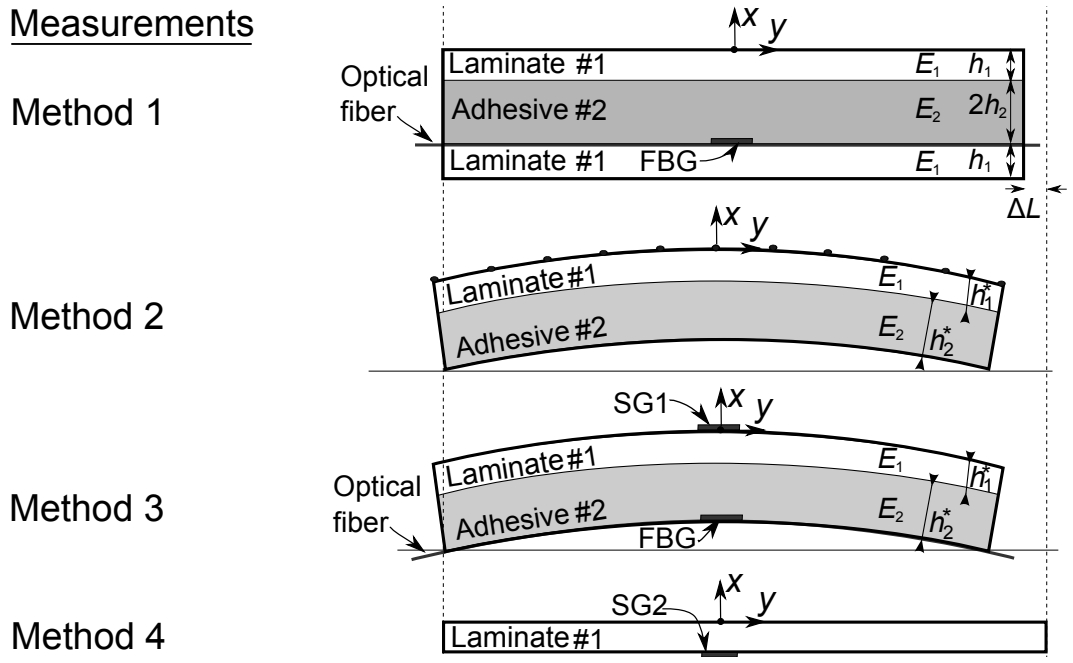

Figure 6: Approach that includes four experimental methods to determine the residual stress of the adhesive after curing. Method 1: Measure strains with FBG. Method 2: Measure curvature with dial gauge. Method 3: Determine curvature with FBG and SG1. Method 4: Measure in-plane strains by SG1 on free laminate. Note, $h_1^* = h_1$ and $h_2^* = 2h_2$.

5.3. Method 1 - based on strains measured by FBG on sandwich specimen

The procedure for Method 1 is: (see the three steps in Figure 5)

- Attach the FBG to the laminate and read off the absolute wavelength of the FBG (Step 1).
- Inject the adhesive in-between two laminates in order to cast a sandwich specimen (Step 2).
- After curing of the adhesive, measure absolute wavelength of the FBG for the sandwich specimen (Step 3).

All measurements should be made at room temperature unless a temperature compensation is applied. The measured absolute wavelength before injection of the adhesive is used as a reference value. After injection- and curing of the adhesive, the FBG measures an absolute wavelength that can be converted to an in-plane strain, ϵ_{FBG}, by using the FBGs gauge factor and the reference value. An equilibrium condition between the forces in the adhesive and the laminate can be used to determine the residual stress as demonstrated in Appendix A. Thus, the stress in the adhesive of the sandwich specimen, $\sigma_{yy,2}$, can be calculated by:

$$\sigma_{yy,2} = \frac{-\bar{E}_1 \epsilon_{FBG}}{\zeta_2} \tag{15}$$

where $\bar{E}_1$ is the plane strain Young's modulus of the substrate. The misfit stress in the adhesive can be determined by rewriting equation 6 as:

$$\sigma_T = -\sigma_{yy,1}\left(\frac{1}{\zeta_2} + \Sigma_2\right) = \sigma_{yy,2}\left(1 + \zeta_2 \Sigma_2\right) \tag{16}$$

where $\sigma_{yy,1}$ is the normal stress in the substrate acting in the y-direction.

5.4. Method 2 - based on dial gauge to measure curvature of bi-layer specimen

The procedure for Method 2 is:

- After curing of the adhesive, peel off one of the laminates of the sandwich specimen.
- Measure beam height at points on the top surface by a dial gauge (Method 2 in Figure 6).
- Fit circle to the points on the beams top surface to determine the radius of curvature, r.
- Determine the curvature, $\kappa = 1/r$.

Having determined κ, of the bi-layer specimens the misfit stress can be determined from [13]:

$$\sigma_T = \frac{(\Sigma_2 \zeta_{2*}^2 - 1)^2 + 4\Sigma_2 \zeta_{2*}(1 + \zeta_{2*})^2}{6\zeta_{2*}^2(1 + \zeta_{2*})} \left[\frac{E_2 h_2 \kappa}{\Sigma_2(1 - \nu_2)}\right] \tag{17}$$

5.5. Method 3 - based on strain gauge and FBG to measure curvature of bi-layer specimen

The procedure for Method 3 is:

- After curing of the sandwich specimen, zero the strain gauge and read off the absolute wavelength of the FBG (reference value).
- Peel off the bottom laminate of the sandwich specimen.
- Measure the strain, ϵ_{SG1}, on the top surface by strain gauge SG1 and measure the absolute wavelength by the FBG on the bottom surface. Convert the absolute wavelength to strain, ϵ_{FBG}, using the FBGs gauge factor and the reference wavelength.
- Determine the curvature based on measured strains.

The curvature, κ, of the bi-layer specimen can be determined by the measured strains from the strain gauge SG1, ϵ_{SG1}, on the top of the beam and the strain measured by the FBG on the bottom of the beam. The relation between the beam normal strain, ϵ_{yy}, and the beam curvature, κ, is:

$$\epsilon_{yy} = \kappa x \tag{18}$$

where x is the distance from the elastic center to the point of interest. For the determination of κ, the position of the neutral axis is not needed since it is the sum of the thickness $(h_1^* + h_2^*)$ that enters the equation (SG1 and FBG are mounted on the top and bottom surface, respectively):

$$\kappa = \frac{(\epsilon_{SG1} - \epsilon_{FBG})}{(h_1^* + h_2^*)} \tag{19}$$

where ϵ_{SG1} is a positive value and ϵ_{FBG} is a negative value. Based on κ, the misfit stress can then be determined from equation 17.

5.6. Method 4 - based on strains measured by strain gauge on free laminate

The procedure for Method 4 is:

- After curing of the sandwich specimen, mount the strain gauge (SG2) on the bottom laminate.
- Peel off the bottom laminate from the sandwich and measure the tensile strain by SG2.

Strain gauge SG2 measures ϵ_{SG2} on the free laminate that is peeled off from the sandwich specimen as shown in Figure 6. The stress in the adhesive of the sandwich can then be determined by assuming perfect bonding of the adhesive/laminate interface in the sandwich specimen and by using an equilibrium condition between the forces in the laminate and the adhesive as demonstrated in Appendix A. Thus, the stress in the adhesive of the sandwich specimen, $\sigma_{yy,2}$, can be determined by:

$$\sigma_{yy,2} = \frac{\bar{E}_1 \epsilon_{SG2}}{\zeta_2} \tag{20}$$

For Method 4, the misfit stress in the adhesive can finally be determined by equation 16.

5.7. Method 5 - based on estimate using a reference temperature

The misfit stress in the adhesive can be estimated based on the temperature difference between a reference temperature, T_r, e.g. the curing or the post curing temperature, and the current test temperature, T_t [13]. Thus, the misfit stress for Method 5 is denoted $\sigma_T^{\Delta\alpha}$ and it can be calculated as:

$$\sigma_T^{\Delta\alpha} = \epsilon_T^{\Delta\alpha} \frac{E_2}{(1-\nu_2)} = (\alpha_1 - \alpha_2)(T_t - T_r) \frac{E_2}{(1-\nu_2)} \tag{21}$$

where α_1 and α_2 are the coefficients of thermal expansion of the substrate and the adhesive, respectively. T_r can be assumed to be the post curing temperature or the peak curing temperature of the adhesive. In Method 5, it is assumed that the chemical shrinkage of the adhesive happens when the adhesive is viscous or visco-elastic, and thus does not contribute to the build up of residual stresses. It is also assumed that all deformation is elastic [13].

5.8. Misfit stress reference value

A misfit stress reference value, $\sigma_T^{\Delta\alpha}$, is determined by Method 5, where the reference temperature, T_r, is taken to be the post curing temperature, $T_{PC} = 50^{\circ}$C, and the test temperature, T_t, is taken to be the measured room temperature, $T_R = 23^{\circ}$C. The other material properties (α_1, α_2, E_2, ν_2) are measured experimentally in the laboratory on the bulk materials. The predicted result by Method 5 for $\sigma_T^{\Delta\alpha}$ is used as reference value and therefore used for normalisation of the misfit stress measurements obtained by the other methods.

6. Manufacturing

Two sandwich specimen configurations with laminates of different layup (fibre architechture) were used for the present study, namely Laminate A and Laminate B. These laminates were primarily made of uni-directional glass fibres oriented in the y-direction and the stiffness were comparable. The same type of adhesive was used for all specimens. The exact properties of the laminates and adhesive are confidential and therefore the results will be presented in a non-dimensional form.

6.1. Manufacturing of sandwich specimens

First the laminates were manufactured of glass fibre non-crimp fabrics in a VARTM process in the laboratory and subsequently the laminates were post cured. Hereafter, as shown in Figure 7, the adhesive was injected through a 10 mm hole drilled in the middle of the laminate. Following the injection, the sandwich (laminates+adhesive) was stored for 20 hours at room temperature, T_R. The temperature of the adhesive during curing, T_C, was measured by a thermo-couple in the middle of the adhesive layer through the injection hole and at the four corners of the sandwich. The peak curing temperature of the adhesive was measured by the thermo-couple to $\approx 45^{\circ}\text{C} \pm 5^{\circ}\text{C}$ and slightly lower

at the corners of the sandwich. Therefore, the post curing temperature, T_{PC}, was set to $T_{PC} = 50^{\circ}$C for 24 hours as standard in order to ensure uniform temperature and -curing over the entire sandwich plate. The sandwich plate was cut into rectangular specimens following the dotted cutting lines shown in Figure 7.

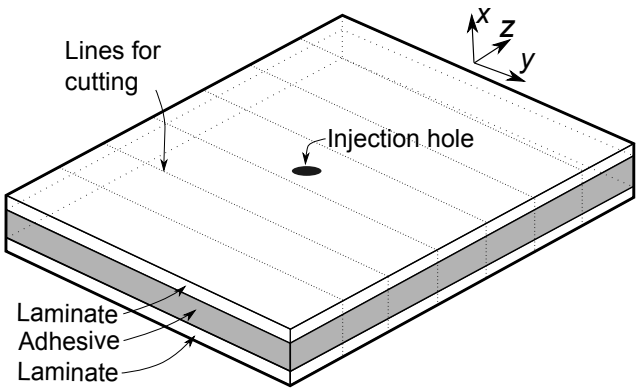

Figure 7: Manufacturing of standard sandwich specimens consisting of two laminates bonded by an adhesive. A hole in the middle is used for injection of the adhesive and for measuring the temperature with a thermo-couple.

6.2. Manufacturing of bi-layer specimens with FBGs

In the manufacturing of the bi-layer specimens, one of the laminates of the sandwich plates was cast with a thin peel ply on, as shown in Figure 8, to create a weak interface that enable separation after manufacturing.

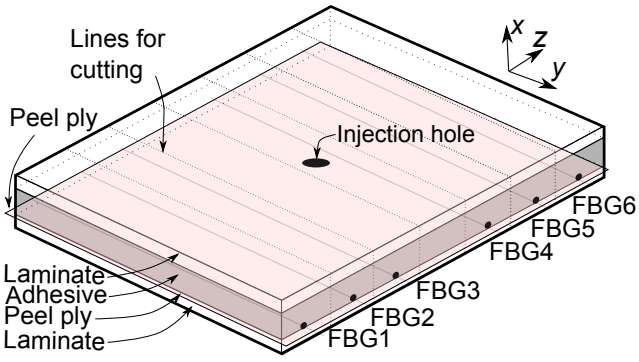

Figure 8: Manufacturing of bi-layer specimens made from a sandwich plate (laminate/adhesive/laminate) and with FBGs embedded.

The optical fibers with FBGs were bonded to the peel ply using a Lock-tide type adhesive near the edges of the plates such that the FBGs were free to move at the gauge section where the strain was to be measured. The purpose of attaching the optical fibers was to avoid movement of the optical fibers

during injection of the adhesive. Thus, misalignment between the optical fibers and the primary fiber direction of the laminate (y-direction in Figure 8) could be avoided. Finally, the adhesive was injected through the hole and the sandwich was cured and post cured.

6.3. Manufacturing of bi-layer and sandwich specimens for different post curing temperatures

Bi-layer specimens were manufactured using a procedure similar to that described in section 6.2. Six plates with sandwich specimens were manufactured and post-cured at temperatures of 50°C, 70°C and 90°C for 24 hours for sandwich specimens with Laminate A and -B, respectively. For half of the sandwich plate, a peel ply was cast with the laminate in order to ease the removal of the laminate for the six bi-layer specimens. The bi-layer specimens were cut out from the same plate as the sandwich specimens according to Figure 9. Thus, the misfit stress results determined by the bi-layer specimens (Method 2) will be a direct measure of the misfit stress in the sandwich specimens.

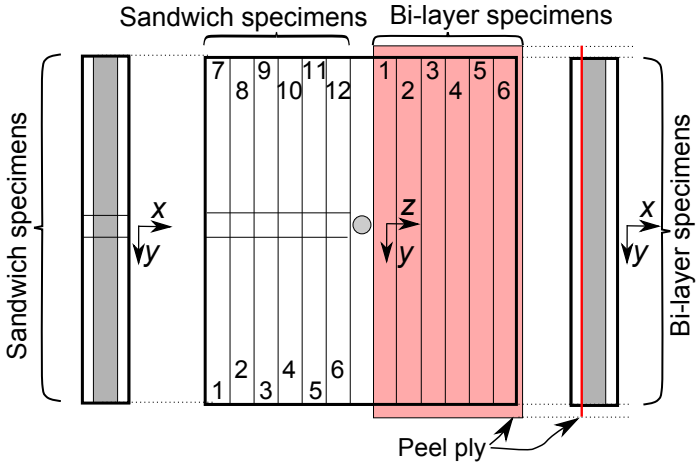

Figure 9: Manufacturing of 12 sandwich specimens and 6 bi-layer specimens from a single sandwich plate.

7. Experimental procedure

7.1. Experimental procedure - bi-material specimens to measure residual stress

The instrumentation of the sandwich specimens used for determination of the residual stress in the adhesive is presented in Figure 10 (A). The strain gauges (type: HBM 6/350 LY11) and FBGs (type: HBM Fiber Bragg Grating K-SYS-FSA) measure over a gauge length of 6 mm and 8 mm, respectively. The curvatures of the bi-layer specimens are measured using a dial gauge (type, Mitutoyo with ID-U1025). Generally, between 6 and 10 specimens were tested in each series of test specimens.

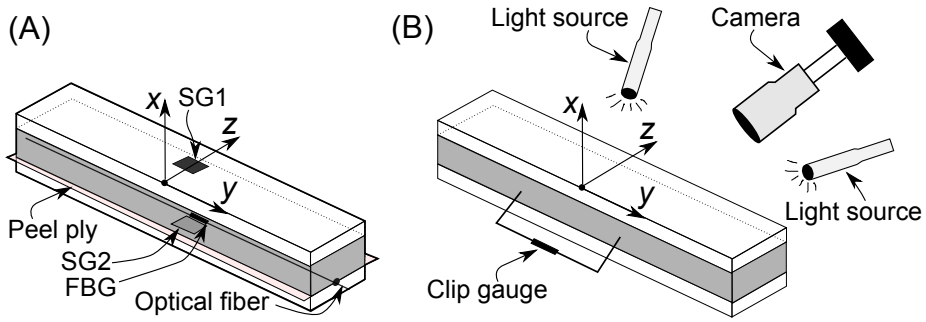

Figure 10: Instrumentaion of specimens: (A) Bi-material specimen to measure residual stress. (B) Sandwich specimen for tensile tests.

7.2. Experimental procedure - static tensile tests of sandwich specimens

Tensile tests were conducted in order to determine the strain corresponding to the appearance of the first crack in the adhesive layer. The tensile test setup and instrumentation of the sandwich specimens are presented in Figure 10 (B). For all tests the strains were measured by a clip gauge, which was attached to the adhesive as shown in Figure 10 (B). The specimens were loaded in quasi-static tension with a load rate of 1 mm/min using a test machine (type: Instron AE08145) with a load cell. 5-8 specimens were tested in each series. During loading the mechanical strain, ϵ_m, increased linearly with time until the first crack appeared in the adhesive. This strain was denoted the mechanical strain at first crack, $\epsilon_{m,fc}$. The appearance of first crack in the adhesive was detected by a sudden drop in the measured force-strain curve, but also on images taken during the test using a digital camera (Nikon D500 with 2784x1856 pixel resolution). Four series of sandwich specimens were loaded inside a climate chamber at low test temperatures of $T_t \approx -20^{\circ}$C, -30°C, -40°C, -50°C. The Young's modulus of the adhesive, E_2, was measured using a dog bone specimen tested at 23°C and -40°C following the standard "ISO 527-2: 2012".

7.3. Experimental procedure - cyclic loaded tests of sandwich specimens

Sandwich specimens were loaded cyclic (load control) in tension-tension with a load R-ratio of $R = 0.1$ where the test temperature was 23°C. 7-8 sandwich specimens were tested in each series. Images were taken with a frequency such that approx. 50-100 images were captured per test. In order to detect cracks, the images were taken by stopping the test and loading the sandwich specimen to 90% of the maximum applied strain i.e. $0.9\epsilon_{m,max}$. Each stop took 5 seconds.

8. Results from residual stress measurements

8.1. Results - FBG strain measurements during manufacturing

In the manufacturing, the FBGs were measuring the straining of the sandwich specimens during the different steps in the bonding process. The three main steps were presented in Figure 5. The measurements in Figure 11 (A-B) are numbered to indicate the corresponding manufacturing step:

1. After mounting of the FBG on the laminate.
    - FBGs were mounted and the recorded strain (wavelength) was used as reference for zero since the optical fibre was taken to be stress free.
2. After injection of the adhesive.
    - A few minutes after injection of the adhesive, the measured strain increased.

3a. After curing at room temperature (before demoulding).

- The measured strain decreased after the adhesive had cured at room temperature for 20 hours.

3b. After demoulding (plates were removed from bonding fixture).

- The measured strain was not affected significantly by demoulding (no trend identified).

3c. After post curing (the specimens were still in one sandwich plate).

- The measured strain decreased after post curing.

3d. After cutting of the sandwich plate into specimens.

- After the sandwich specimens were cut out from the sandwich plate, the measured strains decreased.

In the above list, Step 3 in Figure 5 is divided into sub steps in order to cover additional measurements. All FBG strains were measured at room temperature in the laboratory, but in Step 2 the adhesive had just begun to generate exothermal heat according to the temperature measurements. The manufacturing Step 3c (post curing) was identified, based on Figure 11 (A-B), as the manufacturing step where the primary residual stress builds up.

8.2. Misfit stress results for methods 1 to 5

The misfit stress results determined using Method 1 to 5 are presented in Figure 12 for different test series with Laminate A and Laminate B. The measurements for 1.0A, 2A, 3A and 4A in Figure 12 are from the same series of specimens (from same sandwich plate) and similarly for 1.0B, 2B, 3B and 4B. Series 1.1A and 1.1B are two additional series of specimens from two separate sandwich plates with FBGs.

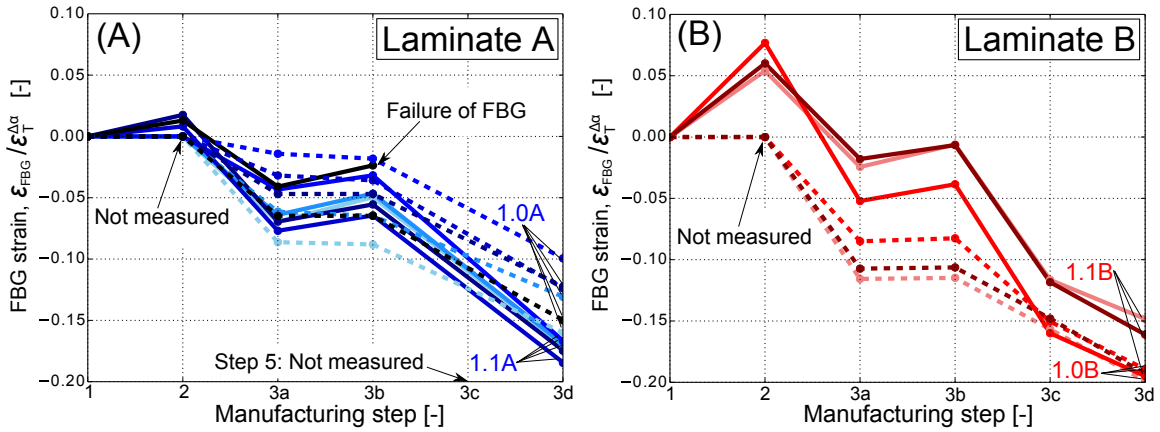

Figure 11: Strain measured with FBG during the manufacturing steps with four different test series of sandwich specimens: (A) Two test series with Laminate A (1.0A with dashed lines and 1.1A with solid lines). (B) Two test series with Laminate B (1.0B with dashed lines and 1.1B with solid lines).

The results based on FBG measurements from test series 1.0A, 1.0B, 1.1A and 1.1B in Figure 12 are taken from the last measurement with FBG (manufacturing Step 3d in Figure 11) i.e. four different test series with 3-6 samples each. The error bars indicate the standard deviation for each test series i.e. the specimen-to-specimen variations.

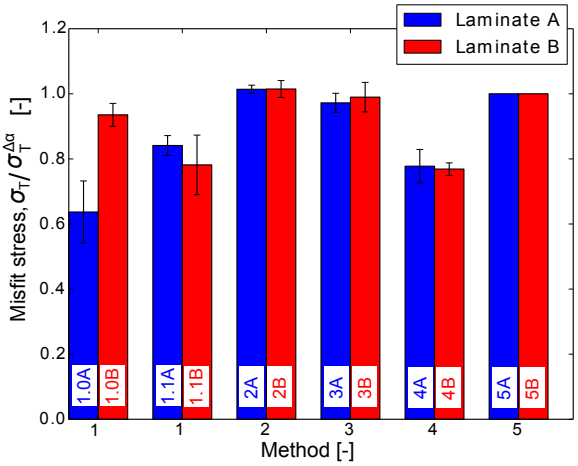

Figure 12: Misfit stress results determined experimentally by the methods 1 to 5, where $\sigma_T^{\Delta\alpha}$ is the misfit stress determined by Method 5 (used as reference value for normalisation).

The results from Method 1 (FBG in sandwich) and Method 4 (strain gauge on free laminate), which are based on strain measurements, are lower than the misfit stresses determined by the other methods. Results from Method 2 (bi-layer curvature measured by dial gauge) and Method 3 (bi-layer curvature measured by strain gauge and FBG) are both based on the determined curvature of the bi-

layer specimen and these results are in close agreement. It is noticeably that the results from Method 2, 3 and 5 are relatively close and with a small standard deviation as indicated by the error bars in Figure 12.

8.3. Misfit stress measured for different post curing temperatures

The effect of post curing temperature on the magnitude of misfit stress is determined using bi-layer specimens manufactured by the procedure described in section 6.3. The misfit stress results are determined at 23°C using Method 2 (bi-layer curvature measured by dial gauge) and presented in Figure 13 for different post curing temperatures. Clearly, the misfit stress increases (almost linearly) with increasing post curing temperature.

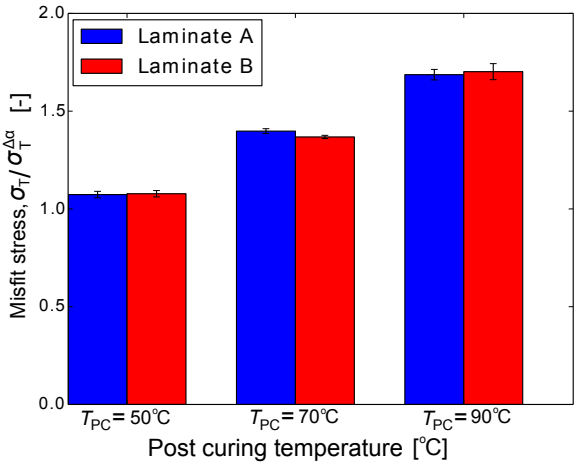

Figure 13: Misfit stress results determined at room temperature based on bi-layer specimens using Method 2 (bi-layer curvature measured by dial gauge) for post curing temperatures of 50°C, 70°C and 90°C.

9. Results from tensile tests of sandwich specimens under quasi-static loading

9.1. Results for stress in the adhesive at first crack - comparison of prediction with experimental tests

Propagation of a crack from a small void in the adhesive of the sandwich specimens was observed on images taken during the experimental tensile test e.g. as shown in Figure 14. However, crack propagation from the void towards the adhesive-laminate interface was rapid, and instantaneously the crack propagated across the full width of the specimen (in z-direction). The stress in the adhesive at onset of propagation of first transverse crack from a small void, σ_{fc}, was determined at temperatures of 23°C and −40°C using the two different methods in point (i) and (ii) of the approach in Figure 2 i.e. based on "(i) Model predictions" and "(ii) Experimental tests".

Input parameters for the two methods were measured experimentally on the bulk materials in the laboratory. The material properties of the adhesive were measured at temperatures of 23°C and −40°C on specimens that were manufactured under similar process conditions as the sandwich specimens. The mode-I critical stress intensity factor, K_{IC}, was measured by a compact tension test of the bulk adhesive using the standard "ASTM D5045" at temperatures of 23°C and −40°C. The Young's modulus of the adhesive, E_2, was measured by a dog bone specimen using the standard "ISO 527-2: 2012" at temperatures of 23°C and −40°C.

(i) Prediction: The stress in the adhesive at first crack of the sandwich specimen shown in Figure 1 (B) was predicted based on the FE model and equation 3. As an approximation the crack length, $2a$, was taken to be the maximum measured void sizes in the adhesive of the sandwich specimens. The size of the six largest voids on the surface of the adhesive in Figure 14 was measured to $a/(h_1 + h_2) \approx 0.042$ with a standard deviation of ± 0.01. Thus, the value of the non-dimensional function, F, was determined based on the modeling result in Figure 4 to $F \approx 1$. Having determined K_{IC}, F and a, the value of σ_{fc} could be determined by equation 3.

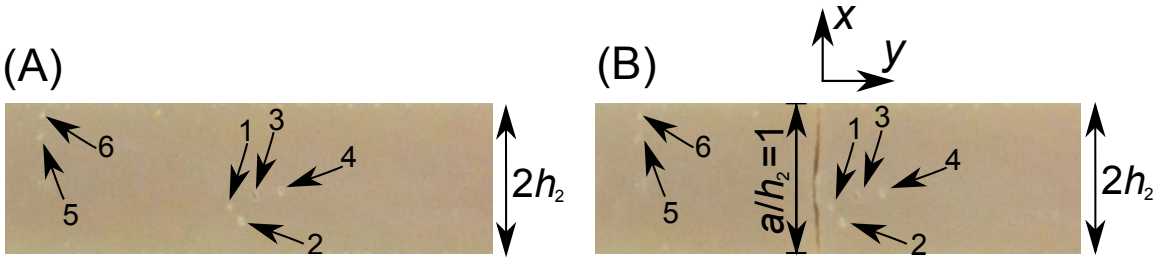

Figure 14: The sizes of six voids in the adhesive layer of a sandwich specimen were measured on the photo. The time interval between (A) and (B) is six seconds. The laminate thickness was $h_1/h_2 = 0.45$, but the laminates are not shown in the photo due to confidentiality.

(ii) Experimental test: For experimental tests of two series of test specimens (23°C and −40°C), the stress in the adhesive at first crack for the sandwich specimen shown in Figure 1 (B) was taken to be the sum of the residual stress and the mechanical stress as shown in equation 4. Here, $\sigma_{m,fc}$ was determined based on the measured mechanical strain from the clip gauge, $\epsilon_{m,fc}$, using equation 5. The misfit stress was determined at 23°C using Method 2 (section 5.4) and at −40°C by Method 5 (section 5.7). Thus, the residual stress, σ_r, could be determined based on equation 6 and finally σ_{fc} could be calculated by equation 4.

(iii) Comparison: A comparison between the predicted results and the experimental results for σ_{fc} at temperatures of 23°C and −40°C is presented in Figure 15. It was a hypothesis that equation 3 could be used to predict σ_{fc} although the FE model was developed for an infinitely sharp start-crack using LEFM whereas the shape of the pre-existing cracks in the adhesive layer of the sandwich

specimens were more uncertain. However, this hypothesis cannot be rejected since the error bars for the "Experimental" and "Prediction" in Figure 15 overlaps i.e. the prediction is close to the experimental results for both 23°C and −40°C. Since results from two independent methods determined at two very different temperatures are consistent, the methods seem to be promising for the determination of the stress in the adhesive at first crack for the sandwich specimens. Therefore in the next sections, the experimental method in Figure 2 (ii) is applied to investigate the effect of different parameters (post curing temperature, test temperature, laminate thickness) on the magnitude of σ_{fc}.

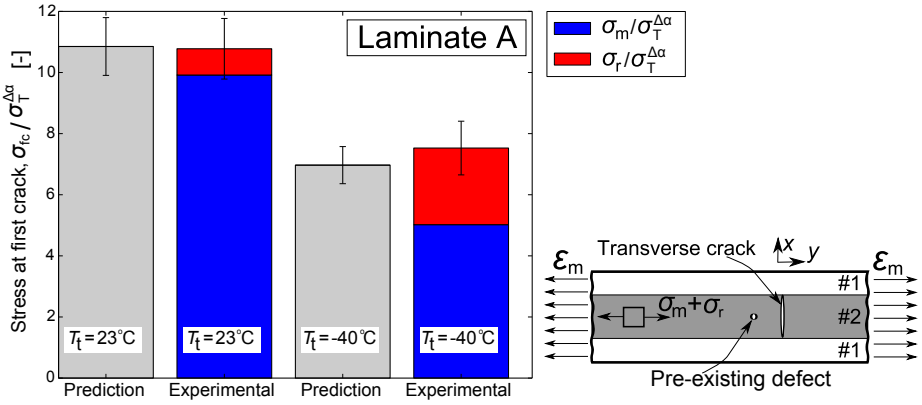

Figure 15: Results for stress in the adhesive at first crack for temperatures of 23°C and −40°C. Comparison of prediction with experimental test results using the approach in Figure 2.

9.2. Stress in the adhesive at first crack - effects of post curing temperature

The effect of post curing temperature on the stress in the adhesive at first crack was investigated by static tensile tests using the sandwich specimens shown in Figure 9. The sandwich specimens were post cured at 50°C, 70°C and 90°C and the residual stresses were measured by Method 2 on bi-layer specimens that were cut out from the same plate as the sandwich specimens, see Figure 9, i.e. in specimens manufactured under similar process conditions. From the results of the tensile tests presented in Figure 16, it can be seen that with increasing post curing temperature, the stress in the adhesive at first crack decreases in a nearly linear manner. This trend can to some extend be explained by an increase in residual stresses (if it is assumed that $T_r = T_{PC}$). However, since σ_{fc} differs for the different tests the material properties of the adhesive (e.g. strength, toughness) might have changed slightly for the different post curing temperatures tested.

9.3. Stress in the adhesive at first crack - effects of low test temperatures

The effect of low temperatures on the stress in the adhesive at first crack was investigated by testing the sandwich specimens shown in Figure 7. The results presented in Figure 17 show that as the test

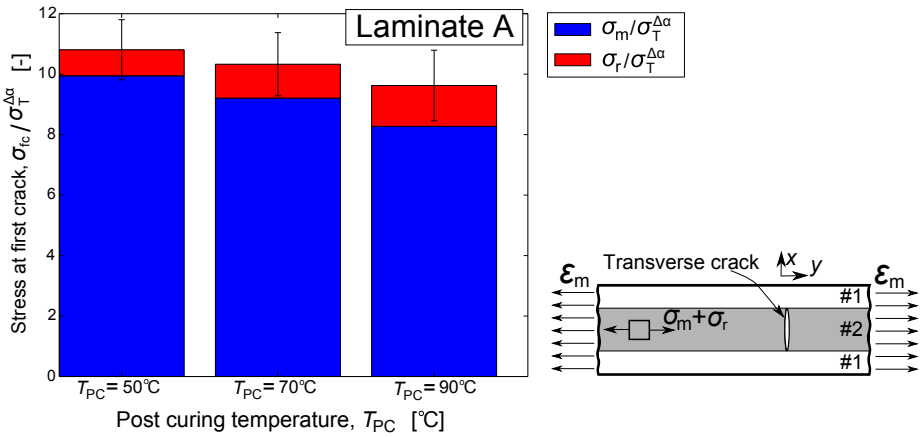

Figure 16: Results for stress in the adhesive at first crack of the sandwich was determined by: $\sigma_{fc} = \sigma_r + \sigma_{m,fc}$. Here, $\sigma_{m,fc}$ was determined from the measured mechanical strain in the tensile test and σ_r was determined from the measurements for Laminate A in Figure 13. For these tests $0.08 \leq \sigma_r/\sigma_{fc} \leq 0.14$.

temperature decreases, the stress in the adhesive at first crack decreases in a nearly linear way. This tendency can to a certain extend be explained by an increase in residual stresses according to equation 21. The finding that the magnitude of σ_{fc} differs for the different test temperatures suggests that the material properties of the adhesive (e.g. strength, toughness) are temperature dependent.

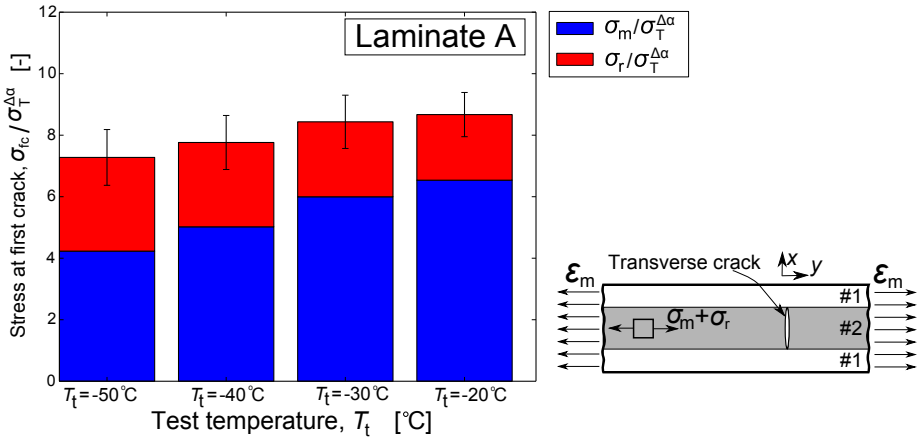

Figure 17: Results for stress in the adhesive at first crack was determined by: $\sigma_{fc} = \sigma_r + \sigma_{m,fc}$. Here, $\sigma_{m,fc}$ was determined based on the measured mechanical strain in the tensile test and σ_r was predicted using Method 5 at different T_t and with $T_r = 50$°C. For these tests $0.25 \leq \sigma_r/\sigma_{fc} \leq 0.41$.

9.4. Stress in the adhesive at first crack - effects of laminate thickness

The stress in the adhesive at first crack of the sandwich specimen with Laminate B was determined experimentally for different laminate thickness ($h_1/h_2 = 0.45$, $h_1/h_2 = 0.65$, and $h_1/h_2 = 0.85$). The

sandwich specimens were manufactured using $T_{PC} = 50^{o}$C and the adhesive thickness was similar for all specimens. Figure 18 (A) shows that the effect of laminate thickness on the stress in the adhesive at first crack is relatively small. Equation 6 and the misfit stress determined by Method 2 (series 2B in Figure 12) were used to determine the residual stress result in Figure 18 (B). As shown by equation 6, when $\Sigma_2 \to 0$ and $\zeta_2 \to 0$ then $\sigma_r \to \sigma_T$. Equivalently, for the specimen shown in Figure 18 (B) where the laminate stiffness is high ($E_1/E_2 \approx 12.0$), this means that when $h_1/h_2 \to \infty$ then $\sigma_r \to \sigma_T$. For all cases $\sigma_r \leq \sigma_T$. Thus, worst case is when the residual stress value reaches the magnitude of the misfit stress since the misfit stress can be interpreted as the upper limit for the residual stress in the adhesive of the sandwich specimen in Figure 18 (B). For these tests the ratio of residual stress to stress in the adhesive at first crack was between $0.10 \leq \sigma_r/\sigma_{fc} \leq 0.11$.

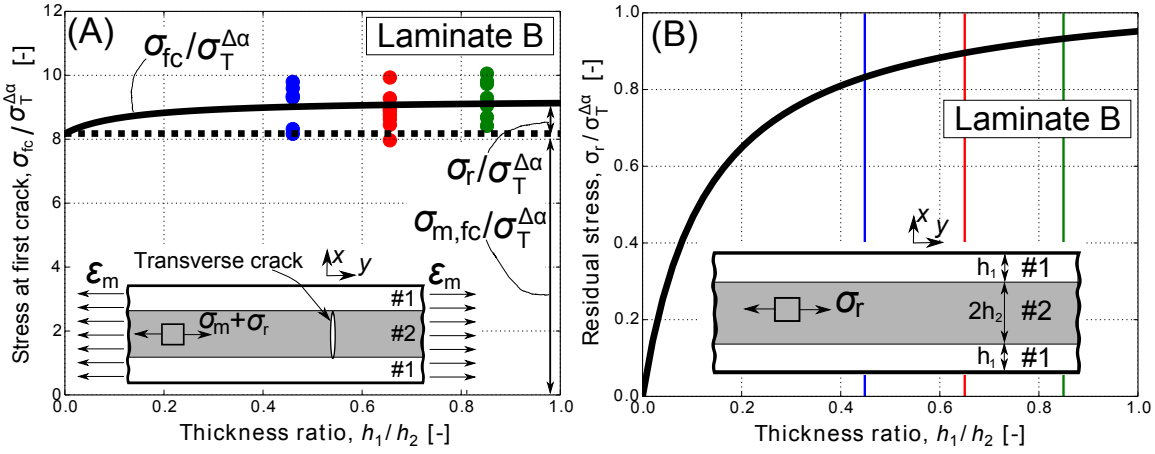

Figure 18: (A) Results for stress in the adhesive at first crack from static tensile tests of sandwich specimens with different thicknesses of the laminates. Dots are measurements and the dashed line is the average of σ_m for all tests and the solid line is the prediction by equation 6. (B) Residual stress model (equation 6) for different thickness ratio based on misfit stress determined experimentally by Method 2 in Figure 12. Vertical lines indicate the h_1/h_2 values of interest.

10. Results from tensile tests of sandwich specimens under cyclic loading

10.1. Results from tests of sandwich specimens under cyclic loading - effects of laminate thickness

The effect of laminate thickness on the number of cycles to first crack in the adhesive layer of the sandwich specimens with Laminate B were tested for three configurations including $h_1/h_2 = 0.45$, $h_1/h_2 = 0.65$ and $h_1/h_2 = 0.85$. The residual stress in the adhesive of the sandwich specimen was determined from the misfit stress measurement by Method 2 (series 2B in Figure 12) and by equation 6. Residual stress increased the mean stress in the adhesive, but not the stress amplitude. Thus, the load R-ratio ($R = \sigma_{min}/\sigma_{max}$) experienced by the adhesive increased from $R = 0.1$ to $R \approx 0.2 - 0.3$.

The maximum mechanical strain, $\epsilon_{m,max}$, applied in the cyclic loaded test was normalised by the average mechanical static strain at first crack, $\bar{\epsilon}_{m,st}$, based on the results in Figure 18 (A). Figure 19 shows that the number of cycles for the first transverse crack to extend across the thickness of the adhesive layer of the sandwich specimen is comparable for the different laminate thickness tested ($h_1/h_2 = 0.45$, $h_1/h_2 = 0.65$, and $h_1/h_2 = 0.85$). This suggests that crack initiation in the adhesive is primarily driven by the stress level and the defect size, and less sensitive to the thickness of the laminate i.e. the constraining effect of the laminate. Figure 20 shows the number of cycles for the occurrence of the first and subsequent cracks for various applied maximum strain levels. It seems that when the maximum applied mechanical strain, $\epsilon_{m,max}$, becomes smaller, the crack density of the adhesive increases. Although the effect is small, the appearance of subsequent cracks seem to occur faster (i.e. at a lower number of cycles) for decreasing substrate thickness.

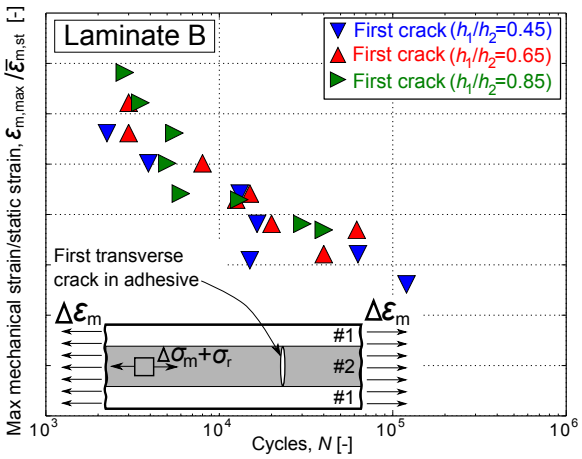

Figure 19: Number of cycles to first crack in the adhesive for different configurations of h_1/h_2.

10.2. Strain energy - comparison of prediction with experimental test

The test with the second highest strain level in Figure 20 (B) with thickness of $h_1/h_2 = 0.65$ is selected for further analysis. The work done by the applied external forces can be used to determine the strain energy of the sandwich specimen experimentally by equation 9 and equation 10 in section 5.1 based the measured force by the load cell, P, and the measured displacement by the clip gauge, δ. Thus, the strain energy was measured for the part of the sandwich specimen volume that was within the gauge length of the clip gauge, see Figure 21 (A). The strain energy during the cyclic loaded test of this specimen is presented in Figure 21 (A), where the current specimen strain energy, U_t, is normalised by the initial specimen strain energy, $U_{no,crack}$.

The first two transverse cracks in the adhesive were identified on images at about 3000 cycles, see Figure 20 (B) and Figure 21 (B-C). The increase in strain energy due to the evolution of Crack 1 and

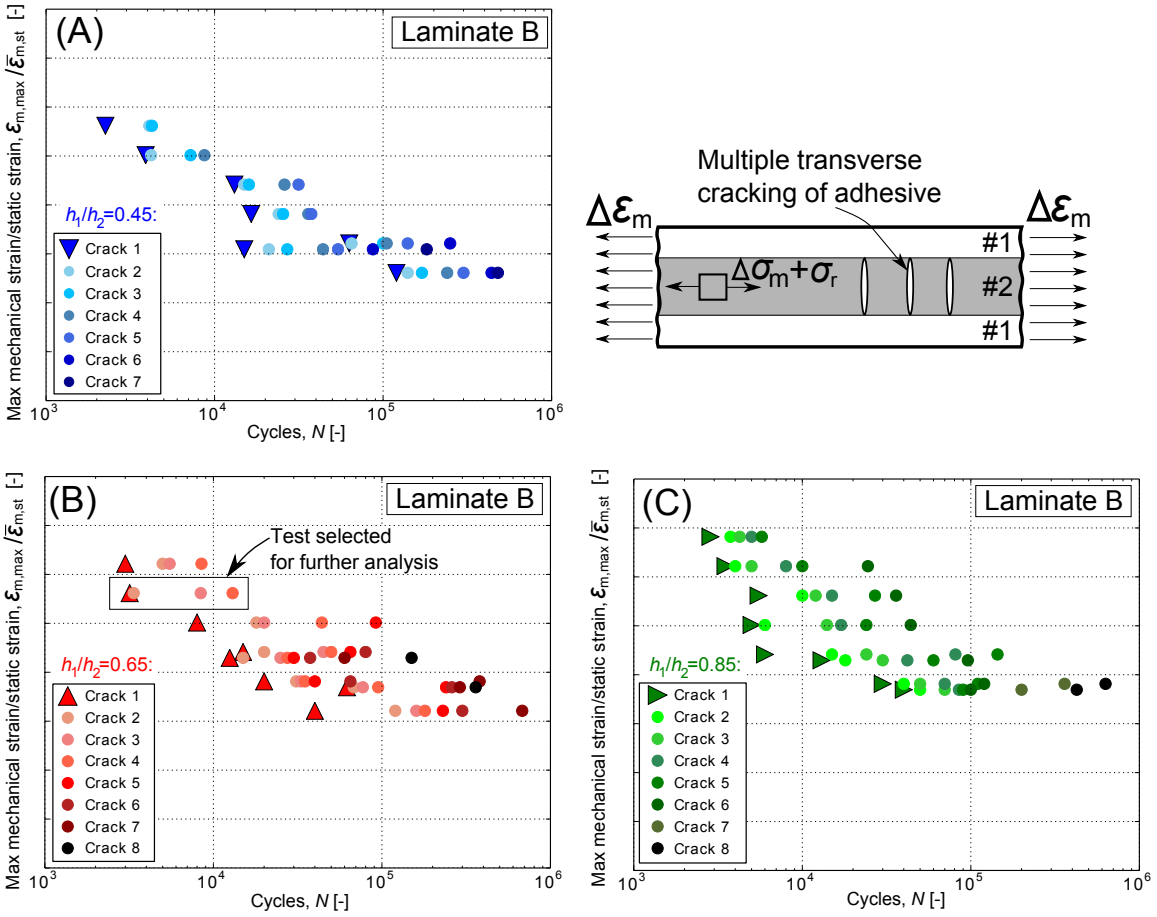

Figure 20: Transverse crack measurements from cyclic loaded tests of sandwich specimens with different thickness of Laminate B. (A) $h_1/h_2 = 0.45$, (B) $h_1/h_2 = 0.65$, (C) $h_1/h_2 = 0.85$.

Crack 2 could be measured by the clip gauge since these two cracks initiated inside the gauge length of the clip gauge (close to the middle of the specimen length). Crack 1 and Crack 2 evolved nearly simultaneously (at $N \approx 3000$ cycles) according to both the measured strain energy in Figure 21 (A) and the images captured during the test. Crack 3 and Crack 4 evolved outside the gauge length of the clip gauge and the change in strain energy caused by Crack 3 and Crack 4 could therefore not be captured by the clip gauge measurement. However, the images and the small bumps on the curve in Figure 21 (A) indicate that Crack 3 and Crack 4 evolved in the adhesive at $N \approx 9000$ cycles and $N \approx 13000$ cycles, respectively.

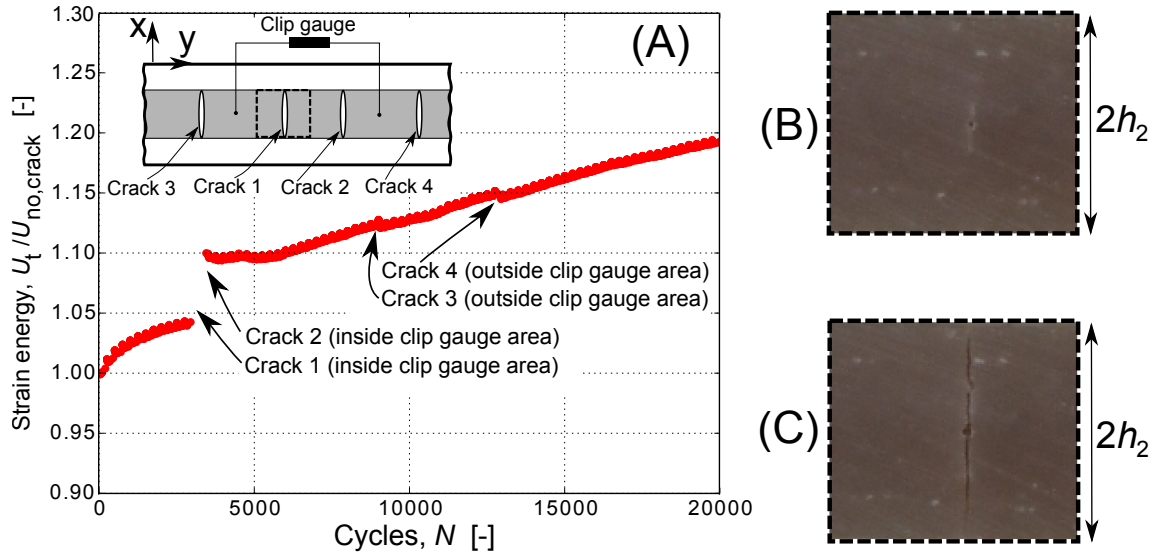

Figure 21: (A) Strain energy measured by clip gauge during the test with strain level of $\epsilon_{m,max}/\bar{\epsilon}_{m,st} \approx 0.48$ in the test series with $h_1/h_2 = 0.65$ i.e. the second highest loaded test in Figure 20 (B). (B) Photo near Crack 1 at 2500 cycles ($a < h_2$). (C) Photo near Crack 1 at 3000 cycles ($a = h_2$).

When the first two cracks appeared across the width of the adhesive layer in the beginning of the test in Figure 21 (A), the increase in strain energy due to the crack, U_{crack}, could be determined by equation 13. Using the inputs from the test in Figure 21 ($h_1/h_2 = 0.65$, $E_1/E_2 = 12$, $\sigma_{yy,2}$) together with the function, F, in Figure 4 gives a predicted strain energy of $U_{crack}/U_{no,crack} = 0.055 \pm 0.01$ (for two cracks). In this model prediction it was assumed that the inputs to equation 13 ($h_1/h_2 = 0.65$, $E_1/E_2 = 12$, $\sigma_{yy,2}$) could be determined within an accuracy of $\pm 5\%$. Note in Figure 4 that when $E_1/E_2 \gtrsim 8.0$, the sensitivity of E_1/E_2 on F is small.

Comparing $U_{crack}/U_{no,crack} = 0.055$ with the measured increase in strain energy $U_t/U_{no,crack}$ in Figure 21 (A) for two transverse cracks at $N \approx 3000$ cycles gives a relative deviation of $\sim 2\%$ between the strain energy prediction of $U_{crack}/U_{no,crack}$ and the measured change in $U_t/U_{no,crack}$. Thus, the strain energy prediction is consistent with the measurement.

11. Discussion

11.1. Discussion of the residual stress results

It is expected that measurement of small strains in comparison with measurement of large strains, is more sensitive to uncertainties in the measurement procedure and equipment. For the methods based on strain measurements (Method 1,3,4), the gauge length was short (6-8 mm) and thus the measurements may be sensitive to local variations. In Method 3, the strain measurements by the strain gauge SG1 and the FBG were used to determine the curvature. In the curved bi-layer specimen (Method 3), the measured strain values were approx. a factor two higher than the measured in-plane strains in the sandwich specimen by FBG (Method 1) and the free laminate by SG2 (Method 4). It is therefore expected that the strain measurements from the bi-layer curvature specimens (Method 3) are less influenced by measurement inaccuracies i.e. strain gauge/FBG accuracy, -signal noise and -misalignment during mounting. The curvature in Method 2 was measured by the dial gauge over the entire specimen length, which was more than 500 mm. Thus, the result can be assumed to average out local variations in e.g. thicknesses and stiffnesses. This suggests that the misfit stress results determined by Method 2 and -3 are the most accurate. This is supported by the estimate by Method 5 according to Figure 12.

One of the difficulties in Method 5 is to measure the right value of reference temperature, T_r, where the adhesive shifts from liquid state to solid and starts behaving elastically with fixed stiffness. The stiffness buildup is expected to take place gradually during the curing process, which complicates the determination of T_r. Therefore, it is most likely not completely accurate to select T_r as the temperature where the cross linking occurs, the peak temperature during curing or the post curing temperature. Time dependency of the adhesive is another uncertainty in the test. At high temperatures and in the early stages of curing, the adhesive is assumed to be visco-elastic and to relax stresses by creep. However, the time dependency of the specific adhesive is unknown. It is likely that the time from manufacturing to test might have an effect on the resulting measurements. E.g. in the bi-layer test, the misfit stress might decrease over time due to creep and stress relaxation in the adhesive when the adhesive is bonded to a stiffer laminate. It is therefore suggested to track the thermal history of the adhesive joint in order to characterise and improve the adhesive material systems in the future.

An uncertainty might be misalignment between the FBG and the primary fiber direction since the FBG were free to move at the gauge section when the adhesive was injected. Quantification of this uncertainty is difficult since the FBG was embedded inside the non-transparent adhesive. Uncertainties in the present experimental study with FBGs includes furthermore temperature changes during the different process steps, and tolerances for the adhesive thickness.

We believe that the most accurate quantification of residual stress is to measure the residual stress

directly on the adhesive joint component or in a very similar specimen that are manufactured under comparable process conditions. Therefore, we believe that it is more accurate to determine the residual stress in the sandwich specimens than measuring on the neat adhesive in an unconstrained state [55] or using the ASTM D2566 standard, where the adhesive is cast into an open half pipe shaped steel mould. The steel mould used in ASTM D2566 cannot reproduce the thermal- and mechanical boundary conditions of the adhesive joint component correct.

Future studies of residual stresses related to the present work could include measuring the misfit stress at low temperatures although this would require knowledge of the stiffness properties of the adhesive at the corresponding temperatures. Investigations of the creep behavior of the adhesive including stress relaxation at medium high temperatures could be a relevant future study as well.

11.2. Discussion of the tensile test results

Comparing the misfit stress results for the different post curing temperatures in Figure 16 with the misfit stress results for the different test temperatures in Figure 17, suggests that the change in residual stress per post curing temperature (σ_r/T_{PC}) is comparable to the change in residual stress per test temperature (σ_r/T_t). Thus, these two distinct types of temperatures seem to have the same effect on the residual stress in the adhesive.

Alia *et al.* [3] measured the elongation at break for a bulk adhesive (Bisphenol A-epoxy vinylester adhesive) as a function of different post curing temperatures using dog bone specimens tested according to the test standard ISO R527-1-966. They found that the elongation at break decreased with approx. 10% over post curing temperatures ranging from 50°C to 90°C. This result can be compared with the measurement in the present paper in Figure 16 (post cured at different temperatures) if the residual stress in the adhesive of the sandwich specimens are taken into account. Furthermore for comparison, it is a prerequisite that the dog bone specimens tested by Alia *et al.* [3] are free of residual stresses and the distribution of defects are comparable. Since, the determined stress in the adhesive at first crack in Figure 16 decreases with approx. 11 % from 50°C to 90°C of post curing temperature, the tendency of the results in the present paper are consistent with the measurements by Alia *et al.* [3] for a comparable adhesive material system.

The variation of stress in the adhesive at first crack in each test series was relatively large. This might be attributed the details of the pre-existing defects. The distribution of defect size and shape from specimen to specimen was not measured, but it is reasonable to assume that there is some specimen-to-specimen variation. The effect of laminate thickness on the stress in the adhesive at first crack (shown in Figure 18 (B)) was relatively small, which might be explained by the relatively small residual stresses for the range of laminate thicknesses tested (at room temperature). The results for stress in the adhesive at first crack, presented in Figure 16 and Figure 17, are experimentally determined

and illustrate the effect of different process parameters on the material properties (strength, fracture toughness) of the adhesive. However, the consistency of the results in Figure 15 suggests that the stress in the adhesive at first crack can be predicted sufficiently accurate by the approach in Figure 2 if the material properties of the test specimens are measured under the same process conditions and temperatures.

12. Summary and conclusions

Dependent on the test temperature and processing conditions, the residual stress in the adhesive layers was determined to ∼8-40% of the stress in the adhesive at first crack in the sandwich specimens. This shows that the residual stresses were of relative significant magnitude, especially at low test temperatures. The post curing of the adhesive was identified by the FBG measurements as the step in the bonding process where the major part of the residual stress builds up.

Prediction of the stress in the adhesive at first crack in the sandwich specimen loaded in tension, using a novel bi-material FE model, was found to be consistent with experimental results obtained at temperatures of 23°C and −40°C. The cyclic loaded tests confirmed that the design of the sandwich specimen was damage tolerant since multiple cracking of the adhesive developed in a stable manner. Other main conclusions of this study are:

- The effect of post curing temperature:
  - The misfit stress increased with increasing post curing temperature.
  - The stress in the adhesive (mechanical+residual stress) at first transverse crack decreased with increasing post curing temperature.
- The effect of test temperature:
  - The stress in the adhesive (mechanical+residual stress) at first transverse crack decreased with decreasing test temperature.
- The effect of laminate thickness:
  - The stress in the adhesive (mechanical+residual stress) at first transverse crack under static loading was relatively insensitive to the thickness of the laminate.
  - The evolution of first crack in the adhesive under cyclic loading was relatively insensitive to the thickness of the laminates.

Based on the conclusions the following design rules are proposed:

- To keep the residual stresses low, avoid post curing at very high temperatures.
- To reduce the residual stresses (especially at low operation temperatures), minimise the mismatch in coefficient of thermal expansion between the adhesive and the laminate.
- To increase the applied mechanical stress in the adhesive to initiate the first transverse crack, post cure at temperatures that are not too high.
- To increase the applied mechanical stress in the adhesive to initiate the first transverse crack, avoid low operation temperatures.

Acknowledgements

Acknowledgements to the staff at the LM Wind Power laboratory for help manufacturing and testing the specimens. Thanks to the technicians at DTU Wind Energy for help mounting strain gauges on the bi-layer specimens. Thanks to Gilmar Ferreira Pereira and Marco Aurelio Miranda Maduro for help assisting with the mounting and measuring with the fiber Bragg gratings. This research was primarily supported by grant no. 4135-00010B from Innovation Fund Denmark. This research was also supported by the Danish Centre for Composite Structures and Materials for Wind Turbines (DCCSM), grant no. 0603-00301B, from Innovation Fund Denmark.

Appendix A. Derivation of misfit stress in adhesive for sandwich specimen

The procedure to determine the normal stress, $\sigma_{yy,2}$, and the misfit stress, σ_T, in the adhesive of the symmetric sandwich specimens for Method 1 and Method 4 are presented. Method 1 and Method 4 are illustrated in Figure 6 in section 5.2. The procedure to determine the misfit stress in the adhesive of the sandwich specimen based on the strain measurement is in short:

- Measure the straining of the specimen.
- Determine the force in the substrate based on the strain measurement (equation A.1).
- Set up the force balance between the substrate and the adhesive (equation A.2).
- Determine the stress in the adhesive (equation A.4 and equation A.5).
- Determine the misfit stress in the adhesive (equation A.6).

The procedure to determine the normal stress and the misfit stress in the adhesive of the sandwich specimen is exemplified for Method 1, where the strain is measured by the FBG. The procedure is similar for Method 4 except that the strain in Method 4 is measured by the strain gauge SG2, see

Figure 6. The first step in the procedure is to determine the force in one of the substrates, $P_{yy,1}$, which can be calculated based on the strain measurement, ϵ_{FBG}, and Hooke's law as:

$$P_{yy,1} = \bar{E}_1 h_1 \epsilon_{FBG} \tag{A.1}$$

where $\bar{E}_1$ is the plane strain Young's modulus of the substrate and h_1 is the thickness of the substrate as shown in Figure A.22 (A). ϵ_{FBG} is the change in strain in the sandwich specimen measured by the FBG after curing of the adhesive as shown in Figure A.22 (B). By assuming perfect bonding at the adhesive-substrate interface, the forces in the two substrates, $2P_{yy,1}$, and the force in the adhesive, $P_{yy,2}$, must be in equilibrium both before and after solidification of the adhesive such that:

$$P_{yy,2} = -2P_{yy,1} \tag{A.2}$$

The force balance between the adhesive and the substrate is also illustrated graphically in Figure A.22 (C). Now the stress per unit width in the substrate and in the adhesive can be determined, respectively:

$$\sigma_{yy,1} = \frac{P_{yy,1}}{h_1} \tag{A.3}$$

$$\sigma_{yy,2} = \frac{P_{yy,2}}{2h_2} \tag{A.4}$$

Equation A.4 for the in-plane normal stress in the adhesive of the sandwich specimen, $\sigma_{yy,2}$, can be rewritten by inserting (A.1) in (A.2), and then inserting (A.2) in (A.4) as:

$$\sigma_{yy,2} = \frac{-\bar{E}_1 \epsilon_{FBG}}{\zeta_2} \tag{A.5}$$

where $\zeta_2 = h_2/h_1$ is the adhesive to substrate thickness ratio. The misfit stress in the adhesive, σ_T, can be determined by rewriting equation 6 in section 3 to give:

$$\sigma_T = -\sigma_{yy,1}\left(\frac{1}{\zeta_2} + \Sigma_2\right) = \sigma_{yy,2}\left(1 + \zeta_2 \Sigma_2\right) \tag{A.6}$$

The relation between the normal stresses in the adhesive and the substrates is given by $\sigma_{yy,2} = -\sigma_{yy,1}/\zeta_2$, which is determined based on equilibrium considerations by inserting equation (A.3) and (A.4) into equation (A.2).

References

[1] J. L. Hart-Smith, Adhesive Bonded Joints for Composites - Phenomenological Considerations, in: Conference on Advanced Composites Technology, 1978, pp. 1–18.

[2] R. J. C. Carbas, L. F. M. da Silva, E. A. S. Marques, A. M. Lopes, Effect of post-cure on the glass transition temperature and mechanical properties of epoxy adhesives, Journal of Adhesion Science & Technology 27 (23) (2013) 2542–2557. doi:10.1080/01694243.2013.790294.

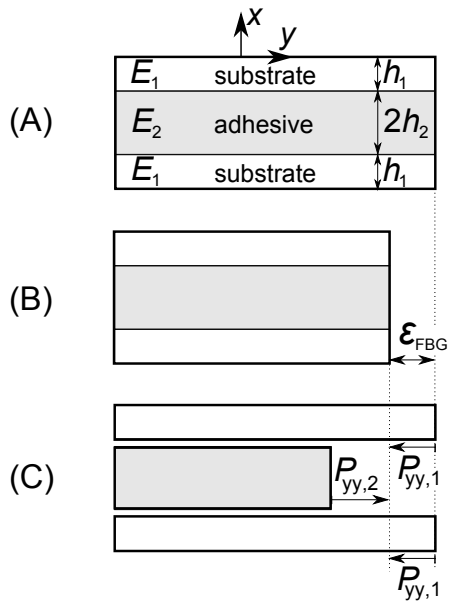

Figure A.22: Force balance and strain measured during curing of the adhesive by the FBG, ϵ_{FBG}. (A) Initial state where the adhesive is liquid. (B) Equilibrium state after curing of the adhesive where the adhesive is solid. (C) Force balance.

[3] C. Aliá, J. A. Jofre-Reche, J. C. Suárez, J. M. Arenas, J. M. Martín-Martínez, Influence of post-curing temperature on the structure, properties, and adhesion of vinyl ester adhesive, Journal of Adhesion Science and Technology 29 (6) (2015) 518–531. doi:10.1080/01694243.2014.995910.

[4] P. J. Withers, H. K. D. H. Bhadeshia, Residual stress part 1 - Measurement techniques, Materials Science and Technology 17 (4) (2001) 355–365. doi:10.1179/026708301101509980.

[5] P. J. Withers, H. K. D. H. Bhadeshia, Residual stress part 2 - Nature and origins, Materials Science and Technology 17 (4) (2001) 366–375. doi:10.1179/026708301101510087.

[6] P. J. Withers, Residual stress and its role in failure, Reports on Progress in Physics 70 (12) (2007) 2211–2264. doi:10.1088/0034-4885/70/12/R04.

[7] W. A. Zdaniewsky, J. C. Conway, H. P. Kirchner, Effect of Joint Thickness and Residual Stresses on the Properties of Ceramic Adhesive Joints: II. Experimental Results, J. Am. Ceram. Soc. 70 (2) (1987) 110–118.

[8] R. Ming-Hwa, L. Wen-Sen, H. Jer-Ming, Residual stresses in symmetric double lap and double strap joints, International Journal of Solids and Structures 28 (4) (1991) 449–469. doi:10.1016/0020-7683(91)90059-O.

[9] R. G. Humfeld, D. A. Dillard, Residual stress development in adhesive joints subjected to thermal cycling, The Journal of Adhesion 65 (1-4) (1998) 277–306. doi:10.1080/00218469808012250.

[10] M. K. Apalak, R. Gunes, S. Eroglu, Thermal residual stresses in an adhesively bonded functionally graded tubular single lap joint, International Journal of Adhesion and Adhesives 27 (1) (2007) 26–48. doi:10.1016/j.ijadhadh.2005.09.009.

[11] A. Mubashar, I. A. Ashcroft, G. W. Critchlow, A. D. Crocombe, A Method of Predicting the Stresses in Adhesive Joints after Cyclic Moisture Conditioning, The Journal of Adhesion 87 (9) (2011) 926–950. doi:10.1080/00218464.2011.600675.

[12] J. A. Nairn, Energy release rate analysis for adhesive and laminate double cantilever beam specimens emphasizing the effect of residual stresses, International Journal of Adhesion and Adhesives 20 (1999) 59–70.

[13] A. G. Evans, J. W. Hutchinson, The Thermomechanical Integrity of Thin Films and Multilayers, Acta metall. mater. 43 (7) (1995) 2507–2530.

[14] M. A. Eder, R. D. Bitsche, Fracture Analysis of Adhesive Joints in Wind Turbine Blades, Wind Energy 00 (2012) 1–18. doi:10.1002/we.

[15] M. A. Eder, R. D. Bitsche, M. Nielsen, K. Branner, A practical approach to fracture analysis at the trailing edge of wind turbine rotor blades, Wind Energy 17 (2014) 483–497. doi:10.1002/we.

[16] P. Haselbach, K. Branner, Effect of Trailing Edge Damage on Full-Scale Wind Turbine Blade Failure, in: Proceedings of the 20th International Conference on Composite Materials, 2015, pp. 1–12.

[17] P. Haselbach, K. Branner, Initiation of trailing edge failure in full-scale wind turbine blade test, Engineering Fracture Mechanics 162 (2016) 136–154. doi:10.1016/j.engfracmech.2016.04.041.

[18] S. M. M. Slütter, Crack formation of adhesive bonded joints in wind turbine blades, Tech. rep., Aeronautical Engineering of Inholland University of Applied Sciences at Delft (2013).

[19] S. Ataya, M. M. Ahmed, Damages of wind turbine blade trailing edge: Forms, location, and root causes, Engineering Failure Analysis 35 (2013) 480–488. doi:10.1016/j.engfailanal.2013.05.011.

[20] A. A. Gawandi, L. A. Carlsson, T. A. Bogetti, J. W. Gillespie, Mechanics of discontinuous ceramic tile core sandwich structure: Influence of thermal and interlaminar stresses, Composite Structures 92 (1) (2010) 164–172. doi:10.1016/j.compstruct.2009.07.022.

[21] K. S. Alfredsson, A. A. Gawandi, J. W. Gillespie, L. A. Carlsson, T. A. Bogetti, Stress analysis of axially and thermally loaded discontinuous tile core sandwich with and without adhesive filled core gaps, Composite Structures 93 (7) (2011) 1621–1630. doi:10.1016/j.compstruct.2011.01.015.

[22] K. S. Alfredsson, A. A. Gawandi, J. W. Gillespie, L. A. Carlsson, T. A. Bogetti, Flexural analysis of discontinuous tile core sandwich structure, Composite Structures 94 (5) (2012) 1524–1532. doi:10.1016/j.compstruct.2011.11.028.

[23] J. W. Gillespie, L. A. Carlsson, A. A. Gawandi, T. A. Bogetti, Fatigue crack growth at the face sheet-core interface in a discontinuous ceramic-tile cored sandwich structure, Composite Structures 94 (11) (2012) 3186–3193. doi:10.1016/j.compstruct.2012.05.021.

[24] K. W. Garret, J. E. Bailey, Multiple transverse fracture in 90 cross-ply laminates of a glass fibre-reinforced polyester, Journal of Materials Science 12 (1977) 157–168.

[25] R. Talreja, Fatigue of composite materials: damage mechanisms and fatigue-life diagrams, Proc. R. Soc. Lond. A. 378 (1981) 461–475. doi:10.1098/rspa.1983.0054.

[26] J. A. Nairn, The Strain Energy Release Rate of Composite Microcracking: A Variational Approach, Journal of Composite Materials 23 (11) (1989) 1106–1129. doi:10.1177/002199838902301102.

[27] J. Varna, L. Berglund, Multiple transverse cracking and stiffness reduction in cross-ply laminates, Journal of Composites Technology and Research 13 (2) (1991) 97–106. doi:10.1520/CTR10213J.

[28] R. Talreja, S. Yalvac, L. D. Yats, D. G. Wetters, Transverse cracking and stiffness reduction in cross ply laminates of different matrix toughness, Journal of Composite Materials 26 (11) (1992) 1644–1663.

[29] J.-M. Berthelot, Transverse cracking and delamination in cross-ply glass-fiber and carbon-fiber reinforced plastic laminates: Static and fatigue loading, Applied Mechanics Reviews 56 (1) (2003) 111–147. doi:10.1115/1.1519557.

[30] B. F. Sørensen, J. W. Holmes, P. Brøndsted, K. Branner, Blade materials, testing methods and structural design, in: W. Tong (Ed.), Wind Power Generation and Wind Turbine Design, Vol. 44, WIT Press, Boston, 2010, Ch. 13, pp. 417–460. doi:10.2495/978-1-84564-.

[31] G. Marsh, The challenge of wind turbine blade repair, Renewable Energy Focus 12 (4) (2011) 62–66. doi:10.1016/S1755-0084(11)70104-1.

[32] D. Cripps, The future of blade repair, Reinforced Plastics 55 (1) (2011) 28–32. doi:10.1016/S0034-3617(11)70034-0.

[33] C. Kong, T. Kim, D. Han, Y. Sugiyama, Investigation of fatigue life for a medium scale composite wind turbine blade, International Journal of Fatigue 28 (10 SPEC. ISS.) (2006) 1382–1388. doi:10.1016/j.ijfatigue.2006.02.034.

[34] X. Liu, Dynamic Response Analysis of the Blade of Horizontal Axis Wind Turbines, Journal of Mechanical Engineering 46 (12) (2010) 128. doi:10.3901/JME.2010.12.128.

[35] K. K. Jin, M. Ghulam, J. H. Kim, S. K. Ha, B. Lopez, A. Gorostidi, Life Prediction of Wind Turbine Blades, in: International Conferences on Composite Materials, 2009, pp. 1–12.

[36] D. Salimi-Majd, V. Azimzadeh, B. Mohammadi, Loading Analysis of Composite Wind Turbine Blade for Fatigue Life Prediction of Adhesively Bonded Root Joint, Applied Composite Materials 22 (3) (2014) 269–287. doi:10.1007/s10443-014-9405-4.

[37] C. C. Ciang, J.-R. Lee, H.-J. Bang, Structural health monitoring for a wind turbine system: a review of damage detection methods, Measurement Science and Technology 19 (12) (2008) 122001. doi:10.1088/0957-0233/19/12/122001.

[38] H. F. Zhou, H. Y. Dou, L. Z. Qin, Y. Chen, Y. Q. Ni, J. M. Ko, A review of full-scale structural testing of wind turbine blades, Renewable and Sustainable Energy Reviews 33 (2014) 177–187. doi:10.1016/j.rser.2014.01.087.

[39] X. Chen, W. Zhao, X. L. Zhao, J. Z. Xu, Preliminary failure investigation of a 52.3m glass/epoxy composite wind turbine blade, Engineering Failure Analysis 44 (11) (2014) 345–350. doi:10.1016/j.engfailanal.2014.05.024.

[40] M. McGugan, G. Pereira, B. F. Sørensen, H. Toftegaard, K. Branner, Damage tolerance and structural monitoring for wind turbine blades, Phil. Trans. R. Soc. A 373 (2035) (2015) 1–16. doi:10.1098/rsta.2014.0077.

[41] D. Li, S.-C. M. Ho, G. Song, L. Ren, H. Li, A review of damage detection methods for wind turbine blades, Smart Materials and Structures 24 (3) (2015) 033001. doi:10.1088/0964-1726/24/3/033001.

[42] G. Pereira, M. McGugan, L. P. Mikkelsen, Method for independent strain and temperature measurement in polymeric tensile test specimen using embedded FBG sensors, Polymer Testing 50 (2016) 125–134. doi:10.1016/j.polymertesting.2016.01.005.

[43] G. Pereira, L. P. Mikkelsen, M. McGugan, Fibre Bragg Grating Sensor Signal Post-processing Algorithm: Crack Growth Monitoring in Fibre Reinforced Plastic Structures, in: P. Ribeiro, M. Raposo (Eds.), Springer Proceedings in Physics - Photoptics 2015, Vol. 181, 2016, pp. 63–80. doi:10.1007/978-3-319-30137-2.

[44] J. Güemes, J. Sierra-Perez, Fiber optic sensors, Springer, 2013. doi:10.1134/S0018143908070096.

[45] W. Ostachowicz, J. Güemes, New Trends in Structural Health Monitoring, Springer, 2013. doi:10.1134/S0018143908070096.

[46] H. Tada, P. C. Paris, G. R. Irwin, The Stress Analysis of Cracks Handbook, 3rd Edition, ASME Press, New York, 2000.

[47] B. F. Sørensen, H. Toftegaard, S. Linderoth, M. Lundberg, S. Feih, Strength and failure modes of ceramic multilayers, Journal of the European Ceramic Society 32 (16) (2012) 4165–4176. doi:10.1016/j.jeurceramsoc.2012.06.012.

[48] J. Beuth, Cracking of thin bonded films in residual tension, Int. J. Solids Structures 2 (13) (1992) 1657–1675.

[49] S. Fenster, A. Ugural, Advanced Strength and Applied Elasticity, 4th Edition, Prentice Hall, Upper Saddle River, New Jersey, 2003.

[50] R. D. Cook, D. S. Malkus, M. E. Plesha, R. J. Witt, Concepts and applications of finite element analysis, 4th Edition, Wiley, United States, 2001.

[51] A. Love, A Treatise on the Mathematical Theory of Elasticity, 4th Edition, At the University Press, Cambridge, 1927.

[52] S. S. Timoshenko, History of Strength of Materials, The maple press company, New York, 1953. doi:10.1016/0022-5096(54)90010-1.

[53] J. R. Rice, P. C. Paris, J. G. Merkle, Some further results of J-integral analysis and estimates, Progress in Flaw Growth and Fracture Toughness Testing 536 (536) (1973) 231–245. doi:10.1520/STP49643S.

[54] G. Irwin, D. Washington, Analysis of Stresses and Strains Near the End of a Crack Traversing a Plate, Journal of Applied Mechanics 24 (1957) 361–364.

[55] J. Hüther, P. Brøndsted, The Influence of the Curing Cycles on the Fatigue Performance of Unidirectional Glass Fiber Reinforced Epoxy Composites, IOP Conference Series: Materials Science and Engineering 139 (2016) 1–11. doi:10.1088/1757-899X/139/1/012023.

APPENDED PAPER P2

The effect of buffer-layer on the steady-state energy release rate of a tunneling crack in a wind turbine blade joint

Jeppe B. Jørgensen, Bent F. Sørensen and Casper Kildegaard
Composite Structures
Submitted, 2017

The effect of buffer-layer on the steady-state energy release rate of a tunneling crack in a wind turbine blade joint

Jeppe B. Jørgensen[a,b,*], Bent F. Sørensen[b], Casper Kildegaard[a]

[a] *LM Wind Power, Østre Alle 1, 6640 Lunderskov, Denmark.*
[b] *The Technical University of Denmark, Dept. of Wind Energy, Frederiksborgvej 399, 4000 Roskilde, Denmark.*

Abstract

The effect of a buffer-layer on the steady-state energy release rate of a tunneling crack in the adhesive layer of a wind turbine blade joint, loaded in tension, is investigated using a parametric 2D tri-material finite element model. The idea of embedding a buffer-layer in-between the adhesive and the basis glass fiber laminate to improve the existing joint design is novel, but the implications hereof need to be addressed.

The results show that it is advantageous to embed a buffer-layer near the adhesive with controllable thickness- and stiffness properties in order to improve the joint design against propagation of tunneling cracks. However, for wind turbine blade relevant material combinations it is found more effective to reduce the thickness of the adhesive layer since the stiffness mismatch between the existing laminate and the adhesive is already high. The effect of material orthotropy was found to be relatively small for the blade relevant materials.

Keywords: Tunneling crack, Adhesive bonded joints, Fracture mechanics, Polymer matrix composites, Finite element analysis

Nomenclature

E_1	Young's modulus of substrate
E_2	Young's modulus of adhesive
E_3	Young's modulus of buffer-layer
$\bar{E}_1$	plane strain Young's modulus of substrate
$\bar{E}_2$	plane strain Young's modulus of adhesive

*Corresponding author
Email address: jbj@lmwindpower.com (Jeppe B. Jørgensen)

$\bar{E_3}$	plane strain Young's modulus of buffer-layer
F	non-dimensional function
$\mathcal{G}_{ss}$	mode-I steady-state energy release rate
G_{xy}	shear modulus
h_1	thickness of substrate
h_2	half thickness of the adhesive layer
h_3	thickness of buffer-layer
x, y, z	coordinates
α_{12}	first Dundurs' parameter (substrate/adhesive)
α_{32}	first Dundurs' parameter (buffer-layer/adhesive)
β_{12}	second Dundurs' parameter (substrate/adhesive)
β_{32}	second Dundurs' parameter (buffer-layer/adhesive)
δ_{cod}	crack opening displacement profile
λ	first orthotropy parameter
ν	Poisson's ratio
ρ	second orthotropy parameter
$\sigma_{yy,2}$	stress in the adhesive (y-direction)
Biax	bi-axial
FE	finite element
UD	uni-directional

1. Introduction

A typical wind turbine blade joint is manufactured of a structural adhesive layer that is bonding two glass fiber laminated shells meaning that the structural adhesive is constrained in-between stiffer laminates. This is exemplified in Figure 1 (A) for a trailing-edge joint in a wind turbine blade. Observations from full scale blade tests of this joint with tensile stresses, $\sigma_{yy,2}$, in the adhesive, show that cracks can initiate at the free-edge and propagate through the adhesive layer as a so-called tunneling crack. The tunneling crack is constrained by the laminates as shown in the sketch in Figure 1 (A) and the photo in Figure 1 (B).

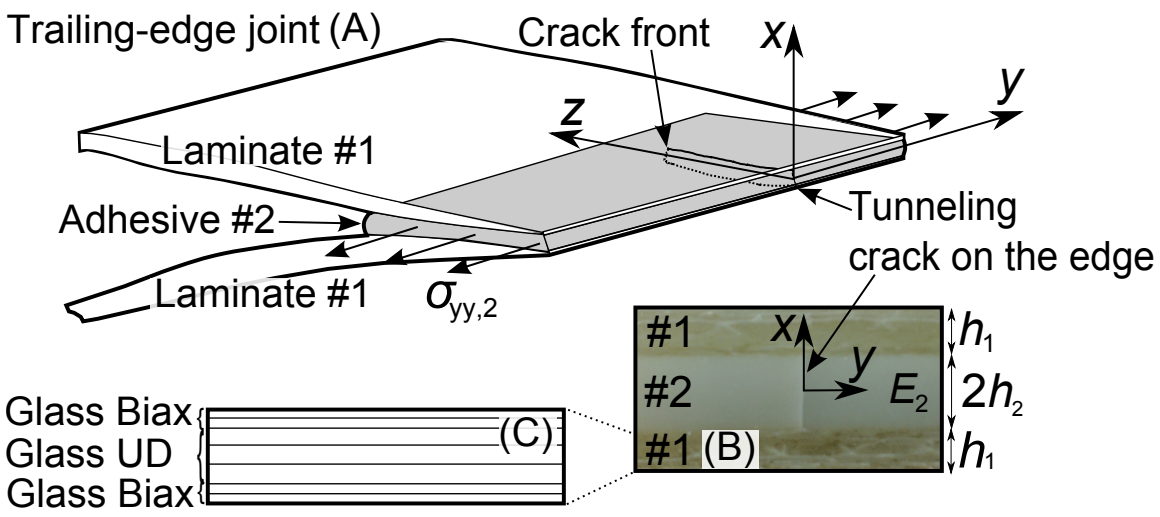

Figure 1: (A) Trailing-edge joint with a tunneling crack propagating across the adhesive layer in the z-direction. (B) Photo of a tunneling crack in a trailing-edge wind turbine blade joint. (C) Typical layers in a glass fiber laminate used in a wind turbine blade joint.

Novel models are desired for establishing design rules for an improved joint design in order to prevent tunneling cracks propagating across the wind turbine blade joint in Figure 1 (A). An improved joint design aims at decreasing the energy release rate for tunneling cracks in the joint and thus enable a reduction in the amount of reinforcement needed in the laminates. This leads to a reduction in blade mass and thus a decrease in the cost of energy since lighter blades are more efficient and can save structural reinforcement in the other wind turbine components e.g. nacelle, hub, tower and foundation [1].

Generally, the process of tunneling crack propagation includes three-dimensional effects. However, when the crack in Figure 1 (A) reaches a certain length from the edge (in z-direction), the energy release rate becomes steady-state meaning that the energy release rate no longer depends on the crack length. The problem of steady-state propagation of a tunneling crack was analysed for an isotropic bi-material model by Ho and Suo [2, 3]. Although tunneling cracking is a 3D problem, the steady-state energy release rate, can be determined exact from a 2D solution by [2, 3]:

$$\mathcal{G}_{ss} = \frac{1}{2}\frac{\sigma_{yy,2}}{2h_2}\int_{-h_2}^{+h_2}\delta_{cod}(x)dx \tag{1}$$

where $\sigma_{yy,2}$ is the far field stress in the cracked adhesive layer (uniform applied stress) and the adhesive thickness is $2h_2$ according to Figure 1. $\delta_{cod}(x)$ is the crack opening displacement profile for the plane strain crack far behind the crack front. For the elementary case of a central crack in an infinitely large plate subjected to remote tensile stresses (Griffith crack), the crack opening displacement is [3]:

$$\delta_{cod} = \frac{4\sigma_{yy,2}}{\bar{E}_2}\sqrt{(h_2^2 - x^2)} \tag{2}$$

where $\bar{E}_2$ is the plane strain Young's modulus of the plate. Inserting equation 2 into equation 1 and evaluating the integral gives [2, 3]:

$$\mathcal{G}_{ss} = \frac{\pi}{4}\frac{\sigma_{yy,2}^2 2h_2}{\bar{E}_2} \qquad \textit{(asymptotic limit)} \tag{3}$$

This asymptotic limit, established by Ho and Suo [2, 3] in equation 3, is representing the mode-I steady-state energy release rate of a tunneling crack in a homogenous structure with infinitely thick substrates. Therefore, it is convenient to normalise other energy release rate results with this elementary case i.e. $[(\sigma_{yy,2}^2 2h_2)/(\bar{E}_2)]$.

The tunneling crack models by Ho and Suo [2, 3] were extended to account for debonding [4, 5, 6], transient effects for short crack lengths [7] (although first demonstrated for thin film [8, 9]) and material orthotropy [10, 11]. Yang *et al.* [10] studied the effect of ply angles on the critical stress to propagate a tunneling crack embedded in the central layer of a carbon-epoxy laminate. It was found that the critical stress to propagate the tunneling crack were highest when the uni-directional fibers were oriented perpendicular to the tunneling crack i.e. fibers oriented in the y-direction in Figure 1. Beom *et al.* [11] presented results for the case where only the adhesive layer was modelled with material orthotropy i.e. the modelling results were limited to substrates with isotropic material properties of infinitely thickness.

In a wind turbine blade joint the adhesive can be assumed isotropic, but the substrates consist of several layers of different type, typically uni-directional- (UD) and bi-axial (Biax) glass-fiber layers as exemplified in Figure 1 (B-C). The in-plane orthotropy of these materials can be described by two dimensionless parameters [12]:

$$\lambda = \frac{E_{xx}}{E_{yy}}, \qquad \rho = \frac{(E_{xx}E_{yy})^{1/2}}{2G_{xy}} - (\nu_{xy}\nu_{yx})^{1/2} \tag{4}$$

which reduces to $\lambda = \rho = 1$ for an isotropic material [12]. The material directions of the laminate are in accordance with the coordinate system in Figure 1, where E_{xx} and E_{yy} are the Young's modulus, G_{xy} is the shear modulus, and ν_{xy} and ν_{yx} are the Poisson's ratio.

The substrates, constraining the adhesive, can be modified in order to prevent the propagation of tunneling cracks since the substrates are layered composite materials. Thus, one way of improving the adhesive joint design is to modify the ply-thickness and stiffness of the individual layers of the laminates. However, modification of the original layup might have a negative effect on the existing blade design that is designed such that the joint can withstand the various other load cases e.g. bending, compression and torsion.

Another way to prevent tunneling crack propagation across the adhesive layer of the joint is to add a new layer, called a buffer-layer, near the adhesive and control the properties of this layer. The buffer-layer design philosophy is attractive since the original joint design can be maintained and at

the same time, by adding the buffer-layer, the joint design can be improved against the propagation of tunneling cracks. Furthermore, it is well known for thin films that it is the thickness and stiffness of the layer closest to the adhesive that has the greatest constraining effect on the crack [13].

The objective of this research is to study the effect of in-plane stiffness, E, and layer-thickness, h, on the steady-state energy release rate, $\mathcal{G}_{ss}$, using finite element (FE) models. More specifically, it is the aim to determine the effect of a buffer-layer on the steady-state energy release rate for an isolated tunneling crack in the adhesive layer of a wind turbine blade joint. This should lead to design rules for an improved bonded joint design. The primary applicability is for wind turbine blade relevant joint design and -material combinations since there is a high demand for novel design rules for adhesive joints in the wind turbine blade industry.

The design idea of a buffer-layer for improvement of a wind turbine blade joint is novel and the implications and effects of this buffer-layer need to be investigated before potential implementation in the future joint design. Therefore, parameter studies with a new symmetric tri-material FE model is used to address the design challenge. Furthermore, the study of steady-state tunnel cracking for a multi-layered sandwich structure with orthotropic substrates has not been addressed in the literature. This includes the applicability on wind turbine blade joints with realistic material combinations.

The paper is organised as follows. In section 2 the materials and the problem are defined, and in section 3 the finite element modelling techniques are described. Hereafter, tunneling cracking in a generalised perspective is analysed using first bi-material FE models in section 4 and tri-material FE models in section 5 (see Figure 2). In section 6, a case study with blade relevant materials demonstrates how a wind turbine blade joint design are influenced by the presence of a buffer-layer including the effect of material orthotropy. Finally, a discussion and conclusion highlights the major findings of the present study.

2. Problem definition

The problem we investigate in the present study is that of an isolated tunneling crack in Figure 2 (A), which is used to clarify the effect of substrate stiffness- and thickness, and used to test the implementation of the numerical models. This model is extended by embedding a buffer-layer, named material #3 in Figure 2 (B), to analyse the effect of buffer-layer thickness and -stiffness on the steady-state energy release rate of a tunneling crack. The model is limited to three layers since more layers complicate the modelling unnecessarily. The effect of material orthotropy of the substrates is investigated in order to test whether it is feasible to model blade relevant materials as isotropic materials.

Since stress is applied as boundary condition in the tunneling crack models, Dundurs' parameters

can be introduced to reduce the number of elastic parameters controlling the stress field [14, 15]:

$$\alpha_{i2} = \frac{\bar{E}_i - \bar{E}_2}{\bar{E}_i + \bar{E}_2} \qquad and \qquad \beta_{i2} = \frac{\bar{E}_i f(\nu_2) - \bar{E}_2 f(\nu_i)}{\bar{E}_i + \bar{E}_2} \tag{5}$$

For the bi-material model in Figure 2 (A), $i = 1$ represents the substrate and for the tri-material model in Figure 2 (B), $i = 1, 3$ denotes the substrate and buffer-layer respectively. ν_i is Poisson's ratio and E_i is the in-plane Young's modulus. $\bar{E}_i = E_i/(1-\nu_i^2)$ and $f(\nu_i) = (1-2\nu_i)/[2(1-\nu_i)]$ are for plane strain, and $\bar{E}_i = E_i$ and $f(\nu_i) = (1-2\nu_i)/2$ are for plane stress. The Young's modulus of the UD composite in the fiber direction, E_{yy}, is used for the computation of α for the orthotropic materials. $\bar{E}_2$ is the plane strain Young's modulus of the adhesive.

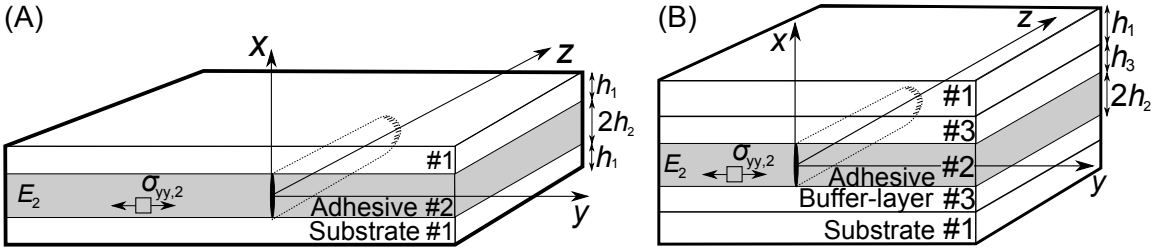

Figure 2: (A) Bi-material model. (B) Tri-material model.

The primary stiffness of a bi-axial glass fiber laminate (Glass Biax), a uni-directional glass fiber laminate (Glass UD) and a uni-directional carbon-fiber laminate (Carbon UD) are used in the present study. These materials, referred to as "blade relevant materials", are modelled as both isotropic and orthotropic with the material parameters presented in Table 1. The constitutive properties of Glass UD and Glass Biax laminates are comparable to those presented by Leong *et al.* [16], whereas for the Carbon UD laminate the properties are close to those of the carbon-epoxy laminate used by Yang *et al.* [10]. The in-plane stiffness, E_{yy}, for Glass UD and Carbon UD are also comparable to the values used in the wind turbine blade design by Mikkelsen [17]. For the cases with isotropic materials ($\lambda = \rho = 1$), the Young's modulus of the substrate, E_1, is set equal to the Young's modulus of a UD composite in the fiber direction, E_{yy}, since this is the primary stiffness parameter constraining the crack. For all models the adhesive is modelled as isotropic and $\nu_i = 1/3$ such that for plane strain $\beta_{i2} = \alpha_{i2}/4$.

	Isotropic				Orthotropic			
Material name	α_{i2}	β_{i2}	λ	ρ	α_{i2}	β_{i2}	λ	ρ
Glass Biax	0.54	0.13	1.00	1.00	0.54	0.13	1.00	0.67
Glass UD	0.85	0.21	1.00	1.00	0.85	0.21	0.26	1.62
Carbon UD	0.94	0.23	1.00	1.00	0.94	0.23	0.11	2.69

Table 1: Material properties for "blade relevant materials".

3. Finite element modelling of a tunneling crack

In the present study $\delta_{cod}(x)$ in equation 1 is determined by a 2D FE model with eight-noded plane strain elements simulated in Abaqus CAE 6.14 (Dassault Systemes). Numerical integration is used to evaluate the integral in equation 1. The steady-state energy release rate, $\mathcal{G}_{ss}$, for the tunneling crack in the bi-material structure, shown in Figure 2 (A), is determined by:

$$\frac{\bar{E}_2 \mathcal{G}_{ss}}{\sigma_{yy,2}^2 2h_2} = F(\alpha_{12}, \beta_{12}, h_1/h_2) \tag{6}$$

where $F(\alpha_{12}, \beta_{12}, h_1/h_2)$ is a non-dimensional function, determined numerically, that accounts for the stiffness mismatch and geometry [2]. The steady-state energy release rate for the tunneling crack in the tri-material structure, shown in Figure 2 (B), can be written as:

$$\frac{\bar{E}_2 \mathcal{G}_{ss}}{\sigma_{yy,2}^2 2h_2} = F(\alpha_{12}, \alpha_{32}, \beta_{12}, \beta_{32}, h_1/h_2, h_3/h_2) \tag{7}$$

where again the non-dimensional function, F, is determined numerically. For both the bi- and tri-material models, the smallest element side length is $0.025h_2$ and approximately 80 elements (eight-noded plane strain) are used across the thickness of the adhesive.

4. Results from tunneling crack bi-material FE model

Figure 3 (B) shows finite element results; $F(\alpha_{12}, \beta_{12} = \alpha_{12}/4, h_1/h_2)$ decreases with increasing substrate stiffness and -thickness. Comparing the FE results for $h_1/h_2 = 2.0$ with the results by Ho and Suo [2] shows that the maximum deviation is below 2%, which indicates that the numerical implementation is sufficiently accurate. The maximum deviation is identified for very compliant substrates. For $\alpha_{12} = 0.0$ in Figure 3 (A), the deviation between the numerical solution and the *asymptotic limit* (Ho and Suo [2]) of $\pi/4$ in equation 3 is less than 0.3% when $h_1/h_2 \geq 6.0$. Furthermore, Figure 3 (A) shows that for decreasing elastic mismatch, α_{12}, the larger h_1/h_2 must be for $\mathcal{G}_{ss}$ to reach a constant value. In Figure 3 (B) an approximate asymptotic limit is identified; when $\alpha_{12} \to 1.0$ and $h_1/h_2 \to \infty$ then $F(\alpha_{12}, \beta_{12} = \alpha_{12}/4, h_1/h_2) \approx 1/2$.

Figure 4 shows the effect of increasing substrate thickness on $F(\alpha_{12}, \beta_{12} = \alpha_{12}/4, h_1/h_2)$ for blade relevant materials. For all types of substrates, where the stiffness of the blade relevant materials are relatively high in comparison with the adhesive, $F(\alpha_{12}, \beta_{12} = \alpha_{12}/4, h_1/h_2)$ starts high, decays and approaches a steady level when $h_1/h_2 \geq 4.0$, see Figure 4. The maximum relative deviation between the models with isotropic- and orthotropic material properties in Figure 4 are 1.9%, 6.0% and 7.2% for Glass Biax, Glass UD and Carbon UD, respectively.

For orthotropic Glass Biax (for which $\rho < 1.0$ i.e. the shear modulus, G_{xy}, is larger for the orthotropic material than for the corresponding isotropic material) the curve in Figure 4 is slightly

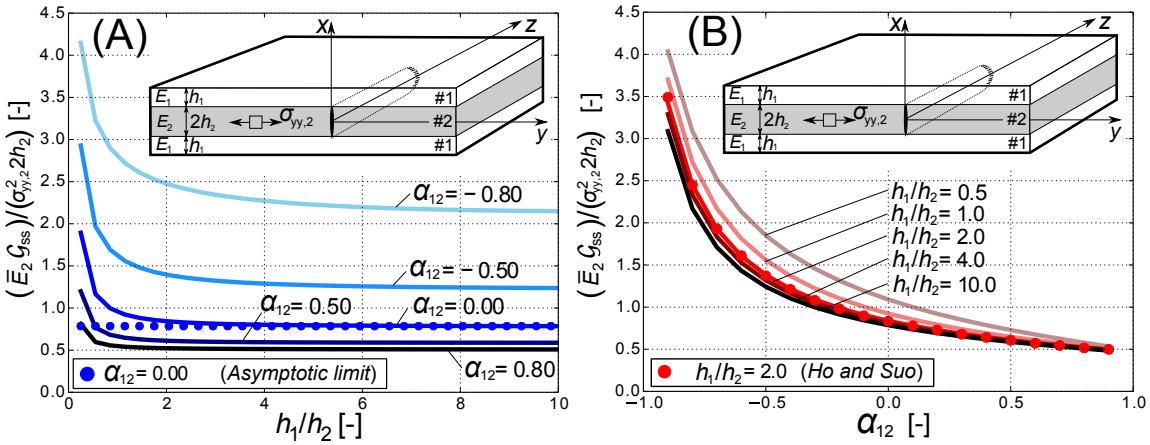

Figure 3: Steady-state energy release rate results for different h_1/h_2 and α_{12}: (A) from bi-material FE model compared with the asymptotic limit ($\pi/4$) from Ho and Suo [2] that is valid for infinitely thick substrates. (B) from bi-material FE model compared with the results by Ho and Suo [2]. Note, for both models $\beta_{12} = \alpha_{12}/4$.

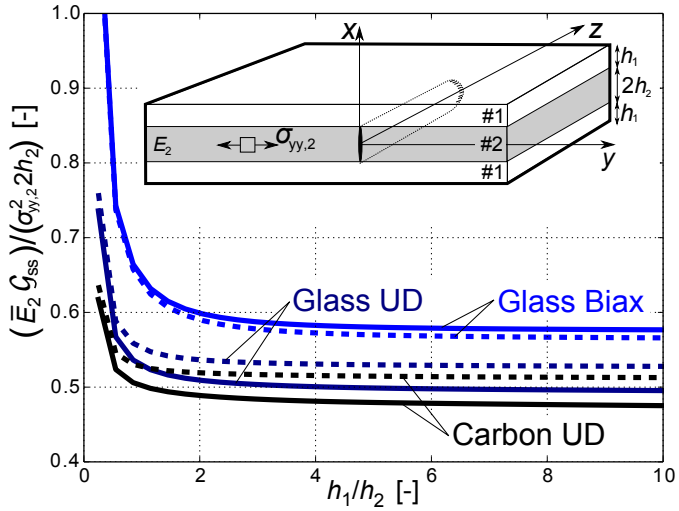

Figure 4: Steady-state energy release rate results from a bi-material FE model for "blade relevant materials" for different stiffness mismatch and with $\beta_{12} = \alpha_{12}/4$. Solid lines and dashed lines represent isotropic- and orthotropic material properties, respectively.

below the curve of the isotropic material. For Glass UD and Carbon UD where $\rho > 1.0$, the energy release rate is higher for the orthotropic case than for the isotropic case.

5. Results from tri-material FE model - generalised joint design

Figure 5 illustrates the influence of buffer-layer thickness and -stiffness on $\mathcal{G}_{ss}$ when $h_1/h_2 = 1.0$. For all cases in Figure 5 it is evident that an increase in α_{32} decreases $\mathcal{G}_{ss}$. It is seen that an increase of buffer-layer thickness, h_3/h_2, decreases $\mathcal{G}_{ss}$ if $\alpha_{32} \gtrsim \alpha_{12}$. Note, that the limit values indicated by arrows in Figure 5 are determined using the bi-material FE model at $h_3/h_2 = 10$. These limit values are identical to the results from the bi-material FE model in Figure 3 at $h_1/h_2 = 10$ indicating that for high buffer-layer thickness, the buffer-layer is the primary layer controlling $\mathcal{G}_{ss}$ (not the substrate).

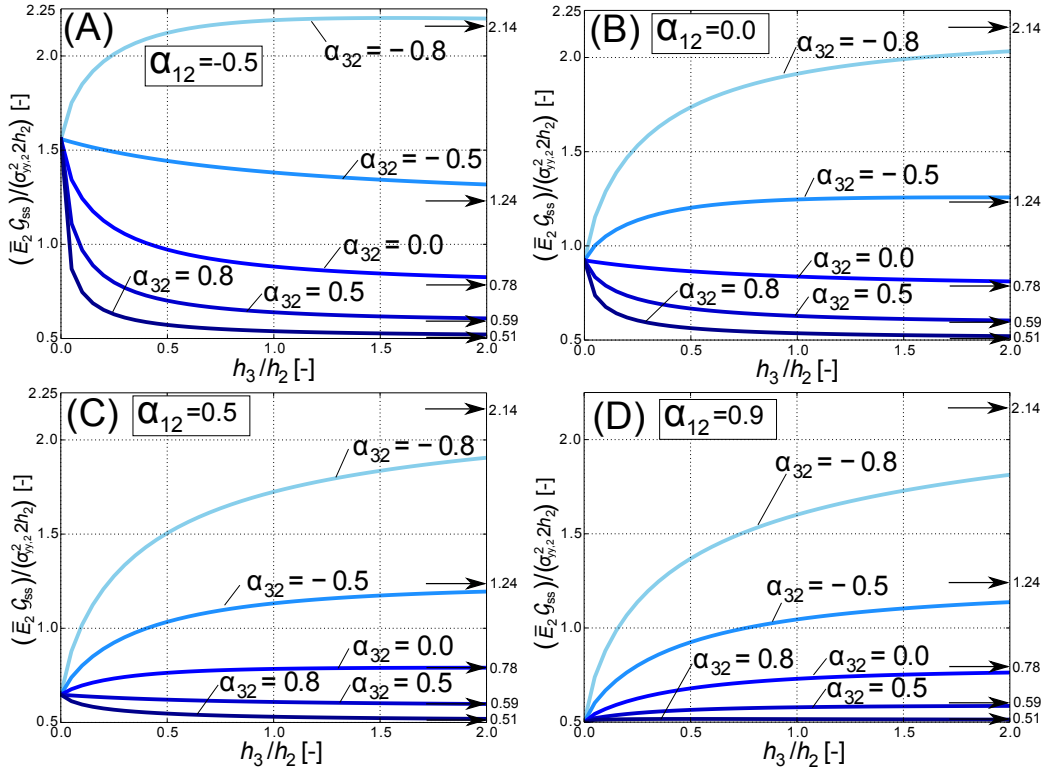

Figure 5: Steady-state energy release rate results from a symmetric tri-material FE model with isotropic materials and selected parameters fixed: $\beta_{i2} = \alpha_{i2}/4$, $h_1/h_2 = 1.0$. Substrate stiffness mismatch of: (A) $\alpha_{12} = -0.5$, (B) $\alpha_{12} = 0.0$, (C) $\alpha_{12} = 0.5$ and (D) $\alpha_{12} = 0.9$.

Further design curves are presented in Figure 6 where α_{32} is varied for different h_3/h_2 and α_{12}. The design curves in Figure 6 for each stiffness mismatch, α_{12}, intersect at a specific point, namely the "point of intersection" (PoI) that is marked with "X" in Figure 6. On the right hand side of the "point of intersection" ($\alpha_{32} >$ PoI), it is advantageous to increase the buffer-layer thickness, whereas on the

left hand side of the "point of intersection" ($\alpha_{32} <$ PoI), it is advantageous to decrease the buffer-layer thickness. It is also evident from Figure 6 that with increasing α_{12} the "point of intersection" moves to the right (to a larger α_{32} value).

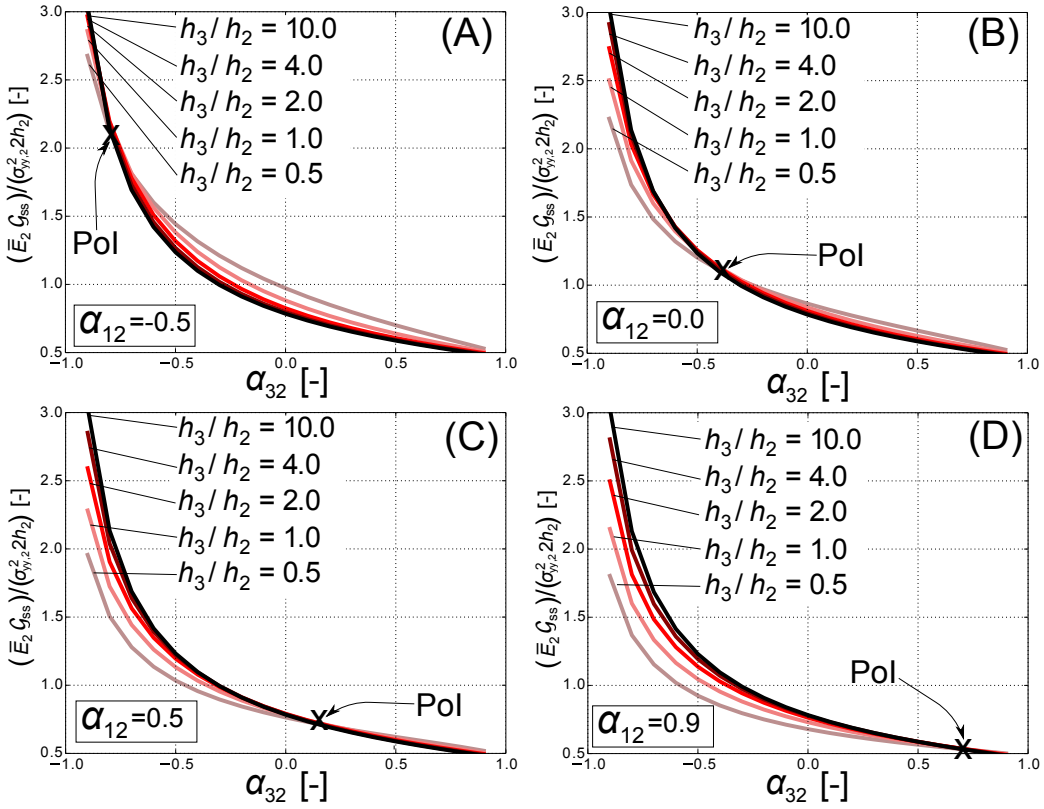

Figure 6: Steady-state energy release rate results from a symmetric tri-material FE model with isotropic materials and selected parameters fixed: $\beta_{i2} = \alpha_{i2}/4$, $h_1/h_2 = 1.0$. Substrate stiffness mismatch of: (A) $\alpha_{12} = -0.5$, (B) $\alpha_{12} = 0.0$, (C) $\alpha_{12} = 0.5$ and (D) $\alpha_{12} = 0.9$.

The best choice (i.e. the one that gives the lowest energy-release rate) of buffer-layer thickness and stiffness depends on the stiffness of the basis substrate, α_{12}. Without prior knowledge of the modeling result it would be expected that the stiffness of the buffer-layer should be a least the stiffness of the substrate in order to reduce the energy release rate. However, the value of α_{32} at the "point of intersection" is less than the value of α_{12} in the models in Figure 6. For instance, it is seen in Figure 6 (C) that the PoI is located at $\alpha_{32} \approx 0.25$, whereas $\alpha_{12} = 0.5$ for the model in Figure 6 (C). Thus, the "point of intersection" must be determined accurately in order to ensure that $\mathcal{G}_{ss}$ decreases with increasing h_3/h_2. An additional study of the transition at the "point of intersection" is presented in Appendix A. In the overall picture, changing the stiffness of the basis substrate (α_{12}) has a small effect on the steady-state energy release rate of the tunneling crack.

6. Results for case study with blade relevant materials

The parametric 2D plane strain FE model of an isolated tunneling crack with a buffer-layer, denoted material #3 in Figure 7, is used to investigate the effect of buffer-layer thickness and -stiffness on $\mathcal{G}_{ss}$ for blade relevant material combinations including the effect of material orthotropy. The stiffness of the substrate (material #1) is equal to that of Glass UD ($\alpha_{12} = 0.85$).

First the results for the case where the stiffness of the buffer-layer (material #3) is similar to that of Glass Biax ($\alpha_{32} = 0.54$) is presented. The curves in Figure 7 for Glass Biax shows that an increase of the buffer-layer thickness, h_3, actually increases $\mathcal{G}_{ss}$ although the total thickness of the substrate ($h_1 + h_3$) becomes larger. This can be understood in that with increasing h_3, the stiffer material #1 is moved further away from the tunneling crack tip hence reducing the constraint, but also by the decreased stiffness of the layer closest to the adhesive.

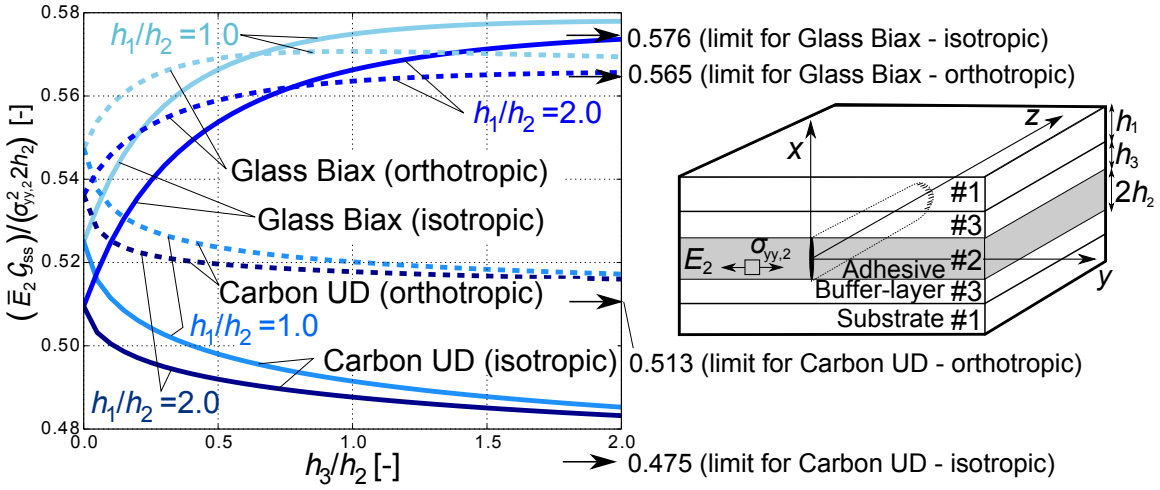

Figure 7: Steady-state energy release rate results from a symmetric tri-material FE model with blade relevant material combinations. Solid lines and dashed lines represent isotropic- and orthotropic material properties, respectively. The limit values indicated by arrows are determined using the results of the bi-material FE model at $h_3/h_2 = 10$ in Figure 4.

Figure 7 also includes results for a buffer-layer with stiffness of a Carbon UD laminate ($\alpha_{32} = 0.94$). The thickness, h_3, of material #3 is varied and the results show that a design for reducing $\mathcal{G}_{ss}$ would consist of a thick and stiff layer closest to the adhesive e.g. a Carbon UD laminate. $\mathcal{G}_{ss}$ is decreased by approx. 5% for by adding the carbon UD buffer-layer with thickness $h_3/h_2 = 1.0$ to the Glass UD substrate ($h_1/h_2 = 1.0$). The largest deviation between Carbon UD isotropic and -orthotropic is approximately 7%, whereas the largest deviation between buffer-layers of Glass Biax and Carbon UD (isotropic) in Figure 7 is about 18%. Note, that the limit values indicated by arrows in Figure 7 are determined using the results of the bi-material FE model at $h_3/h_2 = 10$ in Figure 4.

The results in Figure 7 for Carbon UD can also be used to determine the best compromise between

buffer-layer thickness, -stiffness, and -price since too many Carbon UD layers would be costly in comparison with the constraining effect achieved. However, adding Carbon UD layers to an already stiff Glass UD laminate will only decrease $\mathcal{G}_{ss}$ by approx. up to 6-10% according to Figure 7. Instead, since the steady-state energy release rate scales linearly with the thickness of the adhesive layer, see equation 7, for the present case, it is more effective to decrease the energy release rate by decreasing the thickness of the adhesive layer.

7. Discussions

The implications and effects of the buffer-layer are discussed. In order to design a reliable adhesive joint, specific requirements for the properties of the buffer-layer must be set. If the tunneling crack initially confined in the adhesive, shown in Figure 8 (A), extends through the buffer-layer (Figure 8 (B)) then the energy release rate of the tunneling crack becomes higher since both the thickness- and the stiffness of the cracked layer increase (if $E_3 > E_2$). Thus, cracking through the buffer-layer increases the steady-state energy release rate of the tunneling crack dramatically. Therefore, the strength and fracture toughness of the buffer-layer must be sufficiently high to avoid cracking during the tunneling crack propagation across the bondline. Fortunately, laminates used in wind turbine blades have both higher stiffness and -strength than the typical structural adhesives used in wind turbine blades. Models for crack penetration of interlayers are available in the literature [18, 19, 20]; they can be used to set the requirements for the additional material properties of the buffer-layer. If the buffer-layer is a composite material with long aligned fibres, then it will be unlikely that a crack penetrates through the buffer-layer as a sharp crack. Instead, the tunneling crack will more likely cause damage to a larger zone and initiate splitting and delaminations of the laminates.

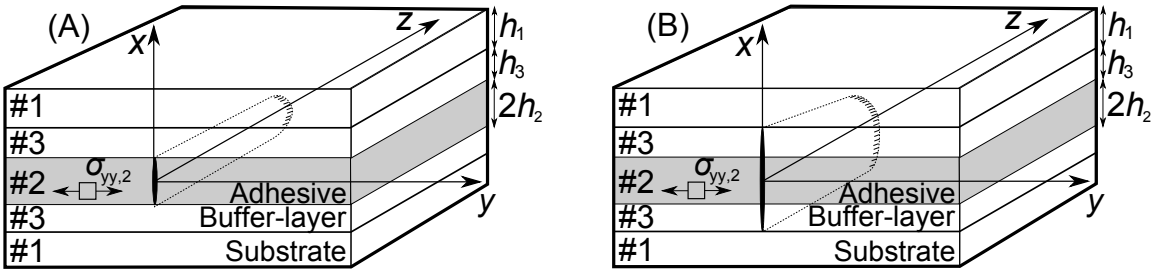

Figure 8: (A) Tunneling crack confined in the adhesive layer. (B) Tunneling crack extended through the buffer-layer.

The load required to propagate a tunneling crack is lower than the load to initiate a tunneling crack from a small void in the adhesive [2]. Thus, the use of the tunneling models as design criteria for bondlines containing voids (no real sharp cracks) is regarded as being conservative. Furthermore, if a tunneling crack initiates at a free edge then the tunneling crack must reach a certain length (dependent

on elastic mismatch) to become steady-state [7]. The energy release rate increases with crack length until the steady-state value is attained [2], which is another reason why the steady-state tunneling crack models are conservative.

For future work, the tri-material model in the present study may be extended to include the effect of adhesive-laminate debonding for both static and cyclic loadings [5, 6, 4] and extended to include multiple cracking [2, 21].

8. Conclusions

Generally, it was found favourable to embed a buffer-layer near the adhesive with controllable thickness- and stiffness properties in order to improve the joint design against the propagation of tunneling cracks. The results from the tri-material FE model showed that it was desirable to increase the thickness of the buffer-layer if the stiffness of the buffer-layer is higher than the "point of intersection" in Figure 6. In any case, it was advantageous to increase the stiffness of the buffer-layer in order to decrease the energy release rate of the tunneling crack.

For blade relevant materials, the effect of material orthotropy on the steady-state energy release rate was found to be relatively small (2-7%). Similarly, the effect of using a Carbon UD laminate as buffer-layer was relatively small (6-10%) since the stiffness of the original Glass UD laminate was already high. Instead, it is proposed to reduce the thickness of the adhesive layer in the wind turbine blade joint.

Acknowledgements

This research was primarily supported by grant no. 4135-00010B from Innovation Fund Denmark. This research was also supported by the Danish Centre for Composite Structure and Materials for Wind Turbines (DCCSM), grant no. 0603-00301B, from Innovation Fund Denmark.

Appendix A. Additional design curves from tri-material FE model

Additional design curves determined by the tri-material FE model are presented in Figure A.9 and Figure A.10. From these curves the transition at the "point of intersection" is investigated further i.e. for the energy release rate increasing with buffer-layer thickness to the energy release rate decreasing with buffer-layer thickness. This transition is difficult to identify from Figure A.9. Therefore, the design curves in Figure A.9 for $-0.5 < \alpha_{32} < 0.0$ are magnified and presented individually in Figure A.10. In Figure A.10, it is seen that the shape of the curve is very dependent on the magnitude of α_{32}. A peak is identified in Figure A.10 (B-G). The peak is reduced with increasing α_{32} (closer to zero). In

Figure A.10 (H-I) the peak vanish and for increasing h_1/h_2, a continuous decreasing trend is attained. It is of interest that a peak in Figure A.10 (A-G) exists since it is typically desired to minimise or maximise the energy release rate dependent on the application.

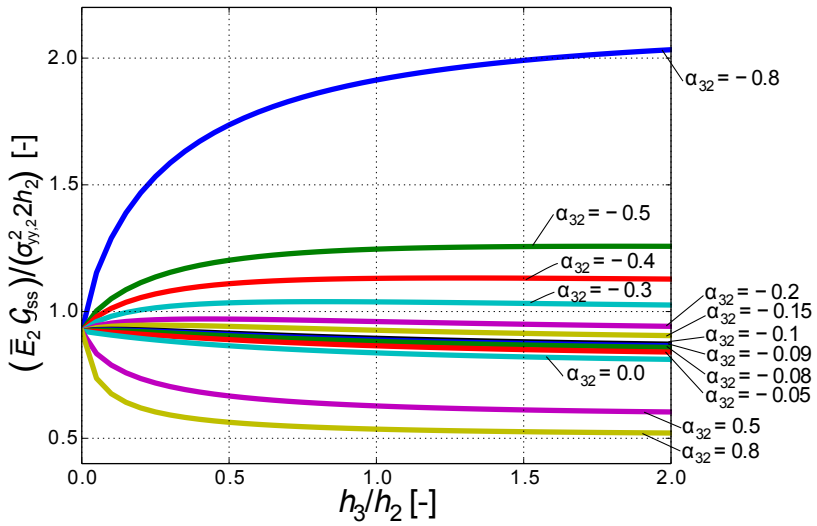

Figure A.9: Steady-state energy release rate results from a tri-material FE model with selected parameters fixed: $\beta_{i2} = \alpha_{i2}/4$, $h_1/h_2 = 1.0$, and substrate stiffness mismatch of: $\alpha_{12} = 0.0$.

References

[1] J. Z. Hansen, The effects of fibre architecture on fatigue life-time of composite materials, Ph.D. thesis, Technical University of Denmark. Dept. of Wind Energy, (2013).

[2] S. Ho, Z. Suo, Tunneling cracks in constrained layers, J. Appl. Mech 60 (1993) 890–894.

[3] Z. Suo, Failure of brittle adhesive joints, Appl. Mech 43 (5) (1990) 275–279.

[4] K. Chan, M. He, J. Hutchinson, Cracking and stress redistribution in ceramic layered composites, Materials Science and Engineering A167 (1993) 57–64.

[5] A. S. J. Suiker, N. A. Fleck, Crack tunneling and plane-strain delamination in layered solids, International Journal of Fracture 125 (1) (2004) 1–32. doi:10.1023/B:FRAC.0000021064.52949.e2.

[6] A. S. J. Suiker, N. A. Fleck, Modelling of fatigue crack tunneling and delamination in layered composites, Composites Part A: Applied Science and Manufacturing 37 (10) (2006) 1722–1733. doi:10.1016/j.compositesa.2005.09.006.

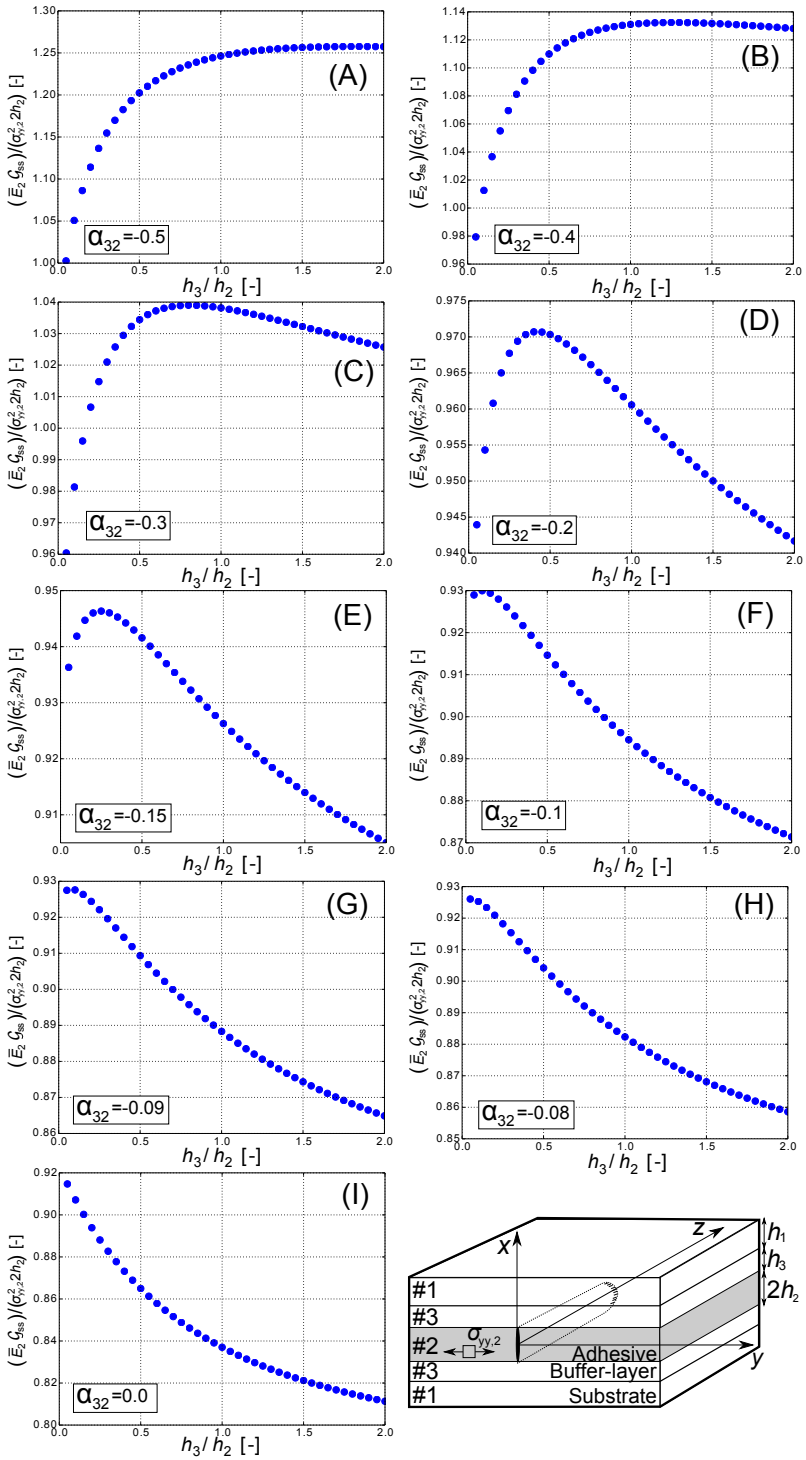

Figure A.10: Steady-state energy release rate results from a tri-material FE model with selected parameters fixed: $\beta_{i2} = \alpha_{i2}/4$, $h_1/h_2 = 1.0$, and substrate-adhesive stiffness mismatch of: $\alpha_{12} = 0.0$.

[7] J. Andersons, P. H. M. Timmermans, J. Modniks, Mechanics of tunnelling cracks in trilayer elastic materials in tension, International Journal of Fracture 148 (3) (2008) 233–241. doi:10.1007/s10704-008-9197-3.

[8] T. Nakamura, S. M. Kamath, Three-dimensional effects in thin film fracture mechanics, Mechanics of Materials 13 (1) (1992) 67–77. doi:10.1016/0167-6636(92)90037-E.

[9] J. M. Ambrico, M. R. Begley, The role of initial flaw size, elastic compliance and plasticity in channel cracking of thin films, Thin Solid Films 419 (2002) 144–153. doi:10.1016/S0040-6090(02)00718-6.

[10] T. Yang, Y. Liu, J. Wang, A study of the propagation of an embedded crack in a composite laminate of finite thickness, Composite Structures 59 (4) (2003) 473–479. doi:10.1016/S0263-8223(02)00284-2.

[11] H. Beom, X. Zhuo, C. Cui, Tunneling cracks in the adhesive layer of an orthotropic sandwich structure, International Journal of Engineering Science 63 (2013) 40–51. doi:10.1016/j.ijengsci.2012.11.001.

[12] Z. Suo, G. Bao, B. Fan, T. Wang, Orthotropy rescaling and implications for fracture in composites, Int. J. Solid Structures 28 (2) (1991) 235–248.

[13] T. Y. Tsui, A. J. McKerrow, J. J. Vlassak, Constraint effects on thin film channel cracking behavior, Journal of Materials Research 20 (2005) 2266–2273. doi:10.1557/jmr.2005.0317.

[14] J. Dundurs, Edge-bonded dissimilar orthogonal elastic wedges under normal and shear loading, Journal of Applied Mechanics 36 (3) (1969) 650–652.

[15] J. Parmigiani, M. Thouless, The effects of cohesive strength and toughness on mixed-mode delamination of beam-like geometries, Engineering Fracture Mechanics 74 (17) (2007) 2675–2699. doi:10.1016/j.engfracmech.2007.02.005.

[16] M. Leong, L. C. T. Overgaard, O. T. Thomsen, E. Lund, I. M. Daniel, Investigation of failure mechanisms in GFRP sandwich structures with face sheet wrinkle defects used for wind turbine blades, Composite Structures 94 (2) (2012) 768–778. doi:10.1016/j.compstruct.2011.09.012.

[17] L. P. Mikkelsen, A simplified model predicting the weight of the load carrying beam in a wind turbine blade, IOP Conference Series: Materials Science and Engineering 139 (2016) 1–8. doi:10.1088/1757-899X/139/1/012038.

[18] M. Y. He, J. W. Hutchinson, Crack deflection at an interface between dissimilar elastic materials, Int. J. Solid Structures 25 (9) (1989) 1053–1067.

[19] M. Y. He, A. G. Evans, Crack deflection at an interface between dissimilar elastic materials: Role of residual stresses, Int. J. Solids Structures 31 (1994) 3443.

[20] J. Parmigiani, M. Thouless, The roles of toughness and cohesive strength on crack deflection at interfaces, Journal of the Mechanics and Physics of Solids 54 (2) (2006) 266–287. doi:10.1016/j.jmps.2005.09.002.

[21] J. W. Hutchinson, Z. Suo, Mixed mode cracking in layered materials, Advances in applied mechanics 29 (1992) 63.

APPENDED PAPER P3

Tunneling cracks in full scale wind turbine blade joints

Jeppe B. Jørgensen, Bent F. Sørensen and Casper Kildegaard
Engineering Fracture Mechanics
Accepted, 2017

Tunneling cracks in full scale wind turbine blade joints

Jeppe B. Jørgensen[a,b], Bent F. Sørensen[b], Casper Kildegaard[a]

[a] *LM Wind Power, Østre Alle 1, 6640 Lunderskov, Denmark.*
[b] *The Technical University of Denmark, Dept. of Wind Energy, Frederiksborgvej 399, 4000 Roskilde, Denmark.*

Abstract

A novel approach is presented and used in a generic tunneling crack tool for the prediction of crack growth rates for tunneling cracks propagating across a bond-line in a wind turbine blade under high cyclic loadings.

In order to test and demonstrate the applicability of the tool, model predictions are compared with measured crack growth rates from a full scale blade fatigue test. The crack growth rates, measured for a several metre long section along the blade trailing-edge joint during the fatigue test, are found to be in-between the upper- and lower-bound predictions.

Keywords: Bonded joints, Fatigue crack growth, Residual stresses, Polymer matrix composites, Finite element analysis

Email address: jeppbj@dtu.dk (Jeppe B. Jørgensen)

Nomenclature

a	crack length
C	Paris law coefficient
da/dN	crack growth rate
E_1, E_2	Young's modulus (substrate, adhesive)
$\bar{E}_1, \bar{E}_2$	plane strain Young's modulus (substrate, adhesive)
(EI)	bending stiffness of DCB specimen arms
f	non-dimensional function
F	function that relates ΔK with da/dN
G_{ss}	mode-I steady-state energy release rate
h_1, h_2	thickness for sandwich (substrate, adhesive)
h_1^*, h_2^*	thickness for bi-layer (substrate, adhesive)
$\bar{h}_2$	average thickness of adhesive in blade section
J	J-integral
K	stress intensity factor
L_b	blade length
L_c	crack spacing
$\bar{L}_c$	average crack spacing
L_r	roller distance for DCB

m	Paris law exponent
M	bending moment
M_{xx}	edgewise bending moment
N	cycles
P	load
q	non-dimensional function
r	radius
R	load R-ratio
t	width of cracked area for DCB
x, y, z	coordinates
α	first Dundurs' parameter
β	second Dundurs' parameter
δ_{ext}	extensometer opening
δ_{cod}	crack opening displacement profile
$\epsilon_T, \epsilon_{yy}$	strain (misfit, adhesive/substrate)
ζ, ζ_*	thickness ratio (sandwich, bi-layer)
κ	curvature of bi-layer
ν_1, ν_2	Poisson's ratio (substrate, adhesive)
σ_m	mechanical stress
σ_r	residual stress

σ_T	misfit stress
$\sigma_{yy,2}$	stress in adhesive
Σ, Σ_*	stiffness ratio (sandwich, bi-layer)
CAD	computer-aided design
DCB	double cantilever beam
FE	finite element
LEFM	linear elastic fracture mechanics
VARTM	vacuum-assisted-resin-transfer-moulding

1. Introduction

Full-scale structural blade testing is the main method used for testing the life-time performance of wind turbine blades and is commonly used for blade certification [1]. The main purposes of full-scale static blade testing are to test that new blade designs meet requirements and to gain insight into the failure mechanisms [2, 3, 4, 5, 6, 7]. Publications of full-scale blade testing under cyclic loadings are limited due to confidentiality and the few testing laboratories that are actually able to perform the test [5]: DTU Wind Energy, LM Wind Power, Siemens Wind Power, Blaest (all in Denmark), CRES in Greece, WMC in Netherlands, NREL, LBR&TF, WTTC (all in USA), NaREC in UK, Fraunhofer in Germany and SGS in China.

A wind turbine life-time is typically designed for 20 years or more [8, 9, 10, 11]. Thus, a wind turbine blade in operation is affected by cyclic loadings

i.a. caused by gravity loads, see edge-wise bending moment, M_{xx} in Figure 1. The adhesive joints are one of the critical structural details in large wind turbine blades. In particular, the trailing-edge is critical since it is located far from the elastic center of the blade and therefore experiences significantly higher strains, ϵ_{yy} when subject to edge-wise bending.

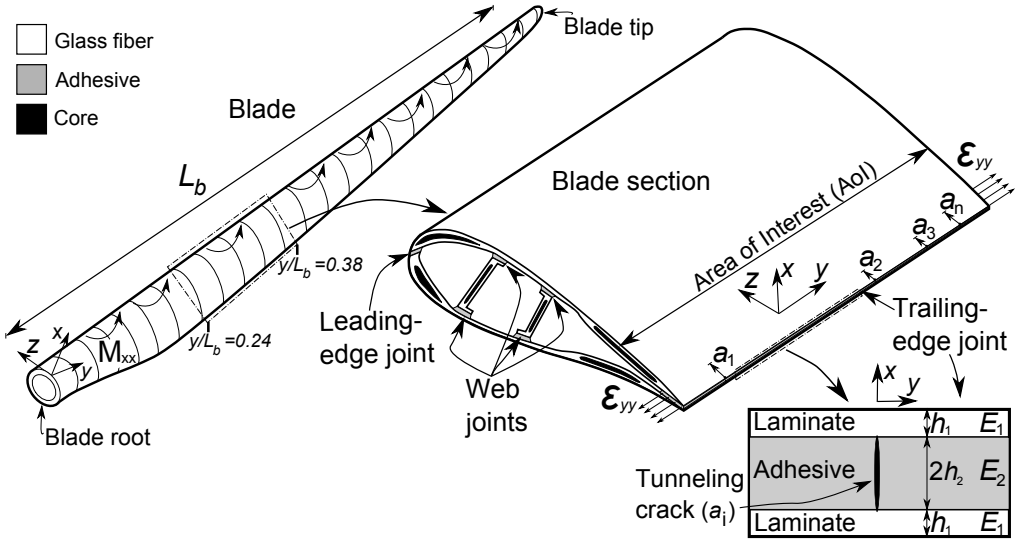

Figure 1: Blade with edge-wise bending moments, M_{xx} distributed over blade length, L_b. Blade section includes web-, leading-edge-, and trailing-edge joints.

During excessive high cycle loading, tunneling cracks may initiate in the trailing-edge adhesive joint as shown in Figure 2, where a tunneling crack in the adhesive is encircled by red marker on the edge of the joint. The tunneling cracks propagate in the z-direction as shown by a_1, a_2, ..., a_n in Figure 1. Each tunneling crack with length, a_i, has a unique configuration of laminate stiffness, E_1, adhesive stiffness, E_2, laminate thickness, h_1, adhesive thickness, $2h_2$ and strain level, ϵ_{yy} dependent on specific location of the crack tip in the y-z plane. Note, the average adhesive thickness along the length

of the blade section is denoted $2\bar{h}_2$.

Ataya *et al.* [12] documented the presence of transverse cracks, of lengths 20 mm to 50 mm, in trailing-edge joints on wind turbine blades operating in the field with working life ranging between 6.5x10^7 and 1.1x10^8 cycles. It was not documented how these transverse (tunneling) cracks initiated and developed. The traditional understanding of transverse cracking is that the cracks start from an edge-flaw and propagate across the adhesive layer. The adhesive is constrained by stiff laminates, primarily with uni-directional fibers, oriented in blade length, i.e. the y-direction in Figure 1. Thus, the tunneling crack in the brittle adhesive layer is constrained in-between laminates with higher stiffness and strength. Tunneling cracks propagating across a bond-line, loaded quasi-static or cyclic, are comparable with propagating off-axis matrix tunneling cracks in composite structures e.g. cross ply laminates [13, 14, 15, 16, 17, 18, 19, 20, 21].

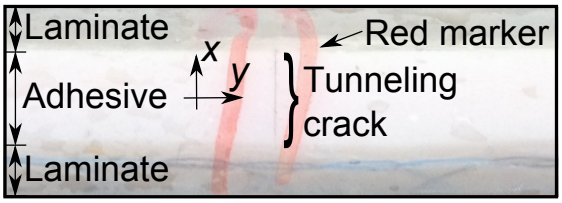

Figure 2: Tunneling crack identified in the trailing-edge joint of a full scale test blade.

Tunneling cracks have been modelled extensively through the last three decades using linear elastic fracture mechanics (LEFM) [22, 23, 24, 25, 19, 26, 27]. From a modelling perspective, this cracking mechanism is closely related to channeling cracks in thin films [28, 29, 30, 31, 32]. One of the first models of a single tunneling crack embedded in-between thick substrates were

developed using 2D finite element (FE) modelling and LEFM [22, 23, 24]. 3D FE models were used for transient modelling of channeling/tunneling cracks since the crack length must reach a certain length for the crack to become steady-state [33, 34, 35, 26]. It is well known [36, 37] that the stress field of bi-material problems with stresses as boundary conditions (not displacement boundary conditions) depends on only two (not three E_1/E_2, ν_1, ν_2) non-dimensional elastic parameters (Dundurs' parameters):

$$\alpha = \frac{\bar{E}_1 - \bar{E}_2}{\bar{E}_1 + \bar{E}_2} \qquad and \qquad \beta = \frac{\bar{E}_1 \frac{(1-2\nu_2)}{2(1-\nu_2)} - \bar{E}_2 \frac{(1-2\nu_1)}{2(1-\nu_1)}}{\bar{E}_1 + \bar{E}_2} \tag{1}$$

where for plane strain $\bar{E} = E/(1-\nu^2)$. ν_1 and ν_2 are the Poisson's ratio of the substrate and adhesive, respectively. In order to apply Dundurs' parameters, it is also a prerequisite that the materials are isotropic, linear-elastic and deformations are planar i.e. either plane strain or plane stress [38, 36]. These prerequisites are satisfied for the sandwich in Figure 2 if the adhesive and laminates are assumed isotropic, linear-elastic and the tunneling crack has reached a certain length from the edge (in z-direction) i.e. steady-state.

Nucleation and propagation of tunneling cracks in the adhesive layer is the first mode of damage of the joint and would not represent catastrophic failure of the blade, or even any significant loss in performance. However, if the tunneling cracks were to initiate delaminations in the laminates or large debonds at the adhesive-laminate interface, this would be far more critical. Tracking and prediction of tunneling cracks propagation are important in order to detect the early stage of damage and to quantify the level of damage before it transforms into a more critical state such as delamination. A safe and conservative joint design is thus designed against the propagation of a

tunneling crack across the bond-line. Therefore, it is relevant to develop rigorous tools for the prediction of tunneling crack propagation in a full scale wind turbine blade joint, especially under cyclic loading.

2. Approach and problem definition

In this paper a novel approach is presented for the prediction of crack growth rates of tunneling cracks in a wind turbine blade joint. The approach includes a generic tunneling crack tool that is exemplified and tested on a trailing-edge joint in a full scale wind turbine blade fatigue test.

The approach enables prediction of crack growth rates for tunneling cracks in adhesive bond-lines, e.g. for wind turbine blade joints, based on information of the tunneling crack state (geometry, start-crack-length, loads and constitutive properties). Crack growth rates (Paris law) for the adhesive are measured by a double cantilever beam (DCB) specimen in laboratory, where the adhesive is loaded cyclic in mode-I [39, 40]. This is elaborated in Section 3.

In adhesive bonded joints residual stresses might develop in the adhesive during the manufacturing process i.a. attributed chemical shrinkage of the adhesive and mismatch in coefficient of thermal expansion between adhesive and laminate. Generally, residual stresses originate from misfits between different material regions or phases [41, 42, 43]. The misfit stress, σ_T, (defined in Section 4) is determined using measured curvature of a bi-layer specimen in the laboratory. The misfit stress is converted to a residual stress, σ_r, in the adhesive, using an analytical sandwich model, to account for local thicknesses and stiffnesses in the blade according to specific crack locations (y, z). It is

advantageous to express the residual stress through a misfit stress since the description of the misfit stress only depends on the adhesive properties and is independent of the application (e.g. thicknesses), whereas the residual stress is application dependent. Thus, the use of the misfit stress is convenient since the misfit stress can be scaled through a non-dimensional function, q, to give the residual stress for the application of interest [44]. This is presented in details in Section 4.

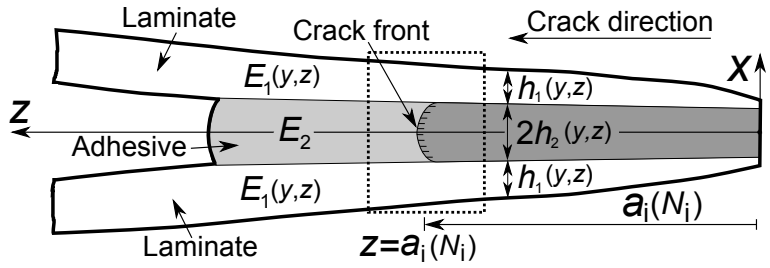

Figure 3: Tunneling crack in trailing-edge joint. The dashed square at position $z = a_i(N_i)$ shows the crack configuration that is analysed using a plane strain condition and LEFM modelling.

The tunneling crack tool takes the local -stiffness and -geometry input from blade models/measurements, shown in Figure 3, including mechanical stress, σ_m, and residual stress, σ_r, in the adhesive. In the real structural blade application, these many parameters dependence on crack tip location (y,z) for each tunneling crack complicates the modelling significantly. Combining these inputs, using LEFM and a plane strain assumption, enables determination of the mode-I steady-state energy release rate, G_{ss} for a single

isolated tunneling crack [24]:

$$G_{ss}(y,z) = \frac{[\sigma_m(y) + \sigma_r(y,z)]^2 2h_2(y,z)}{\bar{E}_2} f\left[\alpha(y,z), \beta(y,z), h_1(y,z)/h_2(y,z)\right] \tag{2}$$

where subscripts 1 and 2 refer to substrate and adhesive, respectively. f is a non-dimensional function that will be determined in the present paper by 2D finite element simulations. Since the loading is cyclic, G_{ss}^{min} and G_{ss}^{max} are converted to a cyclic stress intensity factor range, ΔK using an analytical model as elaborated in Section 5. Combining the tunneling crack modelling results with the measured residual stresses and the measured Paris law for the adhesive, gives the prediction of the crack growth rate for each tunneling crack along the blade section. The steps of the approach, presented in Figure 4, are summarized:

(i) **DCB**: Double cantilever beam specimen fatigue tested in laboratory to measure Paris law (da/dN, ΔK) for a mode-I crack in the adhesive.

(ii) **Bi-layer**: Residual stress (σ_r) determination in the adhesive of the joint using misfit stress (σ_T) that is determined by measuring the curvature of bi-layer specimens.

(iii) **Blade**: Characterization of geometry ($h_1, 2h_2$), crack length for each crack (a_i), cycles for each crack (N_i), constitutive properties (E_1, E_2, ν_1, ν_2), and mechanical stresses ($\sigma_m^{min}, \sigma_m^{max}$) from blade inspection/model, CAD model, aero/FE model or similar.

(iv) **Modelling**: Tunneling cracks modelled using finite elements to determine ΔK_i as a function of blade geometry/properties, mechanical stress, and residual stress ($h_1, 2h_2, E_1, E_2, \nu_1, \nu_2, \Delta\sigma_m, \sigma_r$) for each tunneling crack configuration (a_i, N_i) dependent on location (y, z).

(v) **Blade prediction**: Prediction of da_i/dN_i for each tunneling crack in the blade using ΔK_i from tunneling crack model and Paris law (da/dN) for the adhesive that is measured by a DCB test in laboratory. Note, F is a function that relates ΔK with da/dN.

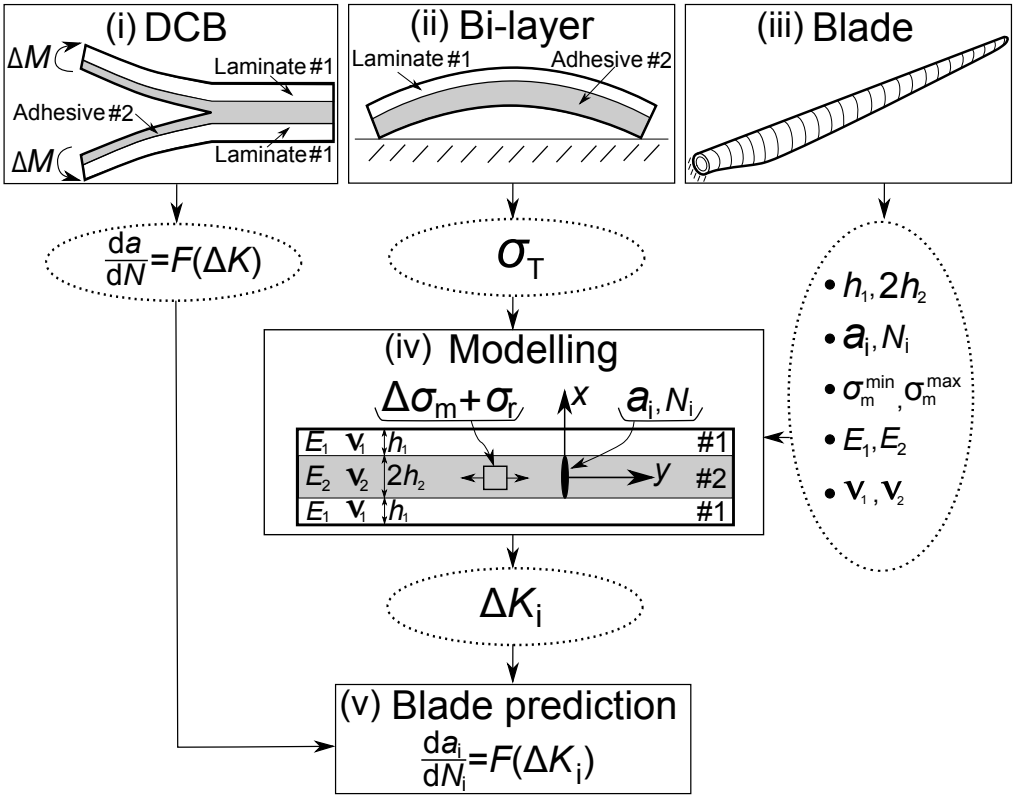

Figure 4: Approach for prediction of crack growth rate for each tunneling crack in a wind turbine blade joint. Step (i) and (ii) are material characterisation whereas step (*iii*), (*iv*) and (*v*) are repeated for each crack with length, a_i.

The properties of the adhesive are characterized in step (i) and (ii), whereas step (iii), (iv) and (v) are repeated for crack number $i = 1$ to $i = n$ according to each cracks specific location (y, z) in the blade. In order to test

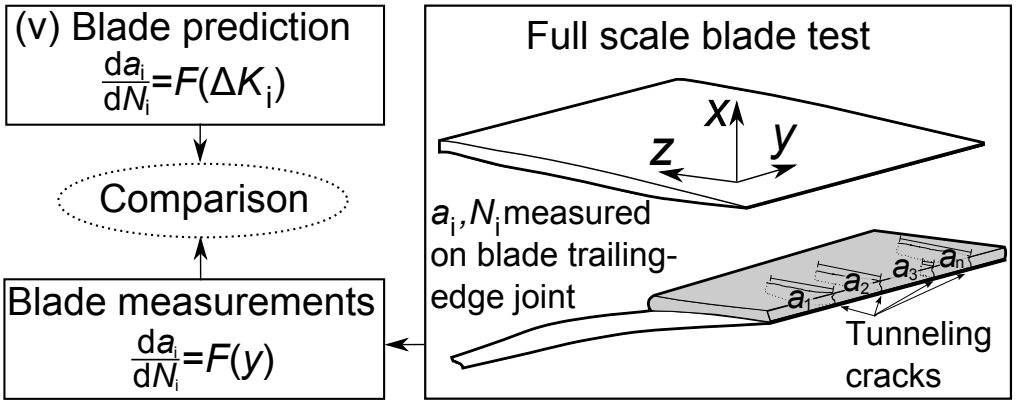

Figure 5: Experimental demonstration for tunneling cracks in a trailing-edge joint. The prediction of crack growth rate for each tunneling crack is tested and compared with the actual measurement on a generic research blade.

the accuracy of the proposed approach, the predicted crack growth rates are compared with crack growth rates measured on a generic research blade as shown in Figure 5. The equations and procedures used for the approach are implemented in a Python program using primarily the Numpy (numerical) and Pandas (data analysis) packages [45, 46]. Thus, it is easy to change the loads, the number of cracks etc. if predictions on other joints in the blade are desired.

3. Theoretical framework: DCB tests to measure Paris law for the adhesive

The DCB specimen is tested by applying a cyclic bending moment to determine the mode-I Paris law for the adhesive using the test setup presented in Figure 6. The J-integral for the moment-loaded DCB specimen is [47, 48]:

$$J = \frac{M^2}{(EI)t} \tag{3}$$

where $M = PL_r$ and t is the width of the cracked area. P is the measured load and L_r is the outer distance between rollers according to Figure 6. The bending stiffness, EI is determined by a layered model of the laminate and adhesive using classical laminate theory [49]. The mode-I stress intensity factor for an isotropic material can be related to the mode-I energy release rate using the well-known Irwin relation [50]:

$$K = \sqrt{G\bar{E}_2} \tag{4}$$

ΔK can be related to fatigue crack growth through the empirical Paris-Erdogan law [39, 40]:

$$da/dN = C(\Delta K)^m \tag{5}$$

The parameters in the power law, C and m are material constants that are determined using a curve fit to actual test data. The use of the Paris law requires that the linear-elastic fracture mechanics assumptions are satisfied meaning that the material must be linear elastic, isotropic, and the fracture process zone must be small in comparison with the other specimen dimensions. Note, Paris law is an empirical relation rather than theoretically based [51].

The DCB specimen with side-grooves, shown in Figure 6, is designed based on initial experiments, which shows that the crack grows to the adhesive-laminate interface if no side-grooves are present. The test setup, presented in Figure 6, has some advantages: 1) energy release rate being independent of crack-length so that crack growth is stable under displacement (rotational) control, 2) easy analytical evaluation of the J-integral. Furthermore, a full range of mode mixities can be tested from pure mode-I to nearly pure

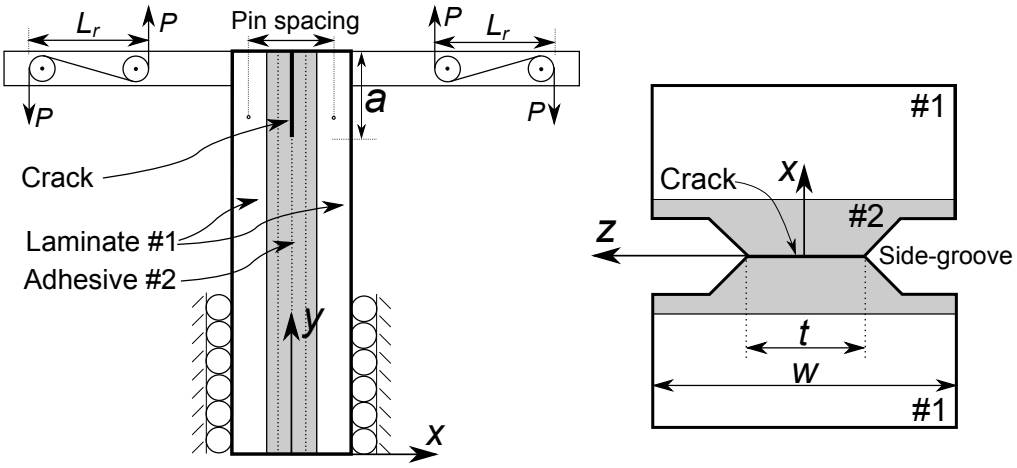

Figure 6: DCB specimen loaded cyclic with even bending moments in mode-I.

mode-II. For the present work and purpose the setup is kept in mode-I since the tunneling cracks in the adhesive, which is assumed isotropic, propagates under mode-I conditions.

For experiments conducted under displacement control, the magnitude of the moment, M decreases as the crack length increases. Thus, a test in displacement control gives information of crack growth rate for the full range of load levels using only a single test specimen. Therefore, in the present study the DCB specimen is loaded cyclic using a constant range of extensometer opening, $\Delta\delta_{ext}$ since it is desired to measure the full Paris law.

4. Theoretical framework: Measuring residual stresses using bi-layer specimen

The residual normal stress, σ_r, e.g. in a symmetric sandwich far from edges as shown in Figure 7, can be related to the misfit stress, σ_T through a

non-dimensional function, q [44]:

$$\sigma_r = q\sigma_T \tag{6}$$

where σ_T is defined as the stress induced in an infinitely thin film adhered to an infinitely thick substrate in a bi-layer material. q is a non-dimensional function accounting for e.g. geometry and elastic properties. The misfit stress cannot be predicted by modelling - it must be measured experimentally [44] unless the mechanism of inelastic strain is known and modelled.

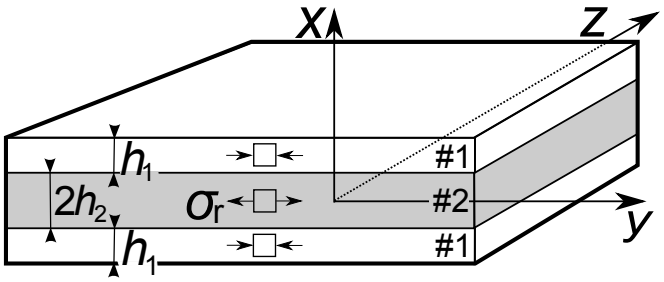

Figure 7: Sandwich specimen used for residual stress modelling.

The misfit stress can be measured using the bi-layer specimen shown in Figure 8 [44, 52, 53]. The curvature, κ is determined by fitting a circle to a number of points measured on top of the surface of the curved beam. The radius of the fitted circle, determined using a least square fit to the measured points along the curved surface, expresses the curvature through the radius, r as; $\kappa = 1/r$. The misfit stress, σ_T can then be determined by [44]:

$$\sigma_T = \frac{\left(\sum_* \zeta_*^2 - 1\right)^2 + 4\sum_* \zeta_*(1+\zeta_*)^2}{6\zeta_*(1+\zeta_*)} \left[\frac{E_2 h_2^* \kappa}{(1-\nu_2)}\right] \tag{7}$$

where $\sum_* = \frac{E_1/(1-\nu_1)}{E_2/(1-\nu_2)}$ and $\zeta_* = h_1^*/h_2^*$ according to Figure 8 for the bi-layer specimen.

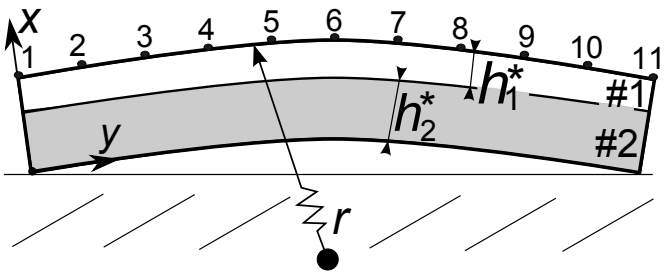

Figure 8: Curvature specimen including positions for measuring beam height.

Knowing σ_T, the stress in the adhesive of the sandwich specimen, shown in Figure 7, can be derived by equilibrium considerations (perfect bonding between the substrates and the adhesive layer), and by Hooke's law in plane stress (in the x-direction):

$$\sigma_r = \frac{-\sigma_T}{\sum + \frac{1}{\zeta}} \tag{8}$$

where $\sum = \frac{E_1/(1-\nu_1)}{E_2/(1-\nu_2)}$ and $\zeta = h_1/h_2$ according to Figure 7 for the sandwich specimen. The energy release rate of the tunneling crack in the sandwich specimen can be expressed as:

$$G_{ss} = (\sigma_m + \sigma_r)^2 \frac{2h_2}{\bar{E}_2} f(\alpha, \beta, h_1/h_2) = \left(\sigma_m + \frac{-\sigma_T}{\sum + \frac{1}{\zeta}}\right)^2 \frac{2h_2}{\bar{E}_2} f(\alpha, \beta, h_1/h_2) \tag{9}$$

where $f(\alpha, \beta, h_1/h_2)$ is determined in the next section.

5. Theoretical framework: Modelling of tunneling cracks

The steady-state energy release rate of an isolated tunneling crack can be expressed using a non-dimensional function, f to account for stiffness and thickness of the materials [24]:

$$\frac{G_{ss}\bar{E}_2}{\sigma_{yy,2}^2 2h_2} = f(\alpha, \beta, h_1/h_2) \tag{10}$$

where the effective stress in the adhesive remote from the crack is designated $\sigma_{yy,2}$. For simplicity, it is assumed that Poisson's ratio for substrates and adhesive are similar, $\nu_1 = \nu_2 = 1/3$, leading to $\beta = \alpha/4$. The steady-state energy release rate, which is constant along the entire tunneling crack front, is determined by [22, 24]:

$$G_{ss} = \frac{1}{2}\frac{\sigma_{yy,2}}{2h_2}\int_{-h_2}^{+h_2} \delta_{cod}(x)dx \tag{11}$$

where $\delta_{cod}(x)$ is the crack opening displacement profile for the plane strain crack, which is determined by FE modelling. Trapezoidal integration is applied to evaluate the integral numerically.

The results from the tunneling crack bi-material FE model, simulated in Abaqus CAE 6.14 (Dassault Systemes) with eight-noded plane strain elements, are compared with the results of Ho and Suo [24] for a thickness ratio of $h_1/h_2 = 2.0$ as shown in Figure 9.

The difference between the FE model results and those of Ho and Suo [24] are less than 2%. As the stiffness and thickness of the substrates increase, $f(\alpha, \beta, h_1/h_2)$ becomes smaller. This is in agreement with the conventional models [23, 24, 27]. Different thickness ratio, h_1/h_2 are modelled hence $f(\alpha, \beta, h_1/h_2)$ for tunneling cracks at different locations can be determined. Figure 9 is the main theoretical result and the relevant stiffness ratio for typical wind turbine blade joints is large as highlighted with the dashed square ($0.7 \leq \alpha \leq 0.9$).

The anisotropy of the glass fiber laminates is assumed negligible since it is assumed that the high in-plane laminate stiffness of the uni-directional fibers in the y-direction is the main constraint to prevent the tunneling crack propagation [27]. ΔK for an isotropic material can be related to ΔG_{ss} in

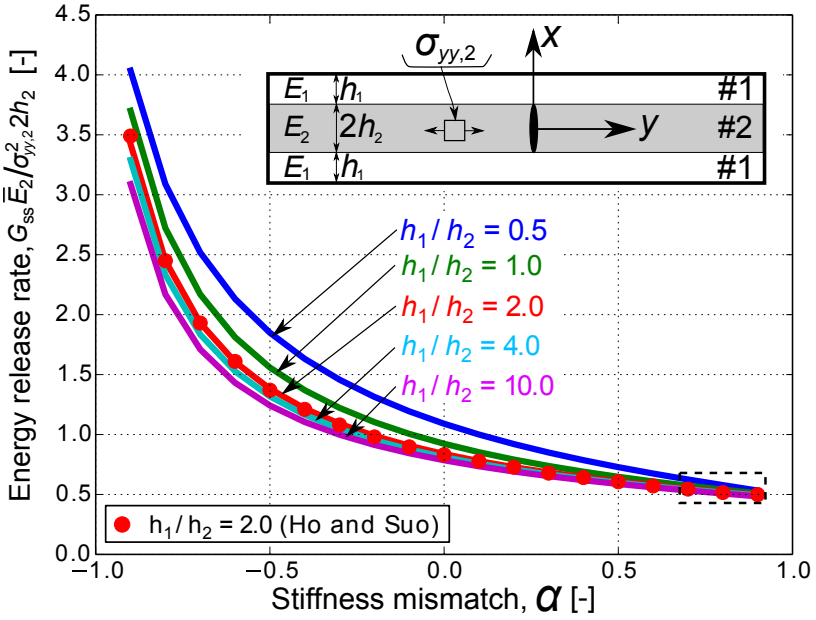

Figure 9: Results from tunneling crack bi-layer FE model and comparison with the model by Ho and Suo [24] for $h_1/h_2 = 2.0$ and $\beta = \alpha/4$.

mode-I using the Irwin relation [19, 50, 51]:

$$\Delta K = \sqrt{G_{ss}^{max}\bar{E}_2} - \sqrt{G_{ss}^{min}\bar{E}_2} = \Delta\sigma_{yy,2}\sqrt{2h_2 f(\alpha,\beta,h_1/h_2)} \qquad (12)$$

that is applicable for tension-tension loading where the load R-ratio ($R = \sigma^{min}/\sigma^{max}$) is $0 \leq R < 1$. However, for tension-compression loading where $R < 0$, equation 12 reduces to:

$$\Delta K = \sqrt{G_{ss}^{max}\bar{E}_2} = \sigma_{yy,2}^{max}\sqrt{2h_2 f(\alpha,\beta,h_1/h_2)} \qquad (13)$$

For compression-compression loading with $R > 1$, the stress intensity factor range becomes zero i.e. $\Delta K = 0$. With the coefficient C and exponent m determined earlier from the DCB test, the crack growth rate (da/dN) of each crack can be determined from equation 5. The stress range can be expressed as a function of load R-ratio, and residual stress (σ_r) can be added to the mechanical stresses (σ_m^{min}, σ_m^{max}) as shown in Figure 10.

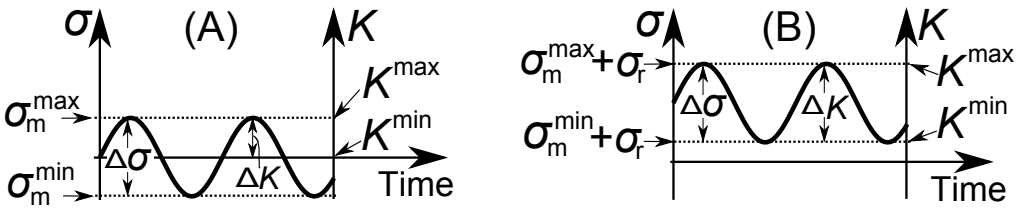

Figure 10: Definition of σ_m^{min}, σ_m^{max}, $\Delta\sigma$, K^{min}, K^{max} and ΔK including a schematic illustration of how ΔK depends on the R-ratio. (A) with $R = -1$, and (B) with $0 \leq R < 1$.

For negative R-ratio ($R < 0$) a part of the stress cycle is negative hence causing crack closure. In that case, only the positive part of the stress cycle is used in the computation of ΔK as illustrated in Figure 10. For the example in Figure 10, for the same applied stress range, ΔK is doubled if R-ratio increases from $R = -1$ to $0 \leq R < 1$. Thus, Figure 10 illustrates the effect of increasing residual stresses on R-ratio and ΔK.

6. Experimental demonstration: Test of full scale research blade

A generic full scale research blade, with length of more than 40 m, was manufactured and tested for approx. 5 million cycles in edge-wise direction with high loads. This corresponds to a full-life fatigue test. Hereafter, the blade was further tested with higher edge-wise cyclic loadings for approx. 1 million cycles, i.e. tested with loads beyond design limits to initiate tunneling cracks. The trailing-edge were loaded in tension-compression fatigue by a load R-ratio of $R = -1$ during the tests. It is unknown when the tunneling cracks initiated, but it was observed and documented that the tunneling cracks propagated through the second test with loadings higher than typical design loads. The experiment was paused 5 times, where the trailing-edge was inspected for cracks and the crack lengths were measured.

The outer trailing-edge thicknesses are measured at four locations (A, B, C, D) in z-direction for each meter along the blade length (y), see Figure 11. The outer thickness measurements are used in combination with the laminate layup from a blade model to determine the actual adhesive thickness for each measurement.

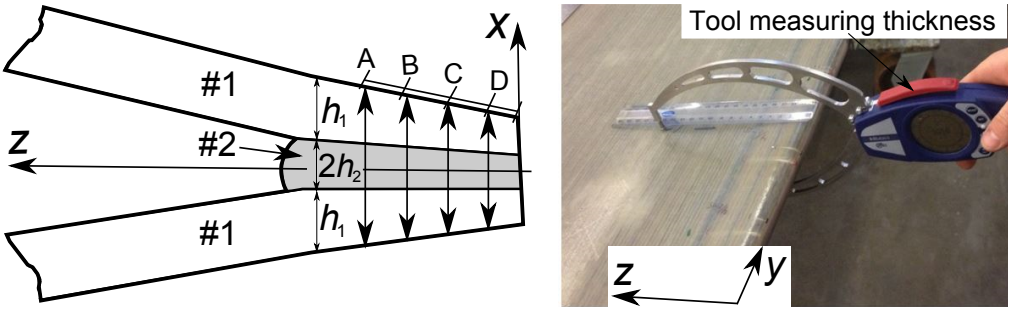

Figure 11: Thickness measurement of the trailing-edge joint at four points for each section.

The stiffness and thickness of the laminates near each crack tip depends on the position in both y- and z- directions as a result of the ply drops in both transverse- and longitudinal blade directions, see Figure 3, Figure 12 and Figure 13. The points in Figure 12 near $y/L_b = 0.28$ and $y/L_b = 0.32$ are not outliers. They are a result of large crack lengths hence the crack tip reach a location where the laminates are thicker, see also Figure 3 and Figure 18.

The average substrate-to-adhesive stiffness ratio, α at each crack position, presented in Figure 13, is determined using linear interpolation (y, z). The number of uni-directional plies is dominant hence the average stiffness is simply a small reduction of the uni-directional ply stiffness due to some biaxial layers surrounding the uni-directional plies. The exact laminate and adhesive properties in the generic research blade are confidential.

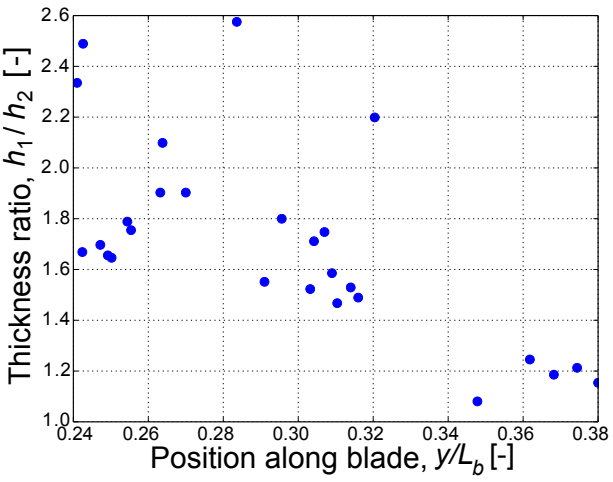

Figure 12: Laminate-adhesive thickness ratio determined at each tunneling crack position along blade length.

The strain range, $\Delta\epsilon_{yy}$ $(= \epsilon_{yy}^{max} - \epsilon_{yy}^{min})$ is measured using strain gauges

located at every second meter along the blade length (y). Variations of strains across the width of the trailing-edge joint (z) are insignificant since the trailing-edge bond-line width is small compared with the distance from the elastic center of the blade to the trailing-edge location. The measured strains are post-processed through a "Rain-flow count algorithm" and sorted into bins dependent on the strain range magnitude [54]. The individual strain ranges are counted for each bin. The mechanical stress range, $\Delta\sigma_m$ in the adhesive is determined using Hooke's law and a plane strain assumption in the y-direction of the blade:

$$\Delta\sigma_m = \bar{E}_2 \Delta\epsilon_{yy} \tag{14}$$

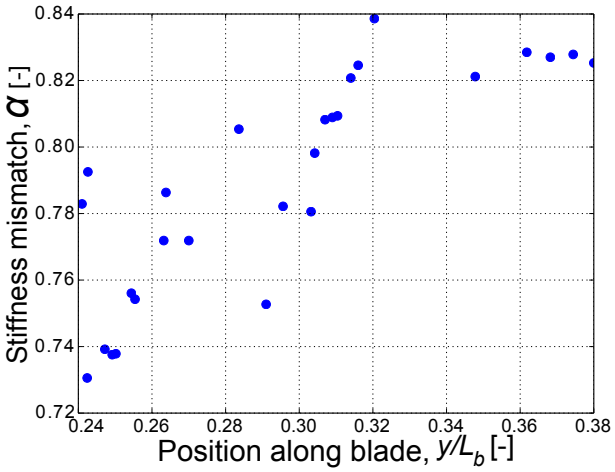

Figure 13: Laminate-adhesive stiffness mismatch determined at each tunneling crack position along blade length.

7. Experimental demonstration: DCB tests to determine Paris law for the adhesive

Two laminates of glass fiber reinforced polyester are cast using vacuum-assisted-resin-transfer-moulding (VARTM). The laminates are post cured and placed in a fixture where a vinylester adhesive is injected to bond the two laminates. Subsequently, the adhesive and laminate are post cured and cut into specimens. The side-grooves are CNC machined to meet the design in Figure 6. The adhesive and laminates are manufactured under laboratory conditions, but the exact properties are confidential.

An extensometer is attached to pins mounted on each beam as shown in Figure 6 to measure the extensometer opening. A servo-hydraulic cylinder applies the load, P to the wires that are attached to two arms on the sides of the DCB specimen hence a pure bending moment is applied cyclic [55]. The end of each cable is attached to a load cell that measures the load, P on each wire individually. Load frequency is set to 3 Hz and mode mixity to 0 degree using same arm length, L_r as shown in Figure 6. The R-ratio is varied between $R \approx 0.3$ and $R \approx 0.5$, which is also the R-ratio in the section of the blade joint when including residual stresses in the adhesive. Images are captured at adequate intervals following a log-scale. The crack length, a is measured on the images with help from a program implemented in Python [45, 46].

The DCB test is controlled by the extensometer opening, δ_{ext}. A fixed value of δ_{ext}^{min} and δ_{ext}^{max} is applied in the duration of the DCB test to maintain a constant $\Delta\delta_{ext}$. Thus, as the crack grows (increasing a), the measured moment range, ΔM decreases and a series of ΔK values can be computed

by equation 3, equation 4 and the first part of equation 12.

Before starting the cyclic test, a static pre-test is performed to create a sharp start-crack; a clamp is mounted on the specimen to constrain the crack from propagating too long and a static moment is applied monotonic until a sharp pre-crack is formed. The clamp is removed and the specimen is now prepared for the cyclic loaded tests. The subsequent cyclic loaded tests on the same specimen continues without further static tests.

The measured Paris laws for the adhesive are presented in Figure 14. The Paris law parameters are determined by a least square fit to the measured data points in the log-log space (ΔK, da/dN) on the form given by equation 5. The best fit in Figure 14 is used to determine parameters C and m. The upper- and lower fit gives the upper- and lower bounds for da/dN as shown in Figure 14 by the dashed and dotted lines, respectively.

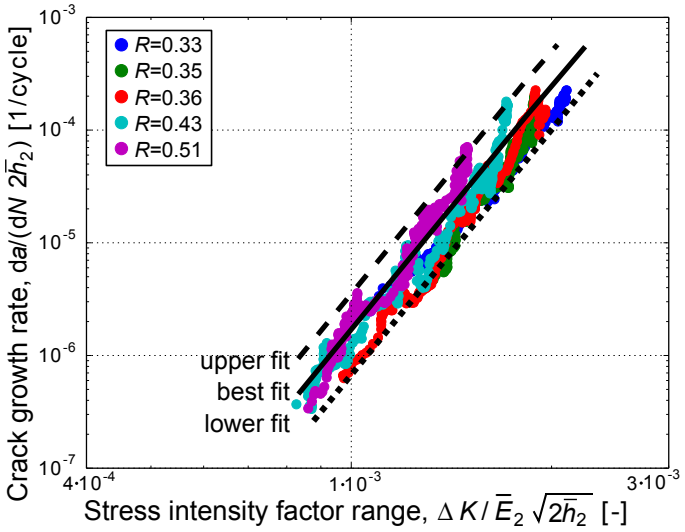

Figure 14: Cyclic loaded DCB test for adhesive including Paris law best fit. The axes are normalised by the average thickness of the adhesive measured on the blade section, $2\bar{h}_2$.

Some R-ratio effect is observed for the present adhesive [56], but this effect is small for the narrow band of R-ratio tested. It is decided to describe the fatigue crack growth rates by ΔK [51]. Different other approaches to describe fatigue crack growth are presented by Pascoe *et al.* [40], but it is out of the scope to investigate this further.

In terms of constitutive properties and fracture toughness the adhesive is comparable to epoxy resins in the published literature [56, 57, 58, 59], but the exact properties of the adhesive used in the present work is confidential. From the DCB test it is found that the crack growth rates of the adhesive is comparable to those of epoxy resins [56, 60, 61, 62, 63, 57, 58, 59, 64], especially those tested in [56, 57, 58, 59].

8. Experimental demonstration: Residual stress determination

Solidification of the vinylester adhesive during curing is an exo-thermal process. The adhesive heats up, shrinks and builds up tensile residual stresses caused by the constraining effect from the laminates since the adhesive cannot freely contract. The procedure to measure the residual stress using the bi-layer specimen is summarized:

- Manufacture sandwich specimen of two laminates bonded by adhesive.
- Peel-off one of the laminates, and measure curvature and geometry of the bi-layer specimen.
- Calculate residual stress through misfit stress from equation 7 and equation 8.

The adhesive and laminates are manufactured under laboratory conditions. Two laminates of uni-directional glass fiber reinforced polyester are cast using VARTM. The laminates are post cured and placed in a fixture where a foam spacer is placed along the edges to control the adhesive thickness to be 8 mm. One of the laminates are covered by a thin foil to create a weak adhesive/laminate interface. The adhesive is injected through a 10 mm hole in the middle of the plate and cured.

After post curing of the adhesive, the plate is cut into 13 specimens of length 500 mm and one of the laminates is peeled off using the thin foil since a weak plane enables separation. Removing one of the laminates cause the beam to bend due to tensile residual stresses in the adhesive. As indicated in Figure 8, the displacement of the top surface of the 13 beams is measured at 11 equal-spaced points using a dial gauge (type, Mitutoyo with ID-U1025). The laminate thickness, h_1^* and adhesive thickness, h_2^* of the bi-layer specimen are measured using a caliper in an optical microscope. Using equation 7, the average misfit stress, σ_T of the 13 curvature specimens is determined and presented non-dimensionally as misfit strain: $\epsilon_T = -0.00218 \pm 0.00013$ [44]. The misfit stress is used to determine the residual stress, σ_r at the various positions along the blade using equation 8.

The residual stress in the adhesive, for each combination of measured $\alpha(y,z)$ and $h_1(y,z)/h_2(y)$ at each tunneling crack location in the blade section, is presented in Figure 15. Here, the residual stress is normalised by the maximum mechanical stress, σ_m^{max} that is introduced by equation 14 and Figure 10. The trend is that closest to the blade root (small y) the residual stresses are highest, which is attributed h_1/h_2 increasing towards the

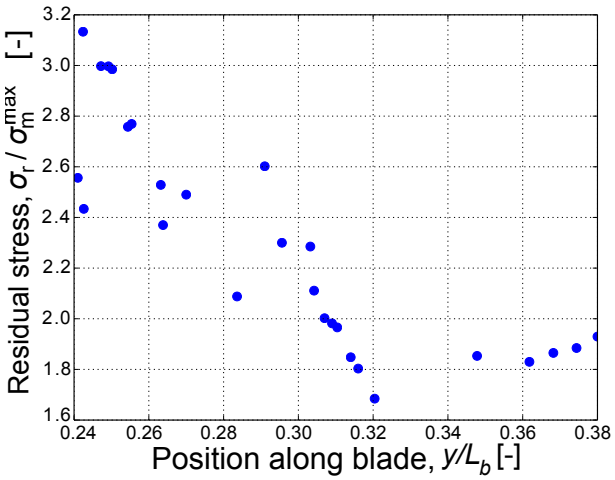

Figure 15: Normalised residual stress in the adhesive of the generic research blade at each tunneling crack position along the blade length.

blade root according to Figure 12. Note, σ_r is large in comparison with σ_m^{max}, especially closest to the blade root where the laminates are thick.

9. Experimental demonstration: Modelling of tunneling cracks

Curves for energy release rate, determined by the tunneling crack tool, are presented in Figure 16 including the corresponding "Experimental points" that are calculated based on data from the generic research blade test ($\alpha, \beta = \alpha/4, h_1/h_2$). The "Experimental points" are determined for each tunneling crack configuration ($z = a_i(N_i)$) according to Figure 3. Thus, α and h_1/h_2 are determined for each crack tip location and based on linear interpolation between the curves in Figure 16, the energy release rate can then be read off for each point.

Ply drops in both the y- and z-direction of the blade joint complicates the tunneling crack analysis. However, it is impractical to define a single finite

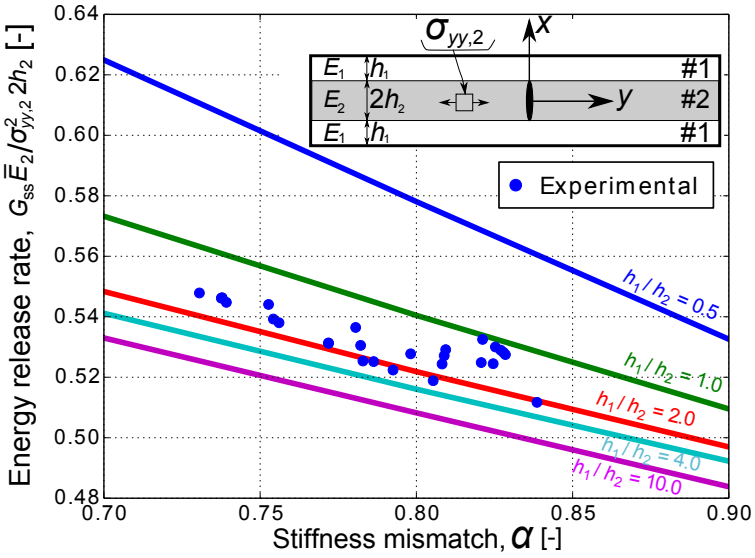

Figure 16: Results from tunneling crack bi-layer FE model with $\beta = \alpha/4$ (part of Figure 9). "Experimental points" are calculated for each tunneling crack configuration.

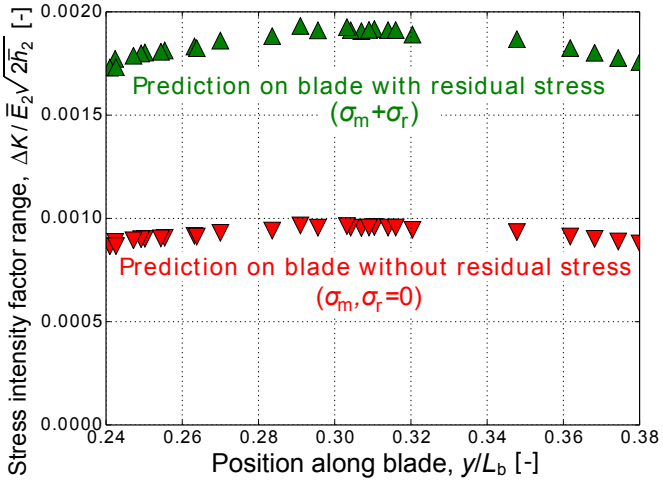

Figure 17: Prediction of ΔK based on data measured on the full scale blade joint at each tunneling crack position along blade length. ΔK is normalised by the plane strain modulus of the adhesive, $\bar{E}_2$ and by the average thickness of the adhesive measured on the generic blade section, $2\bar{h}_2$.

element model, e.g. with 5-12 different layers, for each crack observed and change the laminate stacking sequence for each crack analysed. Instead, the tunneling crack tool is made generic thus it can handle a series of isolated tunneling cracks and be applied to other blade joints as well. Therefore, the thickness ratio, h_1/h_2 and the average laminate stiffness are interpolated linearly in y- and z-directions based on the actual crack tip location in the joint.

ΔK is determined based on equation 12 and presented in Figure 17 with- and without including the magnitude of residual stress, σ_r. ΔK varies only moderately along y, being highest for $y/L_b \approx 0.30$. The inclusion of residual stresses doubles ΔK since the R-ratio changes from $R = -1$ to $R \approx 0.4$, see Figure 10 and Figure 17.

10. Experimental demonstration: Inspection of cracks in full scale blade test

The crack length, measured by a caliper on the trailing-edge joint, for each tunneling crack is presented in Figure 18 and Figure 19 for the number of cycles where the test of the generic research blade is paused for inspection. The a-N measurements in Figure 19 are fitted with a straight line for each crack and the slopes (da/dN) are presented in Figure 20.

11. Experimental demonstration: Prediction of fatigue crack growth rates on the blade joint

Tunneling crack growth rates are predicted using the approach in Figure 4 and presented in Figure 20 together with the measured crack growth rates

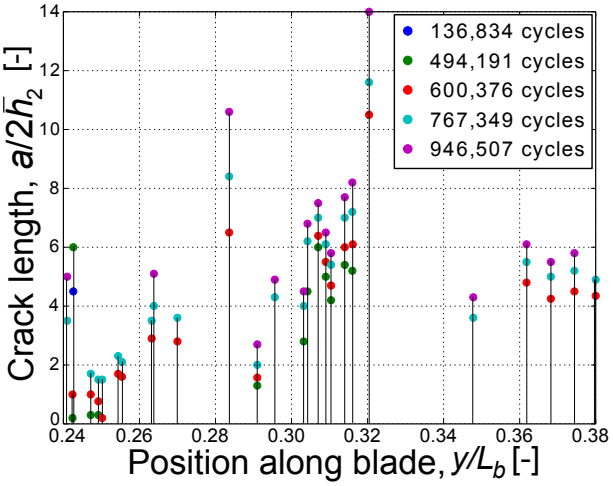

Figure 18: Normalised crack length, $a/2\bar{h}_2$ measured along blade length, y.

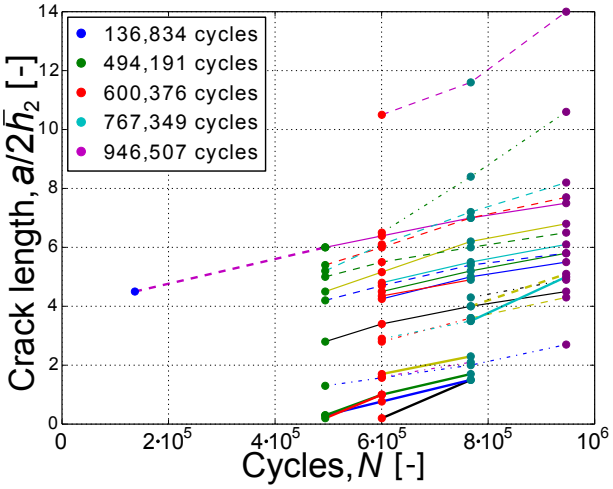

Figure 19: Normalised crack length, $a/2\bar{h}_2$ for cycles, N measured on blade.

on the trailing-edge joint from the test of the generic research blade. The predicted crack growth rates varies relative to crack location (y, z) due to the variations in; $\alpha, h_1/h_2, \Delta\sigma_m$ and σ_r. However, this variation is small meaning that the state of each individual tunneling crack is similar. Also, the crack growth rates, measured individually for each tunneling crack, in the blade are similar, which can be explained by the small variations in load levels and geometry along the blade section (AoI).

The crack growth rates predicted on the blade joint falls above and below the crack growth rates measured on the blade. The crack growth rates predicted without including residual stress are closest to the crack growth rates measured on the blade.

12. Discussion

The crack-to-crack variation for the da/dN predictions in Figure 20 is small since the variation of the mechanical stress and the energy release rate for each crack in Figure 16 is small: $\left(\bar{E}_2 G_{ss}\right) / \left(\sigma^2_{yy,2} 2h_2\right) \approx 0.53 \pm 0.02$. This suggests that a future approximate approach is to use; $\left(\bar{E}_2 G_{ss}\right) / \left(\sigma^2_{yy,2} 2h_2\right) \approx 0.5$ for all tunneling cracks in the blade, which will simplify the modelling significantly. The effect of misfit stress, σ_T is significant since the inclusion of residual stress doubles ΔK as shown in Figure 17.

The DCB- and bi-layer test specimens are manufactured under process conditions in the laboratory that are different from the manufacturing of the generic research blade. This difference in manufacturing process is an uncertainty in the cyclic crack growth prediction on the blade joint.

Another explanation for the deviation between blade prediction and ac-

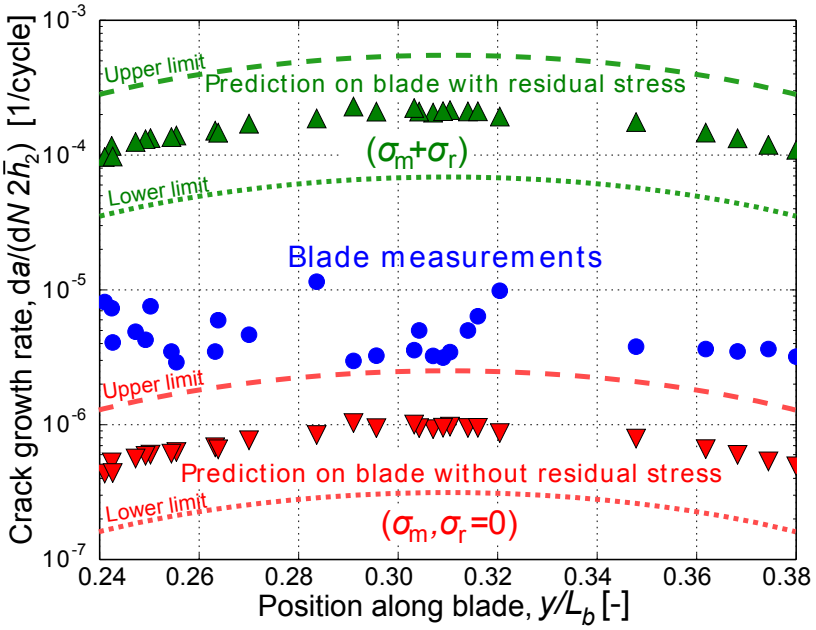

Figure 20: Comparison of predicted crack growth rates (triangles) with the crack growth rates measured (circles) on the full scale blade joint. Dashed lines indicate the upper limits and dotted lines the lower limits for the uncertainty of the predictions based on Figure 14 since the main uncertainty comes from the measured Paris law for the adhesive. Note, da/dN are normalised by the average thickness of the adhesive measured on the blade section, $2\bar{h}_2$.

tual blade measurements could be time dependency of the adhesive (stress relaxation, creep, visco-elasticity), which is unknown. The time scale for the laboratory tests of the bi-layer specimens is in the order of a few weeks whereas the generic full scale research blade is tested over several months. The time scale may influence the level of residual stress, which again affects the R-ratio, ΔK and finally the da/dN prediction. The effect of stress relaxation in the adhesive in the duration of the full scale blade test is unknown. The crack growth rates determined for the tunneling cracks including residual stress must therefore be seen as an upper bound. On the other hand, the crack growth rates predicted without residual stress should be seen as a lower bound if all residual stresses are relaxed during the fatigue test.

Multiple cracking of the adhesive is an other stress relaxing process especially if the crack spacing is small. The tunneling cracks can with good accuracy be modelled without including interaction between the cracks since the crack spacing and the stiffness of the substrates are large ($0.72 \leq \alpha \leq 0.84$) [23, 24]. Crack interaction is only relevant for very compliant substrates [24]. The 27 cracks distributed over the length of the blade section ($0.24 \leq y/L_b \leq 0.38$) gives a normalised inverse average crack spacing of $2\bar{h}_2/\bar{L}_c = 0.038$, where $\bar{L}_c$ is the average crack spacing. This number (0.038) and stiffness mismatch ($0.72 \leq \alpha \leq 0.84$), according to Fig. 5 in Ho and Suo [24], means that crack interaction is insignificant for the present case.

12.1. Tunneling crack model assumption

It is appropriate to investigate whether the approach of averaging the stiffness has a significant effect on the tunneling crack energy release rate since the layers closest to the adhesive is a few number of biaxial layers that

are more compliant than the uni-directional layers. The layer closest to the adhesive, called buffer-layer, is the most important layer since it is well known that the stiffness and thickness of this layer gives the primary constraining effect of the tunneling crack [31].

The effect of buffer layer is tested using a tri-layer tunneling crack FE model. A biaxial layer is added to the existing uni-directional laminate, which decreases the overall average stiffness ratio to $\alpha_{ave} = 0.80$ from $\alpha_{UD} = 0.85$ since the added biax-to-adhesive stiffness ratio is $\alpha_{biax} = 0.54$.

Modelling the problem using the average stiffness instead of the actual stiffnesses of the individual layers gave an energy release rate that was approx. 4 % higher, which is acceptable for the present application. It is concluded that the energy release rate is relatively insensitive to specific layup configurations for the present case since the uni-directional layers are relatively stiff. This is also illustrated by the small variations for the experimental data in Figure 16. Thus, from a practical point of modelling the use of average stiffness is reasonably.

12.2. Tunneling cracks in full scale blade section

In a full scale blade test many factors play a role on the state of the tunneling crack mechanism. One important factor is the assumption that loading is pure tensile in the trailing-edge, see ϵ_{yy} in Figure 1. Thus, the cracks in the adhesive are assumed to propagate under pure mode-I conditions, which is reasonably to assume in a homogeneous material. The mode-I dominance is supported by the image in Figure 2 of the tunneling crack that is perpendicular to the laminate. However, it is not measured whether the trailing-edge joint is loaded in shear as well e.g. caused by large rotations/displacements

("pumping effect") of the trailing-edge balsa panel [65]. Measuring mixed mode effects on the tunneling cracks may require additional strain gauges mounted during the blade test. Models for shear loaded tunneling cracks (oblique cracks) are available in the literature [24, 66].

The measured crack lengths vary significantly along the length of the blade. The two cracks with the largest crack growth rates are found in the highest loaded region. The different crack lengths measured may be a result of the different times/cycles to crack initiation along the blade length (y). The initiation is governed by pre-exising defects, but the exact time (load cycle number) of crack initiation is unknown. For the shortest cracks measured, see Figure 19, the effect of crack length on energy release rate could be accounted for using 3D FE simulations [34, 26]. However, for large elastic mismatch this transient effect is small [35].

12.3. Proposed extensions of the present work

The effect of residual stress on R-ratio and Paris law parameters is not well documented in the literature for polymeric materials. Further work for the adhesive loaded cyclic by different residual stress magnitudes and R-ratio including different models for fitting the crack growth rates is proposed as a future study [53, 40].

The tunneling crack tool can be extended to account for delamination during the tunneling process [67, 25, 19] or expanded to handle gel coat channeling cracks in wind turbine blade surfaces during cyclic loading [68]. It may also be applied to tunneling cracks in grid-scored balsa/foam panels used in wind turbine blades, where the crack tunnels through the resin filled grid-scores [65]. The generic tool is demonstrated on a trailing-edge adhesive

joint, but could be applied to the leading-edge- or web joints as well.

13. Conclusion

The parameters for the mode-I Paris law for the adhesive, measured by the cyclic moment-loaded DCB specimen, was found to be comparable to those published for epoxy resin systems. The energy release rate of a tunneling crack is relatively unaffected by substrate thickness when the substrate stiffness is large. Furthermore, the energy release rate of a tunneling crack is relatively insensitive to specific layup near the adhesive since the stiffness of the primary uni-directional laminate is high.

The crack growth rates predicted for tunneling cracks in a wind turbine blade trailing-edge joint were found to agree well with the crack growth rates measured on a full scale test blade. This suggests that the tunneling crack tool can predict crack growth rates for tunneling cracks in a wind turbine blade trailing-edge joint within acceptable accuracy.

Acknowledgements

Acknowledgements to the LM Wind Power lab for help manufacturing the test specimens used for the bi-layer tests and the cyclic DCB tests. Thanks to Jan Sjølin at DTU Wind Energy for help testing the DCB specimens. Also, thanks to the test engineers and -technicians at LM Wind Power for help with the measurements during the full scale blade test. This research was supported by the Danish Centre for Composite Structure and Materials for Wind Turbines (DCCSM), grant no. 0603-00301B, from Innovation Fund

Denmark. This research was also supported by grant no. 4135-00010B from Innovation Fund Denmark.

References

[1] DNV GL, DNVGL-ST-0376 Standard - Rotor blades for wind turbines, Tech. Rep. December, DNV GL (2015).

[2] F. M. Jensen, B. G. Falzon, J. Ankersen, H. Stang, Structural testing and numerical simulation of a 34 m composite wind turbine blade, Composite Structures 76 (1-2) (2006) 52–61. doi:10.1016/j.compstruct.2006.06.008.

[3] L. C. T. Overgaard, E. Lund, O. T. Thomsen, Structural collapse of a wind turbine blade. Part A: Static test and equivalent single layered models, Composites Part A: Applied Science and Manufacturing 41 (2) (2010) 257–270. doi:10.1016/j.compositesa.2009.10.011.
URL http://dx.doi.org/10.1016/j.compositesa.2009.10.011

[4] J. Yang, C. Peng, J. Xiao, J. Zeng, S. Xing, J. Jin, H. Deng, Structural investigation of composite wind turbine blade considering structural collapse in full-scale static tests, Composite Structures 97 (2013) 15–29. doi:10.1016/j.compstruct.2012.10.055.
URL http://dx.doi.org/10.1016/j.compstruct.2012.10.055

[5] H. F. Zhou, H. Y. Dou, L. Z. Qin, Y. Chen, Y. Q. Ni, J. M. Ko, A review of full-scale structural testing of wind turbine blades, Renewable and Sustainable Energy Reviews 33 (2014) 177–187. doi:10.1016/j.rser.2014.01.087.

[6] X. Chen, W. Zhao, X. L. Zhao, J. Z. Xu, Preliminary failure investigation of a 52.3m glass/epoxy composite wind turbine blade, Engineering Failure Analysis 44 (11) (2014) 345–350. doi:10.1016/j.engfailanal.2014.05.024.
URL http://dx.doi.org/10.1016/j.engfailanal.2014.05.024

[7] X. Chen, X. Zhao, X. Jianzhong, Revisiting the structural collapse of a 52.3 m composite wind turbine blade in a full-scale bending test, Wind Energy 20 (6) (2017) 1111–1127.

[8] C. Kong, T. Kim, D. Han, Y. Sugiyama, Investigation of fatigue life for a medium scale composite wind turbine blade, International Journal of Fatigue 28 (10 SPEC. ISS.) (2006) 1382–1388. doi:10.1016/j.ijfatigue.2006.02.034.

[9] X. Liu, Dynamic Response Analysis of the Blade of Horizontal Axis Wind Turbines, Journal of Mechanical Engineering 46 (12) (2010) 128. doi:10.3901/JME.2010.12.128.

[10] K. K. Jin, M. Ghulam, J. H. Kim, S. K. Ha, B. Lopez, A. Gorostidi, International Conferences on Composite Materials, in: Life Prediction of Wind Turbine Blades, 2009, pp. 1–12.

[11] D. Salimi-Majd, V. Azimzadeh, B. Mohammadi, Loading Analysis of Composite Wind Turbine Blade for Fatigue Life Prediction of Adhesively Bonded Root Joint, Applied Composite Materials 22 (3) (2014) 269–287. doi:10.1007/s10443-014-9405-4.

[12] S. Ataya, M. M. Ahmed, Damages of wind turbine blade trailing edge: Forms, location, and root causes, Engineering Failure Analysis 35 (2013) 480–488. doi:10.1016/j.engfailanal.2013.05.011.
URL http://linkinghub.elsevier.com/retrieve/pii/S1350630713001878

[13] K. W. Garret, J. E. Bailey, Multiple transverse fracture in 90 cross-ply laminates of a glass fibre-reinforced polyester, Journal of Materials Science 12 (1977) 157–168.

[14] Y. Korczynskyj, J. G. Morley, Constrained cracking in cross-ply laminates, Journal of Materials Science 16 (1981) 1785–1795.

[15] J. A. Nairn, The Strain Energy Release Rate of Composite Microcracking: A Variational Approach, Journal of Composite Materials 23 (11) (1989) 1106–1129. doi:10.1177/002199838902301102.
URL http://jcm.sagepub.com/cgi/doi/10.1177/002199838902301102

[16] J. Varna, L. Berglund, Multiple transverse cracking and stiffness reduction in cross-ply laminates, Journal of Composites Technology and Research 13 (2) (1991) 97–106. doi:10.1520/CTR10213J.
URL http://www.scopus.com/inward/record.url?eid=2-s2.0-0026171255{\&}partnerID=tZOtx3y1

[17] R. Talreja, S. Yalvac, L. D. Yats, D. G. Wetters, Transverse cracking and stiffness reduction in cross ply laminates of different matrix toughness, Journal of Composite Materials 26 (11) (1992) 1644–1663.

[18] J.-M. Berthelot, Transverse cracking and delamination in cross-ply glass-fiber and carbon-fiber reinforced plastic laminates: Static and fatigue loading, Applied Mechanics Reviews 56 (1) (2003) 111–147. doi:10.1115/1.1519557.
URL http://dx.doi.org/10.1115/1.1519557

[19] A. S. Suiker, N. a. Fleck, Modelling of fatigue crack tunneling and delamination in layered composites, Composites Part A: Applied Science and Manufacturing 37 (10) (2006) 1722–1733. doi:10.1016/j.compositesa.2005.09.006.
URL http://linkinghub.elsevier.com/retrieve/pii/S1359835X05003751

[20] J. Varna, Modelling mechanical performance of damaged laminates, Journal of Composite Materials 47 (20-21) (2012) 2443–2474. doi:10.1177/0021998312469241.
URL http://jcm.sagepub.com/cgi/doi/10.1177/0021998312469241

[21] M. Quaresimin, A damage-based approach for the fatigue design of composite structures, IOP Conference Series: Materials Science and Engineering 139 (2016) 012006. doi:10.1088/1757-899X/139/1/012006.
URL http://stacks.iop.org/1757-899X/139/i=1/a=012006?key=crossref.98da71596a191dfd02cdc2b30cfdd12d

[22] Z. Suo, Failure of brittle adhesive joints, Appl. Mech 43 (5) (1990) 275–279.

[23] J. W. Hutchinson, Z. Suo, Mixed Mode Cracking in Layered Materials, Advances in Applied Mechanics 29 (1992) 63–191.

[24] S. Ho, Z. Suo, Tunneling cracks in constrained layers, Mem. ASME 60 (1993) 890–894.

[25] A. S. Suiker, N. a. Fleck, Crack tunneling and plane-strain delamination in layered solids, International Journal of Fracture 125 (1) (2004) 1–32. doi:10.1023/B:FRAC.0000021064.52949.e2.
URL http://link.springer.com/10.1023/B:FRAC.0000021064.52949.e2

[26] J. Andersons, P. H. M. Timmermans, J. Modniks, Mechanics of tunnelling cracks in trilayer elastic materials in tension, International Journal of Fracture 148 (3) (2008) 233–241. doi:10.1007/s10704-008-9197-3.
URL http://link.springer.com/10.1007/s10704-008-9197-3

[27] H. Beom, X. Zhuo, C. Cui, Tunneling cracks in the adhesive layer of an orthotropic sandwich structure, International Journal of Engineering Science 63 (2013) 40–51. doi:10.1016/j.ijengsci.2012.11.001.
URL http://linkinghub.elsevier.com/retrieve/pii/S0020722512001978

[28] M. Thouless, Crack Spacing in Brittle Films on Elastic Substrates, J. Am. Ceram. Soc. 73 (7) (1990) 2144–46.

[29] J. Beuth, Cracking of thin bonded films in residual tension, Int. J. Solid Structures 2 (13) (1992) 1657–1675.

[30] J. J. Vlassak, Channel cracking in thin films on substrates of finite thickness, International Journal of Fracture 119/120 (1979) (2003) 299–323. doi:10.1023/A:1024962825938.

[31] T. Y. Tsui, A. J. McKerrow, J. J. Vlassak, Constraint Effects on Thin Film Channel Cracking Behavior, Journal of Materials Research 20 (2005) 2266–2273. doi:10.1557/jmr.2005.0317.

[32] H. G. Beom, H. S. Jang, Effect of elastic constants on crack channeling in a thin film bonded to an orthotropic substrate, Archive of Applied Mechanics 83 (11) (2013) 1577–1589. doi:10.1007/s00419-013-0766-1.
URL http://link.springer.com/10.1007/s00419-013-0766-1

[33] T. Nakamura, S. M. Kamath, Three-dimensional effects in thin film fracture mechanics, Mechanics of Materials 13 (1) (1992) 67–77. doi:10.1016/0167-6636(92)90037-E.
URL http://linkinghub.elsevier.com/retrieve/pii/016766369290037E

[34] Z. C. Xia, J. W. Hutchinson, Crack patterns in thin films, Journal of the Mechanics and Physics of Solids 48 (2000) 1107–1131.

[35] J. M. Ambrico, M. R. Begley, The role of initial flaw size, elastic compliance and plasticity in channel cracking of thin films, Thin Solid Films 419 (2002) 144–153. doi:10.1016/S0040-6090(02)00718-6.

[36] J. Dundurs, Edge-Bonded Dissimilar Orthogonal Elastic Wedges Under Normal and Shear Loading, Journal of Applied Mechanics 36 (3) (1969) 650–652.

[37] J. Parmigiani, M. Thouless, The effects of cohesive strength and toughness on mixed-mode delamination of beam-like geometries, Engineering Fracture Mechanics 74 (17) (2007) 2675–2699. doi:10.1016/j.engfracmech.2007.02.005.
URL http://linkinghub.elsevier.com/retrieve/pii/S0013794407000677

[38] J. Dundurs, Effect of elastic constants on stress in a composite under plane deformation, Journal of Composite Materials 1 (1967) 310–322. doi:10.1177/002199836700100306.

[39] P. Paris, F. Erdogan, Closure to Discussions of A Critical Analysis of Crack Propagation Laws', Journal of Basic Engineering 85 (4) (1963) 534. doi:10.1115/1.3656903.
URL http://fluidsengineering.asmedigitalcollection.asme.org/article.aspx?articleid=1431540

[40] J. A. Pascoe, R. C. Alderliesten, R. Benedictus, Methods for the prediction of fatigue delamination growth in composites and adhesive bonds - A critical review, Engineering Fracture Mechanics 112-113 (2013) 72–96. doi:10.1016/j.engfracmech.2013.10.003.
URL http://dx.doi.org/10.1016/j.engfracmech.2013.10.003

[41] P. J. Withers, H. K. D. H. Bhadeshia, Residual stress part 1 - Measurement techniques, Materials Science and Technology 17 (4) (2001) 355–365. doi:10.1179/026708301101509980.
URL http://www.scopus.com/inward/record.url?

eid=2-s2.0-0034923107{\&}partnerID=40{\&}md5=
814ec6ced08c67e3e5ac9d2ebc9027b2

[42] P. Withers, H. Bhadeshia, Residual stress. Part 2 Nature and origins, Materials Science and Technology 17 (4) (2001) 366–375. doi:10.1179/026708301101510087.

[43] P. J. Withers, M. Turski, L. Edwards, P. J. Bouchard, D. J. Buttle, Recent advances in residual stress measurement, International Journal of Pressure Vessels and Piping 85 (3) (2008) 118–127. doi:10.1016/j.ijpvp.2007.10.007.

[44] A. G. Evans, J. W. Hutchinson, The Thermomechanical Integrity of Thin Films and Multilayers, Acta metall. mater. 43 (7) (1995) 2507–2530.

[45] H. P. Langtangen, Python Scripting for Computational Science, 2nd Edition, Springer, 2008.

[46] H. P. Langtangen, A Primer on Scientific Programming with Python, 4th Edition, Springer, 2014.

[47] B. F. Sørensen, K. Jørgensen, T. K. Jacobsen, R. C. Østergaard, A general mixed mode fracture mechanics test specimen : The DCB-specimen loaded with uneven bending moments, Int J Fract 141 (2006) 163–176.

[48] B. F. Sørensen, L. P. Mikkelsen, R. C. Østergaard, S. Goutianos, From interface laws to composite behaviour, in: Interface Design of Polymer Matrix Composites Mechanics, Chemistry, Modelling and Manufacturing, Risø, 2007, pp. 55–74.

[49] R. M. Jones, Mechanics of composite materials, 2nd Edition, Taylor and Francis, 1999.

[50] G. Irwin, D. Washington, Analysis of Stresses and Strains Near the End of a Crack Traversing a Plate, Journal of Applied Mechanics 24 (1957) 361–364.

[51] C. Rans, R. Alderliesten, R. Benedictus, Misinterpreting the results: How similitude can improve our understanding of fatigue delamination growth, Composites Science and Technology 71 (2) (2011) 230–238. doi:10.1016/j.compscitech.2010.11.010.

[52] J. A. Nairn, P. Zoller, The Development of Residual Thermal Stresses in Amorphous and Semicrystalline Thermoplastic Matrix Composites, ASTM STP 937 (1987) 328–341.

[53] J. A. Nairn, Energy release rate analysis for adhesive and laminate double cantilever beam specimens emphasizing the effect of residual stresses, International Journal of Adhesion and Adhesives 20 (1999) 59–70.

[54] R. Stephens, A. Fatemi, R. R. Stephens, H. Fuchs, Metal fatigue in engineering, 2nd Edition, John Wiley & Sons, Inc, 2001.

[55] J. W. Holmes, L. Liu, B. F. Sorensen, S. Wahlgren, Experimental approach for mixed-mode fatigue delamination crack growth with large-scale bridging in polymer composites, Journal of Composite Materials 48 (25) (2014) 3111–3128. doi:10.1177/0021998313507613.

[56] C. Kanchanomai, A. Thammaruechuc, Effects of stress ratio on fatigue crack growth of thermoset epoxy resin, Po-

lymer Degradation and Stability 94 (10) (2009) 1772–1778. doi:10.1016/j.polymdegradstab.2009.06.012.
URL http://dx.doi.org/10.1016/j.polymdegradstab.2009.06.012

[57] E. N. Brown, S. R. White, N. R. Sottos, Fatigue crack propagation in microcapsule-toughened epoxy, Journal of Materials Science 41 (19) (2006) 6266–6273. doi:10.1007/s10853-006-0512-y.

[58] A. Boonyapookana, K. Nagata, Y. Mutoh, Fatigue crack growth behavior of silica particulate reinforced epoxy resin composite, Composites Science and Technology 71 (8) (2011) 1124–1131. doi:10.1016/j.compscitech.2011.02.015.
URL http://dx.doi.org/10.1016/j.compscitech.2011.02.015

[59] M. H. Kothmann, R. Zeiler, A. Rios De Anda, A. Brückner, V. Altstädt, Fatigue crack propagation behaviour of epoxy resins modified with silica-nanoparticles, Polymer (United Kingdom) 60 (2015) 157–163. doi:10.1016/j.polymer.2015.01.036.

[60] S. A. Sutton, Fatigue crack propagation in an epoxy polymer, Engineering Fracture Mechanics 6 (3) (1974) 587–595. doi:10.1016/0013-7944(74)90015-0.

[61] R. A. Gledhill, A. J. Kinloch, S. Yamini, R. J. Young, Relationship between mechanical properties of and crack progogation in epoxy resin adhesives, Polymer 19 (5) (1978) 574–582. doi:10.1016/0032-3861(78)90285-9.

[62] M. Dessureautt, J. Spelt, Observations of fatigue crack initiation and propagation in an epoxy adhesive, International Journal of Adhesion and Adhesives 17 (3) (1997) 183–195. doi:10.1016/S0143-7496(96)00044-9. URL http://www.sciencedirect.com/science/article/pii/S0143749696000449

[63] J. Du, M. D. Thouless, A. F. Yee, Effects of rate on crack growth in a rubber-modified epoxy, Acta Materialia 48 (13) (2000) 3581–3592. doi:10.1016/S1359-6454(00)00110-5.

[64] A. Boonyapookana, A. Saengsai, S. Surapunt, K. Nagata, Y. Mutoh, Time dependent fatigue crack growth behavior of silica particle reinforced epoxy resin composite, International Journal of Fatigue 87 (2016) 288–293. doi:10.1016/j.ijfatigue.2016.02.013.

[65] S. Laustsen, E. Lund, L. Kühlmeier, O. T. Thomsen, Development of a high-fidelity experimental substructure test rig for grid-scored sandwich panels in wind turbine blades, Strain 50 (2) (2014) 111–131. doi:10.1111/str.12072.

[66] Z. Xia, J. W. Hutchinson, Mode II Fracture Toughness of a Brittle Adhesive Layer.pdf, Int. J. Solids Structures 31 (8) (1994) 1133–1148.

[67] K. Chan, M. He, J. Hutchinson, Cracking and stress redistribution in ceramic layered composites, Materials Science and Engineering A167 (1993) 57–64.

[68] H. Zhang, J. Jackman, Feasibility of Automatic Detection of Surface

Cracks in Wind Turbine Blades, Wind Engineering 38 (6) (2014) 575–586.

APPENDED PAPER P4

Design of four-point SENB specimens with stable crack growth

Jeppe B. Jørgensen, Casper Kildegaard and Bent F. Sørensen
Engineering Fracture Mechanics
Submitted, 2017

Design of four-point SENB specimens with stable crack growth

Jeppe B. Jørgensen[a,b,*], Casper Kildegaard[a], Bent F. Sørensen[b]

[a] *LM Wind Power, Østre Alle 1, 6640 Lunderskov, Denmark.*
[b] *The Technical University of Denmark, Dept. of Wind Energy, Frederiksborgvej 399, 4000 Roskilde, Denmark.*

Abstract

A four-point single-edge-notch-beam (SENB) test specimen loaded in displacement control (fixed grip) is proposed for studying crack deflection at bi-material interfaces. In order to ensure stable crack growth, a novel analytical model of the four-point SENB specimen in fixed grip is derived and compared with numerical models. Model results show that the specimen should be short and thick, and the start-crack length should be deep for the crack to propagate stable towards the bi-material interface. Observations from experimental tests of four-point SENB specimens with different start-crack lengths, confirmed that the crack grows stable if the start-crack length is deep and unstable if not.

Keywords: Stable crack growth, Bonded joints, Brittle fracture, Adhesive, Finite element analysis

Nomenclature

a	actual crack length
a_0	start-crack length
A	area of cracked surface
b	adhesive layer thickness/beam thickness
B	horizontal distance between load- and support point
c	substrate thickness
C	compliance of beam
D	length of debond crack at interface
E_1, E_2	Young's modulus (substrate, adhesive)
$\bar{E}$	plane strain Young's modulus

*Corresponding author
Email address: jbj@lmwindpower.com (Jeppe B. Jørgensen)

f	non-dimensional function for interface stress
F	Tada F-function
F_δ	F-function for bi-material (fixed grip)
G_I	mode-I energy release rate
G_{IC}	critical energy release rate
G_R	resistance curve (rising critical energy release rate)
h	horizontal distance between crack and load point
I	area moment of inertia per unit width
K_I	mode-I stress intensity factor
K_{IC}	mode-I critical stress intensity factor
L	loading parameter
M	bending moment per unit width
P	force per width
r_p	radius of plastic zone size
S	Tada S-function
t	time
T	shear force
U	strain energy
U_1	strain energy of part 1 of the beam
U_2	strain energy of part 2 of the beam
U_P	strain energy caused by force
U_M	strain energy caused by bending moment
U_T	strain energy caused by shear force
U_{crack}	strain energy caused by crack
$U_{no,crack}$	strain energy in beam without crack
U_t	total strain energy
V	work done by external loads
V_t	total work done by external loads

w	width of beam
x, y, z	coordinates
α	first Dundurs' parameter
β	second Dundurs' parameter
γ	shear strain
δ	displacement
ϵ	normal strain
θ	rotation angle
θ_{crack}	rotation angle caused by introduction of crack
$\theta_{no,crack}$	rotation angle for beam without crack
θ_t	total rotation angle
κ	curvature of beam
λ	first orthotropy parameter
μ	shear modulus
ν	Poisson's ratio
$\bar{\nu}$	modified Poisson's ratio
ρ	second orthotropy parameter
σ	normal stress
σ_{xx}	maximum normal stress
$\sigma_{yy,i}$	normal stress across interface
$\hat{\sigma}_i$	cohesive strength of interface
σ_{YS}	yield stress
$\hat{\sigma}_i$	cohesive strength of the interface
τ	shear stress
Φ	strain energy density
Ω	distance to neutral axis from the bottom of the beam
FE	finite element
LEFM	linear-elastic fracture mechanics

SENB single-edge-notch-beam

1. Introduction

Crack deflection at bi-material interfaces is one of the important cracking phenomena for adhesive joints in large composite structures e.g. wind turbine blades. The bond-line contains defects from which cracks can initiate and turn into transverse cracks in the adhesive. Cracks in the trailing-edge joint, including transverse cracks, are observed in full scale blades in operation as demonstrated by Ataya *et al*. [1]. After a small crack has formed in the adhesive from a pre-existing defect, the typical cracking sequence is as shown in Figure 1.

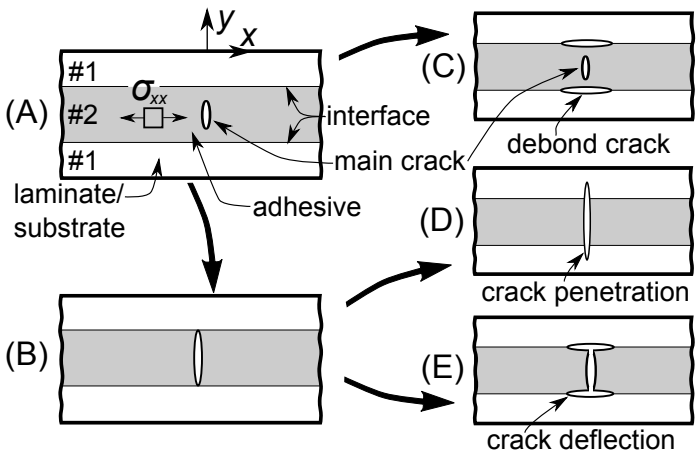

Figure 1: Possible cracking sequences for an adhesive joint loaded in tension. The main crack in the adhesive grows ideally orthogonal towards the adhesive-substrate interface (A). The crack might reach the interface (B) or initiate a new crack at the adhesive-substrate interface (C). If the crack reach the interface it can stop (B), or penetrate into the substrate (D) or deflect along the adhesive-substrate interface (E).

Historically, the cracking mechanisms in Figure 1 have been addressed using various approaches. Models typically describe the problem where the main crack has reached the interface (Figure 1 (B)) and the subsequent crack deflection/penetration process (Figure 1 (D) or Figure 1 (E)). Modelling the deflection of a crack meeting an interface were, at first, based on either stress criteria [2, 3] or energy criteria [4, 5, 6, 7, 8]. The stress criteria and energy based approach can be unified using a cohesive law, which is a traction-separation law that encompasses a peak stress (strength) and work or separation (energy), typically combined with cohesive zone modelling in finite element (FE) simulations [9, 10, 11, 12, 13, 14]. The parameters for the cohesive law can e.g. be measured by the J-integral approach [15, 16]. However, accurate experimental determination of peak stress, $\hat{\sigma}_i$, (cohesive strength)

for bi-material interfaces is challenging, especially for brittle material interfaces with small separations [17], and therefore novel methodologies are desired.

The problem of interface crack initiation in Figure 1 (C) was addressed using modelling based on stress by Cook and Gordon [2]. However, rigorous experimental tests of crack deflection at interfaces, where the crack deflection process is clearly documented are limited [18] since it is difficult to design an experiment where the crack propagates stable towards a bi-material interface. A few have attempted but with limited success [19, 20].

Zhang and Lewandowski [20] tested bi-material four-point single-edge-notch-beam (SENB) specimens with different interfaces. Unfortunately, crack propagation was unstable such that the crack deflection could only be assessed by visual inspection of the cracked specimens after testing i.e. ex-situ. For the cracking mechanism in Figure 1 (C), the bi-material four-point SENB specimen can also be used to measure the cohesive strength of the interface, $\hat{\sigma}_i$, using a recently developed approach [21]. For this purpose and for the study of crack deflection at interfaces, it is advantageous that the crack grows stable in mode-I towards the interface so that the crack deflection process can be observed in-situ e.g. captured on images by a relatively low camera frame rate during loading. Therefore, in the present paper the bi-material four-point SENB specimen is modeled to design an experimental test with stable crack growth.

The parameters defining the four-point SENB test specimen geometry and boundary conditions are presented in Figure 2. The start-crack length is denoted a_0 whereas a is the actual crack length. h is the distance between the crack and the load point, and B is the distance between the load- and support points. The depth in z-direction is denoted w. P is the total applied force and δ is the load-point displacement. θ is the resulting rotation for an applied bending moment, M. The primary parameters can be written in non-dimensional form as: a/b, h/b, and B/b. The dimensionless substrate thickness for the bi-material specimen in Figure 2 (C) is denoted c/b.

In absence of elastic mismatch, the bi-material four-point SENB specimen (Figure 2 (B)) reduces to the homogenous four-point SENB specimen (Figure 2 (A)). The homogenous four-point SENB specimen shown in Figure 2 (A) is a commonly used test specimen during the last five decades e.g. for measuring fracture toughness, but also for other purposes with varying geometry, material and setup [22, 23, 24, 25, 26, 27, 28, 29, 30, 12, 31, 32]. Four-point SENB specimen geometries, found in the literature [15, 27, 33, 20, 30, 12], vary significant from test to test:

- $0.12 < a_0/b < 0.80, \quad 0.60 < B/b < 6.90, \quad 0.50 < h/b < 5.10, \quad 0.22 < w/b < 9.66$

Justification for the choice of a_0/b, B/b, h/b, and w/b are absent in the papers. Crack growth stability were tested experimentally by Tandon *et al.* [33] for three different material systems using homogenous four-point SENB specimens. One of the conclusions was that a smaller h improved the stability of the

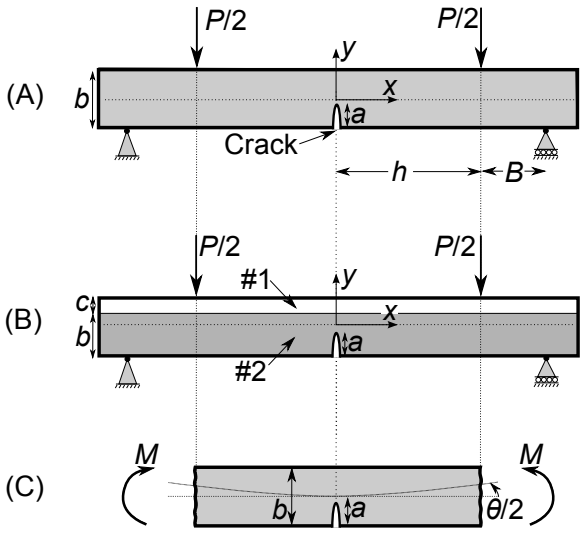

Figure 2: (A) Homogeneous four-point SENB specimen. (B) Bi-material four-point SENB specimen. (C) Homogenous pure bending specimen.

four-point SENB test since the amount of elastic energy in the beam was reduced [33]. The effect of B was not investigated.

Generally, stable crack growth is desirable e.g. when measuring R-curves [34], for tests where a crack initiates from a notch [20, 35] or for tests with sub-critical crack growth [36, 37]. Furthermore, when measuring fracture toughness, stable crack growth enables measuring several values instead of a single one. Often a crack develops from a notch and "pops-in" meaning that initiation of crack growth starts at a higher energy release rate because the starter crack does not have a sufficiently sharp tip leading to an abrupt advance of the crack front and thus an incorrect determination of the critical energy release rate [38]. Furthermore, for the study of crack deflection at bi-material interfaces [20], it should be avoided that the unstable crack growth associated with pop-in extends completely to the interface, which is another reason why stable crack growth is desirable.

A number of models of the four-point SENB specimen loaded with a pure bending moment exist [39, 24, 29]. However, experimental tests are often conducted by applied displacements i.e. displacement control (fixed grip) [20]. Therefore, this paper presents new models (analytical and numerical) of the four-point SENB specimen with applied displacements. More specifically, for displacement control, analytical expressions will be derived for the homogenous specimen (Figure 2 (A)), whereas numerical models will be applied for the bi-material specimen (Figure 2 (B)).

It is the aim to design the specimen geometry including start-crack length dependent on the loading configuration such that the crack grows stable and can be observed in-situ during loading. To enable observation of the crack deflection mechanism it is necessary that the crack can grow stable towards

the bi-material interface. Therefore, novel models are needed in order to explore a relevant parameter space. To summarise, the goals of the present paper is to:

(i) design the homogenous four-point SENB specimen geometry such that crack propagation is stable.

(ii) design the bi-material four-point SENB specimen geometry such that crack propagation towards the bi-material interface is stable.

(iii) determine the normal stress component across the interface of the bi-material four-point SENB specimen.

The latter is needed for the novel approach to determine the cohesive strength of the interface [21]. These points are addressed in the next sections using a model framework, but first the problems and assumptions are specified.

2. Problem definition

The stiffness mismatch for the bi-material specimen in Figure 2 (B) is presented in terms of E_1/E_2 since Dundurs' parameters (α, β) can only be used when boundary conditions are prescribed as tractions (not displacement boundary conditions) [40]. For simplicity, the materials are assumed isotropic and Poisson's ratio are set constant ($\nu_1 = \nu_2 = 1/3$) i.e. in terms of Dundurs' parameters in plane strain, $\beta = \alpha/4$ [40, 41]. For small-scale yielding the energy- and stress intensity approach are related by the Irwin relation [42]:

$$G_I = \frac{K_I^2}{\bar{E}} \tag{1}$$

where $\bar{E} = E$ is for plane stress and $\bar{E} = E/(1-\nu^2)$ is for plane strain.

To enable observations of crack propagation (and the crack deflection mechanism) during loading, the main crack must propagate in a stable manner i.e. in small increments. Dependent on the specimen geometry, material properties and loading configuration, the crack will propagate stable or dynamic once the magnitude of the critical energy release rate, G_{IC}, is reached [43]. For a material exhibiting R-curve behavior, i.e. a material with rising fracture resistance, the condition for continued crack extension is $G = G_R(\Delta a)$, where G is the applied energy release rate. G_R versus Δa is the resistance curve of a material when the crack has extended an amount Δa to the current crack length, a, under quasi-static loading. To ensure stable crack propagation (not dynamic), the following generalised condition must be satisfied [43, 29]:

$$\left[\frac{\partial G}{\partial a}\right]_{\mathrm{L}} < \left[\frac{dG_R}{d\Delta a}\right] \tag{2}$$

where L is the loading parameter that is kept constant while the crack advances a small increment [43]. A mode-I crack in a perfectly brittle material will propagate under constant G_I hence the condition

for stable crack growth reduces to [43]:

$$\left[\frac{\partial G_I}{\partial a}\right]_{\mathrm{L}} < 0 \tag{3}$$

In words, the mode-I energy release rate, G_I, must decrease with crack length. This general condition for stable crack growth in a perfectly brittle material can be specified for fixed displacement loading (fixed grip) as:

$$\left[\frac{\partial G_I}{\partial a}\right]_{\delta} < 0 \tag{4}$$

or for a fixed loading condition (dead load) as:

$$\left[\frac{\partial G_I}{\partial a}\right]_{\mathrm{P}} < 0 \tag{5}$$

Note, for fixed displacement the energy release rate depends on load point displacement and crack length i.e. $G_I(\delta, a)$ and similarly for fixed loading i.e. $G_I(P, a)$.

The specimens in Figure 2 are analysed for load control, displacement control, and test configuration since the first derivative of energy release rate, $\partial G_I/\partial a$, depends on load conditions, geometry, and stiffness properties/mismatch. It is therefore non-trivial to determine the best possible test setup and rigorous models are needed.

The simple pure bending specimen in Figure 2 (A) is analysed in rotation control in Appendix B. The homogenous four-point SENB specimen in Figure 2 (B) are analysed using analytical expressions that are derived and used to determine a specimen design with stable crack growth for displacement control (fixed grip). The assumptions used in the derivations are listed here:

(1) Shear force- and moment distribution are assumed to take the form depicted in Figure C.19 in Appendix C.
(2) Static equilibrium (no dynamic effects).
(3) LEFM assumptions are satisfied:
    (a) Linear-elastic and isotropic material properties.
    (b) Brittle material or only small-scale yielding near the crack tip.
(4) Assumptions from Bernoulli-Euler beam theory are fulfilled:
    (a) Cross-sections which are plane and normal to the longitudinal axis remain plane and normal to it after deformation.
    (b) Small displacements and small rotations.

The latter requires that linear-elasticity and superposition applies. Numerical models are used to test the accuracy/limitations of the analytical models and to design the experiment with the bi-material SENB specimen in Figure 2 (C).

3. Analytical model of the homogenous four-point SENB specimen

The standard solution for the stress intensity factor of the crack in the pure bending specimen (Figure 2 (C)) is given for a homogeneous material by Tada *et al.* [29] as:

$$K_I = \sigma_{xx}\sqrt{\pi a}F(a/b), \qquad \sigma_{xx} = \frac{6M}{b^2} \tag{6}$$

where σ_{xx} is the maximum normal stress (bending) in the beam in the x-direction at location $y = -b/2$. The moment, M, is per width, w. $F(a/b)$ is a non-dimensional function determined by an empirical fit to semi-analytical data obtained by the boundary collocation procedure [23]. A fit to semi-analytical data for $F(a/b)$ is given as [24, 29]:

$$F(a/b) = \sqrt{\frac{2b}{\pi a}\tan\left(\frac{\pi a}{2b}\right)}\frac{0.923 + 0.199\left(1 - \sin(\frac{\pi a}{2b})\right)^4}{\cos\left(\frac{\pi a}{2b}\right)} \tag{7}$$

which has an accuracy of better than 0.5% for any a/b. The energy release rate, G_I, of a mode-I crack can be determined using equation 6 and the Irwin relation in equation 1 [42]:

$$G_I = \frac{K_I^2}{\bar{E}} = \frac{1}{\bar{E}}\sigma_{xx}^2\pi a[F(a/b)]^2 = \frac{1}{\bar{E}}\frac{36M^2}{b^4}\pi a[F(a/b)]^2 \tag{8}$$

For load control, G_I in equation 8 can be written on a non-dimensional form as:

$$\frac{G_I\bar{E}b^3}{M^2} = 36\pi\frac{a}{b}[F(a/b)]^2 \tag{9}$$

In Appendix C an equation for the strain energy of the homogenous four-point SENB specimen is derived as a function of applied displacements (not moments). It is emphasised in equation 10 that the strain energy contributions originate from normal stresses, shear stresses and the presence of the crack according to the principle described by Rice *et al.* [44]:

$$U_t = \frac{P^2}{\bar{E}}\left(\frac{B}{b}\right)^2\left[\underbrace{\frac{B}{b} + 3\frac{h}{b}}_{\text{normal}} + \underbrace{\frac{3}{5}\frac{\bar{E}}{2\mu}\frac{b}{B}}_{\text{shear}} + \underbrace{3S(a/b)}_{\text{crack}}\right] \tag{10}$$

where $S(a/b)$ is presented in equation B.9 in Appendix B based on Tada *et al.* [29]. A relation between moment, M, and displacement, δ, is derived by combining $U_t = P\delta/2$, from equation C.1 and equation C.2 in Appendix C, with the moment, $M = PB/2$, as:

$$M = \frac{U_t B}{\delta} \tag{11}$$

Inserting U_t from equation 10 in equation 11 and then inserting M from equation 11 in equation 8 gives an expression for G_I as a function of applied displacement, δ, as:

$$G_I = \pi a\bar{E}\left[\frac{3}{2}\frac{\delta}{B}\frac{F(a/b)}{\left[\frac{B}{b} + 3\frac{h}{b} + \frac{3}{5}\frac{b}{B}\bar{\nu} + 3S(a/b)\right]}\right]^2 \tag{12}$$

or on a non-dimensional form as:

$$\frac{G_I b}{\bar{E}\delta^2} = \pi \frac{ab}{B^2} \left[\frac{3}{2} \frac{F(a/b)}{\left[\frac{B}{b} + 3\frac{h}{b} + \frac{3}{5}\frac{b}{B}\bar{\nu} + 3S(a/b)\right]} \right]^2 \tag{13}$$

where $\bar{E} = E/(1-\nu^2)$ and $\bar{\nu} = 1/(1-\nu)$ is for plane strain, and $E = \bar{E}$ and $\bar{\nu} = (1+\nu)$ is for plane stress. Note, in displacement control the energy release rate is coupled to the applied displacement through the elastic constants and the geometrical parameters.

4. Introducing the finite element model

A numerical model is developed in order to test the analytical derivation for the homogeneous SENB specimen and to analyse the bi-material SENB specimen, see the specimens in Figure 2 (A-B). The FE model, simulated in Abaqus CAE 6.14 (Dassault Systemes) with eight-noded plane strain elements, is parametrized with the non-dimensional groups, a/b, h/b and B/b. A symmetry condition is imposed at $x = 0$ to reduce the computational time. A focused mesh is applied in the region of $0.5b$ in the x-direction of the beam and 100 elements are used over the distance b.

5. Finite element modelling of homogenous SENB specimen

5.1. Benchmark of analytical derivation with finite element simulations

In the beginning of this section, for different geometries of the FE model and analytical model, two cases are compared; displacement control/load control. The non-dimensional energy release rate results from the parametric linear-elastic FE model of the homogenous four-point SENB specimen is presented in Figure 3 (A-B) for both load- and displacement control. The energy release rate results in Figure 3 (B) for load control are compared with the results of Tada *et al.* [29].

For displacement control, the curves in Figure 3 (A) start from zero at $a/b = 0$, increase to a peak and finally decrease to zero again at $a/b = 1$. Thus, when $a/b \to 1$ then $G_I \to 0$ since the crack approaches a free surface (at $y = b/2$) and the load is applied with fixed displacements. A significant difference is observed in Figure 3 (A) between the results of the analytical- (red curve) and the numerical model (red symbols) for the short and thick specimen loaded in displacement control. When h/b and B/b are relatively large, the results of the analytical model (blue curve) are close to the results from the numerical model (blue dots) as shown in Figure 3 (A). The analytical model becomes inaccurate for small values of h/b and B/b since assumption (1) used in the derivation is not fulfilled.

For load control, the curves in Figure 3 (B) start from zero at $a/b = 0$ and increases as the crack length becomes longer. Thus, for load control (dead load), $G_I \to \infty$ when the crack approaches the free surface, $a/b \to 1$. For load control in Figure 3 (B), the analytical model deviate from the numerical

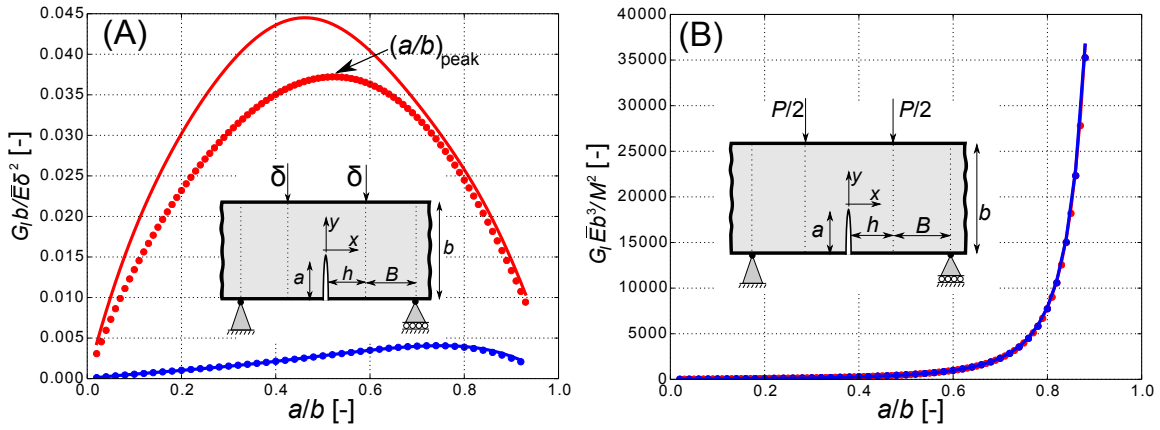

Figure 3: Energy release rate result based on FE model and analytical model. Blue: $h/b = 3.0$, $B/b = 3.0$. Red: $h/b = 0.9$, $B/b = 1.35$. Symbols: FE model, Solid lines: Analytical model. (A) Displacement control. (B) Load control (comparison with Tada *et al.* [29]). The x-y coordinate system is located in the beam centre.

model when a/b becomes high since for small variations of a, the sensitivity of G_I becomes significant, see also Srawley and Brown [22]. The maximum deviations between the numerical and analytical models in Figure 3 (B) are 4.2% and 2.8% for the models with parameters ($h/b = 0.9$, $B/b = 1.35$) and ($h/b = 3.0$, $B/b = 3.0$), respectively. So again, the inaccuracies increases as the beam becomes more compact.

As mentioned in the problem definition, we aim to design the test specimen such that the criterion for stable crack growth in equation 4 is fulfilled. Thus, the energy release rate should decrease with crack length. From Figure 3 (A) it is seen that equation 4 is fulfilled when a exceeds a critical value, denoted $(a/b)_{peak}$. The crack grows stable if the start-crack length is $a_0/b \geq (a/b)_{peak}$ hence the energy release rate decreases with crack length. It is desired that $(a/b)_{peak}$ is as small as possible hence the crack can grow far before reaching the free surface and to enlarge the design space with stable crack growth. Figure 3 (B) shows that the crack grows unstable for load control for any a/b since the stability condition in equation 5 cannot be fulfilled under a fixed loading condition.

A parameter space with a/b, h/b and B/b is explored in Figure 4-7 in order to determine the geometrical parameters effect on G_I and $(a/b)_{peak}$. Based on the dotted lines in Figure 6-7, $(a/b)_{peak}$ is presented in Figure 8. It is evident that the beam should be short (small h and B) and thick (large b) to maximise the design space with stable crack growth i.e. to reduce the value of $(a/b)_{peak}$. Figure 8 shows that $(a/b)_{peak}$ is significantly reduced for $B/b = 2.0$ in comparison with $B/b = 6.0$. Thus, it is demonstrated that crack growth stability for the four-point SENB specimen depends on the start-crack length, load span, support span, and whether the specimen is tested in load- or displacement control.

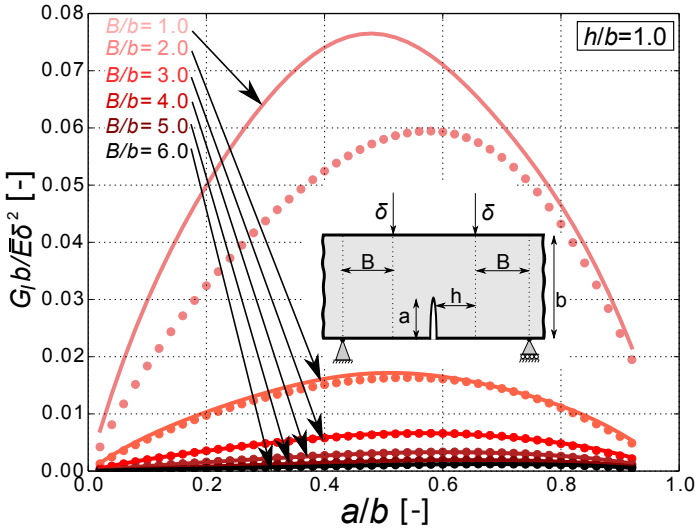

Figure 4: Energy release rate results by plane strain FE model and analytical model for different B/b and a/b for displacement control with $\boldsymbol{h/b = 1.0}$, $E_1/E_2 = 1.0$, $\nu = 1/3$ (lines are analytical results; symbols are FE results).

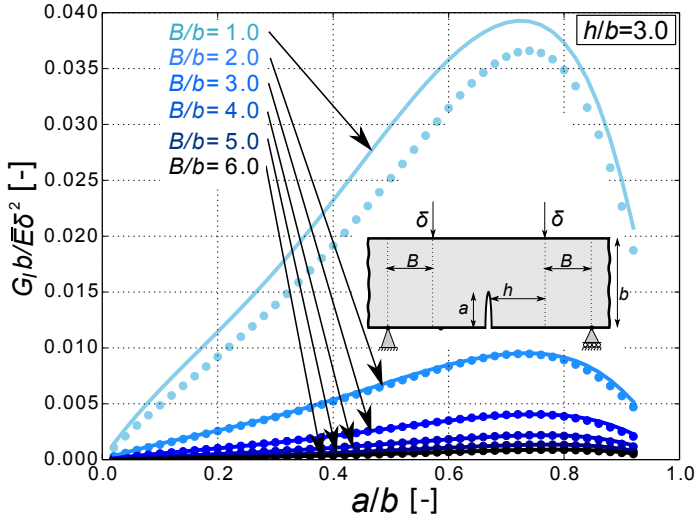

Figure 5: Energy release rate results by plane strain FE model and analytical model for different B/b and a/b for displacement control with $\boldsymbol{h/b = 3.0}$, $E_1/E_2 = 1.0$ and $\nu = 1/3$ (lines are analytical results; symbols are FE results).

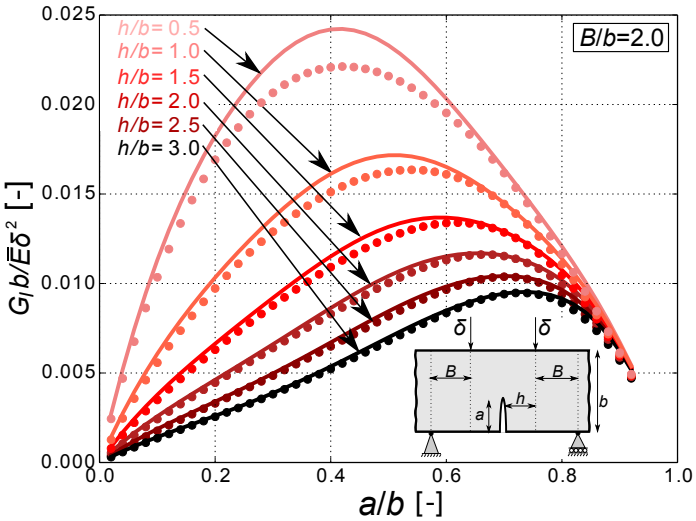

Figure 6: Energy release rate results by plane strain FE model and analytical model for different h/b and a/b for displacement control with $\boldsymbol{B/b = 2.0}$, $E_1/E_2 = 1.0$ and $\nu = 1/3$ (lines are analytical results; symbols are FE results).

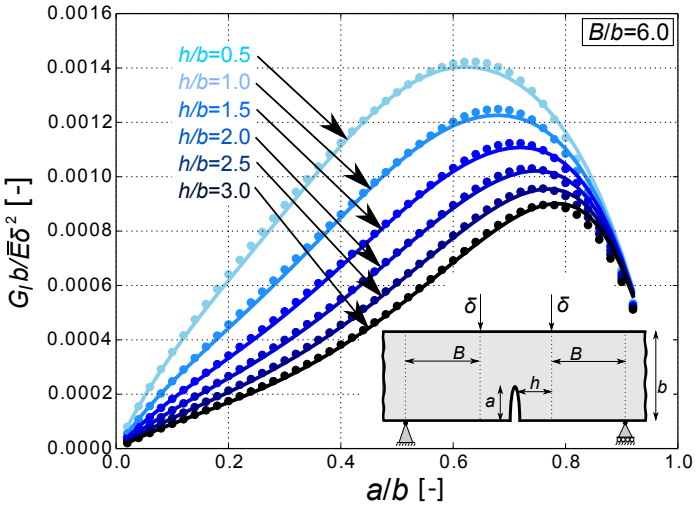

Figure 7: Energy release rate results by plane strain FE model and analytical model for different h/b and a/b for displacement control with $\boldsymbol{B/b = 6.0}$, $E_1/E_2 = 1.0$ and $\nu = 1/3$ (lines are analytical results; symbols are FE results).

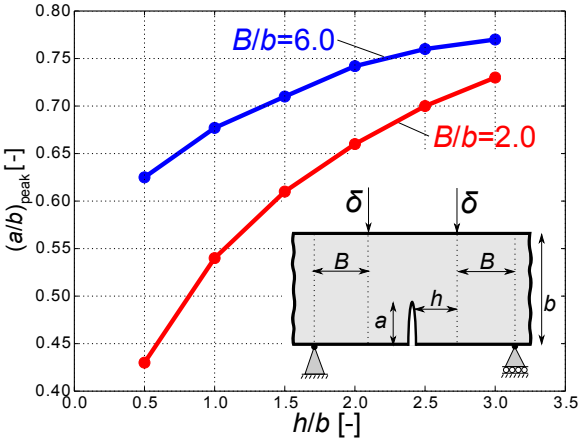

Figure 8: Results from FE model of homogenous four-point SENB specimen that are determined from $(a/b)_{peak}$ in Figure 6 (red curve) and Figure 7 (blue curve).

6. Finite Element Modelling of Bi-material SENB Specimen

A function similar to $F(a/b)$ from Tada *et al.* [29] can be established for the bi-material four-point SENB specimen to account for the presence of a substrate of thickness, c. Thus, for the bi-material specimen, with assumed isotropic adhesive and -substrate, in load control:

$$G_I = \frac{1}{\bar{E}_2}\sigma_{xx}^2 \pi a F(a/(b+c), c/b, E_1/E_2)^2, \qquad \sigma_{xx} = \frac{M E_2 \Omega}{E_1 I_1 + E_2 I_2} \tag{14}$$

where subscript 1 and 2 represent the substrate and adhesive, respectively. As shown in Figure 9, Ω is the distance from the bottom of the beam and to the global neutral axis of the beam (in the specimen without crack) [45]. I_1 and I_2 are the local area moment of inertia for the substrate and adhesive, respectively:

$$I_1 = \frac{c^3}{12} + c\left(\frac{c}{2} + b - \Omega\right)^2, \qquad I_2 = \frac{b^3}{12} + b\left(\Omega - \frac{b}{2}\right)^2, \qquad \Omega = c\frac{1 + 2\frac{E_1}{E_2}\frac{c}{b} + \frac{E_1}{E_2}\left(\frac{c}{b}\right)^2}{2\frac{c}{b}\left(1 + \frac{E_1}{E_2}\frac{c}{b}\right)} \tag{15}$$

The function, F, in equation 14 is determined as shown in Figure 9 by FE simulations, which is compared for $E_1/E_2 = 1$, with the solution by Tada *et al.* [29]. It can be seen that independently of elastic mismatch when; $a/(b+c) \to 0$ then $F(a/(b+c)) \to 1.12$. This limit is similar to the solution for a side-crack in an infinitely large homogenous plate under uni-directional tension [29, 46]. The trend in Figure 9 is comparable to the partial cracked film problem from Beuth [47]. For compliant substrates ($E_1/E_2 \lesssim 3$), F increases monotonic, whereas for stiffer substrates ($E_1/E_2 \gtrsim 9$), F reaches a peak and subsequently starts decreasing (close to $a/(b+c) = 0.8$).

Dimension analysis reveals that the energy release rate of the crack for the bi-material specimen

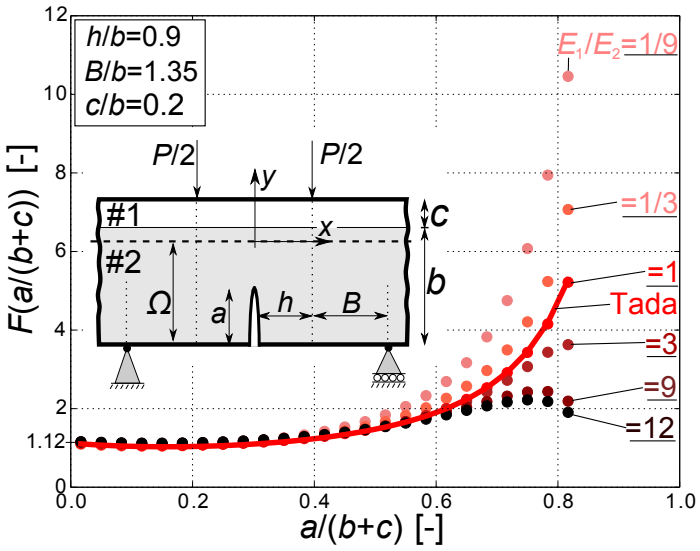

Figure 9: Results for $F(a/(b+c))$ from FE model of bi-material SENB specimen with; $c/b = 0.2$, $h/b = 0.9$ and $B/b = 1.35$ (line is analytical result, symbols are FE results, #1 is substrate, #2 is adhesive). The bi-material interface is located near $a/b \approx 0.83$.

presented in Figure 2 (B) can, when loaded in displacement control, be written as:

$$\frac{G_I(b+c)}{\bar{E}_2\delta^2} = \frac{9\pi}{4}\frac{a(b+c)}{B^2}F_\delta(a/(b+c), h/b, B/b, c/b, E_1/E_2)^2 \tag{16}$$

where the non-dimensional function, F_δ, is determined numerically. F_δ is introduced since it is out of the scope in the paper to derive an expression analytically for the bi-material specimen like in equation 13 for the homogenous specimen.

6.1. Parameter study using the bi-material FE model

To determine a start-crack length, a_0/b, that gives stable crack growth, the requirement in equation 4 needs to be applied on the results of the bi-material FE model in Figure 10-11. From Figure 10-11 it is clear that an increase of the substrate stiffness (E_1/E_2), increases the energy release rate. The effect of elastic mismatch on the magnitude of $(a/b)_{peak}$ is more complex as shown in Figure 12.

The curves in Figure 12 for $c/b = 0.2$ are determined from $(a/b)_{peak}$ of the dotted symbols in Figure 10-11 and similarly for $c/b = 0.1$ and $c/b = 0.3$. Additional points for $E_1/E_2 = 1.5, 3, 6$ are included in Figure 12 to emphasise the trend of the curves, where the data points are connected by lines. Figure 12 shows that $(a/b)_{peak}$ is sensitive to E_1/E_2 and h/b. The graphs in Figure 12 for $h/b = 0.9$ are marked with red colors and the graphs for $h/b = 1.8$ are marked with blue colors. It is seen that $(a/b)_{peak}$ is reduced for the group of $h/b = 0.9$ (red curves) compared with the group of $h/b = 1.8$ (blue curves). This study shows the complexity of the problem since several parameters (h/b, B/b, c/b, E_1/E_2) affects the resulting value of $(a/b)_{peak}$.

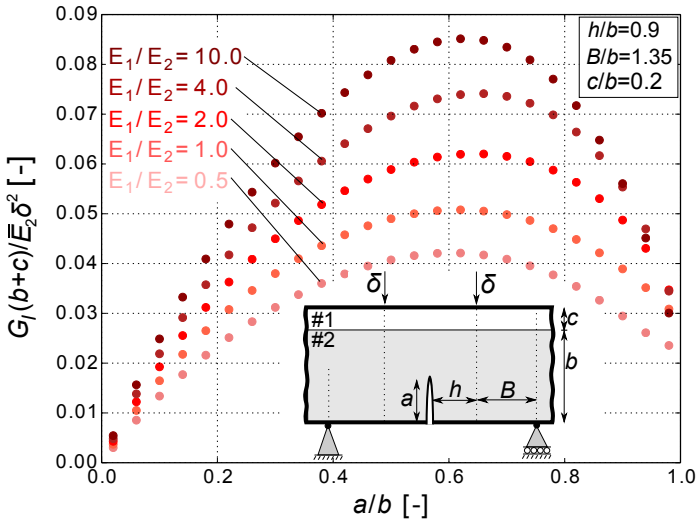

Figure 10: Energy release rate results from FE model for displacement control for E_1/E_2. Other parameters are: $\nu_1 = \nu_2 = 1/3$, $h/b = 0.9$, $B/b = 1.35$ and $c/b = 0.2$ (lines are analytical results; symbols are FE results, #1 is substrate, #2 is adhesive).

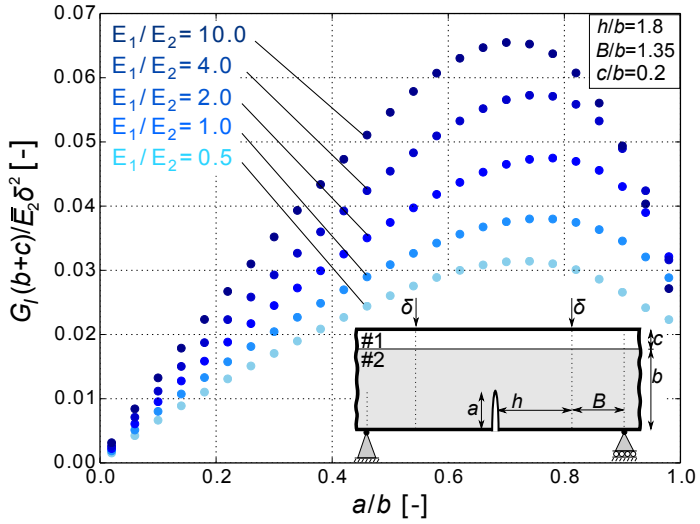

Figure 11: Energy release rate results from FE model for displacement control for E_1/E_2. Other parameters are: $\nu_1 = \nu_2 = 1/3$, $h/b = 1.8$, $B/b = 1.35$ and $c/b = 0.2$ (lines are analytical results; symbols are FE results, #1 is substrate, #2 is adhesive).

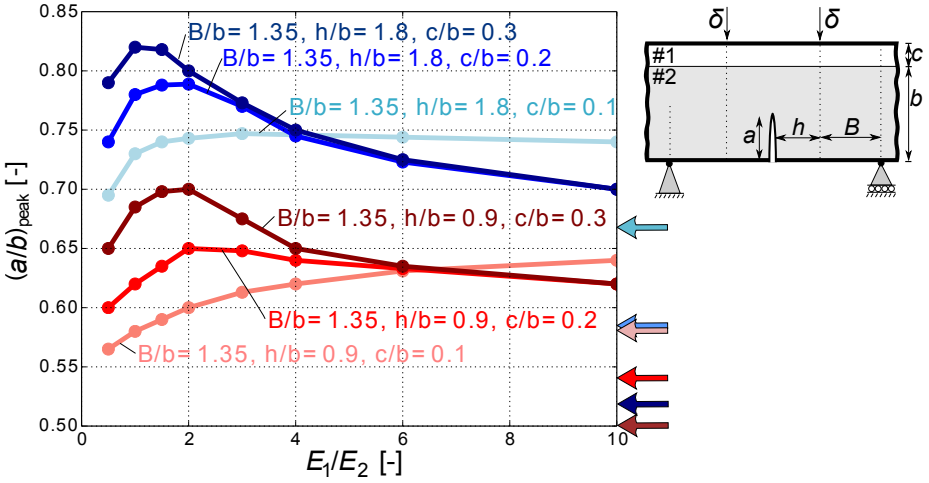

Figure 12: Peak values of a/b from Figure 10-11 are used to determine, $(a/b)_{peak}$, for the bi-material specimen with varying E_1/E_2, h/b, and c/b. The limit value for $(a/b)_{peak}$ is determined for $E_1/E_2 = 100$ as indicated by the colored arrows. (#1 is substrate, #2 is adhesive)

7. Determination of mode-I cohesive strength of interfaces

For the cracking mechanism in Figure 1 (C), at the time where the debond crack at the interface initiates (onset of interface separation), the cohesive strength of the interface, $\hat{\sigma}_i$, is equal to the stress across the interface, $\sigma_{yy,i}$, i.e. $\hat{\sigma}_i = \sigma_{yy,i}$. Using the bi-material FE model of the four-point SENB specimen, $\sigma_{yy,i}$ can be determined by:

$$\frac{\sigma_{yy,i} b^2}{M} = f(a/b, c/b, E_1/E_2) \tag{17}$$

where the non-dimensional function, f, is determined by the FE modelling result in Figure 13-14.

The calculation procedure to determine the cohesive strength of the interface, $\hat{\sigma}_i$, should be read in details in a related paper [21], but it is listed in short here for convenience:

- During the fracture experiment, capture the time of interface crack initiation (onset of interface separation) e.g. by digital image correlation, visually or by other methods.
- From images recorded during the experiment, determine M and a/b at the time of interface crack initiation (onset of interface separation).
- Use measured M and a/b with the FE results in Figure 13-14 and equation 17 to determine the stress across the interface, $\sigma_{yy,i}$ at the onset of interface separation.

Moment, M and crack length, a/b are the only parameters varying during the test. $\sigma_{yy,i}$ scales linearly with M, but non-linearly with a/b as shown in Figure 13-14. Thus, using the measured values of M

and a/b together with the FE simulation results in Figure 13-14, the resulting cohesive strength of a material interface can be determined by equation 17.

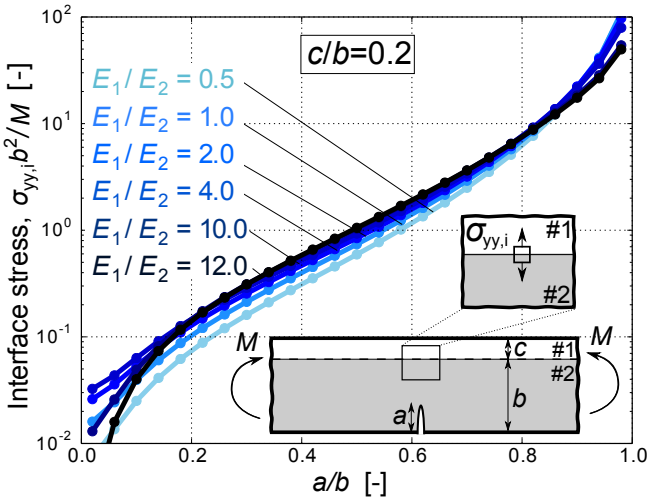

Figure 13: Results for normalised interface stress determined numerically for different E_1/E_2. Other parameters are: $h/b = 0.9$, $B/b = 1.35$ and $c/b = 0.2$.

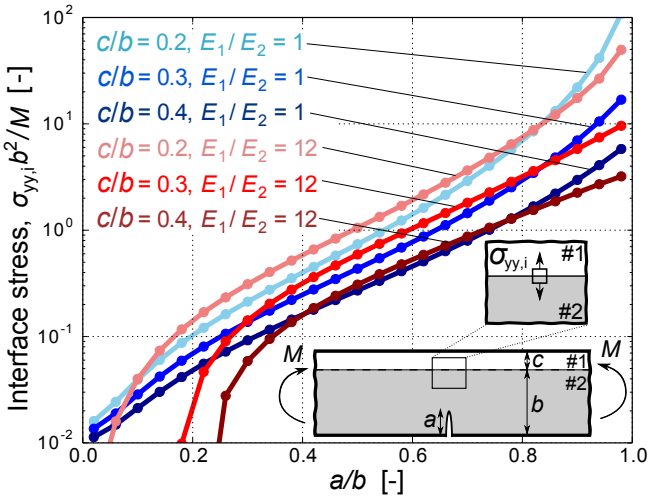

Figure 14: Results for normalised interface stress determined numerically for different E_1/E_2 and c/b. Other parameters are: $h/b = 0.9$ and $B/b = 1.35$.

8. Experimental test of model predictions

In order to test the model predictions for stable growth of the crack, homogenous four-point SENB specimens cast of adhesive were manufactured and tested experimentally in the laboratory.

8.1. Experimental procedure

The four-point SENB specimens were cast by injection of an adhesive in-between two glass plates to create a homogenous plate of adhesive. Prior to the injection, the surfaces of the glass plates were waxed to ease the removal of the cast adhesive plate. The adhesive plate was post-cured and cut into beams with similar outer dimensions ($w/b \approx 0.7$). The adhesive type and processing conditions are proprietary. Start-cracks were cut using an ultra thin razor blade of thickness 76 microns (Ultra-thin single edge, stainless steel blade from Ted Pella, Inc.). The test setup were adjusted with $h/b = 0.9$ and $B/b = 1.35$. The specimens were placed in a four-point bend fixture and loaded by a MTS 858 Mini Bionix II servo-hydraulic test machine at a constant displacement-rate of 0.015 mm/min, where the load is measured by a 1.5 kN load cell. For selected tests, the crack length is measured on images taken during the test by help from a Python script [48, 49].

8.2. Experimental results

The measured bending moment as a function of load point displacement for a selection of test specimens is presented in Figure 15 (A). The curves (bending moment vs load point displacement) show similar trend as those curves reported in the literature [15, 33]. All curves, except of the first ~ 0.05 mm, starts with a linear part until the onset of crack propagation where the moment drops. Onset of crack propagation is identified near the measured maximum moment (the peak) according to images taken during the test. The smooth decrease in M is associated with stable crack propagation. All curves decrease smoothly until zero moment is measured at displacement, $\delta \approx 0.9$-1.0 mm, except of the test with a start-crack length of $a_0/b = 0.34$ (Test 1 in Figure 15 (A)). For this test, the moment initially increases faster with applied displacement since the start-crack length is short. The moment drops instantaneously to zero at displacement, $\delta \approx 0.29$ mm, due to unstable crack growth. In accordance with the model in Figure 15 (B), the sudden drop in moment for this test exemplifies the response of the crack growth when the start-crack length is made too short i.e. unstable crack growth.

The observed unstable crack growth for Test 1 with $a_0/b = 0.34$, shown in Figure 15 (A), agrees fairly well with the prediction by the analytical model presented in Figure 15 (B). The analytical model in Figure 15 (B) at $a_0/b = 0.34$ illustrates that the crack stability criterion in equation 4 is not fulfilled. Thus, at the onset of crack propagation the crack grows unstable. As opposed to the model, in the experiment crack propagation does not become stable again at higher a/b since the

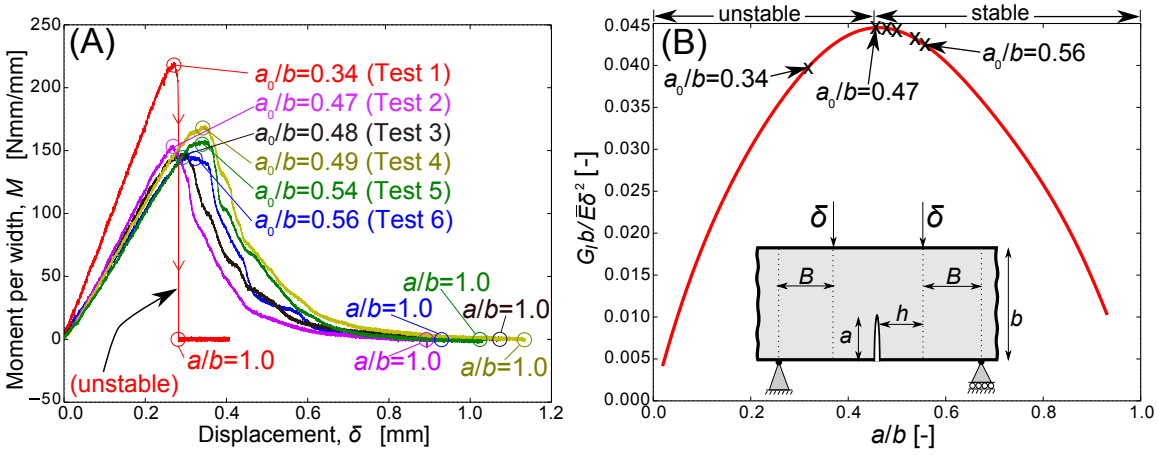

Figure 15: Adhesive four-point SENB specimens (homogenous with $h/b = 0.9$ and $B/b = 1.35$). (A) Experimental test in displacement control. (B) Analytical model of the experiment.

unstable crack growth activates dynamic effects. For the other test specimens with $a_0/b \geq 0.47$, the crack propagates stable as shown by the smoothly decreasing curves in Figure 15 (A) since the crack stability criterion in equation 4 is satisfied. Thus, it is demonstrated experimentally that a proper selection of the start-crack length, e.g. by modelling, is useful for determining a start-crack length that gives stable crack propagation.

The measured bending moment and crack length of another four-point SENB specimen are presented in Figure 16 to investigate the crack propagation in further details. Overall, the bending moment decreases smoothly hence the crack propagates stable and the crack length can be measured on images during the test. However, a small instability is seen in Figure 16 at the onset of crack propagation (at displacement $\delta \approx 0.35$ mm). This unexpected behaviour is attributed the manual cutting of the notch that is not as sharp as a real crack. Thus, the initiation of a crack from the notch gives abrupt crack growth in the beginning i.e. "pop-in" effect [50]. Except of this initiation phenomenon, the remaining growth of the crack is stable as shown by the measured crack length in Figure 16.

9. Discussions

9.1. Discussion of modelling results

When the length of the beam is short, the boundary effects are significant meaning that the moment and shear force distributions are not as idealised as shown in Figure C.19 in Appendix Appendix C. In the analytical model, it is assumed that the normal stress is perfectly linear across the beam thickness and the shear stress distribution is perfectly parabolic, but near the boundaries the shear stress field is not as assumed in the analytical model. While these localised boundary effects are not included in the

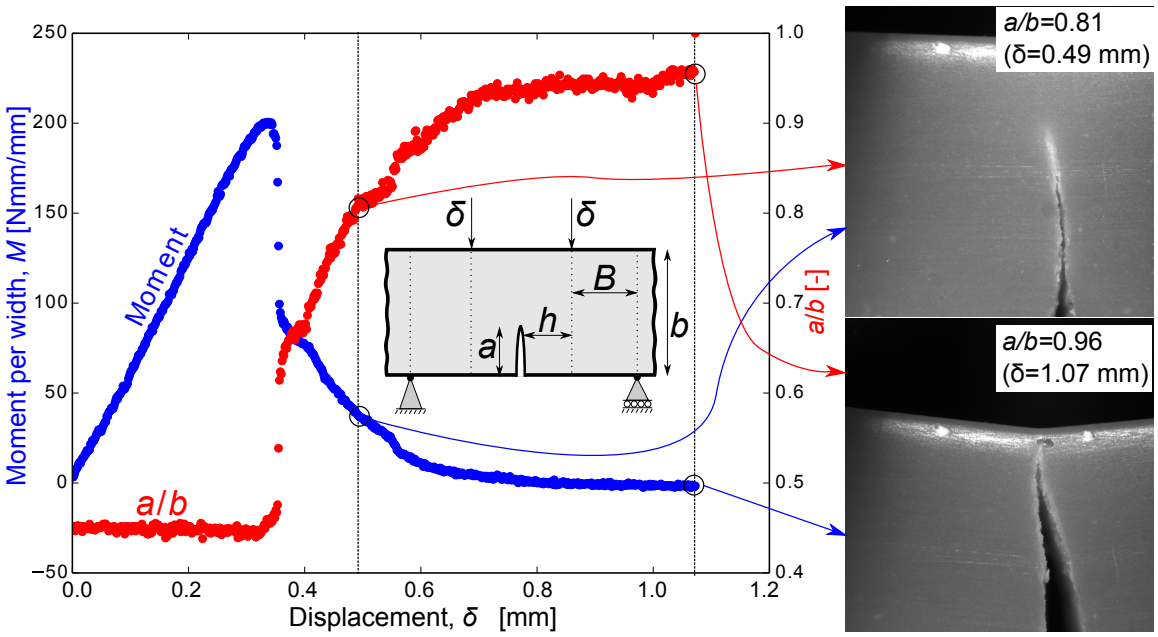

Figure 16: Experimental test of homogenous four-point SENB specimen with stable crack growth and parameters: $a_0/b = 0.47$, $h/b = 0.9$, $B/b = 1.35$.

analytic model, they are included in the numerical model. This is one of the reasons for the deviations between the analytical- and numerical model in Figure 3. This effect is especially significant when the beam is short and thick.

9.2. Small scale yielding assumption

The assumptions from LEFM must be satisfied for the derived analytical model to be accurate for the experimental test specimens. To satisfy brittle fracture conditions (small-scale yielding), the plastic zone size near the crack tip must be small in comparison with the characteristic length scale in the problem i.e. the start-crack length. The first order estimation of the radius of the plastic zone, r_p, is determined for plane strain by [43]:

$$r_p = \frac{1}{3\pi}\left(\frac{K_{IC}}{\sigma_{YS}}\right)^2 \tag{18}$$

The critical stress intensity factor, K_{IC}, was measured by the experimental four-point SENB test in Figure 16, and the yield stress, σ_{YS}, was measured by a dog bone specimen using the standard "ISO 527-2: 2012". Based on equation 18, it is determined that $r_p/a_0 \approx 0.02$ for plane strain. According to the results presented by Charalambides *et al.* [51], a 10% deviation of the stress field from the singular form (K-dominant zone) for a SENB specimen are found to be $r_p/a_0 \approx 0.04$. Thus, a plastic zone size of $r_p/a_0 \approx 0.02$ is judged to be acceptable since it will be embedded in the K-dominant zone.

9.3. Homogenous four-point SENB experiments - uncertainties

The test-to-test variations observed for the initial linear slope in the results of the four-point SENB experiments are primarily attributed the differences in start-crack length. Material variations may affect the measured maximum load. Furthermore, air voids in the adhesive can give variations in the measured curves in Figure 15 (A). The maximum diameter of the voids in the adhesive is measured to about $0.04b$. Voids of this size may accelerate the crack growth in certain regions of the specimens e.g. indicated by the fluctuations and bumps on the smooth curves in Figure 15 (A). Adjustment and alignment of the load rig may affect the shape of the whole curve in Figure 15 (A).

9.4. Stability of crack growth

Typically in the literature, the four-point SENB specimen is used for characterising materials that have a constant fracture toughness (i.e. no R-curve), which not necessarily requires stable crack propagation. However, for many applications, as mentioned in the introduction, stable crack propagation is essential to avoid dynamic effects and enable monitoring crack growth. Furthermore, a test with stable crack growth means that a sharp crack is formed from the start-notch, which in practice cannot be made as sharp as a real crack. According to the test standards ISO-15024:2001(E) and ASTM D5528-01, the start notch should not exceed width of 13 μm when measuring fracture toughness of uni-directional composites. If the start notch is machined it should not exceed a width of 10 μm according to the study of fine grained alumina by Nishida *et al.* [38].

When a sharp crack propagates stable, a more accurate fracture toughness value can be measured since several measurements can be made using just a single test specimen. In any case, stable crack growth is attractive, as it can help uncovering unexpected behavior such as rate dependent- or R-curve behavior. Also, possible errors introduced by having a machined notch as a starter crack, in contrast to a truly sharp crack, is eliminated.

9.5. Discussion of results in relation to existing literature

From the results in Figure 8, the test specimen design by Brinckmann *et al.* [12] can be improved such that crack propagation are stable and can be monitored. For this particular specimen design ($B/b = 6.9$), it is recommended to use a smaller B/b in order to reduce the elastic strain energy of the beam and thereby enhance the probability of stable crack propagation. However, if the substrate is a laminate, the four-point SENB specimen might fail in shear (mode-II shear crack or delamination) in between the support- and load points if B is too small and a weak interface exists in the substrate of the bi-material specimen [26].

9.6. Bi-material model with orthotropic substrate:

As mentioned in the introduction, the methods are also aimed to be applicable for designing experiments with stable crack growth for adhesive-composite joints. Therefore, it is tested, for the bi-material four-point SENB specimen, how accurate it is to model a uni-directional glass-fiber laminate as an isotropic substrate. The in-plane orthotropy can be described by the dimensionless parameters [52]:

$$\lambda = \frac{E_{yy}}{E_{xx}}, \qquad \rho = \frac{(E_{xx}E_{yy})^{1/2}}{2G_{xy}} - (\nu_{xy}\nu_{yx})^{1/2} \tag{19}$$

where $\lambda = 0.3$ and $\rho = 2.5$ are representative for a uni-directional glass-fiber laminate where material directions are following the coordinate system shown in Figure 9. For the FE model with isotropic substrate, E_{xx} and ν_{xy} are the only input of stiffness parameters i.e. $\lambda = \rho = 1$ [52]. Results from a bi-material FE model with a substrate of an isotropic material ($\lambda = \rho = 1$) were compared with a bi-material FE model with a substrate of an orthotropic material ($\lambda = 0.3$ and $\rho = 2.5$) for geometrical parameters of $h/b = 0.9$, $B/b = 1.35$ and $c/b = 0.2$. The energy release rates of the cracks and $(a/b)_{peak}$ are comparable (within 5%) for the isotropic and orthotropic cases. This suggests that the primary stiffness in the x-direction, E_{xx}, is the main stiffness parameter that governs the energy release rate of the crack in the model with orthotropic substrate.

10. Conclusions

An analytical model of the displacement loaded four-point SENB test specimen was derived and found to agree well with FE simulations under certain geometrical conditions. The models (analytical and numerical) were efficient to design the experiment with stable crack growth since stability depends on load configuration, crack length and geometry. These models suggest that the beam should be short and thick, and the start-crack length should be relatively deep for the main crack to propagate stable.

The model predictions for stable crack growth were tested experimentally by homogenous four-point SENB specimens cast of pure adhesive. The experiments showed that crack growth is stable if the start-crack length was made sufficiently long and unstable if not. The stable crack propagation was documented by a series of images captured in-situ during loading. Thus, for the material systems used in the present work, the displacement loaded four-point SENB specimen was found appropriate for studying crack deflection at interfaces since stable crack growth could be achieved.

Acknowledgements

First of all thanks to professor Michael D. Thouless, University of Michigan, for useful discussions about modelling and mechanical testing. Also, thanks to James Gorman, University of Michigan for his

help when testing the specimens in the lab at the Department of Mechanical Engineering, University of Michigan, MI, USA. Also, thanks to Jens Glud, Aalborg University, for the useful discussions about the numerical modelling. Acknowledgements to the LM Wind Power lab for help manufacturing the test specimens and to Fulbright for supporting the research stay at the University of Michigan. This research was primarily supported by grant no. 4135-00010B from Innovation Fund Denmark. This research was also supported by the Danish Centre for Composite Structure and Materials for Wind Turbines (DCCSM), grant no. 0603-00301B, from Innovation Fund Denmark.

Appendix A. Strain energy of cantilever beam

The strain energy density for a three dimensional linear-elastic solid in terms of engineering stresses and strains is [53]:

$$\Phi = \frac{1}{2}\left(\sigma_{xx}\epsilon_{xx} + \sigma_{yy}\epsilon_{yy} + \sigma_{zz}\epsilon_{zz} + \tau_{xy}\gamma_{xy} + \tau_{xz}\gamma_{xz} + \tau_{yz}\gamma_{yz}\right) \tag{A.1}$$

where σ is the normal stress, τ is the shear stress, ϵ is the normal strain and γ is the shear strain. For the cantilever beam loaded by force, P_0, and moment, M_0, shown in Figure A.17, the strain energy density expression in (A.1) reduces to:

$$\Phi = \frac{1}{2}\left(\sigma_{xx}\epsilon_{xx} + \tau_{xy}\gamma_{xy}\right) \tag{A.2}$$

In the following the two terms in (A.2) will be assessed individually.

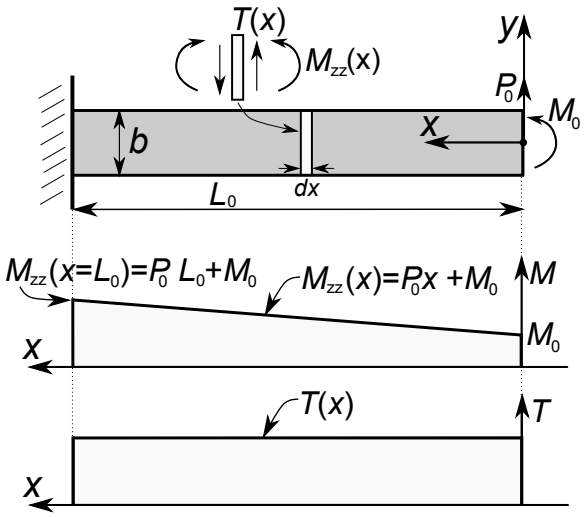

Figure A.17: Cantilever beam with applied bending moment, M_0, and applied force, P_0.

Appendix A.1. Strain energy of cantilever beam due to normal stresses

The strain energy density for the first term in (A.2) due to normal stress is:

$$\Phi(x,y) = \frac{1}{2}\sigma_{xx}\epsilon_{xx} \tag{A.3}$$

Based on the stress across the beam section, $\sigma_{xx}(y) = -M_{zz}y/I$, the strain distribution, $\epsilon_{xx}(y) = -\kappa y$, and Hookes law, $\sigma_{xx} = E\sigma_{yy}$, it can be shown that the total strain energy in a beam under pure bending moments is [53]:

$$U_M = \int_0^{L_0} \left(\frac{M_{zz}^2}{2EI}\right) dx \tag{A.4}$$

where the area moment of inertia per width, I, for a rectangular cross section is; $I = b^3/12$. If the beam is loaded by force, P_0, and moment, M_0, then the cross-sectional moment, $M_{zz}(x)$, varies linearly over the beam length, L_0, as shown in Figure A.17. The strain energy of the cantilever beam in Figure A.17 with an applied moment per width, M_0, and an applied force per width, P_0, is (see p. 726-731 in [54]):

$$U_M = \int_0^{L_0} \left(\frac{M_{zz}(x)^2}{2EI}\right) dx = \int_0^{L_0} \left(\frac{(P_0 x + M_0)^2}{2EI}\right) dx = \frac{6}{b^3 E}\left(\frac{P_0^2}{3} + P_0 M_0 L_0^2 + M_0^2 L_0\right) \tag{A.5}$$

The strain energy in the four-point bend specimen under applied bending forces is ($M_0 = 0$):

$$U_{P_0} = 2\frac{P_0^2}{b^3 E} L_0^3 \tag{A.6}$$

whereas the strain energy in the beam under pure bending moments is ($P_0 = 0$):

$$U_{M_0} = 6\frac{M_0^2}{b^3 E} L_0 \tag{A.7}$$

Appendix A.2. Strain energy of cantilever beam due to shear stresses

The strain energy density for the second term in (A.2) due to shear stress is:

$$\Phi(x,y) = \frac{1}{2}\tau_{xy}\gamma_{xy} = \frac{1}{2}\frac{\tau_{xy}^2}{\mu} \tag{A.8}$$

where the shear stress, τ_{xy}, is given by Hookes law for shear, $\tau_{xy} = \mu\gamma_{xy}$ [54]. Here, μ is the shear modulus and γ_{xy} is the shear strain. For a rectangular cross section, the through thickness shear stress distribution is assumed parabolic on the form (see p. 192 in [46] or p. 392 in [54]):

$$\tau_{xy}(x,y) = \frac{T(x)}{2I}\left(\left(\frac{b}{2}\right)^2 - y^2\right) = \frac{3}{2}\frac{T(x)}{b}\left(1 - \left(2\frac{y}{b}\right)^2\right) \tag{A.9}$$

where the applied shear force is denoted T. The strain energy density becomes:

$$\Phi(x,y) = \frac{1}{2}\frac{\tau_{xy}(x,y)^2}{\mu} = \frac{1}{2\mu}\left[\frac{3}{2}\frac{T(x)}{b}\left(1 - \left(2\frac{y}{b}\right)^2\right)\right]^2 = \frac{1}{2\mu}\left(\frac{3}{2}\frac{T(x)}{b}\right)^2\left(1 + \left(2\frac{y}{b}\right)^4 - 2\left(2\frac{y}{b}\right)^2\right) \tag{A.10}$$

The strain energy of the entire beam due to shear force, T, is determined by integration of the strain energy density over the beam volume. First, the strain energy per unit length of the beam (in the x-direction) is determined by integration of the strain energy density across the beam thickness:

$$\frac{dU_T}{dx} = \int_{-b/2}^{+b/2} \Phi dy = \frac{1}{2\mu}\left(\frac{3}{2}\frac{T(x)}{b}\right)^2 \int_{-b/2}^{+b/2} \left(1 + \left(2\frac{y}{b}\right)^4 - 2\left(2\frac{y}{b}\right)^2\right) dy = \frac{3}{5}\frac{1}{\mu}\frac{T(x)^2}{b} \tag{A.11}$$

Next, the strain energy of the beam is obtained by integrating the strain energy per unit length over the entire beam length:

$$U_T = \frac{3}{5}\frac{1}{b\mu}\int_0^{L_0} T(x)^2 dx \tag{A.12}$$

Thus, the strain energy for a constant shear force, T, over the beam length, L_0, see Figure A.17, becomes:

$$U_T = \frac{3}{5}\frac{T^2 L_0}{b\mu} \tag{A.13}$$

Appendix B. Analytical model of a pure bending specimen

The simplest case possible, the pure bending specimen sketched in Figure B.18 (A), can be described by two non-dimensional geometrical parameters: a/b, h/b. For beam rotations (Figure 2 (C)), the total rotation, θ_t, is the sum of the rotation without a crack, $\theta_{no,crack}$, plus the rotation introduced by the presence of a crack, θ_{crack}, as described by the work of Rice *et al.* [44]:

$$\theta_t = \theta_{no,crack} + \theta_{crack} \tag{B.1}$$

Equivalently, the total strain energy of the beam can be written [44, 29]:

$$U_t = U_{no,crack} + U_{crack} \tag{B.2}$$

Using equation B.1, the work done by the external moment is:

$$V_t = \frac{1}{2}M\theta_t = \frac{1}{2}M(\theta_{no,crack} + \theta_{crack}) = \frac{1}{2}M\theta_{no,crack} + \frac{1}{2}M\theta_{crack} \tag{B.3}$$

The rotation angle for the pure bending specimen with no crack, $\theta_{no,crack}$, is derived by elementary beam theory based on p. 726 in Gere and Goodno [54]:

$$\theta_{no,crack} = \frac{M2h}{\bar{E}I} = \frac{24M}{b^2\bar{E}}\frac{h}{b} \tag{B.4}$$

The change in elastic strain energy per unit extension of the crack is [47]:

$$U(a') = \int_0^{a'} G_I(a) da \tag{B.5}$$

where $U(a') = U_{crack}$ is the change of strain energy when the crack extends from $a = 0$ to $a = a'$. Inserting G_I from equation 8 into equation B.5, the strain energy of the crack becomes:

$$U_{crack} = \frac{1}{2}M\theta_{crack} = \frac{36M^2\pi}{b^4\bar{E}}\int_0^{a'} \left[aF(a/b)^2\right] da \tag{B.6}$$

where we arrive at $U_{crack} = M\theta_{crack}/2$ by combining equation B.2 and equation B.3 through equation C.2. From equation B.6 the rotation angle from the presence of the crack, θ_{crack}, can be determined:

$$\theta_{crack} = \frac{72M}{b^2\bar{E}}\pi \int_0^{a'} \left[\frac{aF(a/b)^2}{b^2}\right] da \tag{B.7}$$

Inserting $M = \sigma_{xx}b^2/6$ from equation 6 into equation B.7 gives:

$$\theta_{crack} = \frac{12\sigma_{xx}}{\bar{E}}\pi \int_0^{a'} \left[\frac{a[F(a/b)]^2}{b^2}\right] da = \frac{4\sigma_{xx}}{\bar{E}} \left(3\pi \int_0^{a'} \left[\frac{a[F(a/b)]^2}{b^2}\right] da\right) = \frac{4\sigma_{xx}}{\bar{E}} S(a/b) \tag{B.8}$$

Thus, from equation B.8 it follows that $S(a/b) = 3\pi \int_0^{a'} \left[\frac{a[F(a/b)]^2}{b^2}\right] da$. $S(a/b)$ is also given as a fit by Tada *et al.* [29]:

$$S(a/b) = \left(\frac{a/b}{1-a/b}\right)^2 \left[5.93 - 19.69(a/b) + 37.14(a/b)^2 - 35.84(a/b)^3 + 13.12(a/b)^4\right] \tag{B.9}$$

The rotation angle, θ_t, can be determined from equation B.1 by adding θ_{crack} (equation B.8) and $\theta_{no,crack}$ (equation B.4). Subsequently, θ_t in equation B.1 can be used in combination with the general compliance relation, $C_t = \theta_t/M$, to derive the compliance, C_t, for the pure bending specimen in Figure B.18 (A) as:

$$C_t = \frac{24}{b^2\bar{E}} \left(\frac{h}{b} + S(a/b)\right) \tag{B.10}$$

The energy release rate, G_I, for the pure bending specimen can be expressed in terms of an applied rotation by inserting C_t in equation B.10 in the general relation for compliance, $M = \theta_t/C_t$, and finally inserting M into equation 8 for G_I:

$$G_I = \frac{1}{\bar{E}}\sigma_{xx}^2 \pi a[F(a/b)]^2 = \frac{1}{\bar{E}}\frac{36M^2}{b^4}\pi a F(a/b)^2 = \frac{1}{16}\frac{\theta_t^2 \bar{E}\pi a F(a/b)^2}{\left(\frac{h}{b} + S(a/b)\right)^2} \tag{B.11}$$

The expression for G_I (equation B.11) can also be written on a non-dimensional form as:

$$\frac{G_I \bar{E} b^3}{M^2} = 36\pi \frac{a}{b}\left[F(a/b)\right]^2 \qquad \text{for load control} \tag{B.12}$$

$$\frac{G_I}{\bar{E}b\theta_t^2} = \frac{1}{16}\frac{a}{b}\frac{\pi\left[F(a/b)\right]^2}{\left(\frac{h}{b} + S(a/b)\right)^2} \qquad \text{for displacement control} \tag{B.13}$$

Equation B.12 and equation B.13, plotted in the graphs in Figure B.18, represent the non-dimensional energy release rate for a pure bending specimen with applied moment and -rotation, respectively. Figure B.18 (B) shows that G_I increases monotonic with a/b. Figure B.18 (C) shows that G_I increases until a peak values is attained, hereafter G_I decreases smoothly towards zero. Note, with increasing h/b, the shape of the curves approaches the shape of the curve for moment control although the specimen is loaded in rotation control. On the other hand, stability is enhanced when h/b is small. Note, the crack approaches a free surface at $a/b = 1.0$. For rotation control; $G_I \to 0$ when $a/b \to 1.0$, and for moment control; $G_I \to \infty$ when $a/b \to 1.0$.

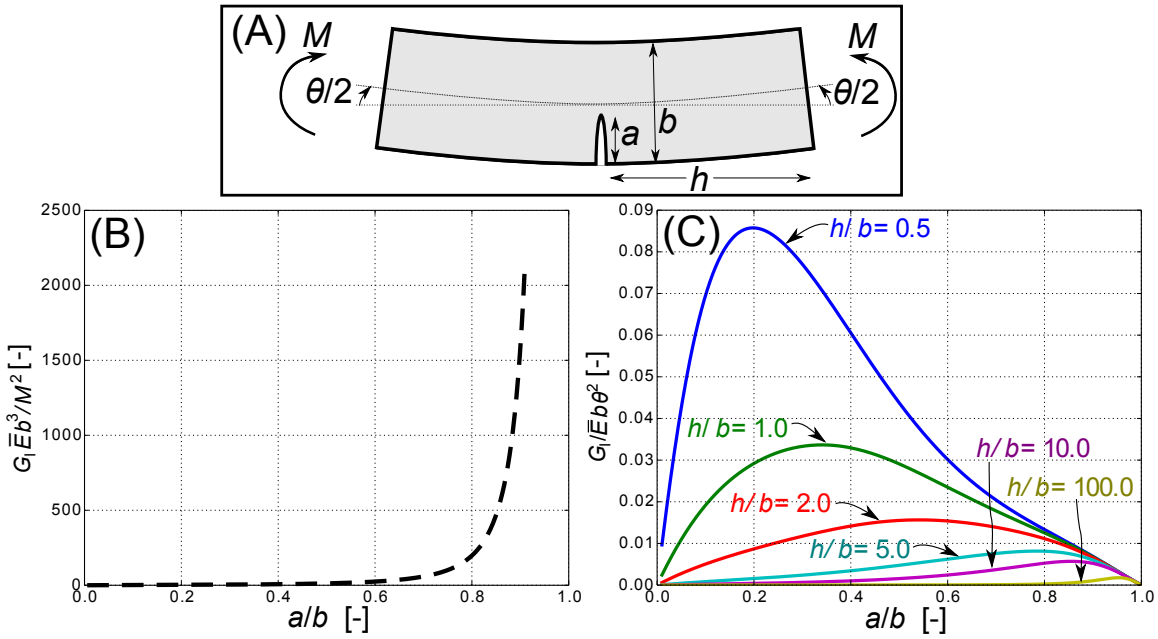

Figure B.18: (A) Analytical model of pure bending specimen. (B) Energy release rate result (equation B.12) in moment control (dashed line). (C) Energy release rate result (equation B.13) in rotation control (solid lines) for different h/b.

Appendix C. Analytical model of a homogenous four-point SENB specimen

The homogeneous four-point SENB specimen in Figure C.19 with applied point loads can be described by three non-dimensional geometrical parameters: a/b, h/b and B/b. Equation 8 presents G_I as a function of applied load i.e. load control (dead load), but when designing experiments to be conducted under displacement control (fixed grip) it is more convenient to express G_I as a function of displacement, δ, of the force(s).

For a linear relationship between load and deflection, the work done by the external forces is (Ugural and Fenster [46] or Cook *et al.* [55]):

$$V_t = \frac{1}{2}P\delta \tag{C.1}$$

where P is the load and δ is the load point deflection. In an elastic beam structure, without energy dissipation i.e. a conservative system, the work done by the external force is equivalent to the total elastic strain energy (Ugural and Fenster [46] or Cook *et al.* [55]):

$$U_t = V_t \tag{C.2}$$

which is also known as Clapeyron's theorem in linear elasticity theory [56, 57]. The total strain energy, U_t, stored in the body of the four-point SENB specimen in Figure C.19 is the sum of the strain energy for the specimen without crack plus the strain energy for the introduction of the crack while holding

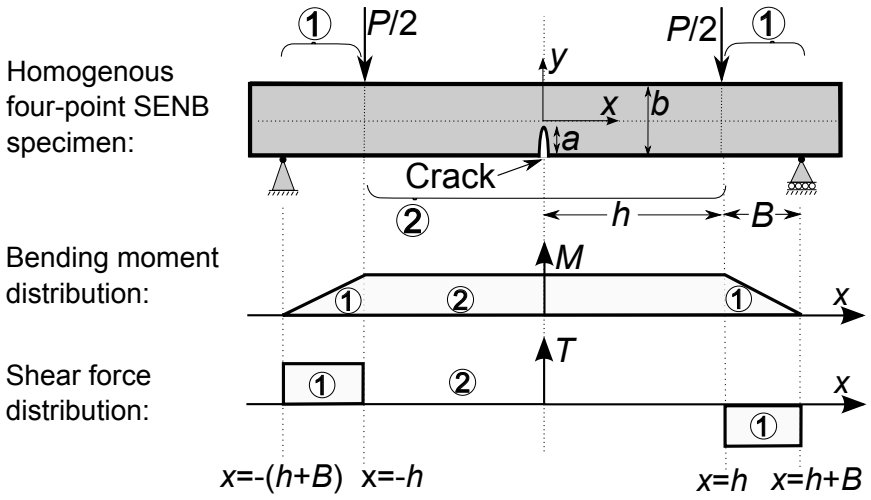

Figure C.19: Four-point bending setup including moment and shear distributions.

the forces constant, see Tada *et al.* [29], Appendix B, Beuth [47] or Rice *et al.* [44]:

$$U_t = U_{no,crack} + \int_0^a \frac{\partial U_t}{\partial a} da \tag{C.3}$$

where $G_I(a) = \partial U_t / \partial a$ [29, 58]. The latter term in equation C.3 is the change in elastic energy per unit cracked area due to the introduction of the crack and related to the ideas by Suo [59] and Beuth [47]. The strain energies from part 1 and part 2 of the beam specimen, marked with encircled numbers in Figure C.19 are added to the strain energy of the crack to form the total strain energy as [44]:

$$U_t = U_{no,crack} + U_{crack} = (U_1 + U_2) + U_{crack} \tag{C.4}$$

Part 1 of the beam spans over the length of, $-(h+B) \leq x \leq -h$ and $h \leq x \leq h+B$, according to Figure C.19. The strain energy of part 1 of the beam, designated U_1, consists of a strain energy contribution from the force, P, causing both bending deformation and shear deformation of the beam i.e. normal stresses and shear stresses. These strain energies are denoted U_P and U_T, respectively. The strain energy contribution based on normal stress in part 1 of the beam (from the force, P) is given by equation A.6 as:

$$U_P = \frac{2(P/2)^2 B^3}{\bar{E} b^3} \tag{C.5}$$

The strain energy based on the shear stresses in part 1 of the beam (from shear force, T) is determined in equation A.13 as:

$$U_T = \frac{3}{5} \frac{(P/2)^2 B}{\mu b} \tag{C.6}$$

where μ is the shear modulus that for an isotropic material is $\mu = E/(2(1+\nu))$. The strain energy for

part 1 of the beam becomes:

$$U_1 = 2(U_P + U_T) = 2\left(\frac{2(P/2)^2 B^3}{\bar{E}b^3} + \frac{3}{5}\frac{(P/2)^2 B}{\mu b}\right) = \frac{P^2 B}{\bar{E}b}\left[\left(\frac{B}{b}\right)^2 + \frac{3}{5}\frac{\bar{E}}{2\mu}\right] \tag{C.7}$$

where the factor "2" outside the parenthesis in equation C.7 is included since two regions of the specimen are numbered 1, see Figure C.19.

Part 2 of the beam in Figure C.19 spans over $-h \leq x \leq h$. The strain energy for part 2 of the beam, with length $2h$ and a pure bending moment applied, is derived using equation A.7 for U_{M_0}. Here, the moment, $M = BP/2$, and the length, $L_0 = 2h$, are inserted in equation A.7 for U_{M_0} to determine the strain energy for part 2 of the beam:

$$U_2 = 3\frac{P^2}{\bar{E}}\frac{B^2 h}{b^3} \tag{C.8}$$

The strain energy contribution from the crack is determined by inserting $\sigma_{xx} = 6M/b^2$ and $M = BP/2$ into $\theta_{crack} = (4\sigma_{xx}S(a/b))/\bar{E}$, which is the rotation due to the presence of the crack from Tada *et al.* [29], to give:

$$U_{crack} = \frac{1}{2}M\theta_{crack} = \frac{1}{2}M\frac{4\sigma_{xx}}{\bar{E}}S(a/b) = 3\frac{P^2}{\bar{E}}\frac{B^2}{b^2}S(a/b) \tag{C.9}$$

where $U_{crack} = \frac{1}{2}M\theta_{crack}$ comes from equation B.6 and $S(a/b)$ is given by an empirical fit in Tada *et al.* [29] and presented in equation B.9 for convenience. Thus, for the homogenous four-point SENB specimen, the strain energy of part 1, part 2, and the crack (equation C.7, C.8, C.9) can now be added to give a single expression for the total strain energy of the beam specimens volume as:

$$U_t = U_1 + U_2 + U_{crack} = \frac{P^2 B}{\bar{E}b}\left[\left(\frac{B}{b}\right)^2 + \frac{3}{5}\frac{\bar{E}}{2\mu}\right] + 3\frac{P^2}{\bar{E}}\frac{B^2 h}{b^3} + 3\frac{P^2}{\bar{E}}\frac{B^2}{b^2}S(a/b) \tag{C.10}$$

This expression (equation C.10) is used in section 3 to determine G_I in displacement control (fixed grip).

References

[1] S. Ataya, M. M. Z. Ahmed, Damages of wind turbine blade trailing edge: Forms, location, and root causes, Engineering Failure Analysis 35 (2013) 480.

[2] J. Cook, J. E. Gordon, C. C. Evans, D. M. Marsh, A mechanism for the control of crack propagation in all-brittle systems, Mathematical and Physical Sciences 282 (1391) (1964) 508–520.

[3] V. Gupta, J. Yuan, D. Martinez, Calculation, measurement, and control of interface strength in composites, J. Am. Ce. Soc. 76 (2) (1993) 305.

[4] M. Y. He, J. W. Hutchinson, Crack deflection at an interface between dissimilar elastic materials, Int. J. Solids Structures 25 (9) (1989) 1053–1067.

[5] M. Y. He, A. G. Evans, Crack deflection at an interface between dissimilar elastic materials: Role of residual stresses, Int. J. Solids Structures 31 (1994) 3443.

[6] V. Gupta, A. S. Argon, Z. Suo, Crack deflection at an interface between two orthotropic media, J. Appl. Mech. 59 (1992) 79.

[7] D. Martinez, V. Gupta, A. S. Argon, Z. Suo, Energy criterion for crack deflection at an interface between two orthotropic media, J. Mech. Phys. Solids. 42 (8) (1994) 1247.

[8] M. D. Thouless, H. C. Cao, P. A. Mataga, Delamination from surface cracks in composite materials, Journal of Materials Science 24 (1989) 1406–1412.

[9] J. Parmigiani, M. Thouless, The roles of toughness and cohesive strength on crack deflection at interfaces, Journal of the Mechanics and Physics of Solids 54 (2) (2006) 266–287. doi:10.1016/j.jmps.2005.09.002.

[10] J. P. Parmigiani, Delamination and deflection at interfaces, Ph.D. thesis, University of Michigan (2006).

[11] J. L. Strom, J. P. Parmigiani, Transition of crack path at bi-material interfaces, Engineering Fracture Mechanics 115 (2014) 13–21. doi:10.1016/j.engfracmech.2013.11.015.

[12] S. Brinckmann, B. Völker, G. Dehm, Crack deflection in multi-layered four-point bending samples, International Journal of Fracture 190 (1-2) (2014) 167–176. doi:10.1007/s10704-014-9981-1.

[13] M. Alam, J. P. Parmigiani, Proc. Appl. Math. Mech., in: Crack propagation at bi-material interfaces, Vol. 15, 2015, pp. 143–144. doi:10.1002/pamm.201510062.

[14] M. Alam, B. Grimm, J. P. Parmigiani, Effect of incident angle on crack propagation at interfaces, Engineering Fracture Mechanics 162 (2016) 155–163.

[15] V. C. Li, R. J. Ward, A novel testing technique for post-peak tensile behavior of cementitious materials, Fracture Toughness and Fracture Energy, Mihashi et al. (eds). (1989) 183.

[16] S. Goutianos, R. Arevalo, B. F. Sørensen, T. Peijs, Effect of Processing Conditions on Fracture Resistance and Cohesive Laws of Binderfree All-Cellulose Composites, Applied Composite Materials 21 (6) (2014) 805–825. doi:10.1007/s10443-013-9381-0.

[17] R. K. Joki, F. Grytten, B. Hayman, B. F. Sørensen, Determination of a cohesive law for delamination modelling - Accounting for variation in crack opening and stress state across the test specimen width, Composites Science and Technology 128 (2016) 49–57. doi:10.1016/j.compscitech.2016.01.026.

[18] W. Lee, W. J. Clegg, The deflection of cracks at interfaces, Key Engineering Materials 116-117 (1996) 1886–1889. doi:10.4028/www.scientific.net/KEM.132-136.1886.

[19] K. Kendall, Transition between cohesive and interfacial failure in a laminate, Proc. R. Soc. Lond.A. 344 (1975) 287–302. doi:10.1098/rspa.1983.0054.

[20] J. Zhang, J. J. Lewandowski, Delamination study using four-point bending of bilayers, Journal of Materials Science 32 (14) (1997) 3851–3856.

[21] J. B. Jørgensen, M. D. Thouless, B. F. Sørensen, C. Kildegaard, Determination of mode-I cohesive strength for interfaces, IOP Conference Series: Materials Science and Engineering 139 (2016) 267–274. doi:10.1088/1757-899X/139/1/012025.

[22] J. E. Srawley, W. F. Brown Jr, Fracture toughness testing methods, ASTM STP 381 (1) (1965) 133–196.

[23] B. Gross, J. Srawley, Stress-intensity factors for single-edge-notch specimens in bending or combined bending and tension by boundary collocation of a stress function., NASA TN D-2603.

[24] W. Brown, J. Strawley, Plane Strain Crack Toughness testing of high strength metallic materials., Astm STP 410 (3) (1966) 1–129. doi:10.1520/STP410-EB.

[25] B. Gross, J. Srawley, Stress-intensity factors by boundary collocation for single-edge-notch specimens subject to splitting forces, NASA TN D-3295.

[26] R. K. Bordia, B. Dalgleish, P. G. Charalambides, A. G. Evans, Cracking and Damage in a Notched Unidirectional Fiber-Reinforced Brittle Matrix composite, J. Am. Ceram. Soc. 74 (11) (1991) 2776–80.

[27] S. Tarafder, M. Tarafder, V. R. Ranganath, Compliance crack length relations for the four-point bend specimen, Engineering Fracture Mechanics 47 (6) (1994) 901–907. doi:10.1016/0013-7944(94)90068-X.

[28] F. Fischer, G. Pusch, Fracture mechanical testing of structural steels - SENB-specimen under four-point-bending, Materialprufung 37 (4) (1995) 115.

[29] H. Tada, P. C. Paris, G. R. Irwin, The Stress Analysis of Cracks Handbook, 3rd Edition, Vol. 3, ASME Press, New York, 2000.

[30] C. Liu, P. J. Rae, C. M. Cady, M. L. Lovato, Damage and fracture of high-explosive mock subject to cyclic loading., Proceedings of the 2011 Annual Conference on Experimental and Applied Mechanics. 3 (2011) 151.

[31] A. D. Wargo, S. Safavizadeh, R. Y. Kim, The use of four-point bending notched beam fatigue tests to rank crack-mitigating interlayers, 8th RILEM International Symposium on Testing and Characterization of Sustainable and Innovative Bituminous Materials. 11 (2016) 359.

[32] M. L. Nguyen, H. Di Benedetto, C. Sauzéat, Crack propagation characterisation of bituminous mixtures using a four-point bending notched specimen test, Road Materials and Pavement Design 17 (1) (2016) 70–86. doi:10.1080/14680629.2015.1063535.

[33] S. Tandon, K. T. Faber, Z. P. Bazant, Crack Stability in the Fracture of Cementitious Materials, in: Mat. Res. Soc. Symp. Proc., Vol. 370, 1995, pp. 387–396.

[34] Z. Suo, G. Bao, B. Fan, Delamination R-curve phenomena due to damage, Mech. Phys. Solids 40 (I) (1992) 1–16.

[35] P. A. Vanniamparambil, U. Guclu, A. Kontsos, Identification of crack initiation in aluminum alloys using acoustic emission, Experimental Mechanics 55 (5) (2015) 837–850. doi:10.1007/s11340-015-9984-5.

[36] A. N. Kumar, B. F. Sørensen, Fracture Resistance and Stable Crack-Growth Behavior of 8-mol%-Yttria-Stabilized Zirconia, Journal of the American Ceramic Society 83 (5) (2000) 1199–1206.

[37] A. N. Kumar, B. F. Sørensen, Fracture energy and crack growth in surface treated Yttria stabilized Zirconia for SOFC applications, Materials Science and Engineering A 333 (1-2) (2002) 380–389. doi:10.1016/S0921-5093(01)01863-9.

[38] T. Nishida, Y. Hanaki, G. Pezotti, Effect of notch-root radius on the fracture toughness of a fine-grained alumina, J. Am. Ceram. Soc. 77 (2) (1994) 707–608.

[39] B. Gross, J. E. Srawley, Stress-Intensity Factors for Single-Edge-Notch Specimens in Bending or Combined Bending and Tension By Boundary Collacation of a Stress Function, NASA Technical note TN D-2603 (January 1965) (1964) 1–17.

[40] J. Dundurs, Edge-Bonded Dissimilar Orthogonal Elastic Wedges Under Normal and Shear Loading, Journal of Applied Mechanics 36 (3) (1969) 650–652.

[41] J. W. Hutchinson, Z. Suo, Mixed mode cracking in layered materials, Advances in applied mechanics 29 (1992) 63.

[42] G. Irwin, D. Washington, Analysis of Stresses and Strains Near the End of a Crack Traversing a Plate, Journal of Applied Mechanics 24 (1957) 361–364.

[43] J. W. Hutchinson, Fundamentals of the Phenomenological Theory of Nonlinear Fracture Mechanics, Journal of Applied Mechanics 50 (4) (1983) 1042–1051. doi:10.1115/1.3167187.

[44] J. R. Rice, P. C. Paris, J. G. Merkle, Some further results of J-integral analysis and estimates, Progress in Flaw Growth and Fracture Toughness Testing 536 (536) (1973) 231–245. doi:10.1520/STP49643S.

[45] Z. Suo, J. W. Hutchinson, Interface crack between two elastic layers, International Journal of Fracture 43 (1990) 1–18.

[46] S. Fenster, A. Ugural, Advanced Strength and Applied Elasticity, 4th Edition, Prentice Hall, Upper Saddle River, New Jersey, 2003.

[47] J. L. Beuth, Cracking of thin films in residual tension, Int. J. Solids Structures 29 (13) (1992) 1657.

[48] H. P. Langtangen, Python Scripting for Computational Science, 2nd Edition, Springer, 2008.

[49] H. P. Langtangen, A Primer on Scientific Programming with Python, 4th Edition, Springer, 2014.

[50] U. P. Singh, S. Banerjee, On the origin of pop-in crack extension, Acta metall. mater. 39 (6) (1991) 1073–1084.

[51] M. Charalambides, A. J. Kinloch, Y. Wang, J. G. Williams, On the analysis of mixed-mode failure, International Journal of Fracture 54 (3) (1992) 269–291. doi:10.1007/BF00035361.

[52] Z. Suo, G. Bao, B. Fan, T. Wang, Orthotropy rescaling and implications for fracture in composites, Int. J. Solid Structures 28 (2) (1991) 235–248.

[53] H. P. Gavin, Strain Energy in Linear Elastic Solids, Tech. rep., Duke University, Department of Civil and Enironmental Engineering (2015).

[54] J. Gere, B. Goodno, Mechanics of Materials, 7th Edition, Cengage learning, 2009.

[55] R. D. Cook, D. S. Malkus, M. E. Plesha, R. J. Witt, Concepts and applications of finite element analysis, fourth edi Edition, Wiley, United States, 2001.

[56] A. Love, A Treatise on the Mathematical Theory of Elasticity, 4th Edition, At the University Press, Cambridge, 1927.

[57] S. S. Timoshenko, History of Strength of Materials, The maple press company, New York, 1953. doi:10.1016/0022-5096(54)90010-1.

[58] C. T. Sun, Z. H. Jin, Fracture Mechanics, 1st Edition, Elsevier, Amsterdam, 2012.

[59] Z. Suo, Failure of brittle adhesive joints, Appl. Mech 43 (5) (1990) 275–279.

APPENDED PAPER P5

Crack deflection at interfaces in adhesive joints for wind turbine blades

Jeppe B. Jørgensen, Bent F. Sørensen and Casper Kildegaard
Composites Part A: Applied Science and Manufacturing
Submitted, 2017

Crack deflection at interfaces in adhesive joints for wind turbine blades

Jeppe B. Jørgensen[a,b,*], Bent F. Sørensen[b], Casper Kildegaard[a]

[a] *LM Wind Power, Østre Alle 1, 6640 Lunderskov, Denmark.*
[b] *The Technical University of Denmark, Dept. of Wind Energy, Frederiksborgvej 399, 4000 Roskilde, Denmark.*

Abstract

Crack deflection at material interfaces is investigated using a new experimental approach by recording images and applying 2D digital image correlation (DIC) on a four-point single-edge-notch-beam (SENB) test specimen. A crack grows from the notch towards the adhesive-substrate interface in mode-I. For six types of test series, measurements from DIC captured three different cracking mechanisms; crack penetration into the substrate, crack deflection along the interface, and initiation of a new crack at the interface ahead of the main crack.

The latter cracking mechanism, i.a. observed in adhesive-composite bi-material specimens, enabled the determination of the mode-I cohesive strength of the material interfaces using a novel approach. The measured cohesive strength of the tested interfaces was found to be low in comparison with the macroscopic strength of the adhesive.

Keywords:
Cohesive interface modelling, Strength, Mechanical testing, Finite element analysis (FEA)

1. Introduction

In typical wind turbine rotor blades, the main parts are two aerodynamic shells and two webs made of glass-fibre reinforced composites produced by a vacuum infusion process. The shells and webs are moulded separately and subsequently bonded in an assembly process using a structural adhesive. The main load carrying adhesive joints are located at the leading-edge, trailing-edge and at the webs [1]. The primary loads acting on the blade can be simplified to flap-wise- and edge-wise bending moments. Figure 1 illustrates that edge-wise bending moments, M_{yy}, can lead to tensile stresses, σ_{xx}, in the adhesive of the trailing-edge joint. The trailing-edge joint is located far from the elastic center of the blade cross section and therefore loaded with significantly higher strains which can cause transverse cracks to evolve from pre-existing flaws in the adhesive.

*Corresponding author
Email address: jbj@lmwindpower.com (Jeppe B. Jørgensen)

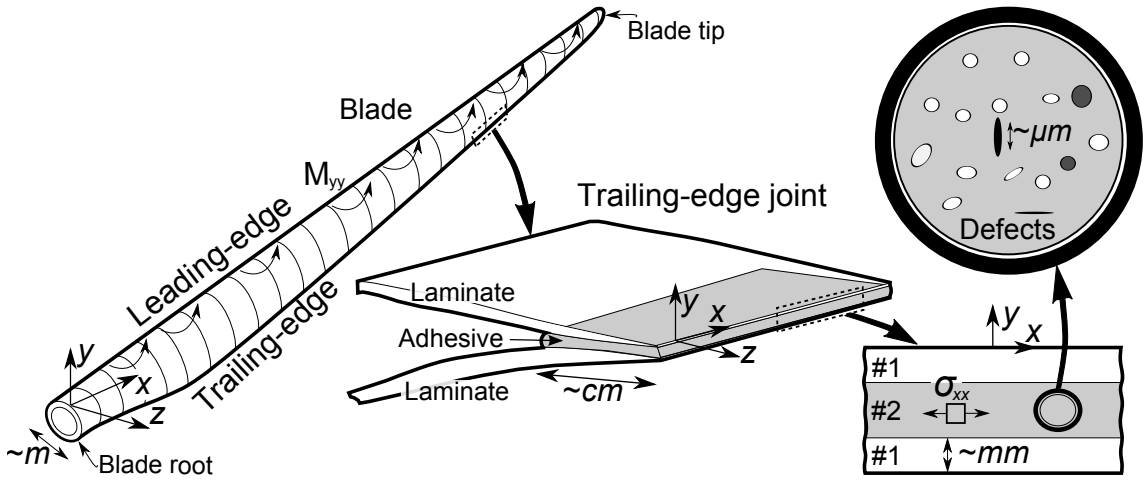

Figure 1: Wind turbine rotor blade with trailing-edge joint loaded in tension due to edge-wise bending moments, M_{yy}. The different order of scale from full scale blade to micro-scale defects in the adhesive layer is exemplified by m, cm, mm, and μm.

Cracks in the trailing-edge joint, including transverse cracks, are observed in full scale blades in operation [2]. After a small crack has formed in the adhesive as shown in Figure 2 (A), the cracking sequence can evolve in three different ways as shown schematically in Figure 2 (B-E). It is the issue of crack deflection/penetration that is in focus of the present study. Crack deflection at interfaces in composite materials is known to act as a toughening mechanism for the overall structure [3, 4] which is why a criterion for deflection is often desired.

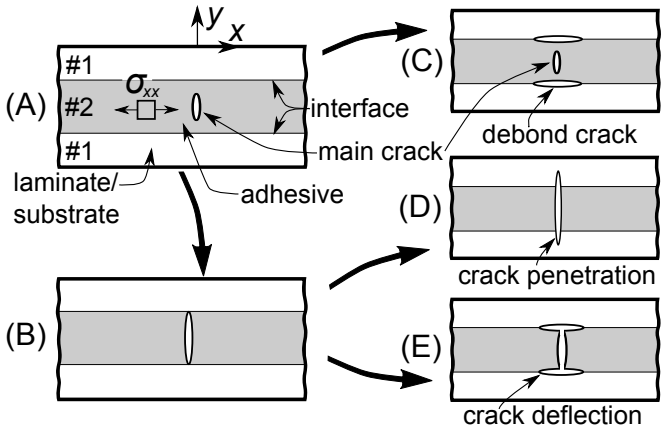

Figure 2: Possible cracking sequence for an adhesive joint loaded in tension. The main crack in the adhesive grows orthogonal towards the adhesive/substrate interface (A). The crack might reach the interface (B) or initiate a new crack at the adhesive/substrate interface (C). If the crack reach the interface it may stop here (B), but it can also penetrate the substrate (D) or deflect along the adhesive/substrate interface (E).

One of the first models for the cracking mechanism in Figure 2 (C) were developed by Cook and Gordon [5]. A stress based criterion was established for an elliptical shaped crack in a homogeneous solid. The Cook-Gordon deflection criterion states that the interface will fail if the interface strength is less than about 1/3 to 1/5 of the bulk material strength. Otherwise, the main crack will propagate across the interface.

Later, a fracture mechanics based approach was applied to predict crack deflection for the cracking mechanism in Figure 2 (B), by introducing an infinitesimal small crack at the interface and in the substrate [6, 7, 8]. In absence of elastic mismatch, the deflection criterion states that the interface-to-substrate toughness ratio should be one fourth or less for the crack to deflect.

The stress based and fracture mechanics based approaches can be unified in a cohesive zone approach. Parmigiani and Thouless [9] studied crack deflection in a thin film on a thick substrate using cohesive zone modelling (CZM) in finite element (FE) simulations and it was concluded that both the cohesive strength and the toughness are important parameters for an accurate crack deflection criterion.

Recently, Brinckmann *et al.* [10] modelled and tested crack deflection in multi-layered four-point bending samples. A cohesive zone model was developed to predict deflection/penetration of the different layers, by varying the cohesive strength and the fracture toughness. They also conclude that both the cohesive strength and the fracture toughness are important parameters for the crack deflection process. Unfortunately for the experiments, crack growth were unstable according to the measured load-displacement curve such that the crack deflection process could not be documented by images [10].

There are only a few rigorous experimental studies where the crack deflection process are well documented [11]. Kendall [12] tested transparent rubber using a single-edge-notch-tension (SENT) specimen to test a derived crack deflection criterion for a Griffith crack [13]. SENT specimens with different interface toughness were manufactured and characterized. Details about the crack deflection process were limited since the crack growth was unstable. Instead, it was assumed that the main crack reached the interface where it, dependent on interface toughness, continued through its path or deflected along the interface.

Later, Lee and Clegg [11] tested crack deflection experimentally. A wedge were moved into the notch of a PMMA laminate while the specimen were placed on a rigid foundation. The foundation were slowly removed whereby a crack started to grow slowly from the notch in a stable manner. It was documented that a new crack formed at the interface before the main crack reached the interface, similarly to the mechanism shown in Figure 2 (C). Different interface toughness were tested and a toughness based criterion were established to predict the interface debond length: The higher interface toughness, the smaller debond length and vice versa.

In order to test crack deflection at interfaces, Zhang and Lewandowski [14] tested three types of four-point single-edge-notch-beam (SENB) specimens with varying interface properties. The aluminum-to-composite adhesion were made by roll bonding, roll bonding with aluminum interlayer and epoxy bonding. Three different cracking mechanisms were assessed in the light of strength as the governing property for crack path selection:

- High interface strength: Crack penetrates into substrate (Figure 2 (D)).
- Intermediate interface strength: Crack reaches the interface and deflects. (Figure 2 (E)).
- Low interface strength: Crack initiation at interface ahead of main crack (Figure 2 (C)).

Unfortunately, stable crack growth could only be attained for the specimens with high interface strength where the crack penetrated the interface. For the other two cases, the crack deflection could only be seen as a sudden jump in the measured moment-displacement curve.

The recent developments of digital image correlation (DIC) suggests that more accurate experimental studies can be made in order to identify crack deflection during loading by in-situ observations. DIC is a white-light full field method using a digital camera and a software package to measure displacements by comparing images of the deformed- and undeformed specimen. DIC is an experimental mechanics method that has been successfully applied on adhesive joints to characterize the damage sequence e.g. for single-lap-joints [15, 16], double-butt-strap-joints [17] or bonded repair patches [18, 19, 20, 21]. DIC has also been used to determine crack tip location during both static and cyclic loading [22, 23] and been applied on bending experiments for various applications e.g. for the four-point SENB specimen [22, 23, 24].

Cohesive laws, also known as traction-separations laws, can conveniently be used in numerical cohesive zone models to simulate both crack initiation that is largely governed by the cohesive strength, $\hat{\sigma}$, and crack propagation that is primarily governed by fracture energy, J_c [25]. Cohesive zone modelling of crack deflection requires input in terms of traction-separations laws with the most important parameters being the fracture energy, the critical separation, δ_{cr}, and the cohesive strength of the interface, $\hat{\sigma}_i$, and -substrate, $\hat{\sigma}_s$, see the example of a traction-separation law in Figure 3. The cohesive law parameters of a straight-growing crack can be measured e.g. using a J-integral approach [26, 27, 28, 29]. Mohammed and Liechti [30] measured the cohesive law parameters for an aluminum-epoxy bi-material interface using a calibration procedure where cohesive zone modelling by finite element simulations were combined with measurements from an experimental test of a four-point bend specimen. However, experimental methods to measure the cohesive law parameters for bi-material interfaces are limited and accurate determination of the cohesive strength magnitude is challenging [31]. A novel approach [32] demonstrated a new way to overcome this problem. Therefore, it is the aim in this paper to apply

the novel approach [32] to determine the cohesive strength, $\hat{\sigma}_i$, of the adhesive-substrate interface using the cracking mechanism in Figure 2 (C).

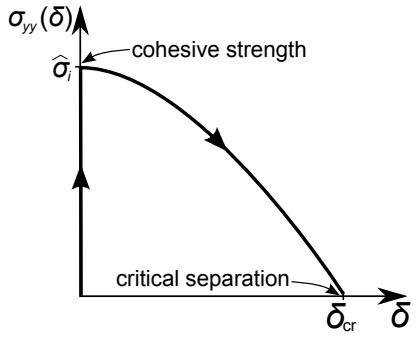

Figure 3: Schematic traction-separation law for a zero-thickness interface.

To summarize, crack deflection at interfaces is one of the primary cracking mechanisms of composite structures and composite-adhesive joints. Also, stable crack growth experiments where the crack deflection process are clearly documented are limited. Thus, it is the goal in the present paper to:

(i) perform stable crack growth experiments for different material systems/interfaces and apply DIC to study cracking mechanisms during loading by in-situ observations.

(ii) apply a novel approach [32] to determine the cohesive strength of the interface, $\hat{\sigma}_i$, for tests with the cracking mechanism shown in Figure 2 (C).

Point (i) is used to clarify experimentally which of the cracking mechanisms (deflection, penetration or initiation of a new crack) in Figure 2 (C-E) that can evolve for a selected range of material systems. Therefore, stable crack growth and in-situ observations are important.

2. Problem definition

For the adhesive-composite sandwich joint design in Figure 2 (A), it is difficult in practice to initiate a center-crack and achieve stable crack growth. Thus, for the purpose of the present paper (to obtain stable crack growth of a crack towards an interface) the center cracked test specimen is not useful [33]. Instead, the four-point SENB specimen in Figure 4 is preferred since the experiment can be designed such that the main crack in the displacement-loaded four-point SENB specimen grows stable towards the bi-material interface [34].

The parameters that define the four-point SENB test specimen geometry are presented in Figure 4, where a_0 is the start-crack-length, a is the actual crack length, h is the horizontal distance between load point and main crack, and B is the horizontal distance between load- and support point. Furthermore, b is the thickness of the adhesive layer, c is the substrate thickness and d is the distance from crack

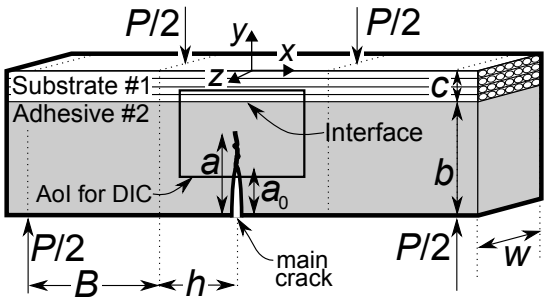

Figure 4: The four-point SENB test specimen geometry with symbols describing the geometry for the bi-material specimens.

tip to interface. The primary geometric parameters can be written in non-dimensional form as: a/b, h/b, B/b and c/b.

The four-point SENB specimen is analyzed in a related paper [34] for load control, displacement control, and test configuration since the mode-I energy release rate, G_I, of the main crack depends on load conditions, geometry, and stiffness mismatch. For all experiments in the present study, we use $h/b = 0.9$ and $B/b = 1.35$, and the specimens are manufactured such that $0.2 \leq c/b \leq 0.3$. To enable observations of the crack deflection mechanism, the main crack should grow in a stable manner towards the interface requiring that the energy release rate of the main crack must decrease with crack length i.e. $\partial G_I/\partial a < 0$. Using this criterion it was determined that the start-crack-length should be $0.55 \leq a_0/b \leq 0.70$ for elastic mismatch of $1.0 \leq E_1/E_2 \leq 12.0$, and substrate thickness of $0.1 \leq c/b \leq 0.3$ using the FE model presented in a related paper [34].

If a crack initiates in the interface between adhesive and substrate as shown in Figure 4, it will do so in pure mode-I since shear stresses, τ_{xy}, are zero along the vertical symmetry line (at $x = 0$). In order to study crack initiation, crack propagation and potentially crack deflection, an optical camera and DIC are applied to measure the displacement field in the area of interest (AoI) shown in Figure 4. The identification of interface crack initiation is the first step in the approach to determine the mode-I cohesive strength of the interface.

3. Approach for determination of mode-I cohesive strength of interfaces

For the cracking mechanism in Figure 2 (C), a novel approach [32] for determination of the cohesive strength of an adhesive-laminate interface, $\hat{\sigma}_i$, was demonstrated using a four-point SENB specimen, DIC, and a FE model. In the present study, the original approach [32] is elaborated and further extended to account for propagation of the main crack as illustrated in Figure 5.

The approach is based on the stress field of a crack tip close to an interface that has the purpose of initiating a new crack at the interface, see Figure 5 (A). Two scenarios can evolve during the test:

- Scenario 1: stationary main crack ($a = a_0$).
- Scenario 2: propagating main crack ($a > a_0$).

During the experiments, the displacement difference, $\Delta\delta$, across the zero-thickness interface is measured by DIC over the gauge length, l_g, between two points on each side of the interface as shown in Figure 6. During loading, the distance between the two points increases due to elastic deformation and initiation of the interface crack. For Scenario 1, where the main crack tip is stationary ($a = a_0$), the displacement difference, $\Delta\delta$, across the interface must increase linearly with applied load (and time, t) in the early stages of the experiment before interface separation, but becomes non-linear at the onset of interface crack initiation at time $t = t^*$ as shown by the sketched graph in Figure 5 (B). The onset of non-linear displacement difference is denoted $\Delta\delta^*$. The corresponding value of a is denoted a^* (in Scenario 1, $a^* = a_0$) and the value of moment, M, is denoted M^*, where the moment is per specimen width. Additionally, for Scenario 1 ($a^* = a_0$), the crack initiation can also be detected by visual monitoring (in-situ). Assuming linear-elastic materials and a zero-thickness interface, the non-linearity in measured displacement difference across the interface is attributed interface separation only.

In Scenario 2, the main crack propagates ($a^* > a_0$), which change the stress field hence the relationship between load and displacement becomes non-linear even though the interface crack remains closed. Thus, visual monitoring is the only way to detect crack initiation at the interface. Therefore, it is important to record the crack length and displacement field simultaneously so that the values of M^* and a^* can be determined.

For a zero-thickness cohesive law and linear elastic materials, no opening is expected before the normal stress, $\sigma_{yy,i}$, reaches the cohesive strength, $\hat{\sigma}_i$, see Figure 3. Assuming that the point of non-linearity in measured displacement difference is the onset of crack initiation at the interface means that the level of stress, $\sigma_{yy,i}$, can be associated with the cohesive strength of the interface, $\hat{\sigma}_i$. Thus, at the time, t^*, where the crack at the interface initiates, the cohesive strength of the interface is equal to the stress across the interface i.e. $\hat{\sigma}_i = \sigma_{yy,i}$.

At the time of crack initiation, t^*, the associated moment, M^*, and crack length, a^*, are measured. These measurements (M^*, a^*/b) are applied to a 2D linear-elastic FE model of the experiment, see Figure 5 (C). The stress across the interface, $\sigma_{yy,i}$, corresponding to debond initiation is determined by:

$$\frac{\sigma_{yy,i} b^2}{M} = f(a/b, c/b, E_1/E_2) \tag{1}$$

The non-dimensional function, f, is determined by the FE model as shown by the results in Figure 7. Details of the FE model are presented in a related paper [34]. Note, the results for the four-point SENB models in Figure 7 depends on a/b, c/b and E_1/E_2, which make interpretation of the results

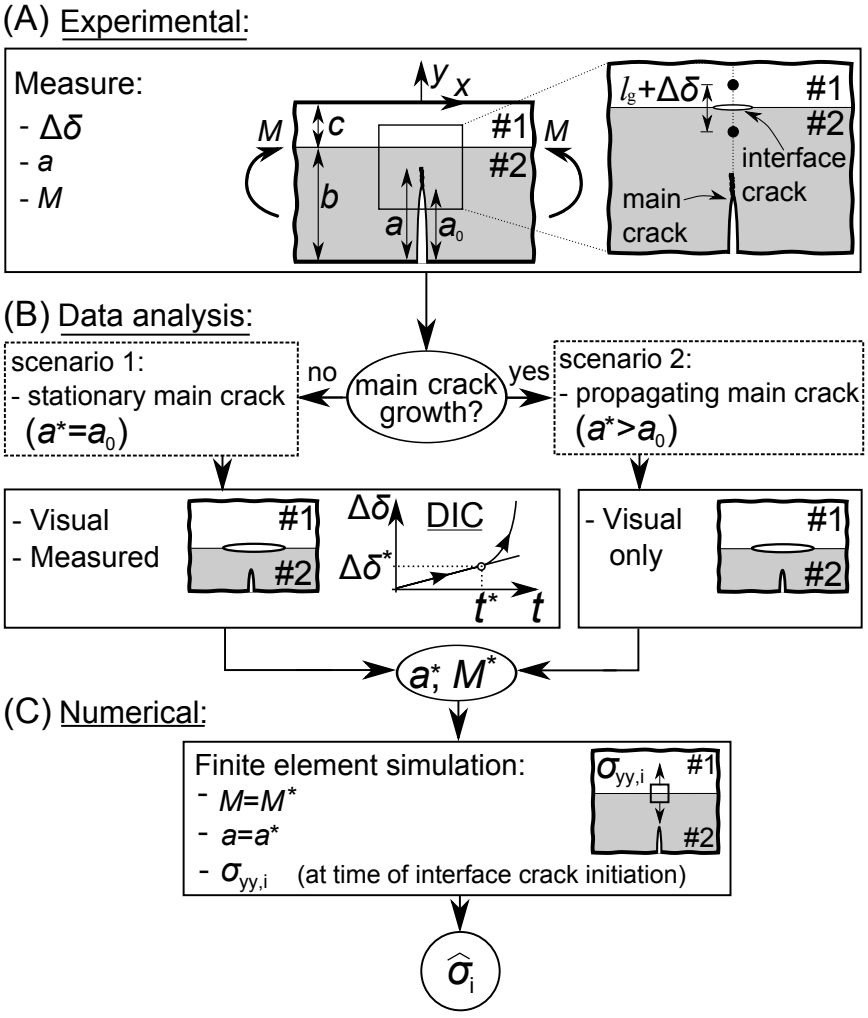

Figure 5: Approach to determine the cohesive strength of the interface, $\hat{\sigma}_i$. (A) Experimental. (B) Data analysis. (C) Numerical.

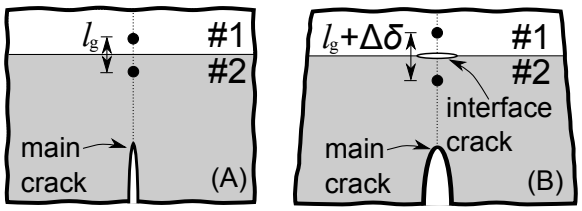

Figure 6: Illustration of l_g and $\Delta\delta$: (A) Undeformed state. (B) Deformed state.

challenging. However, M (and a/b in Scenario 2) are the only parameters in equation 1 that changes with time/loading during the experiment. The interface stress, $\sigma_{yy,i}$, scales linearly with M, but non-linearly with a/b as shown in Figure 7.

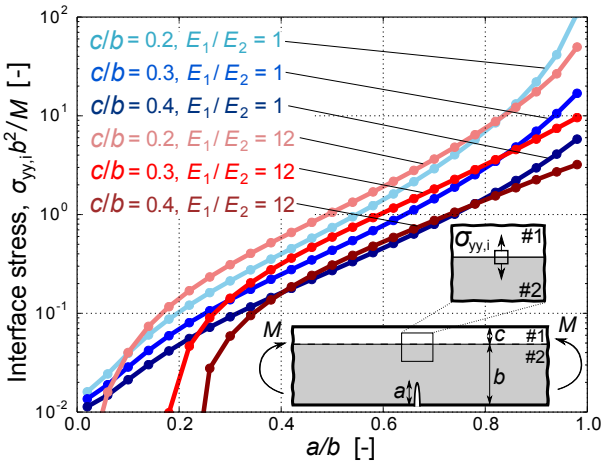

Figure 7: Results for normalised interface stress determined numerically as a function of relative crack length, a/b, and for different E_1/E_2 and c/b (results from [34]). Other parameters are $h/b = 0.9$ and $B/b = 1.35$.

4. Design and manufacturing of specimens for experiments

Six types of different four-point SENB specimens were manufactured and tested (A1, A2, B, C, D, E) as illustrated in Figure 8. Test series A (A1, A2), referred to as "model experiments", was designed for testing crack deflection versus crack penetration. Test series B, C, D, and E, referred to as "cohesive strength experiments", were designed for measuring the cohesive strength of different material interfaces. The specimens in test series A, B and C were moulded by injection of adhesive in-between two glass plates to create a homogenous plate of adhesive. The adhesive plate was post-cured. Prior to casting, the surfaces of the glass plates had been waxed to ease removal of adhesive after casting.

For test series A and C, two pre-cast adhesive plates of different thickness were subsequently bonded using the same type of adhesive. This process enabled that different interfaces could be manufactured; the roughened surface (A1: roughened interface), the smooth surface (A2: smooth interface) and peel ply embedded (C: peel ply interface). "Roughened interface" means that the surface at the interface was roughened with sandpaper of grid 180. "Smooth interface" means that the interface was left untreated, but cleaned. Thus, this surface finish was prepared by the surface of the smooth glass plate. The adhesive, applied in viscous form to bond the two pre-cast adhesive plates, were left for 20 hours to harden at room temperature. Finally, the tri-layer specimens were post cured and cut into

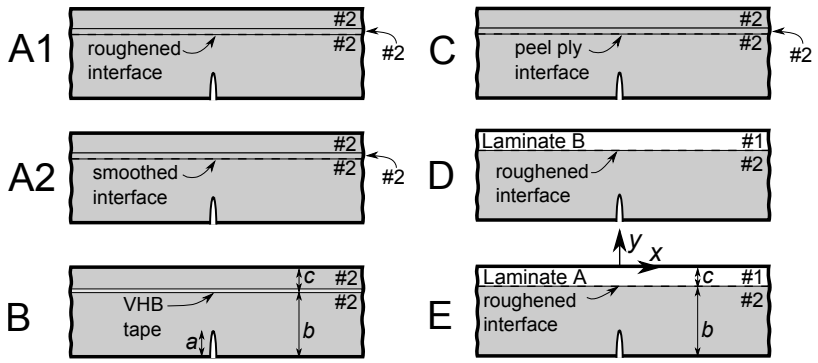

Figure 8: Six types of SENB test specimens divided into different categories. Model experiments: A1: roughened interface. A2: smoothed interface. Cohesive strength experiments: B: VHB tape interface, C: peel ply interface, D: roughened (Laminate B), E: roughened (Laminate A). Dashed lines indicate the material interface. (For bi-material experiments; #1: Laminate, #2: Adhesive).

beams.

For test series B, two pre-cast adhesive beams of different thickness were bonded by Very High Bond (VHB) tape (3M VHB Acrylic Adhesive 100MP).

The bi-material specimens in test series D and -E were manufactured of adhesive and glass-fiber laminates. The laminates were produced of polyester reinforced with non-crimp-fabrics of glass-fiber using vacuum-assisted-resin-transfer-moulding (VARTM). Subsequently, a vinylester adhesive paste was cast onto the laminate, creating a zero-thickness interface between the adhesive and the laminate. The plies were primarily uni-directional with main fiber-orientation in x-direction as shown in Figure 4 and Figure 8. The non-crimp-fabrics of glass fiber used for laminate A and laminate B had different fibre-architecture. The surface on the laminate was roughened with sandpaper of grid 180 to ensure a proper bonding of the adhesive to the surface of the laminate.

Start-cracks of length, a_0, for all test specimen types, were cut using first a thin hack saw, followed by a standard razor blade, and finally an ultra-thin razor blade of thickness 74 microns, see Figure A.21 in Appendix A.

It was the same adhesive type that was used as material #2 for all specimens, see Figure 8. The material systems were manufactured in a laboratory and are not representative for materials used in wind turbine blades. However, exact material properties are confidential and results are therefore presented in normalised form.

5. Test- and DIC setup

The test setup and equipment are presented in Figure 9. Vic 2D DIC system (Correlated Solutions) is employed to measure displacements. Practical guidelines for measuring with DIC and initial

experiments are used to determine the DIC setup and speckle pattern [35]. The settings are primarily inspired by the work of Reu [36, 37, 38, 39, 40, 41, 42], but also by Lava [43], and Pierron & Barton [44], and the guidelines in the Vic manual [45]. The description of preparation of speckle pattern and the settings used for the DIC measurements are presented in Appendix A.

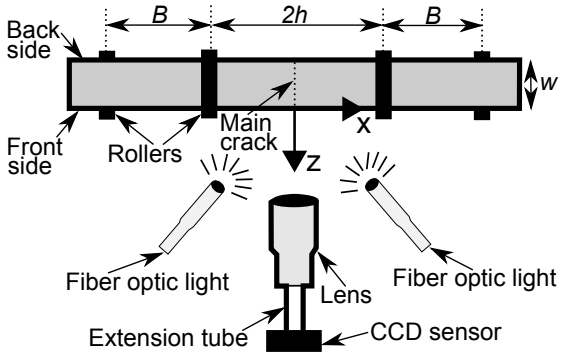

Figure 9: Top-view of the four-point bend test setup and equipment.

5.1. Experimental test setup

A MTS 858 Mini Bionix II servo-hydraulic test machine applied the monotic loading in displacement control. A load cell, calibrated for 1.5 kN, measured the load, P. A CCD sensor of type Grasshopper GRAS-50S5M (2448x2048 pixels) was mounted to a tri-pod and to the Fujinon CCTV Lens (HF50SA-1, 1:1.8/50mm) as shown in Figure 9. Extension tubes were used to achieve a proper magnification [38]. During the experiments, images were recorded with a frequency of 1 Hz.

5.2. Data analysis

Vic-2D (Vic Snap Software) was used to correlate the images by applying a normalized squared differences correlation algorithm (Optimized 8-tap interpolation scheme), see the Vic manual [45]. The displacement and strain fields were determined in the selected AoI thus the main crack tip and the interface were covered simultaneously.

The displacement field is the primary measurement and should preferably be used since it is determined with a better accuracy than the strain field [46]. For the studies of crack deflection, the primary use of DIC strain contours is to capture crack initiation (not to rely on a specific strain value), which by DIC manifests itself as localised strain at the interface. The displacement difference, $\Delta\delta$, is determined as the relative displacement over the initial gauge length, l_g, and thus based on the raw displacement measurements. The crack length, a, was measured directly on the images using a developed Python script [47, 48].

6. Results from model experiments in series A (penetration versus deflection)

The moment measured during the nine experiments in test series A1 is presented as a function of elapsed time in Figure 10. After the rollers have established fully contact, the moment increases linearly until a peak value is attained. A plateau in measured moment is found in the last part of the test. The plateau is located just before the main crack reach the interface. Next, the main crack propagates unstable through the specimen and penetrates into the substrate as indicated by the sudden drop in measured moment.

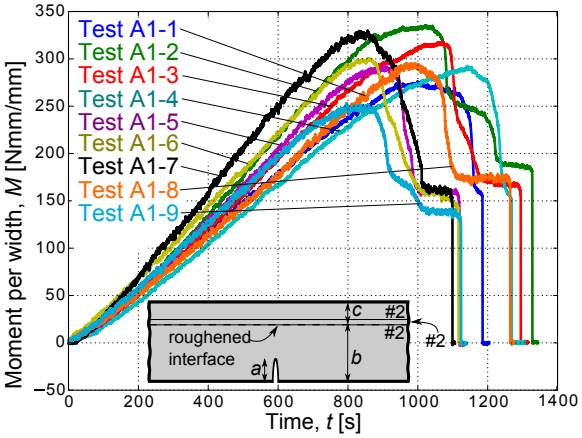

Figure 10: Results for specimens in series A1 with "roughened" interface.

Results from test A1-7 is evaluated in further details. The measured moment, crack length and strain contours for test A1-7 are presented in Figure 11. According to images of the front surface, the main crack grows stable from $a_0/b = 0.64$ to $a/b = 0.92$. The crack speed decreases significantly as indicated by the larger number of data points in the plot for $0.90 \leq a/b \leq 0.92$. From $a/b = 0.92$ and onwards the main crack growth becomes unstable and the crack penetrates into the substrate. Evaluation of the fracture surfaces for test specimen A1-7 shows that the main crack has reached the interface in the center of the specimen (at $z = -w/2$), but not on the front surface (at $z = 0$). Thus, a crack front with shape as a thumbnail is identified and measured to be $a/b = 0.08$ longer in the center than at the front of the specimen.

The measured moment for the five experiments in test series A2 is presented in Figure 12. Test A2-1 is selected for further analysis. The moment and crack length measured for test A2-1 are presented in Figure 13 (A). The moment increases linearly with time until the main crack starts to grow at time $t \approx 1200$ s. The main crack grows stable towards the interface until time $t \approx 1402$ s, see the image in Figure 13 (B), where the crack length is measured to be $a/b = 0.92$. Next, at time $t \approx 1404$ s, it is observed that the main crack deflects along the interface, see Figure 13 (C).

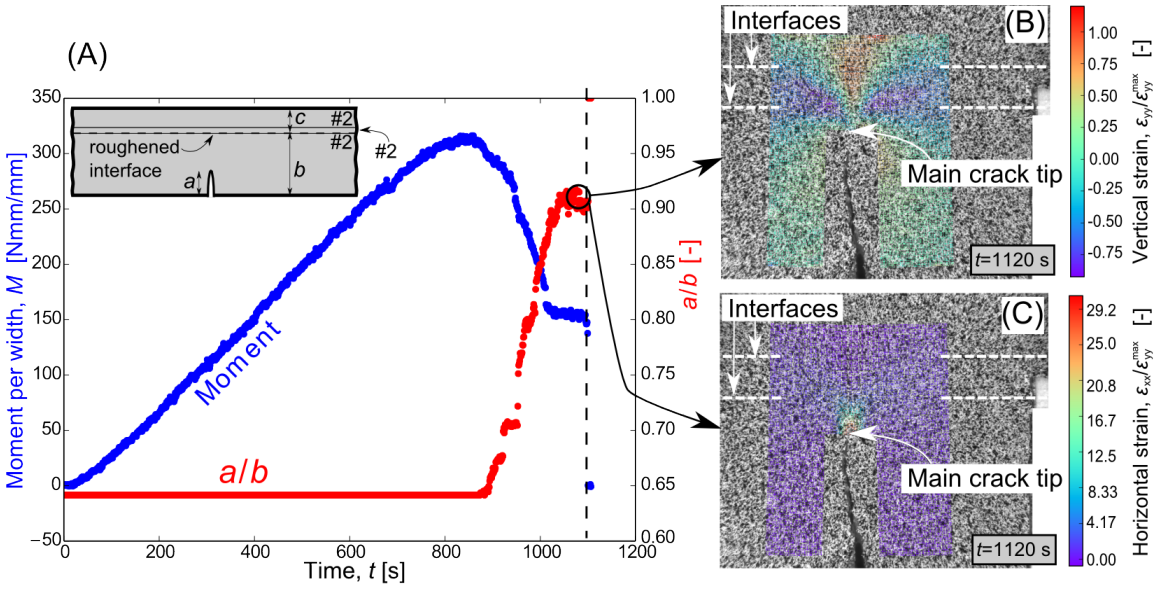

Figure 11: Results for test specimen A1-7 with crack penetration. ϵ_{yy}^{max} is the maximum vertical strain measured measured by DIC in (B). DIC contour plots illustrate: (B) the vertical strain and (C) horizontal strain just before crack penetration.

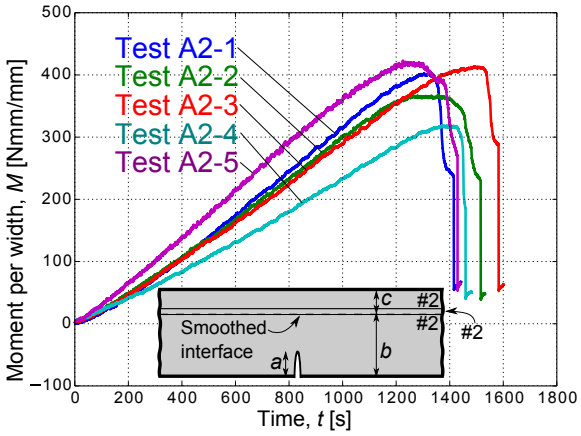

Figure 12: Results for specimens in series A2 with "smooth" interface.

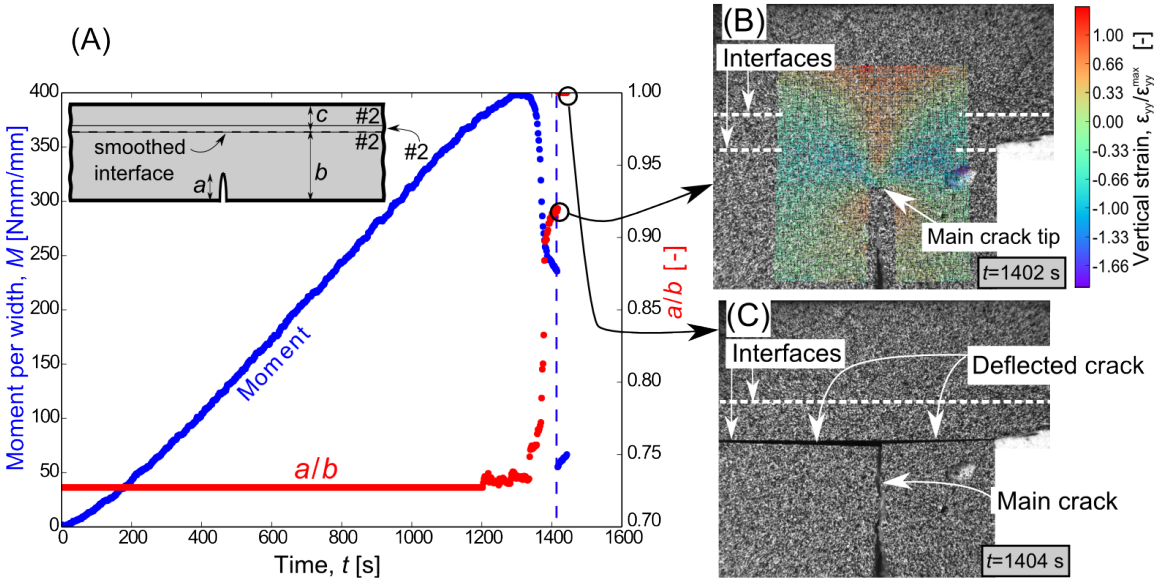

Figure 13: Results for test specimen A2-1 with crack deflection. (A): Moment and crack length. (B): Vertical strain contour. (C): After crack deflection. ϵ_{yy}^{max} is the maximum vertical strain measured by DIC in (B).

A comparison of test A1-7 (rough interface) with test A2-1 (smooth interface) is presented. The geometries are similar and the last crack length measurement for both tests is $a/b = 0.92$ (compare Figure 11 (A) with Figure 13 (A)). This, and evaluation of the fracture surfaces, indicates that a thumbnail shaped crack is $a/b = 0.08$ longer in the center (at $z = -w/2$) than at the edges (at $z = 0$) of both specimens (A1-7 and A2-1). This suggests that the main crack, in test series A2, first reaches the interface and then deflects along the interface.

7. Results for experiments with adhesive tape - series B

Images taken during the test of specimen B-1 with VHB tape embedded in the interface (Figure 14 (A)) are presented in Figure 14 (B-D). As shown in Figure 14, the interface separation starts before the main crack reaches the interface. For test series B, Scenario 2 ($a^* > a_0$) is observed since the main crack has propagated slightly from its initial position, which is measured on the front surface. Thus, a non-linear load-strain relationship cannot be used to determine the onset of interfacial separation. Therefore, the onset of separation (t^*, M^* and a^*) must be identified visually on images, see Figure 14, and a^* must be measured on images accordingly.

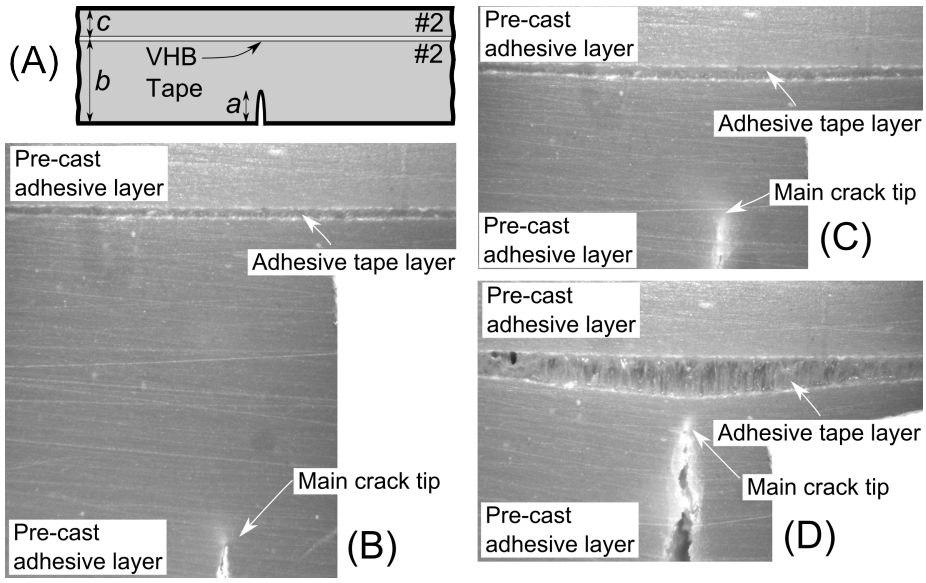

Figure 14: (A) Results from test with specimen B-1 with VHB tape at the interface. (B) Beginning of separation ($M = M^* = 150$ Nmm/mm, $a/b = a^*/b = 0.64$, $\Delta\delta = \Delta\delta^*$). (C) Large interface separation ($M = 61$ Nmm/mm). (D) Very large separation ($M = 32$ Nmm/mm).

8. Results for peel ply experiments - series C

The measured moment for test series C with peel ply interface is presented in Figure 15 (B). Figure 15 (C-E) illustrates images of test C-2 at different time steps. For test specimen C-2 with peel ply interface, Figure 15 (C) shows that the interface separates ($t^* = 1374$ s) after the beginning of main crack growth. Thus, for the specimens in test series C, Scenario 2 is observed ($a^* > a_0$). Just after interfacial debond, the main crack grows unstable towards the interface as shown by the progress from Figure 15 (D) to Figure 15 (E) and from the curves in Figure 15 (B). This behavior is explained by the FE model in Appendix B.

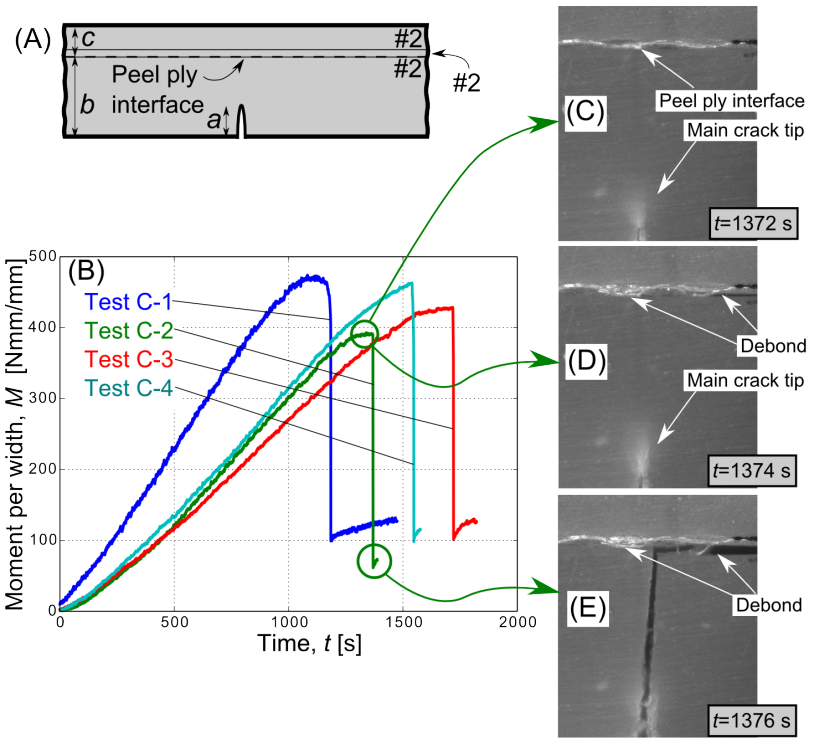

Figure 15: (A) Specimens in series C with "peel ply" interface. (B) Moment as a function of time. (C) Test C-2 before debond at time $t = 1372$ s. (D) Test C-2 after debond initiation at time $t = 1374$ s. (E) Test C-2 after debond and after main crack reach the interface at time $t = 1376$ s.

9. Results for bi-material experiments - series D and E

The measured moment-time relationships for test series D and E are presented in Figure 16 and Figure 17, respectively. For all of these tests, the moment increases linearly after the rollers have established fully contact on the specimen at time $t \approx 50$ s. The main crack grows stable towards the interface until the interface suddenly debonds as indicated by the sudden drop in measured moment in Figure 16-17. Differences in start-crack-length, a_0, and adhesive layer thickness, b, are the main reasons for the specimen-to-specimen variation.

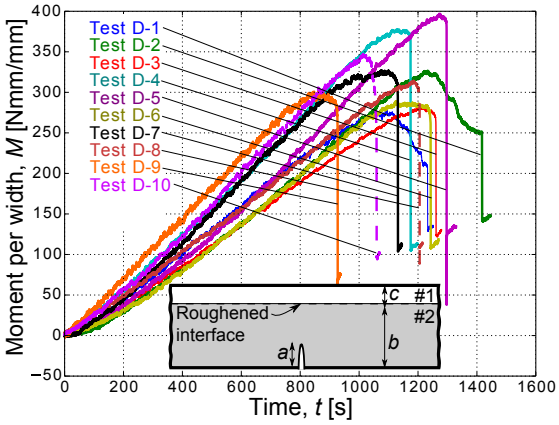

Figure 16: Results for test series D (Laminate B). Presented for 10 test specimens.

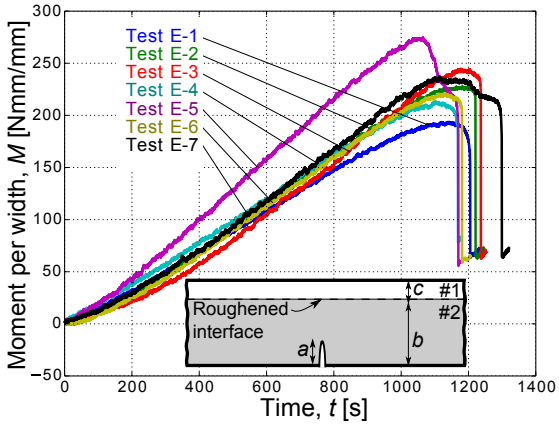

Figure 17: Results for test series E (Laminate A). Presented for 7 test specimens.

Test specimen D-9 is selected for further analysis. The moment and crack length are measured and presented in Figure 18 (A) for test D-9. Figure 18 shows that the main crack grows stable towards the interface until time, $t \approx 957$ s. On the next image at time, $t \approx 958$ s, the main crack has reached the interface ($a/b = 1.0$). A localised strain at the interface is captured by DIC as seen by the vertical

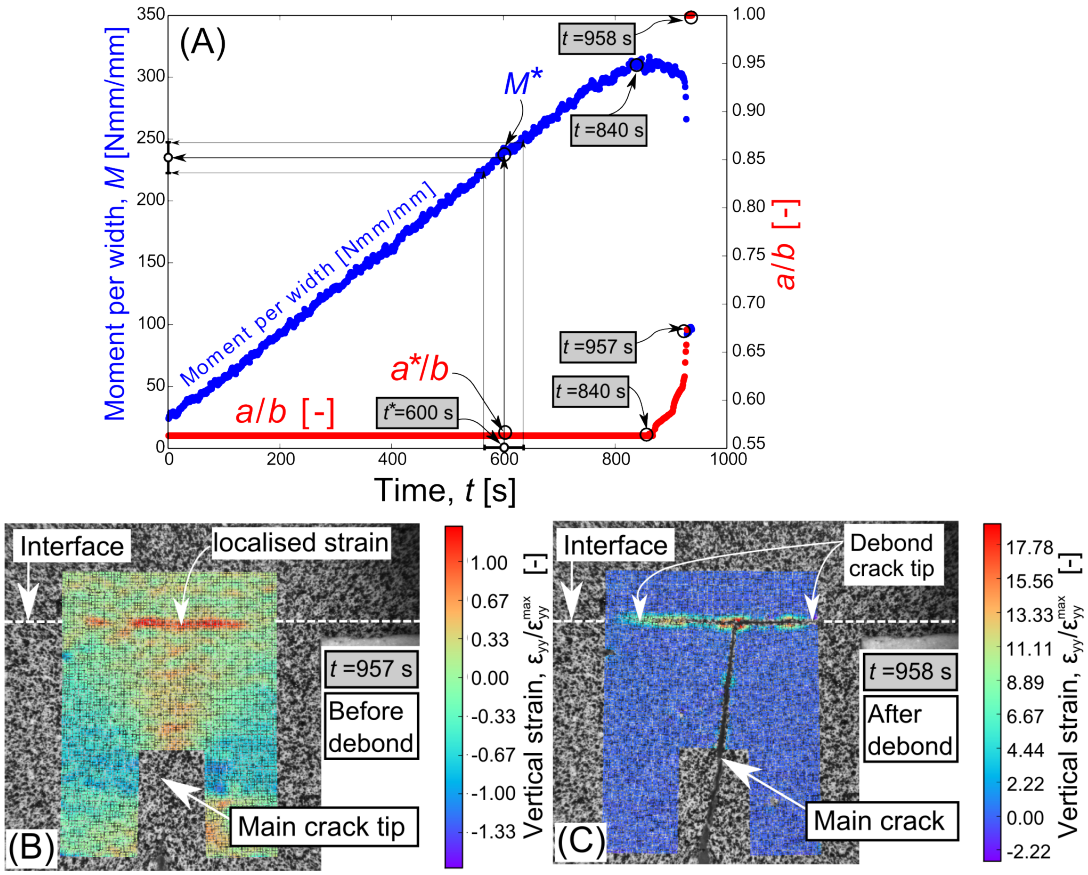

Figure 18: Measurements from test D-9: (A) Moment and crack length. (B) DIC vertical strain contour plot of AoI before debond at time $t = 957$ s. (C) DIC vertical strain contour plot of AoI after debond at time $t = 958$ s. ϵ_{yy}^{max} is the maximum vertical strain measured by DIC in (B).

strain contour plot in Figure 18 (B) for $t = 957$ s for test D-9. This indicate that the interface crack initiated before the main crack reached the interface. Thus, Scenario 1 is observed for the present tests.

In order to determine the onset of interface separation, a displacement is measured by DIC over the gauge length, $l_g = 0.1b$. Thus, determining the displacement difference, $\Delta\delta$, across the interface as shown in Figure 19.

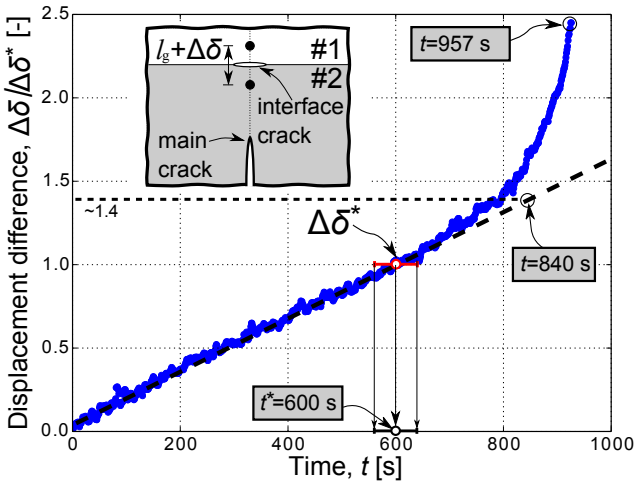

Figure 19: Results of test D-9 with DIC. The displacement difference, $\Delta\delta$, is normalised by the value of the displacement difference at the onset of non-linearity, $\Delta\delta^*$. $\Delta\delta$ is measured over a gauge length of $l_g = 0.1b$. The onset of interface separation begins at time $t^* = 600 \pm 30$ s whereas the main crack starts to propagate at time $t = 840$ s.

The result in Figure 19 is used to identify the time where the interface crack initiates more accurately than what can be seen from the strain contours. A straight line is fitted to the first linear part of the measured displacement difference, $\Delta\delta/\Delta\delta^*$, and it is judged that the measurements deviate from the fitted straight line at time $t \approx 600$ s. Thus, time $t^* \approx 600 \pm 30$ s is identified as the onset of non-linearity in measured displacement difference and the time where the interface crack initiates according to the approach presented in Figure 5.

A forward finite difference approximation of $\Delta\delta$ versus t was used to determine the partial derivatives, $\partial\Delta\delta/\partial t$ and $\partial^2\Delta\delta/\partial^2 t$ in order to determine the point of non-linearity more accurately. It was found that these results were comparable to the determined onset of non-linearity at time $t^* \approx 600$ s in Figure 19 and therefore not presented in further details. However, exact determination of the time of crack initiation is challenging [49, 50] and influenced by some degree of uncertainty as illustrated by the error bar in Figure 19.

10. Determination of mode-I cohesive strength of interfaces

Two examples, one for Scenario 1 and one for Scenario 2, are given to demonstrate the procedure for the determination of the cohesive strength of the interface, $\hat{\sigma}_i$. Since the material systems are confidential, the cohesive strength of the interface, $\hat{\sigma}_i$, will be presented in normalised form. According to the stress based criterion by Cook and Gordon [5] for a homogenous solid, the interface strength should be less than a about 1/3 to 1/5 of the bulk material for the main crack to initiate a new crack at the weaker interface. It is therefore relevant to normalise the cohesive strength of the interface by the cohesive strength of the adhesive. Unfortunately, the cohesive strength of the adhesive has not been measured. Therefore, $\hat{\sigma}_i$ is normalised with the macroscopic strength of the adhesive, $\bar{\sigma}_a$, that was measured by a uni-directional tensile test of a dog bone specimen.

10.1. Example: Determination of cohesive strength - Scenario 1

For the laminate-adhesive specimens (series D and E) with $E_1/E_2 \approx 12.0$, Scenario 1 ($a^* = a_0$) is observed. Thus, for test series D and E, DIC can be applied to determine the onset of interface separation in order to determine the time of crack initiation at the interface, see the approach in Figure 5.

The approach to determine the cohesive strength of the interface for Scenario 1 ($a^* = a_0$) is exemplified by test D-9. For test D-9 a displacement difference is measured by DIC as shown in Figure 19. The point of interfacial separation is identified at time $t^* = 600$ s since this point is identified as the onset of non-linear displacement difference, $\Delta\delta^*$, according to Figure 19. This time measurement ($t^* = 600$ s) is used in Figure 18 (A) to determine $M^* = 240\ Nmm/mm$ and $a^*/b = 0.57$. These parameters ($M^* = 240\ Nmm/mm$, $a^*/b = 0.57$) together with $E_1/E_2 = 12.0$ and $c/b = 0.2$ are used to read off the value for $\sigma_{yy,i}b^2/M$ in Figure 7. From equation 1, the mode-I cohesive strength of the interface can be determined to be $\hat{\sigma}_i/\bar{\sigma}_a = 0.078 \pm 0.004$ for test D-9. The uncertainty is primarily a result of the estimated precision in the value of M^* corresponding to the range of the error bar for $t^* = 600 \pm 30$ s in Figure 19.

10.2. Example: Determination of cohesive strength - Scenario 2

For the specimens in test series B and C, the moment at onset of separation, M^*, is measured just before the interface debonds i.e. using visual inspection in accordance with Scenario 2 ($a > a_0$) in the approach in Figure 5. Thus, a^*/b is measured on the last image before the interface debonds.

An example with Scenario 2 ($a^* > a_0$) is given by test C-2 with peel ply interface. The results for test C-2 is presented in Figure 13. Here, the moment just before debond was measured to $M = 390$ Nmm/mm and the crack length before onset of interface separation is measured to $a/b = 0.78$. Inserting these values ($M^* = 390\ Nmm/mm$, $a^*/b = 0.78$) into equation 1 and using the results

for $E_1/E_2 = 1.0$ and $c/b = 0.3$ in Figure 7 gives the mode-I cohesive strength of the interface: $\hat{\sigma}_i/\bar{\sigma}_a = 0.163 \pm 0.008$ for test C-2. The uncertainty is primarily a result of the estimated accuracy in the determination of the onset of interface separation.

11. Results for the mode-I cohesive strength of the interfaces

The mode-I cohesive strength results for test series B, C, D and E are presented for comparison in Figure 20. It is clear that the cohesive strengths of the interface for the specimens in test series B are smallest. The cohesive strengths of the interfaces for the specimens in test series C and D are intermediate, whereas those in test series E are highest. For all specimens, the cohesive strength of the interface is relatively small in comparison with the macroscopic strength of the adhesive, $\bar{\sigma}_a$.

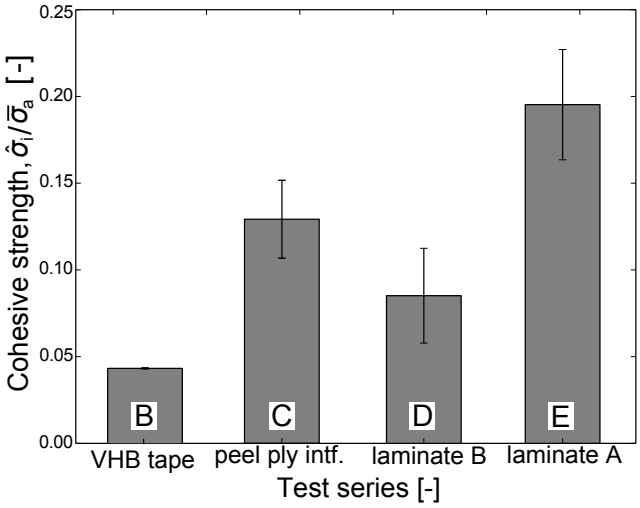

Figure 20: Results for normalised cohesive interface strength for different types of test specimens where the crack at the interface initiated ahead of the main crack. Error bars indicate the standard deviation. The number of specimens are: B: 2 specimens, C: 4 specimens, D: 31 specimens, E: 22 specimens.

12. Discussions

Mohammed and Liechti [30] measured the cohesive strength of an aluminum-epoxy bi-material interface to $\hat{\sigma}_i = 3$ MPa. This value can be normalised with the bulk strength of the epoxy adhesive of $\bar{\sigma}_a = 13.4$ MPa (provided by Mohammed and Liechti [30]) to give $\hat{\sigma}_i/\bar{\sigma}_a = 0.217$. Although the material systems are different, the measured average cohesive strength of the interfaces in test series E of $\hat{\sigma}_i/\bar{\sigma}_a = 0.195$ in Figure 20 is close to the non-dimensional result by Mohammed and Liechti [30]. This close agreement leads confidence in the novel approach applied in the present paper. In order to evaluate the accuracy of the novel approach, the measured cohesive strength of the specific interfaces

could be compared with other independent measurements obtained by another method, e.g. using the J-integral approach on small DCB beam specimens in environmental scanning electron microscope, where the end-opening displacement can be measured with high accuracy [29].

Normalisation of $\hat{\sigma}_i$ by $\bar{\sigma}_a$ is equivalent to the way Cook and Gordon [5] presented their modelling results based on stress. They [5] suggested that the interface strength should be less than about 1/3 to 1/5 of the bulk material strength in order to ensure that a new crack initiates along the weaker interface ahead of the main crack. Although the Cook and Gordon model was established for a homogenous solid, the criterion is consistent with the experimental test results presented in Figure 20 since all measured normalised cohesive strengths of the interfaces in Figure 20 are below 1/5. Since crack penetration into the substrate is observed in test series A1, it is expected based on the Cook-Gordon criterion that the cohesive strength of the interfaces for the specimens in test series A1 is $\hat{\sigma}_i/\bar{\sigma}_a > 1/3$.

In order to determine the cohesive strength of the interface accurately, it is found important to identify the correct load and crack tip location at correct time t^* corresponding to the onset of interface separation. It can be seen in Figure 18 that the maximum moment for test D-9 is measured at time $t = 840$ s, which is 1.4 times M^* determined at time $t^* = 600$ s. Thus, the use of maximum moment as M^*, as proposed by Zhang and Lewandowski [14], would clearly overestimate the determined cohesive strength of the interface, $\hat{\sigma}_i$, since in the experiments the crack initiates before the moment reaches the peak.

For test series C with peel ply interface and the bi-material tests, it is observed shortly after interface crack initiation that the main crack starts to grow unstable towards the interface. The observed instability of the main crack, shown in Figure 18, is attributed the initiation of a new crack at the interface since the energy release rate of the main crack increase when the interface crack is fully developed. This phenomenon is explained by FE simulations in Appendix B.

Possible improvements of the work in the present paper are discussed. One of the limitations of the method is that the main crack should preferably be stationary in order to make the most accurate prediction of the onset of separation i.e. enabling the use of DIC to identify crack initiation. A more thorough numerical study could be made in order to determine the optimum combination of h/b, B/b, and a_0/b for the four-point SENB specimen. The shape of the notch could also be changed e.g. by using an elliptical or circular shaped notch instead of the start-crack in the four-point SENB specimen. Then, the risk of main crack propagation would be reduced.

It is demonstrated that the vertical normal stress, σ_{yy}, in front of the main crack can initiate a new crack at the interface before the main crack reaches the interface, which is similar to the experimental observations by Lee and Clegg [11]. This suggests that the interfacial strength is low in comparison with both the adhesive and the substrate. This cracking mechanism (Figure 2 (C)) enables determination of the cohesive strength of the interface that can be used as input for cohesive

zone models to simulate crack deflection at interfaces in adhesive joints [9, 10]. Thus, experimental tests and numerical simulations can be combined to solve the challenging problem of crack deflection at interfaces.

Based on the literature presented in the introduction, especially the work by Parmigiani and Thouless [9], and the experiments in the present paper, it is judged that the cohesive strength of the interface and the of substrate are important parameters in an accurate crack deflection criterion. However, additional experiments with systematic varying cohesive strength of the interface/substrate is needed to form such a crack deflection criterion.

At present, the initiation of a new crack at the interface cannot be modelled by the available energy based models [6, 7]. Therefore, a criterion for crack initiation at the interface must be based on strength [5, 14] or preferably CZM [9, 10]. Cohesive zone modelling of the competition between main crack growth and initiation of an interface crack is a natural extension of the experimental studies presented in this paper and it may be addressed by models similar to those by Parmigiani and Thouless [9] and Brinckmann *et al.* [10]. This CZM modelling framework can subsequently be used for sub-modelling of adhesive joints in large bonded structures, like a wind turbine blade, to predict crack deflection at interfaces on a sub-component scale.

13. Conclusions

Based on a four-point SENB specimen design with stable crack growth, it was found possible to study the cracking mechanisms during loading by DIC and in-situ observations. Model experiments showed that the crack penetrated into the substrate for the specimen with roughened (strong) interface, whereas for the specimen with smooth (weak) interface the crack deflected along the interface.

Observations by DIC, during four other experiments with different types of four-point SENB specimens, showed that a new crack initiated at the interface before the main crack reached the interface. DIC was succesfully used to determine the onset of interface separation by measuring a displacement difference across the interface. The initiation of the interface crack enabled determination of the cohesive strength of the different material interfaces using a novel approach. The cohesive strength of the interfaces was found to be low in comparison with the macroscopic strength of the adhesive.

Acknowledgements

First of all thanks to professor Michael D. Thouless, University of Michigan, for useful discussions that helped develop the earlier approach [32] that was further refined and applied here. Acknowledgements to the LM Wind Power lab for help manufacturing the test specimens and to Fulbright for supporting the research stay at the University of Michigan. Thanks to James Gorman, University

of Michigan for his help when preparing some of the Python scripts used for the DIC data analysis and for his help when testing the specimens in the lab at the Department of Mechanical Engineering, University of Michigan, MI, USA. This research was primarily supported by grant no. 4135-00010B from Innovation Fund Denmark. This research was also supported by the Danish Centre for Composite Structure and Materials for Wind Turbines (DCCSM), grant no. 0603-00301B, from Innovation Fund Denmark.

Appendix A. DIC setup and settings

Appendix A.1. Field of view

The first step in design of the four-point SENB experiments with DIC is the selection of Field of View (FOV), which together with the camera resolution (2448x2048) defines the displacement accuracy, spatial resolution, and the scaling between pixels and microns (μm or mm) [51]. It is desired to have as many pixels in the measurement area as possible [38], but this is limited by the need of keeping the main crack tip and the interface in the FoV simultaneously. Based on initial experiments, it was found that the scaling between pixels and microns should be approx. 3 $\mu m/pixel$ (or slightly less).

Appendix A.2. Speckle pattern

A speckle pattern was applied to the front surface using an Iwata CM-B airbrush where the aim was to achieve a 50/50 distribution of black/white [42] and build up a surface of multiple thin layers [40]. The speckle pattern equipment (airbrush) had limitations since the smallest achievable speckle size was approx. 5-10 microns. Furthermore, it was desired to have 3-7 pixels per speckle and at least 2-3 speckles in each subset in order to have a suitable trade-off between spatial resolution and noise [52, 53, 54]. The 3 pixels speckle size minimum guideline was to avoid aliasing and the maximum guideline of 7 pixels was to maximise spatial resolution [55]. The contrast, which was defined as the difference in gray level counts between the bright and the dark areas of the speckle pattern, should be maximised [56].

Appendix A.3. Speckle-, subset- and step-Sizes

The speckles, shown in Figure A.21, were measured in an optical microscope to be in the range of ∼8-30 microns. A subset size of about 20 pixels could be used as a good compromise between spatial resolution and noise if speckle sizes of 3-5 pixels were achieved [57]. The average speckle size was measured to ∼3-10 pixels and a larger subset size must therefore be used e.g. a subset size of 25-30 pixels. The guideline of 2-3 unique features in each subset should be followed. The subset size was set relatively small since it was important to capture displacement gradients and it was less important to reduce noise. A rule of thumb was not to set the step size greater than $\sim 1/4$ of the subset size

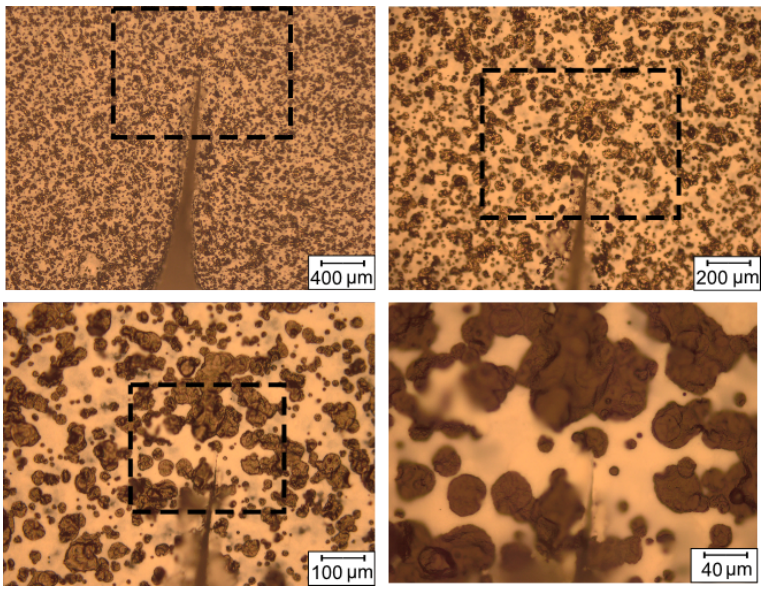

Figure A.21: Speckle pattern near the start crack tip of test D-10 (optical microscope).

since smaller step sizes increased the solution time without adding independent measurements [51]. Therefore, the subset size was set to 25 pixels and the step size to 5 pixels. This gave approx. 100,000 measuring points on the sample. The spatial resolution was 25 pixels. The displacement resolution was 0.02 pixels and the strain resolution was $1.9 \cdot 10^{-4}$ m/m. These values were determined based on 25 still images taken before loading the specimen.

Appendix A.4. Light conditions and camera settings

Fiber optic lights from Cole-Palmer illuminated the specimens front surface as shown in Figure 9. Adequate lightning of the speckle pattern was important [39] and the light should be uniform, bright, and diffuse to capture a good contrast image [41, 37]. Image contrast and noise depends on the interaction of lightning and the speckle pattern [37] and it was a trade-off between light intensity and reflections. For the experiments in this paper, reflections were primarily originating from too thick layers of paint. Missing paint was a minor problem since the surfaces of the adhesive and glass-fiber materials were non-reflective.

The selection of aperture level is a trade-off between gathering light and capturing image depth [35] and typically the aperture is reduced to increase the depth of field [38, 37]. In the present experiments the aperture size was set to a medium level of f/8 where the bounds for the lens was f/22 and f/1.8. At large magnifications, rigid body movement should be minimised in order to achieve high precision DIC results. Therefore, it was advantageous that the load- and support-span were small for the four-point SENB specimen.

Appendix B. The effect of interfacial debond in the four-point SENB specimen

The socalled Cook-Gordon [5] cracking mechanism, sketched in Figure 2 (C), where a debond crack at the interface develops before the main crack reach the interface, is modeled using finite elements in order to determine the effect of the debond crack length, D, on the stability of the main crack propagation. The details of the finite element model is presented in a related paper [34]. The debond crack is initiated by the normal stress component perpendicular to the main crack and located at a weak interface. The Cook-Gordon [5] cracking mechanism is also observed in experimental tests [14, 11, 58]. The non-dimensional energy release rate results for the main crack are presented in Figure B.22 for a substrate with stiffness mismatch of $E_1/E_2 = 12$ (bi-material) that is comparable to the stiffness of a uni-directional glass fiber laminate with a polymer adhesive layer. For short main crack lengths (small a/b), the effect of debond crack is limited. In turn, when the main crack approaches the debond crack, the constraining effect of the main crack is reduced hence the energy release rate of the main crack increases.

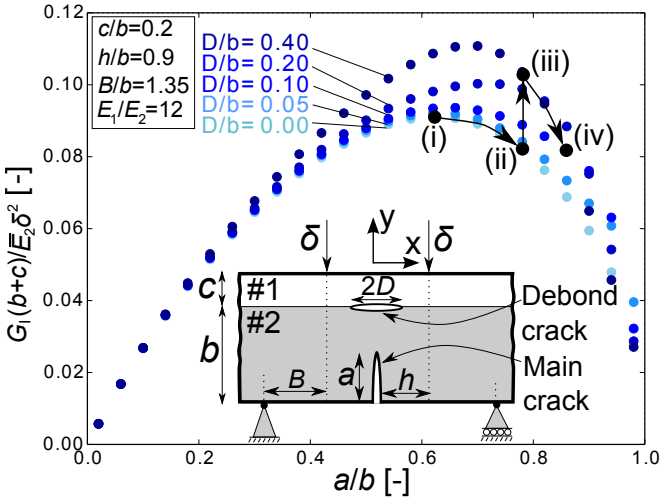

Figure B.22: Results from FE model with debond of different length, D/b. Other parameters are: $E_1/E_2 = 12$, $h/b = 0.9$, $B/b = 1.35$ and $c/b = 0.2$. (#1 is substrate, #2 is adhesive).

To exemplify, recall that the tests are designed so the start-crack length, a_0/b, is slightly larger than $(a/b)_{peak}$ for $D/b = 0.0$ (point (i) in Figure B.22). Then, $\partial G_I/\partial a < 0$ is satisfied and the main crack grows stable under monotonic loading with increasing a/b to point (ii). If an interface crack of a certain length, lets say $D/b = 0.4$, suddenly develops at the interface, then the energy release rate of the main crack increases instantly from point (ii) to point (iii) in Figure B.22. The increase in energy release rate of the main crack will cause the main crack to grow instantaneously to point (iv). Thus, the main crack growth becomes unstable if suddenly a sharp debond crack develops at the interface.

References

[1] B. F. Sørensen, J. W. Holmes, P. Brøndsted, K. Branner, Blade materials, testing methods and structural design, in: W. Tong (Ed.), Wind Power Generation and Wind Turbine Design, 1st Edition, Vol. 44, WIT Press, Boston, 2010, Ch. 13, pp. 417–460. doi:10.2495/978-1-84564-.

[2] S. Ataya, M. M. Z. Ahmed, Damages of wind turbine blade trailing edge: Forms, location, and root causes, Engineering Failure Analysis 35 (2013) 480.

[3] W. J. Clegg, The fabrication and failure of laminar ceramic composites, Acta metall. mater. 40 (11) (1992) 3085.

[4] W. Lee, S. J. Howard, W. J. Clegg, Growth of interface defects and its effect on crack deflection and toughening criteria, Acta. Mater. 44 (1996) 3905.

[5] J. Cook, J. E. Gordon, C. C. Evans, D. M. Marsh, A mechanism for the control of crack propagation in all-brittle systems, Mathematical and Physical Sciences 282 (1391) (1964) 508–520.

[6] M. He, J. W. Hutchinson, Crack deflection at an interface between dissimilar elastic materials, Int. J. Solid Structures 25 (9) (1989) 1053–1067.

[7] M. Y. He, A. G. Evans, Crack deflection at an interface between dissimilar elastic materials: Role of residual stresses, Int. J. Solids Structures 31 (1994) 3443.

[8] M. D. Thouless, H. C. Cao, P. A. Mataga, Delamination from surface cracks in composite materials, Journal of Materials Science 24 (1989) 1406–1412.

[9] J. Parmigiani, M. Thouless, The roles of toughness and cohesive strength on crack deflection at interfaces, Journal of the Mechanics and Physics of Solids 54 (2) (2006) 266–287. doi:10.1016/j.jmps.2005.09.002.

[10] S. Brinckmann, B. Völker, G. Dehm, Crack deflection in multi-layered four-point bending samples, International Journal of Fracture 190 (1-2) (2014) 167–176. doi:10.1007/s10704-014-9981-1.

[11] W. Lee, W. J. Clegg, The deflection of cracks at interfaces, Key Engineering Materials 116-117 (1996) 1886–1889. doi:10.4028/www.scientific.net/KEM.132-136.1886.

[12] K. Kendall, Transition between cohesive and interfacial failure in a laminate, Proc. R. Soc. Lond.A. 344 (1975) 287–302. doi:10.1098/rspa.1983.0054.

[13] A. A. Griffith, The phenomena of rupture and flow in solids, Royal Society of London 221 (587) (1920) 163.

[14] J. Zhang, J. J. Lewandowski, Delamination study using four-point bending of bilayers, Journal of Materials Science 32 (14) (1997) 3851–3856.

[15] Z. Y. Wang, L. Wang, W. Guo, H. Deng, J. W. Tong, F. Aymerich, An investigation on strain/stress distribution around the overlap end of laminated composite single-lap joints, Composite Structures 89 (4) (2009) 589–595. doi:10.1016/j.compstruct.2008.11.002.

[16] T. Sadowski, M. Knec, Application of DIC technique for monitoring of deformation process of SPR hybrid joints, Archives of Metallurgy and Materials 58 (1) (2013) 119–125. doi:10.2478/v10172-012-0161-x.

[17] G. Crammond, S. W. Boyd, J. M. Dulieu-Barton, Evaluating the localised through-thickness load transfer and damage initiation in a composite joint using digital image correlation, Composites Part A: Applied Science and Manufacturing 61 (2014) 224–234. doi:10.1016/j.compositesa.2014.03.002.

[18] M. P. Moutrille, K. Derrien, D. Baptiste, X. Balandraud, M. Grédiac, Through-thickness strain field measurement in a composite/aluminium adhesive joint, Composites Part A: Applied Science and Manufacturing 40 (8) (2009) 985–996. doi:10.1016/j.compositesa.2008.04.018.

[19] R. Srilakshmi, M. Ramji, Experimental investigation of adhesively bonded patch repair of an inclined center cracked panel using DIC, Journal of Reinforced Plastics and Composites 33 (12) (2014) 1130–1147. doi:10.1177/0731684414525245.

[20] M. Kashfuddoja, M. Ramji, Assessment of local strain field in adhesive layer of an unsymmetrically repaired CFRP panel using digital image correlation, International Journal of Adhesion and Adhesives 57 (040) (2015) 57–69. doi:10.1016/j.ijadhadh.2014.10.005.

[21] J. Jefferson Andrew, V. Arumugam, D. J. Bull, H. N. Dhakal, Residual strength and damage characterization of repaired glass/epoxy composite laminates using A.E. and D.I.C, Composite Structures 152 (2016) 124–139. doi:10.1016/j.compstruct.2016.05.005.

[22] C. Liu, P. J. Rae, C. M. Cady, M. L. Lovato, Damage and fracture of high-explosive mock subject to cyclic loading., Proceedings of the 2011 Annual Conference on Experimental and Applied Mechanics. 3 (2011) 151.

[23] A. D. Wargo, S. Safavizadeh, R. Y. Kim, The use of four-point bending notched beam fatigue tests to rank crack-mitigating interlayers, 8th RILEM International Symposium on Testing and Characterization of Sustainable and Innovative Bituminous Materials. 11 (2016) 359.

[24] K. Allaer, I. De Baere, W. Van Paepegem, J. Degrieck, Direct fracture toughness determination of a ductile epoxy polymer from digital image correlation measurements on a single edge notched bending sample, Polymer Testing 42 (2015) 199–207. doi:10.1016/j.polymertesting.2015.01.014.

[25] B. F. Sørensen, Cohesive laws for assessment of materials failure: Theory, experimental methods and application, Risø-R-1736 (EN), 2010.

[26] V. C. Li, R. J. Ward, A novel testing technique for post-peak tensile behavior of cementitious materials, Fracture Toughness and Fracture Energy, Mihashi et al. (eds). (1989) 183.

[27] B. F. Sørensen, T. K. Jacobsen, Large-scale bridging in composites: R-curves and bridging laws, Composites Part A: Applied Science and Manufacturing 29 (1998) 1443–1451. doi:10.1016/S1359-835X(98)00025-6.

[28] T. Andersson, U. Stigh, The stress-elongation relation for an adhesive layer loaded in peel using equilibrium of energetic forces, International Journal of Solids and Structures 41 (2) (2004) 413–434. doi:10.1016/j.ijsolstr.2003.09.039.

[29] S. Goutianos, R. Arevalo, B. F. Sørensen, T. Peijs, Effect of Processing Conditions on Fracture Resistance and Cohesive Laws of Binderfree All-Cellulose Composites, Applied Composite Materials 21 (6) (2014) 805–825. doi:10.1007/s10443-013-9381-0.

[30] I. Mohammed, K. M. Liechti, Cohesive zone modeling of crack nucleation at bimaterial corners, J. Mech. Phys. Solids. 48 (2000) 735.

[31] R. K. Joki, F. Grytten, B. Hayman, B. F. Sørensen, Determination of a cohesive law for delamination modelling - Accounting for variation in crack opening and stress state across the test specimen width, Composites Science and Technology 128 (2016) 49–57. doi:10.1016/j.compscitech.2016.01.026.

[32] J. B. Jørgensen, M. D. Thouless, B. F. Sørensen, C. Kildegaard, Determination of mode-I cohesive strength for interfaces, IOP Conference Series: Materials Science and Engineering 139 (2016) 267–274. doi:10.1088/1757-899X/139/1/012025.

[33] H. Tada, P. C. Paris, G. R. Irwin, The Stress Analysis of Cracks Handbook, 3rd Edition, Vol. 3, ASME Press, New York, 2000.

[34] J. B. Jørgensen, B. F. Sørensen, C. Kildegaard, Design of four-point SENB specimens with stable crack growth, To be published NA (NA) (2017) NA.

[35] M. A. Sutton, J. Orteu, H. W. Schreier, Image Correlation for Shape, Motion and Deformation Measurements, Vol. 1, Springer, 2009. arXiv:arXiv:1011.1669v3, doi:10.1017/CBO9781107415324.004.

[36] P. Reu, Stereo-rig design: Camera selection-part 2, Experimental Techniques 36 (6) (2012) 3–4. doi:10.1111/j.1747-1567.2012.00872.x.

[37] P. Reu, Stereo-rig design: Lighting - Part 5, Experimental Techniques 37 (3) (2013) 1–2. doi:10.1111/ext.12020.

[38] P. Reu, Stereo-rig design: Lens selection - Part 3, Experimental Techniques 37 (1) (2013) 1–3. doi:10.1111/ext.12000.

[39] P. Reu, Speckles and their relationship to the digital camera, Experimental Techniques 38 (4) (2014) 1–2. doi:10.1111/ext.12105.

[40] P. Reu, Points on Paint, Experimental Techniques 39 (4) (2015) 1–2. doi:10.1111/ext.12147.

[41] P. Reu, All about speckles: Contrast, Experimental Techniques 39 (1) (2015) 1–2. doi:10.1111/ext.12126.

[42] P. Reu, All about speckles: Speckle density, Experimental Techniques 39 (3) (2015) 1–2. doi:10.1111/ext.12161.

[43] P. Lava, D. Debruyne, Practical considerations in DIC measurements MatchID : new spin-off company of KULeuven, in: Practical considerations in DIC measurements, Edinburgh, 2015, pp. 1–79.

[44] F. Pierron, Metrology and uncertainty quantification in DIC, Tech. rep., University of Southampton, Southampton (2015).

[45] C. Solutions, Vic-2D Reference Manual, Tech. rep., Correlated Solutions (2009).

[46] P. Reu, Hidden components of 3D-DIC: Triangulation and post-processing - Part 3, Experimental Techniques 36 (4) (2012) 3–5. doi:10.1111/j.1747-1567.2012.00853.x.

[47] H. P. Langtangen, Python Scripting for Computational Science, 2nd Edition, Springer, 2008.

[48] H. P. Langtangen, A Primer on Scientific Programming with Python, 4th Edition, Springer, 2014.

[49] P. A. Vanniamparambil, U. Guclu, A. Kontsos, Identification of crack initiation in aluminum alloys using acoustic emission, Experimental Mechanics 55 (5) (2015) 837–850. doi:10.1007/s11340-015-9984-5.

[50] R. Jiang, F. Pierron, S. Octaviani, P. A. Reed, Characterisation of strain localisation processes during fatigue crack initiation and early crack propagation by SEM-DIC in an advanced disc alloy, Materials Science and Engineering A 699 (May) (2017) 128–144. doi:10.1016/j.msea.2017.05.091.

[51] P. Reu, Stereo-rig design: Creating the Stereo-Rig Layout - Part 1, Experimental Techniques 36 (5) (2012) 3–4. doi:10.1111/j.1747-1567.2012.00871.x.

[52] P. Reu, Virtual Strain Gage Size Study, Experimental Techniques 39 (5) (2015) 1–3. doi:10.1111/ext.12172.

[53] P. Reu, All about speckles: Speckle size measurement, Experimental Techniques 38 (6) (2014) 1–2. doi:10.1111/ext.12110.

[54] G. Crammond, S. W. Boyd, J. M. Dulieu-Barton, Speckle pattern quality assessment for digital image correlation, Optics and Lasers in Engineering 51 (12) (2013) 1368–1378.

[55] P. Reu, All about speckles: Aliasing, Experimental Techniques 38 (5) (2014) 1–3. doi:10.1111/ext.12111.

[56] P. Reu, Hidden components of 3D-DIC: Interpolation and matching - Part 2, Experimental Techniques 36 (3) (2012) 3–4. doi:10.1111/j.1747-1567.2012.00838.x.

[57] P. Reu, Hidden components of DIC: Calibration and shape function - Part 1, Experimental Techniques 36 (2) (2012) 3–5. doi:10.1111/j.1747-1567.2012.00821.x.

[58] R. K. Bordia, B. Dalgleish, P. G. Charalambides, A. G. Evans, Cracking and Damage in a Notched Unidirectional Fiber-Reinforced Brittle Matrix composite, J. Am. Ceram. Soc. 74 (11) (1991) 2776–80.

APPENDED PAPER P6

Determination of mode-I cohesive strength of interfaces

Jeppe B. Jørgensen, Michael D. Thouless, Bent F. Sørensen and Casper Kildegaard
IOP Conf. Series: Materials Science and Engineering, 139, 012025
Published, 2016

IOP Conf. Series: Materials Science and Engineering **139** (2016) 012025 doi:10.1088/1757-899X/139/1/012025

Determination of mode-I cohesive strength for interfaces

J B Jørgensen[1,#], M D Thouless[2], B F Sørensen[3] and C Kildegaard[1]

[1] LM Wind Power, Østre Alle 1, 6640 Lunderskov, Denmark.
[2] The University of Michigan, 3672 G. G. Brown Addition, Ann Arbor, MI, USA.
[3] The Technical University of Denmark, Dept. of Wind Energy, Frederiksborgvej 399, 4000 Roskilde, Denmark.

E-mail: #jbj@lmwindpower.com

Abstract. The cohesive strength is one of the governing parameters controlling crack deflection at interfaces, but measuring its magnitude is challenging. In this paper, we demonstrate a novel approach to determine the mode-I cohesive strength of an interface by using a 4-point single-edge-notch beam specimen. The test specimen is made of a glue cast onto a uni-directional, glass-fiber laminate. A crack is cut in the glue, orthogonal to the interface, which creates a high normal stress across the glue/laminate interface during loading. It is observed that a new crack can be initiated along the interface in response to this stress, before the main crack starts to grow. Observations using 2D digital-image correlation showed that an "apparent" strain across the interface initially increases linearly with the applied load, but becomes non-linear upon the initiation of the interface crack. The cohesive strength is determined, using a 2D, linear-elastic, finite-element model of the experiment, as the stress value where the experimental measured "apparent" strain value becomes non-linear across the interface.

1. Introduction

Crack deflection along interfaces is an important failure mechanism in adhesive bonded joints. Several studies on crack deflection have been presented previously, but with a primary focus on modeling. An early work was by Cook and Gordon [1], who used a stress-based approach to model an elliptical notch situated a short distance from a weak interface in a homogeneous substrate. The peak stresses normal to the interface and normal to the notch were compared to show that the interface fails before the substrate (causing crack deflection), if the interface strength is less than about one fifth of the substrate strength.

Later models of crack deflection used an energy-based approach by applying linear-elastic fracture mechanics (LEFM) [2, 3, 4]. These models indicated that, in the absence of a modulus mismatch, the interface toughness should be less than one fourth of the substrate toughness for the crack to deflect. Thus, modeling the deflection of a crack at an interface was, at first, either based on stress [1] or toughness [2]. These two distinct concepts, strength and toughness, are unified in a cohesive law [5]. It was shown that the cohesive strength of the interface is one of the governing parameters that controls crack deflection [5]. This cohesive strength can be measured experimentally using environmental scanning-electron microscopy (ESEM) [6] in conjunction with the J-integral [7, 8]. Unfortunately, this method requires advanced equipment and specialized loading devices.

Experimental studies of crack deflection at interfaces are very limited, and only a few have been found [9, 10]. Kendall [9] derived a deflection criterion for a Griffith crack, and used single-edge-notch-tension (SENT) specimens made from a brittle and transparent ethylene propylene rubber in which crack propagation could be monitored. Unfortunately, details and images of the crack deflection process were not presented in that paper. A subsequent experiment [10] used a wedge to load a single-edge-notch-beam (SENB) to show that an interface crack was initiated before the main crack reached the interface. This competition between growth of the main crack and initiation of an interface crack is similar to the model proposed by Cook and Gordon [1].

In this paper, crack deflection at an interface is studied using a 4-point SENB specimen. The test specimen is manufactured of a brittle vinylester glue cast onto a uni-directional glass-fiber-reinforced polyester laminate. 2D digital-image-correlation (DIC) is used to measure the full displacement field during loading of the specimen. It is found that a new crack initiates in the interface prior to the main crack reaching the interface. This is similar to the experimental observations of Lee and Clegg [10], but we use this failure mode to develop a new approach to measure the cohesive strength of the interface.

2. Approach

A new approach is proposed in this paper for measuring the cohesive strength of the interface, $\hat{\sigma}$. This approach is summarized in figure 1. The strength is measured using 2D DIC (figure 1(a)), in combination with a linear-elastic finite-element (FE) model of the experiment (figure 1(b)). During the test, measurements of an "apparent" strain, ϵ_{yy}, acting normal to the interface allows the point at which the interface crack is initiated to be identified. ϵ_{yy} is obtained from the displacement difference between two points on either side of the interface divided by gauge length, l_g as shown on Figure 2.

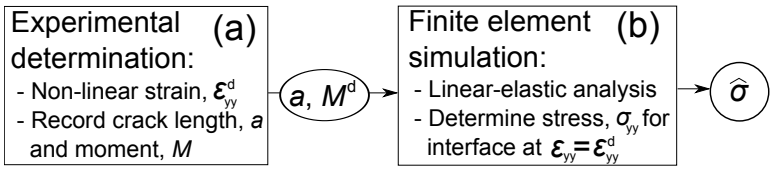

Figure 1. Approach to obtain cohesive strength of the interface.

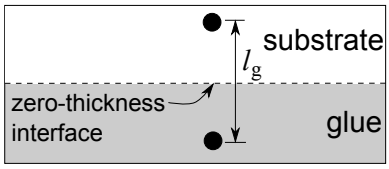

Figure 2. Measuring an "apparent" strain, ϵ_{yy}.

The strain field at the interface increases linearly with load until the point at which the interface crack initiates. The applied bending moment, M^d and the crack length, a at the point when DIC indicates that the "apparent" strain is no longer linear are identified. Linear-elastic materials and a zero-thickness interface are assumed hence the non-linearity in measured "apparent" strain is due to interface separation. Separation of interface is the first step in the crack initiation process and this is the beginning of delamination. These conditions are then used in a linear-elastic finite-element model of the experiment, assuming an orthotropic substrate and an isotropic glue, to calculate the normal stress at the interface. The maximum stress calculated from this numerical analysis is taken to be the cohesive strength of the interface.

3. Methods

The 4-point SENB specimen is illustrated in figure 3, and the dimensions are given in table 1. In this figure and table a_0 is pre-crack length, a is the actual crack length, b is thickness of the glue, c is thickness of the laminate, w is width, and L is the length of the specimen.

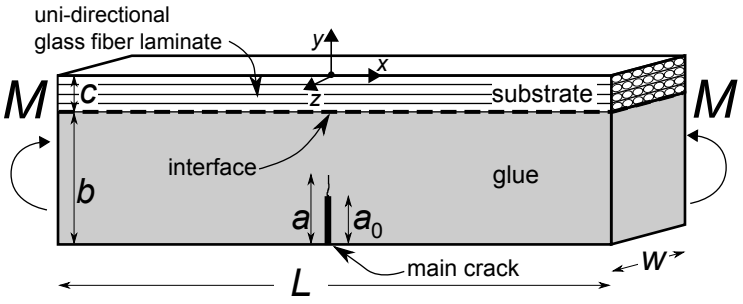

Figure 3. Geometry and nomenclature of the 4 point SENB specimen. The uni-directional fibers are oriented in the x-direction according to the coordinate system.

Table 1. Dimensions of test specimen.

a_0/b [-]	c/b [-]	L/b [-]	w/b [-]
0.6	0.2	6.6	1.1

3.1. Design of experiment by finite element modeling

The purpose of the main crack is to create a high normal stress across the interface. Furthermore, this geometry containing a crack is selected because it can be modeled precisely using FE, allowing the interface stress to be determined accurately. The interface stress is extracted in the symmetry line ($x = 0$, $y = -c$) where the shear stress is zero hence the crack initiation is mode-I. For the approach to work, the interface crack must initiate before the main crack reaches the interface, and, if the main crack starts to grow, it should do so in a stable manner.

The energy-release rate of the main crack, G, shown on figure 3, can be determined for a homogeneous specimen using the results of Tada *et al.* [11]. However, the energy-release rate for the present case of an orthotropic substrate and an isotropic glue depends on the following parameters:

$$a/b, \quad c/b, \quad E_{xx,s}/E_g, \quad E_{yy,s}/E_g, \quad \mu_{xy,s}/E_g, \quad \nu_{xy,s}, \quad \nu_g$$

where E is in-plane stiffness, μ is shear modulus, ν is Poisson's ratio, and the subscripts s and g represent the substrate and glue, respectively.

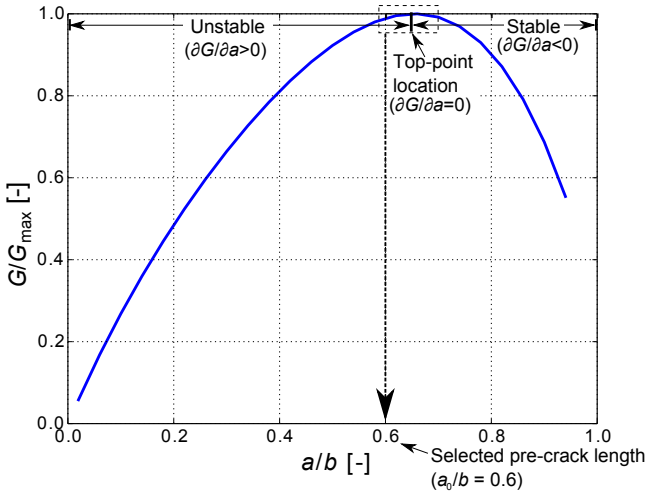

Figure 4. Results from the finite element model of the test specimen geometry, where the normalized energy release rate is determined as a function of relative crack length.

It is important that the main crack grows stably to avoid dynamic effects *i.e.* rapid, unstable crack growth, in the experiment. A 2D plane-strain linear-elastic finite-element model is used

to determine a suitable initial length for the main crack to ensure stable crack growth. The normalized energy-release rate of the main crack is determined as a function of the relative crack length, a/b, from the FE calculations and shown in figure 4.

Stable growth of the main crack is achieved if $\partial G/\partial a < 0$. If the pre-crack is very long then the main crack will grow stably, but it will be very close to the interface. Therefore, from figure 4, a normalized pre-crack length of $a_0/b = 0.6$ is selected as the best compromise between length and stability.

3.2. Test specimen and speckle pattern

The test specimen is manufactured from polyester reinforced with fabrics of uni-directional glass fiber, using vacuum-assisted resin-transfer moulding (VARTM). A brittle vinylester glue is subsequently cast onto the glass-fiber laminate creating a zero-thickness interface. The exact material data are confidential, and the results are, therefore, normalized when presented. The pre-crack is cut in the glue using first a thin hack saw, then a standard razor blade, and finally an ultra-thin razor blade of thickness 74 microns. See figure 5 and figure 6 for images of the pre-crack.

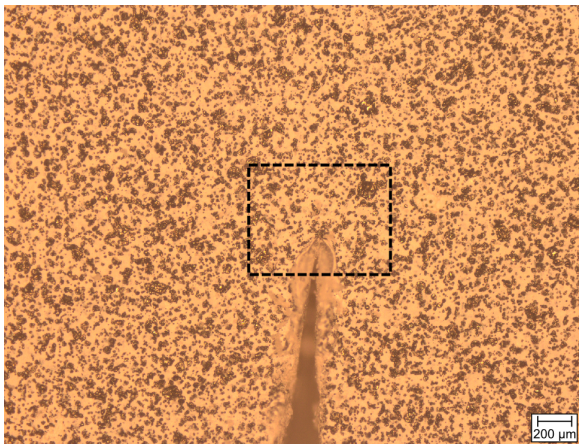

Figure 5. Image taken in optical microscope, of the front of the test specimen showing the pre-crack and speckle pattern.

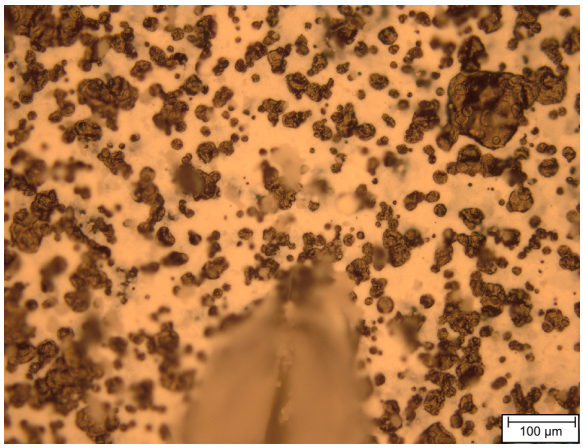

Figure 6. Zoom of the dashed square on figure 5 showing the speckle pattern close to the pre-crack tip.

A speckle pattern is applied to the front surface using an Iwata CM-B airbrush. First, a white baseline paint is applied to cover the front surface of the specimen. Afterwards, a carbon black paint is applied with increased pressure to minimize the speckle sizes. 3-5 pixels across each speckle diameter, and 10 speckles per subset are desired to track displacements accurately, and to maximize the spatial resolution in DIC [12].

It is desirable to have a scaling factor between microns and pixels of about 3 microns/pixel or less to capture the crack initiation accurately. Thus, the speckles should be between 9 microns and 15 microns (3x3 and 5x3). Larger speckles would lower the spatial resolution, since a larger subset should be used to maintain the 10 speckles per subset. After application of the speckle pattern, the speckles are measured in an optical microscope to between 8 and 28 microns, see figure 6. The actual scaling factor is determined, based on a scale bar mounted on the images, to 2.8 microns/px leading to a field of view (FoV) of 6.8 x 5.7 mm (2448x2048 pixels). The pre-crack lengths are measured using a digital vernier caliper with an accuracy of $a_0/b \pm 1\%$, while the crack length is measured during the test using the images, which can be measured with an accuracy of about ± 4 pixels.

3.3. Experimental setup and procedure
A MTS 858 Mini Bionix II servo-hydraulic test machine is used in displacement control to load the specimen at a rate of 0.015 mm/min (0.00025 mm/s) for the cross-head displacement. The specimen is loaded slowly so many images can be captured during the test. The test is conducted at room temperature. Data (time, force, cross head displacement) are collected on a PC at 10 Hz.

Vic-2D DIC system (Vic Snap 8) is used to capture the images with an image frequency of 1 Hz. A CCD sensor of brand Grasshopper GRAS-50S5M and Fujinon CCTV Lens (1:1.8/50mm) are used with the DIC system. A fiber-optic illuminator from Cole-Palmer is used to illuminate the specimen surface. The camera is mounted on a tripod that can be moved in the y-direction and rotated around 3 axes. The lens aperture is set to a medium level of 8, where the minimum is 1.8 and the maximum is 22. This is found to be the best trade-off between capturing surface depth and the amount of light let through the lens.

3.4. Data analysis
Images are correlated with a subset size of 31 pixels and a step size of 3 pixels to obtain the full displacement field using the DIC software, DaVis from LaVision. The subset size is set hence approx. 10 speckles are found in each subset. The step size is set small enough to resolve the fine details of the interface.

The "apparent" strain is determined, by a script, using the displacement at two points across the interface divided by their separation to obtain an average "apparent" strain across the interface. Here a gauge length, l_g of $l_g/b = 0.007$ is used. This method is equivalent to using a virtual strain gauge across the interface in the DIC software. As a check, the normal strain at the interface is also calculated by the DIC software at different points across the interface. The precise location of interface is taken as the point with the largest strain value. The two methods resulted in the same strain value across the interface. The strains are not further post processed since the purpose of the strain measurement is to identify strain non-linearity.

4. Results
Figure 7 illustrates the relative crack length and the normalized moment as a function of time after the start of the experiment. According to figure 7, the moment increases non-linearly with time until about $\sim$ 200 s. This is attributed the establishment of full contact of the rollers on the specimen. Thereafter, the moment increases linearly with time, until the main crack in the glue starts to propagate at $t = 1100$ s. Figure 7 also shows that when the interface crack is fully developed, the main crack grows and reaches the interface to form a doubly-deflected crack at the interface.

The role of the DIC measurements is to identify the "apparent" strain, ϵ_{yy}. These measurements indicate a transition from a linear relationship to a non-linear relationship between the "apparent" strain and the moment at $t = 800$ s (figure 8). The value of the "apparent" strain at which this occurs is designated by ϵ^d_{yy}. This is confirmed by observed changes in strain field by contour plots of the vertical strain, similar to those shown in figure 9.

A comparison between figures 9 and 8 shows that both the normal strain across the interface and the applied moment increase linearly with time until $t = 800$ s. In this regime, the "apparent" strain is proportional to the applied moment, as one would expect for a linear-elastic system.

After this point, the moment continues to increase linearly with time until the main crack in the glue grows at $t = 1100$ s, figure 7. However, even while there is still linear elasticity at the macroscopic scale (800 s $< t <$ 1100 s) the strain across the interface increases significantly - this apparent localization of strain is taken to indicate the onset of interfacial delamination. If it is assumed that this is failure of the zero-thickness interface then the level of stress at which the onset of non-linearity occurs can be associated with the cohesive strength of the interface.

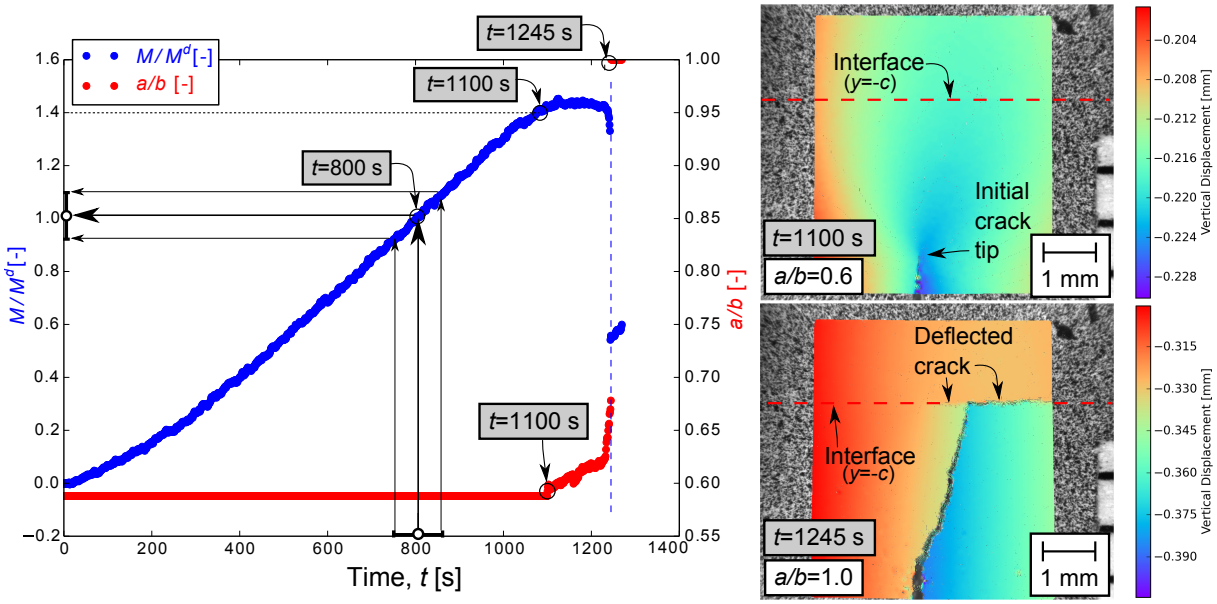

Figure 7. Left: Graph showing normalized moment and relative crack length as a function of elapsed time, t. The vertical blue dashed line indicates the time where the interface crack is fully developed. Right: DIC contour plot of the vertical y-displacement. The top contour plot is at time, $t = 1100$ s and the bottom contour plot is at time, $t = 1245$ s, just after the interface crack is fully developed. The red dashed line indicate the interface location.

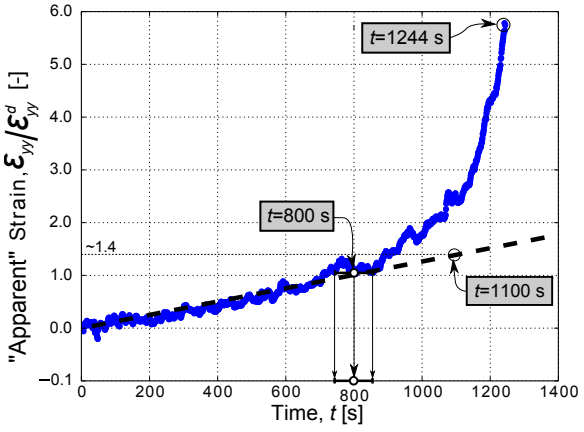

Figure 8. DIC: Normalized "apparent" strain, $\epsilon_{yy}/\epsilon^d_{yy}$, shown as a function of time. The "apparent" strain, ϵ_{yy} is normalized by the value of the "apparent" strain at the onset of non-linearity, ϵ^d_{yy}. The interface is located at $y = -c$, according to figure 3.

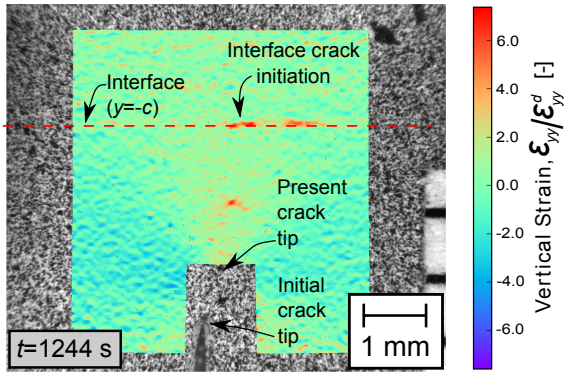

Figure 9. DIC: Contour plot of the vertical strain, normalized by the "apparent" strain at the onset of non-linearity, ϵ^d_{yy}, just before the main crack grows to the interface ($t = 1244$ s). The initiation of the interface crack is clearly identified. The interface is located at $y = -c$ according to figure 3.

The cohesive strength of the interface is determined by using an finite-element model (Section 3.1) to calculate the value of the normal stress across the interface at the conditions under which the onset of a non-linear strain were observed. It is estimated that the time of transition from linear to non-linear strain at the interface can be identified to an accuracy of ± 50 s, the pre-crack length can be measured to an accuracy of $a_0/b \pm 1\%$, and other uncertainties are indicated by error bars in figure 7. As discussed earlier, the material properties that entered into this calculation are confidential information. However, the calculations result in a cohesive strength for the interface of:

$$\hat{\sigma}/\bar{\sigma}_g = 0.081 \pm 0.007 \tag{1}$$

Again, owing to the confidential nature of the system, the cohesive strength has been normalized with the macroscopic strength of the glue, $\bar{\sigma}_g$, which was obtained by a uni-directional tensile test of a dog bone specimen with a gauge length of 115 mm. It would be more appropriate to normalize with the cohesive strength of the glue, but this is not known.

5. Discussion

The cohesive strength can be determined with ESEM using a *J*-integral based approach [6]. This approach requires manufacturing tiny specimens and using specialized and expensive equipment, such as a special fracture mechanics loading stage for ESEM. A benchmark of the new approach with the ESEM and the *J*-integral based approach is proposed as a future study.

One of the advantages with the new approach presented in this paper is that there is no need to use advanced scanning-electron microscope equipment, since a standard 4 point bend rig with a DIC camera system can solve the task. During the last decade DIC has become a relatively easy, cheap, and efficient tool for measuring in-plane deformations, and it is available in most labs at universities [13]. The new approach is not limited to the 4-point SENB specimen, but it can be used with any other test specimen, provided that the interface crack initiation can be captured by DIC and the interface stress can be accurately determined using a model (*e.g.* FE or analytical).

The cohesive strength at the interface is extracted in the symmetry line ($x = 0$, $y = -c$) of the SENB specimen where the shear stress is zero and therefore the crack initiation is mode-I. If the interface crack initiates at other locations along the interface, *e.g.* due to a defect, the crack initiation will be mixed mode. This is also confirmed by the FE model.

It is beneficial that the interface crack initiates before the main crack starts to propagate so that the growth of the main crack does not change the strain field. For an interface cohesive law with a high $\hat{\sigma}$ it may not be possible to initiate the interface crack, but maybe the test specimen could be optimized further in the future to enable this. Another design of the test specimen to determine the cohesive strength could be a SENB geometry with an elliptical notch. The advantage of this geometry is that the stress concentration factor would be known, and it will be harder for the main crack to start growing. This might simplify the analysis. An analysis similar to that of Cook and Gordon [1] could then be used to determine the optimum distance from notch to interface.

6. Conclusion

It can be concluded that the mode-I cohesive strength can be determined using a 4-point SENB test specimen in combination with 2D DIC measurements and linear-elastic finite element modeling. For the material system tested, a normalized cohesive strength is determined to $\hat{\sigma}/\bar{\sigma}_g = 0.081 \pm 0.007$, meaning that the interface cohesive strength is about 0.08 of the macroscopic strength of the glue.

Acknowledgments
Thanks to the LM Wind Power lab for help manufacturing the test specimens and to Fulbright for supporting the research stay at the University of Michigan. Special thanks to James Gorman for his help when conducting the experiments in the lab at the Department of Mechanical Engineering, University of Michigan, Ann Arbor, MI, USA. This research was supported by the Danish Centre for Composite Structure and Materials for Wind Turbines (DCCSM), grant no. 09-067212, from the Danish Strategic Research Council (DSF).

References
[1] Cook J and Gordon J E 1964 *Proc. R. Soc. Lond. A.* **10** 508
[2] He M Y and Hutchinson J W 1989 *Int. J. Solids Structures* **25** 1053
[3] Thouless M D, Cao H C and Mataga P A 1989 *J. Matls. Sci.* **24** 1406
[4] He M Y, Evans A G and Hutchinson J W 1994 *Int. J. Solids Structures* **31** 3443
[5] Parmigiani J P and Thouless M D 2006 *J. Mech. Phys. Solids* **54** 266
[6] Goutianos S, Arevalo R, Sørensen B F and Peijs T 2014 *Appl. Compos. Mater.* **21** 805
[7] Li V C and Ward R J 1989 *Fracture Toughness and Fracture Energy, Mihashi et al. (eds).* 183
[8] Suo Z, Bao G and Fan B 1992 *J. Mech. and Phys. Solids.* **40** 1
[9] Kendall K 1975 *Proc. R. Soc. Lond. A.* **344** 287
[10] Lee W and Clegg W J 1996 *Key Engineering Materials* **116** 193
[11] Tada H, Paris P C and Irwin G R 2000 *The Stress Analysis of Cracks Handbook* 3rd ed (New York: ASME Press)
[12] Crammond G, Boyd S W and Dulieu-Barton J M 2013 *Optics and Lasers in Engineering* **51** 1368
[13] Reedlun B, Daly S, Hector L, Zavattieri P and Shaw J 2013 *Experimental Techniques* **37** 62

$\sqrt{17}$
$\Omega \int \delta e^{i\pi} = -1$
{2.7182818284}
ϑφερτυθιοπσδφγηξκλ
χ^2
$\sum$